SILICIC ERUPTIVE TRANSITIONS OF LAGUNA DEL MAULE

CLAUDIO IGNACIO CONTRERAS HIDALGO

SUPERVISORS:

KATHARINE CASHMAN

ALISON RUST

A dissertation submitted to the University of Bristol in accordance with the requirements for award of the degree of Doctor of Philosophy in the Faculty of Science.

SCHOOL OF EARTH SCIENCES

APRIL 2020

Abstract

The understanding of silicic eruptive transitions is key to mitigating the potential hazards of future eruptions. The diversity of rhyolitic eruptive products formed during a single eruption phase in the Laguna del Maule volcanic complex (LdM) allows the study of the factors governing the eruptive transitions. In this thesis, the reconstruction of the eruption histories, the processes preluding the transitions to effusive phases, the magma permeabilities, and the magmatic storage and ascent conditions are studied for the two first (Laguna del Maule and Los Espejos) and the youngest (Las Nieblas) postglacial rhyolites of LdM. The rhyolite of Laguna del Maule is the most voluminous rhyolitic deposit formed during a high explosive eruption due to the interaction of silicic melts with deeper and hotter mafic-to-intermediate magmas. The younger rhyolites did not interact with mafic magmas and were formed during smaller eruptions. The rhyolite of Los Espejos (*rle*) began with a phreatomagmatic phase followed by a subplinian magmatic eruption which formed a fall deposit which has dense pumices and vesicular obsidian clasts before the transition to an effusive stage. The permeability of the *rle* pumices is high ($>10^{-12}$ m^2) due to their high anisotropy and the localization of the degassing in some wide and elongate bubbles. The permeability localization allowed effective outgassing despite the increasing bubble collapse and densification of magma during ascent. The effective outgassing together with a high total strain and a decrease of the magma ascent rate during the late stage of the subplinian eruption promoted the transition to the effusive phase. Unlike *rle*, the explosive-effusive transition of Las Nieblas (*rln*) eruption was promoted by a rapid decrease of the magma ascent rate based on the glassy groundmass of the obsidian lavas.

Dedication

To Antonia and Santiago, who give me motivation and inspiration to complete this project. Just hearing your voices or looking your faces reloaded my energy to start a new day.

Florencia, thanks for your constant support. We have made many crazy things together. I am sure that other many crazy things are still waiting for us.

I must thank to Kathy Cashman and Alison Rust, my supervisors, for all the support, patience, effort and dedication. I gave them many difficulties during this period. I did not realize (I could not) how difficult was to focus on my thesis while a big part of my mind was looking forward to my family many miles away. Probably, they knew better than me how I really was. I wish to become a better scientist after this period, but certainly I am a better person now. And many thanks for your confidence in me.

Thanks go to the bristolian-latinamerican-multicultural community that I met here in Bristol. Specially, in order of appearance: Irving, Maryory, Juan, Eduardo, Philipp and Julie.

Thanks go to Osvaldo, Víctor, Dani, Javier, Gisela, Fernanda, Gabriel, Catalina, Esteban, Mario, Ximena, Alicia, Pascual, Marianela, Roberto, Soledad, Cecilia, Drina, Octavio and many others who were like unconditional and loyal fans.

To my mum who taught me that nothing is impossible.

Dad, grandma, we're just three lost souls swimming in a fish bowl year after year.

Acknowledgments

This work was supported by Becas Chile PhD scholarship [grant number 72160339 CC]. Thanks go to Luis Torres, local authority of Laguna del Maule, for his assistance on logistics and boat trips; to Barbara Buono-Core, Carolina Geoffroy, Rayen Gho, Christian Pizarro and Florencia Rosas, students of University of Chile, for their assistance in field; to Marcelo Cortés for the use of the He-pycnometer in SERNAGEOMIN; to Chris Pangalos and Charles Clapham for the design and fruitful conversations about the permeability measurements; to Tom Davies for his helpful assistance in the use of the X-ray tomography and the softwares for imaging processing; to Stuart Kearns and Ben Buse for their assistance and guidance with microprobe analysis; to Ángelo Castruccio, Judy Fierstein, Miguel Ángel Parada, Jenny Riker, and Stephen Sparks for her fruitful comments about the volcanic field and fundamentals of volcanic systems; and to my thesis examiners, Prof. Jon Blundy and Dr. Sebastian Watt, for their comments and suggestions which improved this work.

Author’s declaration

I declare that the work in this dissertation was carried out in accordance with the requirements of the University's *Regulations and Code of Practice for Research Degree Programmes* and that it has not been submitted for any other academic award. Except where indicated by specific reference in the text, the work is the candidate's own work. Work done in collaboration with, or with the assistance of, others, is indicated as such. Any views expressed in the dissertation are those of the author.

SIGNED: DATE: 15th April 2020

Contents

List of Tables

List of figures

1. Introduction

The hazards related to silicic volcanic eruptions depend on the eruptive styles. Explosive eruptions can be deadly and can affect infrastructure and agriculture near a volcano due to the ash fall from eruptive columns (Fig. 1.1a) and pyroclastic flows (Fig. 1.1b). More distally, the dispersion of volcanic ash (Fig. 1.1c) and aerosols may affect air traffic, air quality or even change the climate conditions for years. On the other hand, silicic effusive eruptions form lava flows (Fig. 1.1d) and have only relatively minor local effects unless they trigger density currents (e.g. block and ash flows). Despite advances in volcanic monitoring, mitigation of volcanic hazards is still challenging due to the difficulties in predicting the timing and style of volcanic eruptions. Even once an eruption has started, there can be rapid transitions in the eruption style (e.g. convective column, pyroclastic density current, effusion of lava), and thus shifts in the associated hazards.

In silicic eruption sequences, transitions in eruption style are mostly dictated by two factors which are commonly combined: the magma ascent rate and the efficiency of outgassing (Cassidy et al., 2018; Fig. 1.2). The most explosive eruptions are associated with limited outgassing and fast magma ascent (e.g., Bouvet de Maisonneuve et al., 2009). As the magma ascent rate is dynamic, the high explosivity in silicic eruptions is usually transient. However, rapid decompression may keep or increase the eruption intensity (e.g., Mt. St. Helens, 1980, in Endo et al., 1981; Eyjafjallajökull, 2010, in Tarasewicz et al., 2012). The transition from explosive eruptions into an effusive phase is commonly attributed to an increase in the efficiency of outgassing accompanying a decrease of the magma ascent rate (e.g., Chaitén, 2008, in Castro and Dingwell, 2009). As very few rhyolitic eruptions have been witnessed and monitored, however, establishing the histories of previous volcanic events is key to understanding the potential hazards of the possible future eruptions.

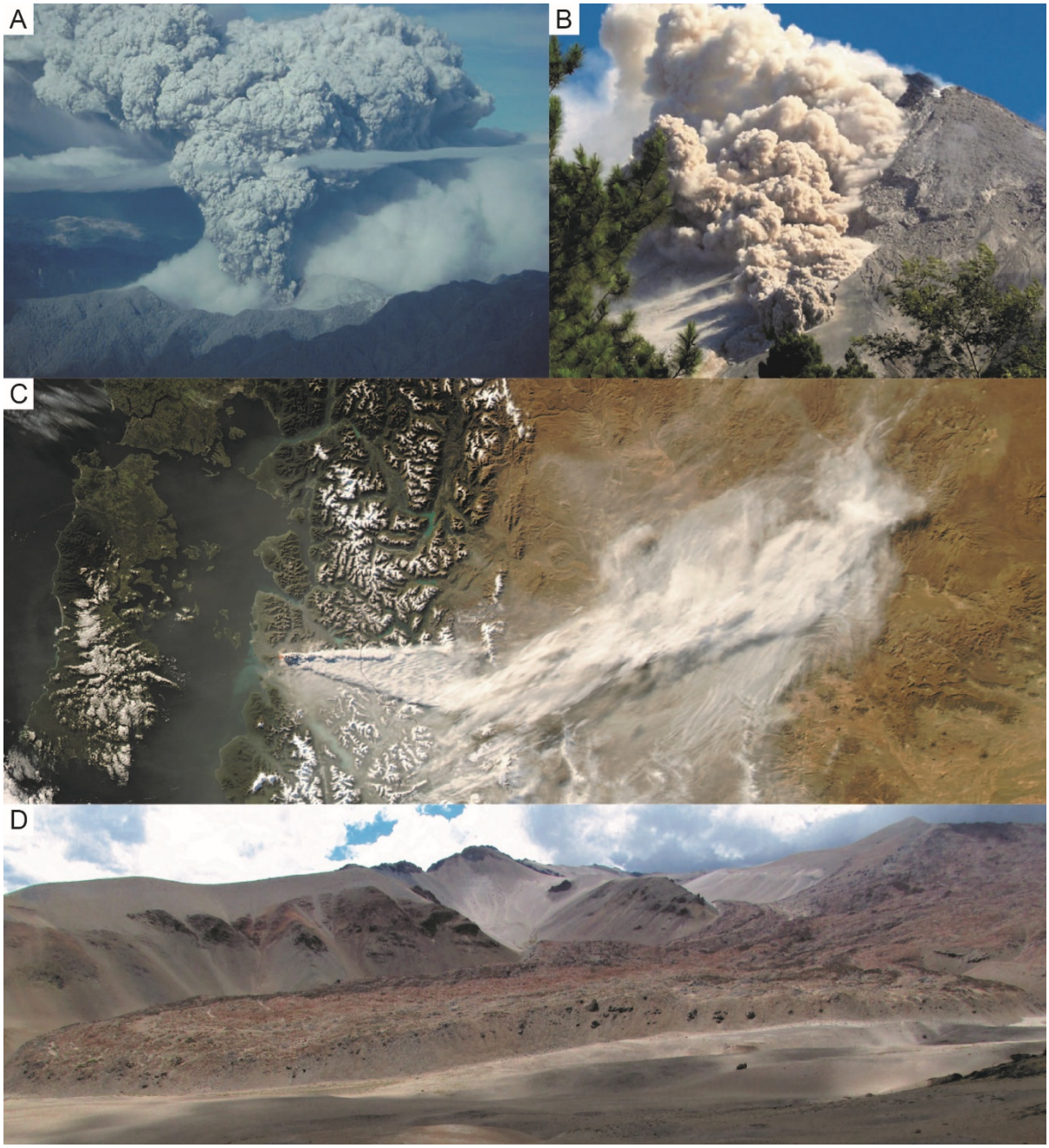

Fig. 1.1: A summary of silicic eruptive styles and their effects in proximal and distal areas. **A** The formation of an eruptive column during the paroxysm of an explosive eruption. Photograph of the 2008 eruption in Chaitén, Chile, ~150 km from vent taken by René P. Fuchslocher and published by emol.com. **B** A pyroclastic flow from the 2006 eruption of Merapi, Indonesia (Report on Merapi, Indonesia, 2007). **C** Satellite image of the ash dispersion from the 2008 Chaitén eruption, Chile (earthobservatory.nasa.gov). **D** Rhyolite lava flow of Cari Launa from the Laguna del Maule volcanic complex, Chile (this work).

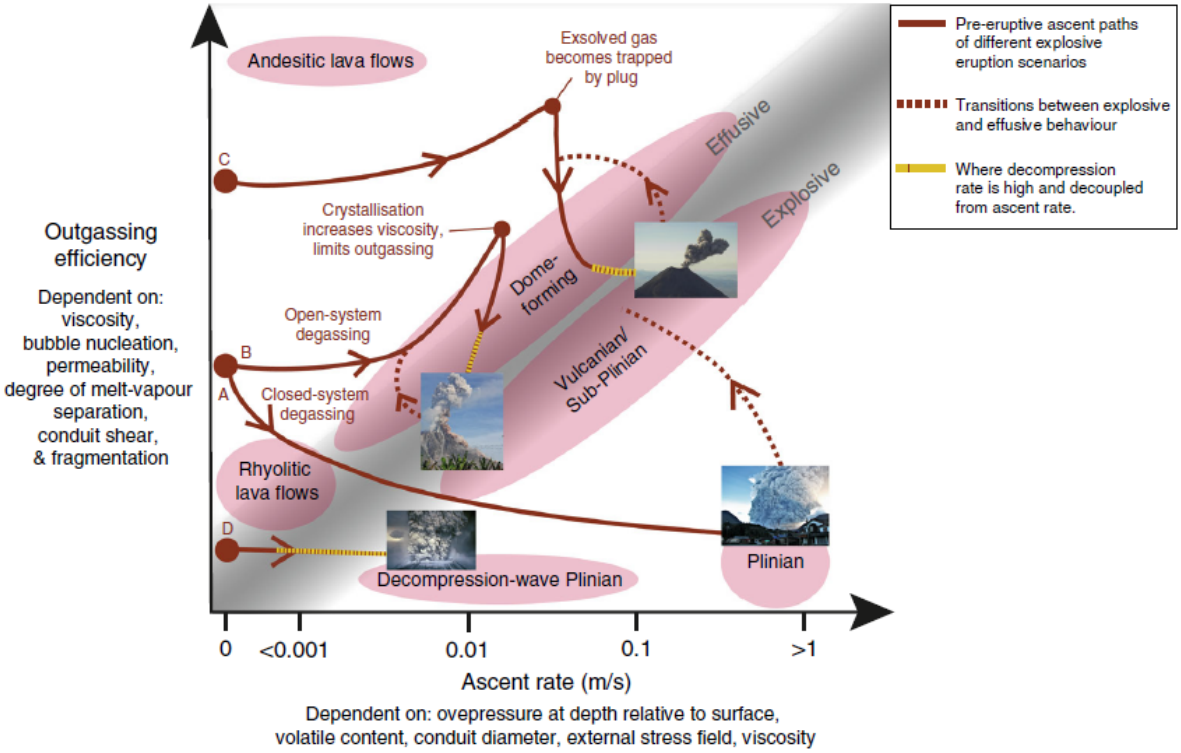

Fig. 1.2: Schematic diagram showing eruption styles and transitions depending on the ascent rate and the outgassing efficiency. Points represent different eruption scenarios, the continuous and dashed red and yellow lines show eruption transitions. From Cassidy et al. (2018).

This thesis focuses on post-glacial rhyolite eruptions of the Laguna del Maule volcanic complex (LdM), Chile. LdM is located 250 km south of Santiago and forms part of the Transitional Southern Volcanic Zone (TSVZ) of the Andes (Fig. 1.3a) which is characterized by an abrupt decrease of the Sr isotopic ratio and a thinner continental crust (~35 km-thick) compared with the northern section (NSVZ; Cembrano and Lara, 2009; Hildreth and Moorbath, 1988; Lopez-Escobar et al., 1995). The stratovolcanoes that form the volcanic arc within both NSVZ and TSVZ commonly erupt dacites to andesites, however, LdM and other caldera systems (e.g., Maipo, Calabozos) occur 20-30 km beyond the volcanic arc and erupt predominantly rhyolites (Fig. 1.3b). In LdM more than 20 rhyolitic eruptive units and the wide diversity of volcanic deposits formed in the last 25 ky allow study of a range of silicic eruption styles and transitions from a single system. Importantly from a hazard perspective, the different rhyolitic eruptive units do not show the same eruptive sequence and not all have lava flows.

This is an important case study for potential hazards related to silicic eruptions because there has been rapid uplift at LdM in the last decade due to magma and/or fluid accumulation within a silicic magma reservoir (Feigl et al., 2014; Singer et al., 2014). The interest in the origin of the current uplift has resulted in studies of the conditions of the magmatic system below LdM (e.g., Andersen et al., 2017) and the physical characteristics of the magma body producing the current uplift (e.g., Miller et al., 2017). However, very few studies of the physical characteristics of the deposits, and these are mostly focused on the lava flows (e.g., Cáceres et al., 2018; Hildreth et al., 2010).

This thesis studies the pyroclastic deposits and physical properties of silicic juvenile clasts from three rhyolite eruptive units. The selected rhyolite eruptive units are the two first and most silicic of the postglacial stage (Fig. 1.3c), the rhyolites of Laguna del Maule (*rdm*; 23 ky in Andersen et al., 2017) and Los Espejos (*rle*; 19 ky in Singer et al., 2000), and the youngest rhyolite of LdM, Las Nieblas (*rln*; 1.8 ky in Fierstein, 2018). The rhyolite of Laguna del Maule is selected because is the most voluminous postglacial volcanic deposit (>20 km^3; Fierstein, 2018), is the only rhyolitic eruptive unit having mafic juvenile and granitoid lithic clasts and has no pyroclastic obsidians or lava flows. Unlike the rhyolite of Laguna del Maule, the rhyolite of Los Espejos is smaller (2-5 km^3 of pyroclastic deposits and lava flows; Gho et al., in prep.; Hildreth et al., 2010), has pyroclastic obsidians and the eruptive sequence finishes with a lava flow; the pyroclastic deposits do not have mafic juveniles or granitoid lithics. Finally, the rhyolite of Las Nieblas is less silicic and more alkaline than *rdm* and *rle;* the sequence starts with a pyroclastic density current deposit followed by a co-erupted fall deposit and lava flow, a second lava flow (the biggest of the postglacial stage; Cáceres et al., 2018) and three minor eruptive centers. The current uplift in LdM is just north of the Las Nieblas lava flow (Fig. 1.3c).

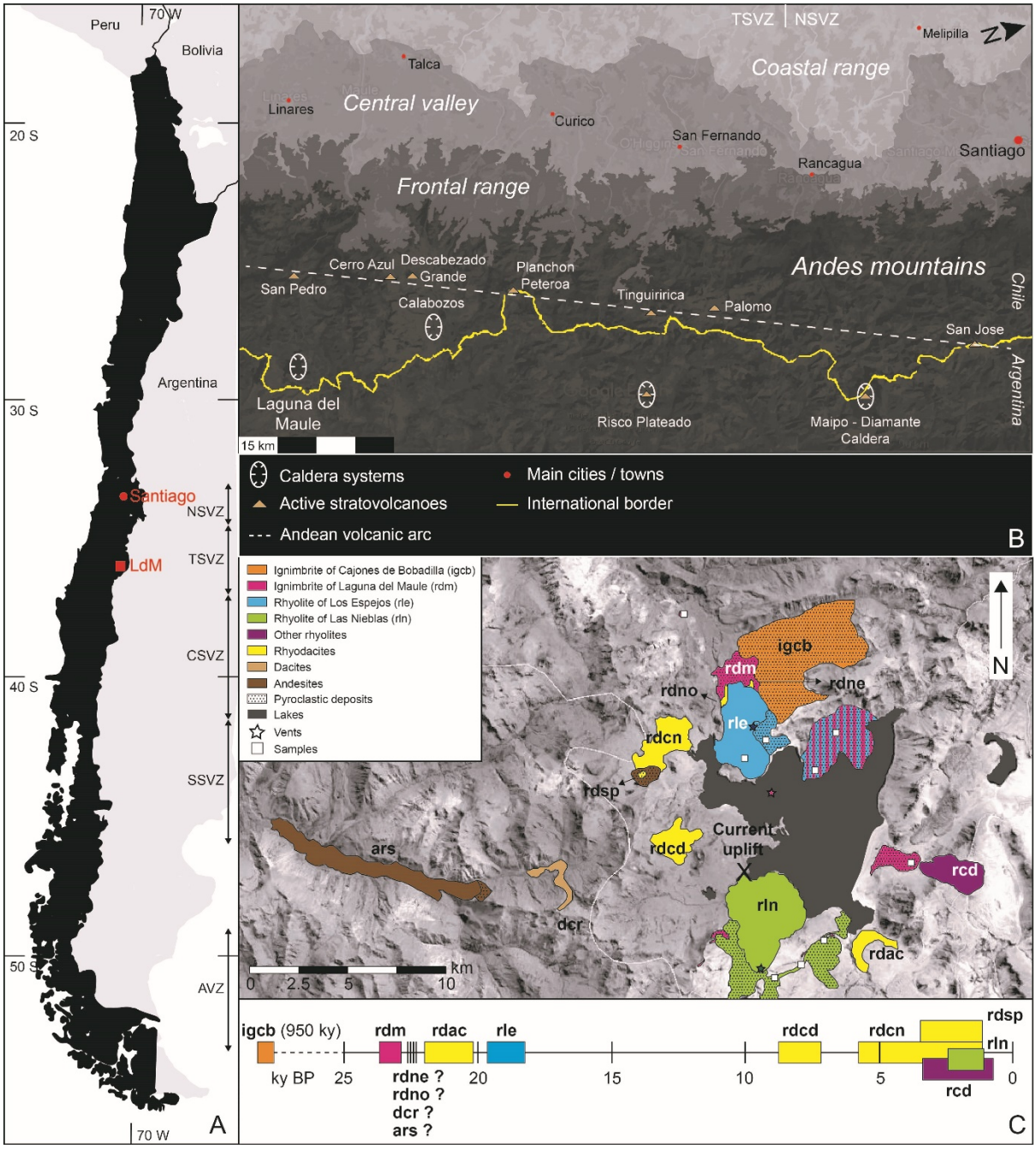

Fig. 1.3: Geological context of the Laguna del Maule volcanic complex. A Map of Chile showing the Andean Southern volcanic zones (SVZ) according to Lopez-Escobar et al. (1995). N- = North; T- = Transitional; C- = Central; S- = South. **B** View on plant of the Central-South Chile showing the main geomorphological units. The volcanic arc consists of stratovolcanoes of intermediate compositions, instead the caldera systems are 10-30 km beyond the arc under a back-arc extensional regime. **C** The Laguna del Maule volcanic complex showing the three rhyolites studied in this thesis. Ages are from Hildreth et al. (2010) and Andersen et al. (2017).

The main goal of this research is to determine the factors governing the transitions in the rhyolitic eruptions of the Laguna del Maule volcanic complex. The main objectives of this thesis are:

1. To characterize the tephrostratigraphy and physical parameters of the rhyolites of Laguna del Maule (*rdm*) and Los Espejos (*rle*) in order to determine stratigraphic subunits.

2. To determine the factors governing the eruption styles and transitions of *rdm* and *rle.*

3. To optimize the X-ray microtomography conditions for imaging the pore structure of silicic pumices.

4. To compare the permeabilities obtained by analytical measurements with those from numerical simulations to understand the factors controlling the permeabilities and the limitations of each approach.

5. To determine the role of bubble textures in the magma permeabilities of the *rdm* and *rle* pumices.

6. To determine the role of the magma permeabilities in the styles and transitions of the *rdm* and *rle* eruptions.

7. To determine the magmatic storage and ascent conditions of the *rdm* and *rle* magmas.

8. To determine the role of the storage and ascent conditions in the eruptive styles and transitions of LdM.

This introduction chapter provides an introduction to the three rhyolite eruptive units studied in this thesis, a general review of the study of silicic eruption transitions, a review of methodologies, and then a geological background and the conditions of the magmatic system below LdM. Finally, I summarize the objectives and results of each chapter of this thesis.

1.1. Chapter 2

1.1.1. The three rhyolite eruptive units studied in this thesis

The three postglacial rhyolite eruption sequences studied as part of this thesis are Laguna del Maule (*rdm*), Los Espejos (*rle*) and Las Nieblas (*rln*). The rhyolite of Laguna del Maule (*rdm*) is the first (23 ky by $^{39}Ar/^{40}Ar$ in Andersen et al., 2017; 16 ky by ^{14}C in Fierstein, 2018), biggest (>20 km^3; Fierstein, 2018) and most silicic (76.4-76.7 wt.% of SiO_2; "rle-ig" in Hildreth et al., 2010) rhyolitic eruption of the postglacial stage and could represent silicic melt segregated from the dacitic mush reservoir (Andersen et al., 2019). *rdm* shows a distinctive componentry: cauliflower-shaped mafic olivine-bearing clasts, massive and reticulated andesitic hornblende-bearing clasts, andesites forming bands with silicic pumices and no obsidian pyroclasts or lava flows (Fierstein, 2018). The *rdm* outcrops are found around the entire lake, always under other postglacial units.

The rhyolite of Los Espejos (*rle*) is the most silicic (75.5-75.7 wt.% of SiO_2) and the first rhyolitic eruption after the rhyolite of Laguna del Maule, with a time gap of ≤4 ka (19 ka by $^{39}Ar/^{40}Ar$; Singer et al., 2000) or 1 ky (15 ka by ^{14}C; Fierstein, 2018). *rle* erupted one of the biggest pyroclastic deposits after *rdm* (~4 km^3; Gho et al., in prep) followed by the third most voluminous (~0.82 km^3) postglacial rhyolitic coulee of LdM. The rle obsidian lavas have plagioclase and biotite phenocrysts, the most common mineral association among the LdM rhyolites. Andersen et al. (2019) suggest that *rle* was produced by remnant rhyolitic magma from *rdm,* based on the similar zircon compositions in both rhyolitic units.

The rhyolite of Las Nieblas (*rln*, 73.0-73.7 wt.% of SiO_2) is the youngest eruption of LdM (1.8 ka BP by ^{14}C; Fierstein, 2018) and erupted ≥1.5 km^3 of a continuous sequence of pyroclastic flows, a synchronic fall deposit and lava flow, and a second lava flow which is the most

voluminous (1.16 km^3) of the postglacial stage. Despite having a similar petrography to *rle*, temperatures estimated by two-oxide thermometry (Andersen et al., 2018) show that *rln* storage conditions were ~30 °C hotter than *rle*.

1.1.2. A brief history of the study of silicic eruptive transitions

Eichelberger and Westrich (1981) proposed that the different styles of an eruption reflect a stratified magma reservoir where a volatile-rich magmatic layer feeds explosive eruptions and a dryer magma portion produces an effusive stage. Later, Eichelberger et al. (1986) suggested that both eruptive styles can come from magmas with the same initial volatile content but experience different degassing histories. Magma degassing requires volatile oversaturation and, thereby, bubble nucleation and growth (Gonnermann and Manga, 2007). With further bubble expansion and shearing, bubbles may coalesce and form connected gas channels (Castro et al., 2012a; Gonnermann and Manga, 2007), making the magma permeable. Pathways for gas escape from magma (outgassing) can also be generated by fracturing of the magma, especially at the margins of the conduit where shear stresses are greatest (Okumura et al., 2009; Papale, 1999). The rate of magma outgassing relative to the rate at which magma ascends can determine the eruptive style (e.g. Cassidy et al., 2018; Degruyter et al., 2010): if the exsolved volatile phase remains coupled to the melt, volatile overpressure may cause magma fragmentation, characteristic of an explosive eruption; on the other hand, if outgassing is efficient, an effusive eruption occurs. Both ductile shearing and brittle fractures may occur in the same time as evidenced by pyroclast-filled fractures (tuffsites) within obsidian lavas (Castro et al., 2012b) and hybrid explosive-effusive activity during the 2012 eruption of Cordón Caulle evidenced by the formation of tube elongate pumices and obsidian lava flows (Schipper et al., 2013).

1.1.3. Pumice porosity and bubble textures

As the magma degassing depends on the porosity and pore framework of the ascending magma, pumice porosity and bubble textures are related to the volatile exsolution and outgassing processes during magma ascent. In this way, the analysis and interpretation of pyroclast bubble textures give insights into the dynamics of the eruptions that generated them (e.g., Alfano et al., 2012). Pumice porosity can be related to the intensity and style of explosive eruptions. For instance, pumice clasts from Plinian eruptions are usually of high porosity (> 0.75) with narrow ranges (0.15 - 0.25) due to the inefficient magma outgassing during these eruptions (e.g., Gonnermann et al., 2017). By contrast, pumices from pulsatory subplinian, pyroclastic flow-forming and vulcanian eruptions may have intermediate average porosities (~0.5) with broader ranges (0.25 - 0.40) due to their pulsatory styles (each magma pulse may have its own vesicularity) and more efficient outgassing (e.g., Mueller et al., 2011). The interaction of water with magma during phreatomagmatic eruptions means that the resulting fragments can have even lower bubble volume fractions with wider ranges than dry vulcanian eruptions (Houghton et al., 2010).

The bubble number density is the number of bubbles in a unit of area (N_A) or volume (N_V) of magma. As the bubbles may expand using the space of the silicic melt, but not deform the previously formed phenocrysts, the number of bubbles is usually normalized by the area of volcanic glass not including the area used by phenocrysts or bubbles. The bubble number density can be linked to the magma decompression rates in explosive eruptions by considering the silica and water contents in magma (Toramaru, 2006). In this way, pumices from more intense eruptions (e.g., Plinian) should show a higher bubble number density than the pumices from more pulsatory eruptions (e.g., subplinian or vulcanian) due to a common late-stage vesiculation that enhances magma buoyancy (Alfano et al., 2012). However, this model assumes a regime of homogeneous nucleation and constant rates of decompression and

therefore should be considered as a comparative tool only. For a set of samples, the bubble number density can be analyzed together with the pumice density to determine the factors controlling bubble formation (e.g., Rotella et al., 2014). For a constant pumice density, if N_A increases the bubble formation was dominated by bubble nucleation, or by contrast, if N_A decreases the bubble formation was dominated by coalescence. Where N_A is constant for a range of pumice densities, the bubble formation was dominated by bubble growth (Fig. 1.4). In this way, the bubble formation can be determined by a combination of nucleation, growth or coalescence according to the trends of N_A with density.

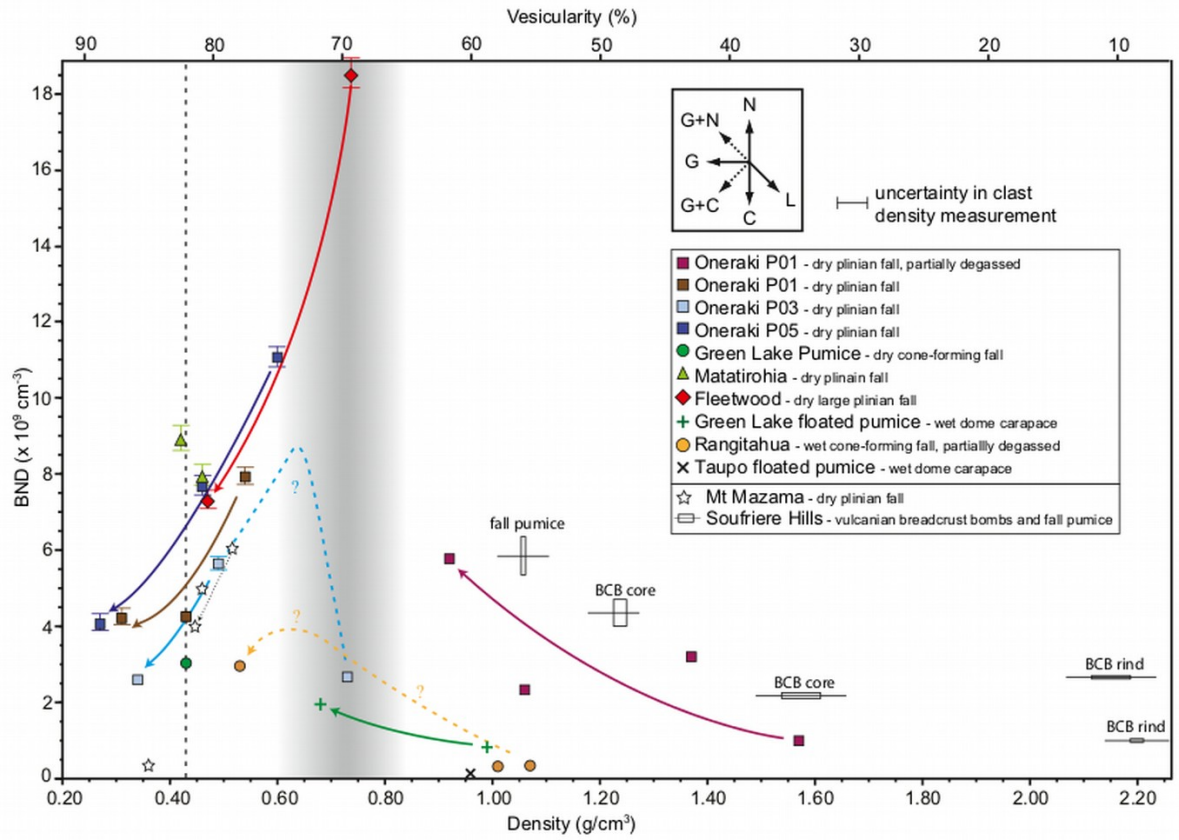

Fig. 1.4: Bubble number density (BND) versus juvenile density (bottom axis) and vesicularity (top axis). The arrows relate samples from the same volcanic layer. In the case of dotted arrows, they link samples from the same pyroclastic layer. The graph at the top represents vesiculation trends as: N, nucleation; G+N, growth and nucleation; G, growth; G+C, growth and coalescence; C, coalescence; L, vesicle loss. Figure from Rotella et al. (2014).

Bubble size distributions compare the number density or volume fraction per bubble size (see a review in Shea et al., 2010). The bubble size can be considered as the long or short axes of

the bubbles or as the equivalent diameter of a circle (in 2D) or a sphere (in 3D). To prevent biasing the size distributions by the selection of a bin size, the data can be plotted as cumulative distributions. Trends and local inflections of the curvature in the cumulative distributions of bubble number density or volume fraction may represent a range of vesiculation processes (rows B and D in Fig. 1.5). For instance, a single stage of nucleation and growth produces a concave curve in the logarithm cumulative number density (Log N > L) vs bubble size (L) plot and a short sigmoidal curve in the cumulative volume fraction (Vf > L) vs bubble size plot. Bubble coalescence causes a straighter curve for Log N > L and a local inflection around the bigger bubbles for Vf > L. By contrast, bubble collapse produces a stretched sigmoidal curve in both Log N > L and Vf > L plot. 2D textural data can be converted to 3D by considering that the bubbles are spherical and other stereological assumptions (e.g., Higgins, 2002; Sahagian and Proussevitch, 1998). I did not use this approach in this thesis because of the bias of this numerical approach on the textural analysis of highly deformed bubbles, and on the resulting interpretations.

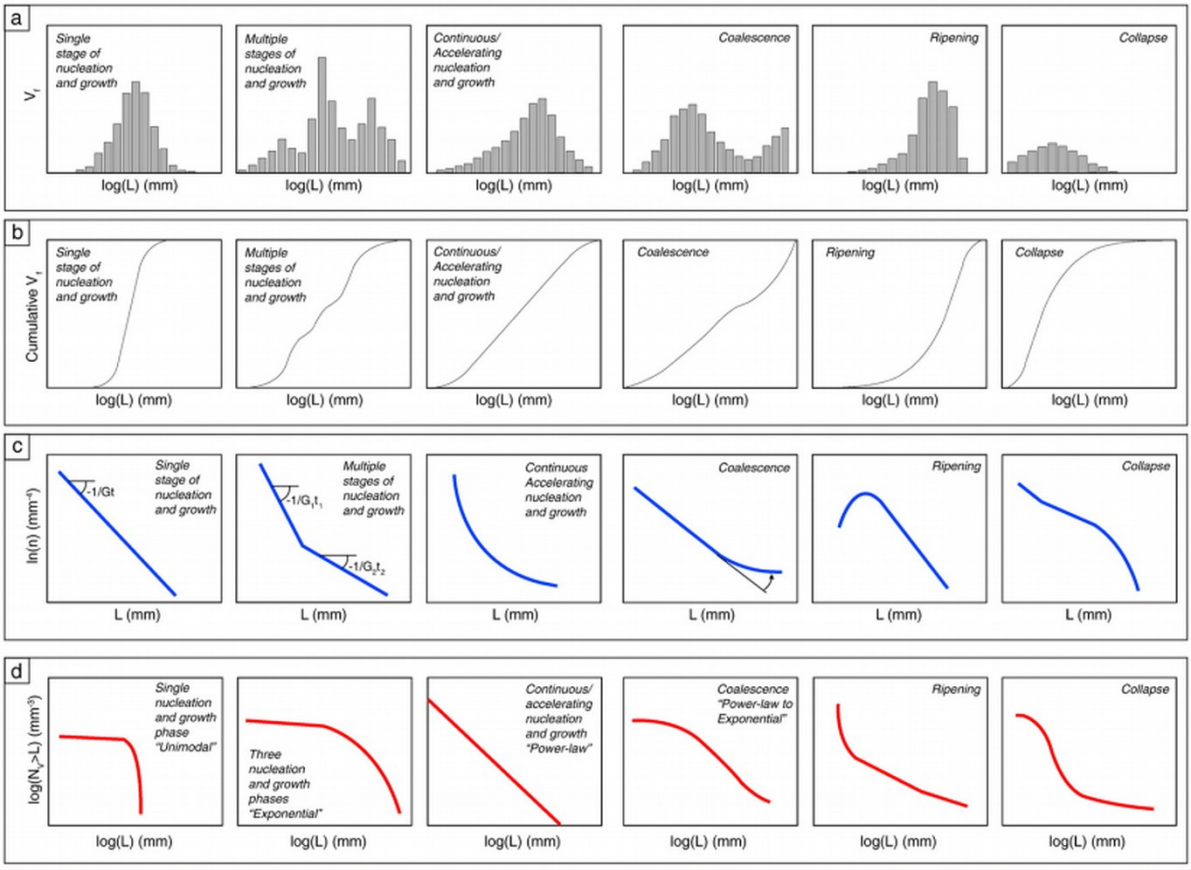

Fig. 1.5: Bubble size distributions (BSD) for various events of vesiculation. The data is represented in different diagrams as **A** volume fraction per bubble size, **B** cumulative volume fraction with bubble size, **C** logarithm of the bubble number density per bubble size, **D** logarithm of the cumulative bubble number density with bubble size. In this thesis I use the plots in **B** and **D** to avoid the bias of the selection of size intervals for the histograms in **A** and **C**. In this figure from Shea et al. (2010), the vesiculation processes plotted are a single nucleation and growth stage, multiple stages of nucleation and growth, continuous accelerating nucleation and growth, bubble coalescence, ripening, and collapse.

1.2. Chapter 3

1.2.1. Application of X-ray tomography analyses to Earth sciences

The analysis of sizes and shapes of crystals, bubbles and pyroclasts has been the objective of petrological and volcanic studies (e.g., Cashman and Marsh, 1988; Liu et al., 2015; Mastrolorenzo and Pappalardo, 2006; Shea and Hammer, 2013). These textural parameters are usually analyzed from 2D images obtained by optical and back-scattered electron microscopes. If all the components have the same shape and convex surfaces, and assuming a fabric index and object cutting probabilities, stereological models can convert the 2D textural data into

corrected 3D datasets (Higgins, 2002; Sahagian and Proussevitch, 1998). A first approach to measure 3D textural parameters was based on a serial sectioning, which required the analysis of several thin sections and the interpolation of components. This supposed the absence of smaller components than the distance between parallel sections (Mock and Jerram, 2005). X-ray tomography systems, in contrast, allow us to obtain a full 3D volume from a set of radiograms (2D images) which are reconstructed by using specialized algorithms (Cnudde and Boone, 2013). Despite the quick performance and the non-destruction of the sample, the application of the X-ray tomography analysis to igneous rocks is recent because of the limited availability of tomographic imaging equipment (e.g., Brown et al., 1999; Ketcham and Carlson, 2001).

There are two types of X-ray tomography systems usually applied to igneous rocks: conventional or tube X-ray tomography and the synchrotron X-ray tomography. The former applies a single beam with polychromatic spectra from a source with tube geometry; while the latter applies a dual beam with monochromatic spectra from a source with plane geometry (Baker et al., 2012). Despite the physical differences between these two systems, the resulting image resolution and imaging artifacts are similar (Baker et al., 2012; Cnudde and Boone, 2013). For instance, both kind of systems can cause ring artifacts that appear as blurry rings at the center of the reconstructed volumes due to problems in the X-ray target, (Cnudde and Boone, 2013; Ketcham and Carlson, 2001). However, the conventional X-ray tomography may present a beam hardening artifact because the low-energy X-rays have a higher probability of being absorbed than high-energy X-rays as it applies a polychromatic spectrum (Cnudde and Boone, 2013). When the beam hardening is high, the tomograms show a higher attenuation coefficient towards the sample rim, or visually, the sample is brighter towards the rim (Ketcham and Carlson, 2001). The X-ray tomography technique applies an X-ray beam to the object to obtain a 3D gray-scale image (tomogram) based on the linear attenuation coefficient,

a function of the atomic number, the sample density and the X-ray energy (Ketcham, 2005; Rivers et al., 1999; Sutton et al., 2002). The first two properties are intrinsic of the sample, but the latter depends on the applied conditions by the user; as a decreasing voltage broadens the difference of the linear attenuation coefficient between different minerals (Fig. 1.6), the image contrast (the capability to separate objects of different composition) may be improved by the user.

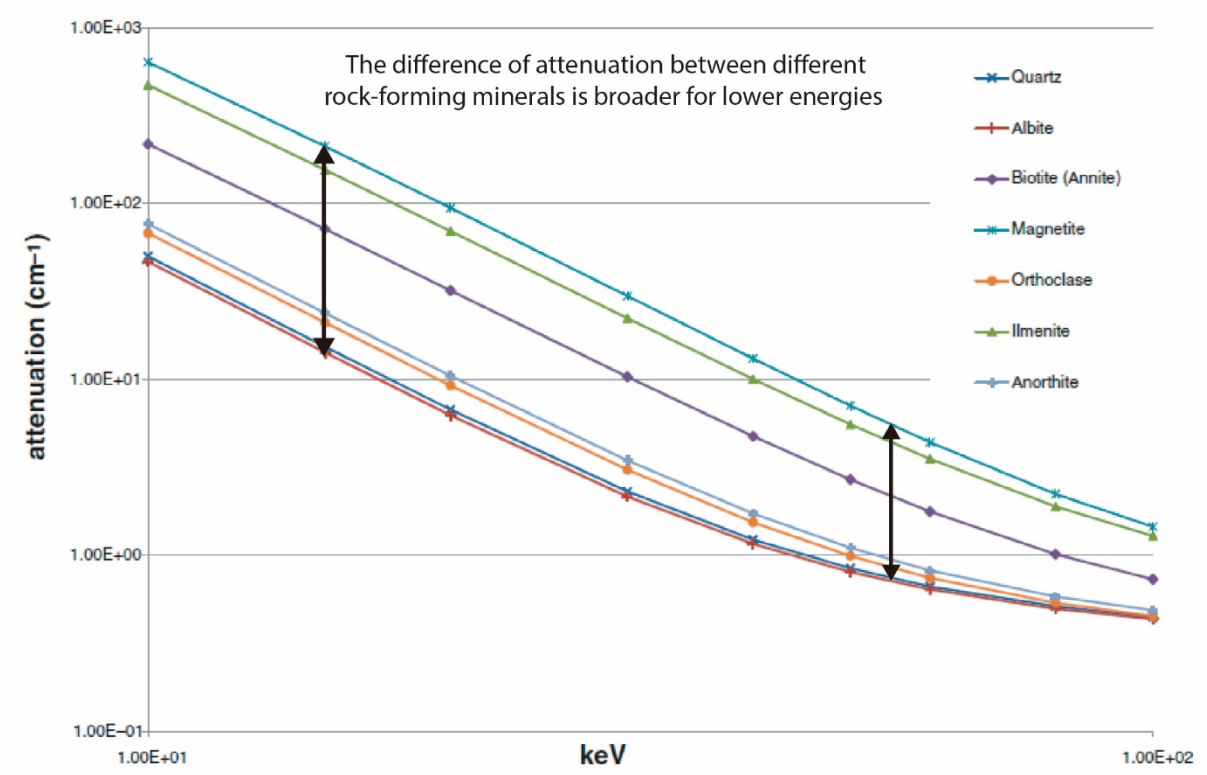

Fig. 1.6: Energy-dependent attenuation coefficient for several rock-forming minerals obtained by X-ray tomography. The attenuation coefficient is high in the oxides (magnetite and ilmenite), intermediate in the mafic silicates (biotite) and low in the felsic silicates (anorthite, orthoclase, quartz and albite). As a high attenuation coefficient is related to bright objects in the tomograms, the grayscales observed in the granites by the X-ray tomography are like those obtained from BSEM images. A lower energy increases the attenuation coefficient and broadens the difference of attenuation coefficient among the rock-forming minerals. Modified from Boone et al. (2011).

1.3. Chapter 4

1.3.1. Recent rhyolitic explosive eruptions in Chile

The 2008 subplinian eruption of Chaitén was unexpected. Prior to the eruption, Chaitén was known as a "Hill" but not as a "Volcano" as it was believed that it had not erupted for several thousands of years (Mandujano and Rodríguez, 2016). Additionally, the onset of volcanic activity was rapid as it appeared only within ~36 hours after the first felt earthquake (Castro and Dingwell, 2009). The eruption started with ash emissions that lasted one day and were followed by explosive activity which produced a 13-16 km-height eruption column over 6 hours (Alfano et al., 2011). The eruption intensity decreased the three following days and was characterized by several explosive events with different intensities and durations, which formed an eruption column of ~10 km. The climactic phase occurred on the sixth day, when the eruption column reached 20 km, producing a fall deposit which consists of 80% of silicic lithics, 10% of pumice, and 10% of fresh obsidian. The pumice clasts are rhyolitic (73-76 wt.% SiO_2), almost aphyric and have a low and limited range of densities (Alfano et al., 2012; Castro and Dingwell, 2009). Textural analyses reveal that magma vesiculation was late due to a fast magma ascent. After two days, activity shifted with dome collapse and lateral blasts accompanied by minor explosive events (Castro et al., 2012b).

Unlike the 2008 Chaitén eruption, seismic activity was reported during two months before the onset of the 2011 Cordón Caulle eruption (Pistolesi et al., 2015). The eruption began with sustained activity characterized by an eruption column 10-12 km-high which lasted 24-30 hours. This climactic phase produced coarse layers which consist of >70% low-density pumice and 5-25% altered clasts. Most pumice clasts are 400 kg m^{-3} but the juvenile density distribution show a large tail of denser clasts characterized by banded pumices, dense juveniles and obsidians (Pistolesi et al., 2015). The low-density pumice clasts are isotropic with nearly

spherical bubbles; in contrast, the denser pumice have heterogeneous bubble textures and evidence of strain localization. The eruption intensity then decreased, and the volcanic activity became pulsatory, characterized by at least five partial collapses of the eruption column to produce PDCs. On the third day the eruption intensity decreased further, producing fall deposits with 30% fresh obsidians. Later explosive activity was pulsatory and characterized by ash emissions. Sixteen days after the onset of the Cordón Caulle eruption, the emission of obsidian lava started (Tuffen et al., 2013). Like the 2008 Chaitén eruption, the beginning of the effusive activity was simultaneous with pulses of minor explosive activity which formed coarse ash characterized by elongate tube pumices (Schipper et al., 2013). The anisotropy of the Cordon Caulle pumice clasts allows a high permeability despite of having a wide range of porosities.

1.3.2. Magma permeabilities

The porosity and permeability of vesiculated volcanic rocks control the efficiency of magma degassing during magma ascent (Degruyter et al., 2010). The relationship between porosity and permeability depends on the history of deformation, decompression, degassing and crystallinity of magma. Magmas of low crystallinity and low porosity can be effectively impermeable. If the bubbles expand and coalesce, the pore connectivities in magmas may increase. Gas can escape from magma ("open-system degassing" or "outgassing") if the porosity exceeds the percolation threshold. The percolation threshold is defined as the critical porosity to consider a volcanic rock as a permeable material (Rust and Cashman, 2004), is variable among different materials, and depends on the pore framework (Burgisser et al., 2017). Importantly bubble deformation during decompression can decrease this critical porosity (Rust and Cashman, 2004).

During effusive eruptions there is open-system degassing whereby exsolved volatiles escape from melt through permeable magmas (Gonnermann and Manga, 2007). During Plinian and

subplinian eruptions, in contrast, magmas degas like closed systems, bubbles remain coupled to the melt, volatiles within bubbles overpressure and the fragmentation threshold is reached (Gonnermann and Manga, 2007). In this way, the relationship between the magma permeability and porosity is related to the eruption style. Most pumices from Plinian and steady subplinian deposits show a narrow range of high porosities and variable permeabilities (e.g., Bouvet de Maisonneuve et al., 2009; Klug et al., 2002) due to an increasing permeability during bubble expansion (Gonnermann et al., 2017). By contrast, pumices from pulsatory subplinian eruptions show a wide range of porosities and high permeabilities (Schipper et al., 2013) due to a lower volatile pressure which produces partial bubble collapse and a high anisotropy of the fabric clasts (Gonnermann et al., 2017). Magmas can be densified by compaction or by surface tension between melt and gas interfaces depending on the magma decompression rate; thus, a sharp decrease of the magma permeability may be linked with a diminishing porosity (Rust and Cashman, 2004).

1.4. Chapter 5

1.4.1. Petrology of the Laguna del Maule volcanic complex

Recent geophysical studies suggest that below LdM lies a 450 km^3 mush reservoir at ~5 km depth, with an estimated crystal fraction of ~0.95 (Le Mevel et al., 2016; Wespestad et al., 2019). As most of the LdM rhyolites follow similar whole-rock geochemical trends and show subtle variations in trace elements, a rhyolite extraction from ephemeral magma batches within the crystal mush reservoir is suggested (Andersen et al., 2017; Miller et al., 2017). In this way, the subtle differences in two-oxide temperatures and mineral compositions among the LdM rhyolites can be explained by the autonomous storage conditions of the small magma batches that fed each eruption (Cáceres et al., 2018). The LdM eruptions come from several vents distributed within a wide area during the early postglacial and Holocene periods but focused

into one volcanic edifice during the interim period (Hildreth et al., 2010). The wide distribution of the volcanic vents and the occurrence of ephemeral magma batches suggest a lateral mobilization of hot and fertile zones within the mush reservoir (Andersen et al., 2018). The origin of these ephemeral small fertile zones is still unclear because the rhyolites do not show evidences of silicic-mafic magma interactions. Some Ba-spikes in unzoned plagioclase crystals could suggest the input and accumulation of fluids derived from the degassing of deeper magmas (Andersen et al., 2018). Unlike rhyolites, rhyodacites to andesites commonly show mafic enclaves suggesting the interaction of different magma compositions coming from different depths below the mush reservoir (Cáceres et al., 2018; Hildreth et al., 2010). These mafic injections can be a source of heating that produce partial localized melting within the crystal-rich mush or directly ascend to the surface to erupt the few small and distal basalts and basaltic-andesites in Laguna del Maule.

1.5. Thesis overview

This thesis studies the eruptive transitions of the first two, and the most recent postglacial rhyolites of the Laguna del Maule volcanic complex (LdM). The starting point was fieldwork and the reconstruction of the past eruptions from the tephrostratigraphy and the interpretation of physical properties. Subsequent work explored, the roles of ascent and storage conditions on eruption transitions and the longer-term evolution of the system. This thesis is presented in four main chapters:

1. In Chapter 2 I describe the tephrostratigraphy of the Los Espejos pyroclastic deposits and quantify the grain size distributions (GSD), componentry, juvenile densities, and bubble textures to determine the eruption history. Here I determine that the eruption started with a phreatomagmatic eruption with pulses of more phreatic and more magmatic activity. This

phase developed into a subplinian magmatic eruption which formed a fall deposit and some minor PDCs. The fall deposit has dense pumices and vesicular obsidians which increase in abundance with stratigraphic height, suggesting an increasing magma densification before the formation of the subsequent lava flow. For comparison I also analyzed some deposits of the rhyolite of Laguna del Maule eruption sequence, which in addition to silicic pumice, have mafic juveniles and granitoid lithics. In contrast to the Los Espejos sequence, there are no obsidian pyroclasts and there is no lava phase, strengthening the interpretation for Los Espejos that the increasing pyroclastic obsidian component erupted during the subplinian phase was part of the transition to the effusive phase.

2. In Chapter 3 I review the X-ray tomography conditions used in studies related to geosciences. As I did not find a common procedure in the application of the Xray tomography conditions, tests of the energy applied, frames per radiogram, exposure time, application of a metal filter, virtual algorithm to reduce beam hardening artefact and ring artefact minimizer were applied to determine their role in the image quality. These tests show that a low energy applied, and a moderate beam hardening filter, improve the image quality and the definition of small objects within the samples. I present bubble textural analyses in silicic pumices of a range of compositions to show how the X-ray tomography conditions may affect the results, and consequently, the interpretations of volcanic processes. I present a detailed procedure to optimize the acquired image quality from X-ray tomography. These conditions are applied for simulations of the viscous permeability through the porous media of silicic pumices in Chapter 4.

3. In Chapter 4 I measure the porosities (total and connected), and permeabilities (viscous and inertial) of pumices from *rdm* and *rle*. To understand how the bubble framework is controlling magma permeability, I select five representative samples to scan in the X-ray tomography.

Based on segmented binary images from the X-ray tomograms, simulations of gas flow through the porous media of pumices were developed to obtain the viscous permeability and to visualize the flow pathways. The X-ray tomograms show that the *rdm* and *rle* pumices are anisotropic and have elongate and oriented bubbles. While the most porous pumices show a homogeneous distribution of the pore apertures, the least porous pumices have <10 wide and straight bubbles per cubic millimeter and thousands of small flattened bubbles with irregular cross-sectional shapes. The permeability simulations show that the degassing is localized in the most elongate and straightest vesicles, regardless of the porosity of the rest of porous medium; this explains the consistently high permeabilities of the Los Espejos pumice clasts despite their variable total and connected porosities. In this chapter I concluded that permeability localization together with decreasing magma ascent rate promote magma densification and the formation of both pyroclastic and lava flow obsidians.

4. In Chapter 5 I describe the crystal textures and the groundmass glass and mineral composition of pumices and pyroclastic and lava obsidians from *rdm*, *rle* and *rln*. Constraints of temperature, pressure and water contents are estimated by the application of mono-mineral, two-mineral and mineral-glass thermometry, barometry and hygrometry methods. After determination of the initial composition forming the silicic magmas, the storage conditions of the *rdm*, *rle* and *rln* magmas are determined. The storage conditions are used as the initial and boundary conditions to simulate the conditions of magma decompression (ascent). Here I found that the samples from the upper sequence of *rdm* ascended at a temperature tens of degrees over the liquidus due to the heating produced by the mafic magmas, whereas the *rle* and *rln* magma erupted at sub-liquidus temperatures. During the effusive stage the *rle* magmas were 10-15 °C cooler than during the explosive stage, whereas the *rln* magmas did not show variations of temperature. In this way, I concluded that subtle variations of the storage and ascent conditions are key to develop different styles and transitions during silicic eruptions.

5. In the last chapter I summarize the key conclusions and recommend future directions to continue the study of the silicic eruptive transitions and their governing factors in the Laguna del Maule volcanic complex.

The results and interpretations of this thesis are my own research in cooperation with my supervisors. Tom Davies assisted with the acquisition of X-ray tomograms and the segmentation of bubbles within the pumices. The samples of the rhyolites of Las Nieblas were provided by and analyzed with Marcelo Cortés and Dr. Angelo Castruccio from the University of Chile. Eduardo Becerra-Torres, PhD student of the University of Bristol, assisted with the analysis of the whole-rock geochemistry of Laguna del Maule, and guided my first approaches to the MELTS simulations.

References

Alfano, F., Bonadonna, C., Gurioli, L., 2012. Insights into eruption dynamics from textural analysis: the case of the May, 2008, Chaiten eruption. Bulletin of Volcanology 74, 2095-2108.

Alfano, F., Bonadonna, C., Volentik, A. C., Connor, C. B., Watt, S. F., Pyle, D. M., Connor, L. J., 2011. Tephra stratigraphy and eruptive volume of the May, 2008, Chaitén eruption, Chile. Bulletin of Volcanology, 73(5), 613-630.

Andersen, N. L., Singer, B. S., Coble, M. A., 2019. Repeated Rhyolite Eruption from Heterogeneous Hot Zones Embedded Within a Cool, Shallow Magma Reservoir. Journal of Geophysical Research: Solid Earth.

Andersen, N. L., Singer, B. S., Costa, F., Fournelle, J., Herrin, J. S., Fabbro, G. N., 2018. Petrochronologic perspective on rhyolite volcano unrest at Laguna del Maule, Chile. Earth and Planetary Science Letters, 493, 57-70.

Andersen, N.L., Singer, B.S., Jicha, B.R., Beard, B.L., Johnson, C.M., Licciardi, J.M., 2017. Pleistocene to Holocene growth of a large upper crustal rhyolitic magma reservoir beneath the active Laguna del Maule volcanic field, central Chile. Journal of Petrology, 58, 85–114.

Baker, D.R., Mancini, L., Polacci, M., Higgins, M.D., Gualda, G.A.R., Hill, R.J., Rivers, M.L., 2012. An introduction to the application of X-ray microtomography to the three-dimensional study of igneous rocks. Lithos 148, 262-276.

Boone, M., Dewanckele, J., Boone, M., Cnudde, V., Silversmit, G., Van Ranst, E., Jacobs, P., Vincze, L., Van Hoorebeke, L., 2011. Three-dimensional phase separation and identification in granite. Geosphere, 7(1), 79-86.

Bouvet de Maisonneuve, C., Bachmann, O., Burgisser, A., 2009. Characterization of juvenile pyroclasts from the Kos Plateau Tuff (Aegean Arc): insights into the eruptive dynamics of a large rhyolitic eruption. Bulletin of volcanology, 71(6), 643.

Brown, M.A., Brown, M., Carlson, W.D., Denison, C., 1999. Topology of syntectonic melt-flow networks in the deep crust: Inferences from three-dimensional images of leucosome geometry in migmatites. American Mineralogist 84, 1793-1818.

Burgisser, A., Chevalier, L., Gardner, J. E., Castro, J. M., 2017. The percolation threshold and permeability evolution of ascending magmas. Earth and Planetary Science Letters, 470, 37-47.

Cáceres, F., Castruccio, Á., Parada, M. A., 2018. Morphology, Effusion Rates, and Petrology of Postglacial Lavas of Laguna del Maule Volcanic Field, Chilean Andes, and Implications for Their Plumbing System. Geochemistry, Geophysics, Geosystems, 19(12), 4925-4944.

Cashman, K.V., Marsh, B.D., 1988. Crystal Size Distribution (CSD) in rocks and the kinetics and dynamics of crystallization. 2. Makaopuhi lava lake. Contributions to Mineralogy and Petrology 99, 292-305.

Cassidy, M., Manga, M., Cashman, K., Bachmann, O., 2018. Controls on explosive-effusive volcanic eruption styles. Nature communications, 9(1), 2839.

Castro, J. M., Burgisser, A., Schipper, C. I., Mancini, S., 2012a. Mechanisms of bubble coalescence in silicic magmas. Bulletin of Volcanology, 74(10), 2339-2352.

Castro, J.M., Cordonnier, B., Tuffen, H., Tobin, M.J., Puskar, L., Martin, M.C., Bechtel, H.A., 2012b. The role of melt-fracture degassing in defusing explosive rhyolite eruptions at volcan Chaiten. Earth and Planetary Science Letters 333, 63-69.

Castro, J. M., Dingwell, D. B., 2009. Rapid ascent of rhyolitic magma at Chaitén volcano, Chile. Nature, 461(7265), 780.

Cembrano, J., Lara, L., 2009. The link between volcanism and tectonics in the southern volcanic zone of the Chilean Andes: a review. Tectonophysics, 471(1-2), 96-113.

Cnudde, V., Boone, M.N., 2013. High-resolution X-ray computed tomography in geosciences: A review of the current technology and applications. Earth-Science Reviews 123, 1-17.

Degruyter, W., Bachmann, O., Burgisser, A., 2010. Controls on magma permeability in the volcanic conduit during the climactic phase of the Kos Plateau Tuff eruption (Aegean Arc). Bulletin of Volcanology, 72(1), 63.
Eichelberger, J. C., Carrigan, C. R., Westrich, H. R., Price, R. H., 1986. Nonexplosive silicic volcanism. Nature 323, 598-602.
Eichelberger, J. C., Westrich, H. R., 1981. Magmatic volatiles in explosive rhyolitic eruptions. Geophysical Research Letters 8, 757-760.
Endo, E., Malone, S., Noson, L., Weaver, C., 1981. The 1980 Eruptions of Mount St. Helens, Washington 93–108, professional paper 1250 (U.S. G.P.O., Washington, DC).
Feigl, K.L., Le Mével, H., Ali, S.T., Cordova, L., Andersen, N.L., DeMets, C., and Singer, B.S., 2014. Rapid uplift in Laguna del Maule volcanic field of the Andean Southern Volcanic Zone (Chile) 2007–2012. Geophysical Journal International, 196, 885–901, doi: 10.1093/gji/ggt438.
Fierstein, J., Postglacial eruptive history established by mapping and tephra stratigraphy provides perspectives on magmatic system beneath Laguna del Maule, Chile, Presented at: AGU Chapman Conference on Merging Geophysical, Petrochronologic, and Modeling Perspectives of Large Silicic Magma Systems, Quinamavida, Chile, 2018.
Global Volcanism Program, 2007. Report on Merapi (Indonesia) (Wunderman, R., ed.). Bulletin of the Global Volcanism Network, 32:2. Smithsonian Institution. https://doi.org/10.5479/si.GVP.BGVN200702-263250.
Gonnermann, H. M., Giachetti, T., Fliedner, C., Nguyen, C. T., Houghton, B. F., Crozier, J. A., Carey, R. J., 2017. Permeability during magma expansion and compaction. Journal of Geophysical Research: Solid Earth, 122(12), 9825-9848.
Gonnermann, H. M., Manga, M., 2007. The fluid mechanics inside a volcano. Annual Reviews of Fluid Mechanics, 39, 321-356.
Higgins, M. D., 2002. Closure in crystal size distributions (CSD), verification of CSD calculations, and the significance of CSD fans. American Mineralogist, 87(1), 171-175.
Hildreth, W., Godoy, E., Fierstein, J., Singer, B.S., 2010. Laguna del Maule volcanic field: eruptive history of a Quaternary basalt to rhyolite distributed volcanic field on the Andean range crest in central Chile. Servicio Nacional de Geología y Minería, Boletin 63.
Hildreth, W., Moorbath, S., 1988. Crustal contributions to arc magmatism in the Andes of central Chile. Contributions to mineralogy and petrology, 98(4), 455-489.
Houghton, B. F., Carey, R. J., Cashman, K. V., Wilson, C. J., Hobden, B. J., Hammer, J. E., 2010. Diverse patterns of ascent, degassing, and eruption of rhyolite magma during the 1.8 ka Taupo eruption, New Zealand: evidence from clast vesicularity. Journal of Volcanology and Geothermal Research, 195(1), 31-47.
Ketcham, R.A., 2005. Three-dimensional grain fabric measurements using high-resolution X-ray computed tomography. Journal of Structural Geology 27, 1217-1228.
Ketcham, R.A., Carlson, W.D., 2001. Acquisition, optimization and interpretation of X-ray computed tomographic imagery: applications to the geosciences. Computers & Geosciences 27, 381-400.
Klug, C., Cashman, K., Bacon, C., 2002. Structure and physical characteristics of pumice from the climactic eruption of Mount Mazama (Crater Lake), Oregon. Bulletin of Volcanology 64, 486–501. http://dx.doi.org/10.1007/s00445-002-0230-5.
Le Mével, H., Gregg, P. M., Feigl, K. L., 2016. Magma injection into a long-lived reservoir to explain geodetically measured uplift: Application to the 2007-2014 unrest episode at Laguna del Maule volcanic field, Chile. Journal of Geophysical Research: Solid Earth, 121, 6092–6108. https://doi.org/10.1002/2016JB013066
Liu, E.J., Cashman, K.V., Rust, A.C., 2015. Optimising shape analysis to quantify volcanic ash morphology. GeoResJ 8, 14-30.

López-Escobar, L., Cembrano, J., Moreno, H., 1995. Geochemistry and tectonics of the Chilean Southern Andes basaltic Quaternary volcanism (37-46 S). Andean geology, 22(2), 219-234.
Mandujano, F., Rodríguez, J. C., 2016. La catástrofe del 2008 en la provincia de Palena: reflexiones sobre sus particularidades e impacto en la Patagonia Occidental. Magallania, 44 (2), 69-85.
Mastrolorenzo, G., Pappalardo, L., 2006. Magma degassing and crystallization processes during eruptions of high-risk Neapolitan-volcanoes: Evidence of common equilibrium rising processes in alkaline magmas. Earth and Planetary Science Letters 250, 164-181.
Miller, C. A., Williams-Jones, G., Fournier, D., Witter, J., 2017. 3D gravity inversion and thermodynamic modelling reveal properties of shallow silicic magma reservoir beneath Laguna del Maule, Chile. Earth and Planetary Science Letters, 459, 14-27.
Mock, A., Jerram, D.A., 2005. Crystal size distributions (CSD) in three dimensions: Insights from the 3D reconstruction of a highly porphyritic rhyolite. Journal of Petrology 46, 1525-1541.
Mueller, S., Scheu, B., Kueppers, U., Spieler, O., Richard, D., Dingwell, D. B., 2011. The porosity of pyroclasts as an indicator of volcanic explosivity. Journal of Volcanology and Geothermal Research, 203(3-4), 168-174.
Okumura, S., Nakamura, M., Takeuchi, S., Tsuchiyama, A., Nakano, T., Uesugi, K., 2009. Magma deformation may induce non-explosive volcanism via degassing through bubble networks. Earth and Planetary Science Letters, 281(3-4), 267-274.
Papale, P., 1999. Strain-induced magma fragmentation in explosive eruptions. Nature 397, 425-428.
Pistolesi, M., Cioni, R., Bonadonna, C., Elissondo, M., Baumann, V., Bertagnini, A., Chiari, L., Gonzales, R., Rosi, M., Francalanci, L., 2015. Complex dynamics of small-moderate volcanic events: the example of the 2011 rhyolitic Cordón Caulle eruption, Chile. Bulletin of Volcanology, 77(1), 3.
Rivers, M.L., Sutton, S.R., Eng, P., 1999. Geoscience applications of x-ray computed microtomography, Conference on Developments in X-Ray Tomography II, Denver, Co, pp. 78-86.
Rotella, M. D., Wilson, C. J., Barker, S. J., Cashman, K. V., Houghton, B. F., Wright, I. C., 2014. Bubble development in explosive silicic eruptions: insights from pyroclast vesicularity textures from Raoul volcano (Kermadec arc). Bulletin of Volcanology, 76(8), 826.
Rust, A.C., Cashman, K.V., 2004. Permeability of vesicular silicic magma: inertial and hysteresis effects. Earth and Planetary Science Letters, 228, 93-107.
Sahagian, D. L., Proussevitch, A. A., 1998. 3D particle size distributions from 2D observations: stereology for natural applications. Journal of Volcanology and Geothermal Research, 84(3-4), 173-196.
Schipper, C. I., Castro, J. M., Tuffen, H., James, M. R., How, P., 2013. Shallow vent architecture during hybrid explosive–effusive activity at Cordón Caulle (Chile, 2011–12): evidence from direct observations and pyroclast textures. Journal of Volcanology and Geothermal Research, 262, 25-37.
Shea, T., Hammer, J.E., 2013. Kinetics of cooling- and decompression-induced crystallization in hydrous mafic-intermediate magmas. Journal of Volcanology and Geothermal Research 260, 127-145.
Shea, T., Houghton, B. F., Gurioli, L., Cashman, K. V., Hammer, J. E., Hobden, B. J., 2010. Textural studies of vesicles in volcanic rocks: an integrated methodology. Journal of Volcanology and Geothermal Research, 190(3-4), 271-289.
Singer, B. S., Andersen, N. L., Le Mevel, H. et al., 2014. Dynamics of a large, restless, rhyolitic magma system at Laguna del Maule, southern Andes, Chile. GSA Today 24, 4–10.

Singer, B., Hildreth, W., Vincze, Y., 2000. 40Ar/39Ar evidence for early deglaciation of the central Chilean Andes. Geophysical Research Letters, 27(11), 1663-1666.
Sutton, S.R., Bertsch, P.M., Newville, M., Rivers, M., Lanzirotti, A., Eng, P., 2002. Microfluorescence and microtomography analyses of heterogeneous earth and environmental materials. Applications of Synchrotron Radiation in Low-Temperature Geochemistry and Environmental Sciences 49, 429-483.
Tarasewicz, J., White, R. S., Woods, A. W., Brandsdóttir, B., Gudmundsson, M. T., 2012. Magma mobilization by downward-propagating decompression of the Eyjafjallajkull volcanic plumbing system. Geophysical Research Letters, 39, 1–5.
Toramaru, A., 2006. BND (bubble number density) decompression rate meter for explosive volcanic eruptions. Journal of Volcanology and Geothermal Research, 154(3-4), 303-316.
Tuffen, H., James, M. R., Castro, J. M., Schipper, C. I., 2013. Exceptional mobility of an advancing rhyolitic obsidian flow at Cordón Caulle volcano in Chile. Nature communications, 4, 2709.
Wespestad, C., Thurber, C. H., Andersen, N. L., Singer, B. S., Cardona, C., Zeng, X., et al., 2019. Magma Body Beneath Laguna del Maule Volcanic Field Imaged with Surface Wave Tomography. Journal of Geophysical Research: Solid Earth, 124. https://doi.org/10.1029/2018JB016485.

2. The link between the eruption transitions and the formation of pyroclastic obsidians in the rhyolites of Laguna del Maule

Abstract

Silicic explosive eruptions can be devastating and affect human settlements and industry for hundreds of kilometers around the volcano. They may switch to a more explosive phase or form lava flows and domes, however, the eruptive dynamics and timings related to the eruption transitions are difficult to predict. In this chapter I study potential indicators of impending changes in the eruptive styles of two rhyolitic eruptions of the Laguna del Maule volcanic complex (LdM). The first and most silicic postglacial eruption of LdM, the Rhyolite of Laguna del Maule (*rdm*), formed the most voluminous pyroclastic deposit (>20 km^3) which has low-density pumices, mafic juvenile clasts, granitoid lithics, no pyroclastic obsidians and no lava flow. Here I analyze the upper sequence of *rdm* and a pyroclastic flow formerly described as an early unit of Los Espejos (*rle*). Los Espejos is the first and most silicic after *rdm*, is much smaller (2-5 km^3) and formed fall deposits which contain high-density pumices and an increasing fraction of vesicular obsidian clasts followed by a lava flow. The analysis of physical characteristics suggest that the eruption styles were controlled by the fragmentation level. A downward propagation of the fragmentation level during the climactic phase of *rdm* eruption produced the interaction of the silicic magma with hotter and deeper mafic magmas which increased the eruption intensity and avoided the formation of obsidians. By contrast, an upward propagation of the fragmentation level during the last stage of the explosive phase of *rle* increased the total strain and the bubble connectivity within the silicic magma which promoted an efficient magma outgassing and the densification of magma. A comparison with recent moderate silicic eruptions suggests that the increasing formation of pyroclastic obsidians is

related to a decrease of the eruption intensity and preludes the formation of lava flow on the order of days.

Keywords

Laguna del Maule volcanic complex; Tephrostratigraphy; Juvenile densities; Bubble textural analysis; Explosive eruptions; Silicic eruptive transitions.

2.1. Introduction

Silicic explosive eruptions comprise most of the largest volcanic events on the Earth surface (Pyle, 2015), can cause the evacuation of entire towns (e.g., Chaitén, 2008; Carn et al., 2009) and may have global effects on climate for years (e.g., Pinatubo, 1991; Self et al., 1993). The capability of silicic magmas to produce large explosive eruptions is mainly related to the high viscosity of the silicic melt and the high volatile content (Cassidy et al., 2018). Diverse factors may trigger silicic explosive eruptions, such as the interaction of silicic magmas with deeper and wet mafic magmas (e.g., Pinatubo, 1991; Pallister et al., 1992), a downward propagation of the fragmentation level (e.g., Eyjafjallajökull, 2010; Tarasewicz et al., 2012), a reservoir overpressured by magma or volatile inputs (e.g., Santorini, 1620 B.C.; Degruyter et al., 2016), volatile saturation driving fast magma ascent rates (e.g., Chaitén, 2008; Castro and Dingwell, 2009), or a rapid unloading and decompression wave (e.g., St. Helens, 1980; Alidibirov and Dingwell, 1996). However, high-intensity phases are intrinsically unstable, and they may switch to an even more intense eruption, with vent widening and the formation of pyroclastic density currents, or to an effusive phase (Cassidy et al., 2018).

The transition from an explosive to an effusive phase in silicic eruptions is mainly dictated by efficient magma outgassing and a decreasing magma ascent rate (Cassidy et al., 2018). Despite

the abrupt stratigraphic records of pyroclastic deposits being overlain by silicic lava flows, however, recent observations reveal that the explosive-effusive transitions may occur over weeks or months (e.g., Alfano et al., 2011; Schipper et al., 2013). This time period is significant for the mitigation of human lives and settlements and gives insights about gradual changes in the eruptive dynamics governing the magma outgassing and ascent rate (Gonnermann and Manga, 2007). Changes of the eruption processes preceding the formation of lava flows are printed as subtle variations of sedimentological and physical parameters at the top of the pyroclastic sequences. For instance, Alfano et al. (2011) have shown that the paroxysm of the 2008 Chaitén eruption (Chile) formed a fall deposit with 80% of silicic lithics and only 10% of silicic pumice clasts; later, the eruption intensity decreased forming fall deposits with smaller clasts and a higher fraction of pumice (<50%) and obsidian clasts (~10%). After ten days, the explosive activity was limited to ash and steam plumes (not forming continuous stratigraphic layers) and synchronous with the initial extrusion of an obsidian dome. Similarly, the pulsatory subplinian eruption of Cordón Caulle (Chile) in 2011 formed pumice-rich fall deposits during the first two days (Pistolesi et al., 2015); the pumice clasts show a diversity of bubble textures from isotropic high-porosity to heterogeneous dense juveniles. In the third day, the eruption intensity decreased and formed an obsidian-rich fall deposit. During two weeks after the climactic phase, the explosive activity was limited to discrete eruptive pulses which formed elongate tube-pumice coarse ash and lapilli (Schipper et al., 2013), and synchronous with the extrusion of an obsidian lava flow (Tuffen et al., 2013). In this chapter, I analyze the subtle sedimentological and physical indicators of eruption transitions in past (non-monitored) silicic eruptions at Laguna del Maule.

Laguna del Maule (LdM) is a caldera-type volcanic complex within a locally extensional area in the Southern volcanic zone of the Andes (Cembrano and Lara, 2009; Hildreth et al., 2010). LdM encompasses a diversity of silicic eruptive products that reflect a range of eruptive styles.

Several pyroclastic deposits and lavas were erupted from the same vent during a single eruption, and therefore experienced syn-eruptive transitions among different eruptive styles (Hildreth et al., 2010). In the last 25 ky (the postglacial eruptive stage), rhyolites have predominated: 20 out of 35 eruptive units have silica contents of 68-78 wt.% (Fierstein, 2018; Hildreth et al., 2010). The postglacial eruptive stage of LdM started with one exceptional silicic eruption, the rhyolite of Laguna del Maule (*rdm*; ~23 ky by $^{39}Ar/^{40}Ar$; Andersen et al., 2017), which has the most voluminous deposit (>20 km^3) and the most silicic rocks (>77 wt.% SiO_2) of LdM (Fierstein, 2018; Hildreth et al., 2010). The *rdm* pyroclastic deposits contain pumice clasts, mafic juveniles and enclaves within pumices, is the only postglacial rhyolite eruption sequence without lava flow(s) and may be the only one without juvenile obsidian clasts in its pyroclastic units. By contrast, the rhyolite of Los Espejos (*rle*; Hildreth et al., 2010) is the first rhyolitic eruption (19 ky by $^{39}Ar/^{40}Ar$; Singer et al., 2000) and the most silicic (75.5-75.7 wt.% of SiO_2; Hildreth et al., 2010) after *rdm* (Fierstein, 2018; Hildreth et al., 2010). Unlike *rdm* and similar to the younger rhyolitic eruptions of LdM (Hildreth et al., 2010), the Los Espejos eruption started with an explosive stage that produced an ash fall deposit and minor pyroclastic density currents of >1 km^3 (Gho et al., in review) containing dense pumices and pyroclastic obsidians, followed by the effusion of a ~0.82 km^3 rhyolitic lava flow (Cáceres et al., 2018). Nowadays, LdM shows a localized high uplift rate in the southern geographic area which is a surface expression of an active magmatic system (Feigl et al., 2014; Singer et al., 2014).

In this chapter, I present a detailed stratigraphic description of the *rle* tephra deposits based on outcrops north of the current lake in order to define layers and volcanic units and correlate them among the stratigraphic stations. Representative layers of each volcanic unit, as well as layers with remarkable sedimentological or physical features, are selected for grain size distributions (GSD), componentry and density analyses. I then reconstruct the eruption history of Los Espejos based on the field descriptions and laboratory analyses. I also present some

descriptions of the deposits and physical parameters from *rdm* to compare them with those from Los Espejos, although, the reconstruction of the eruption history and the interpretation of the factors governing the *rdm* event are beyond the scope of this study. I select representative pumices from *rle* according to the density analysis for bubble textural analysis, including determination of bubble number density and bubble size distributions. The variations of the componentry and bubble textural parameters within pumice clasts with stratigraphic height are used to interpret the eruption processes governing the styles and transitions of Los Espejos event. In particular, this chapter is focused on determining the physical and volcanic processes that formed the pyroclastic obsidians and preceded the formation of the obsidian lava flow in order to give insights into the potential eruptive behavior of future eruptions in LdM.

2.2. Geological background

In this section I describe the rocks underlying the entire LdM and locally preceding *rdm* and *rle* in order to illustrate the physical characteristics and relative age and depth of potential lithics within the studied pyroclastic deposits. I then summarize the eruption sequences and mineralogy of the postglacial rhyodacites and rhyolites and describe some of the main physical characteristics of *rdm* and *rle*. In the end, I present some sedimentological and physical analyses on recent rhyolitic explosive eruptions which were applied to determine the eruption dynamics governing the styles and transitions of those eruptions.

2.2.1. LdM basement and older eruptive units around *rdm* and *rle*

The Laguna del Maule volcanic complex overlies the following volcanogenic formations (Hildreth et al., 2010 and references therein): the late Oligocene to early Miocene Cura-Mallín formation which consists of nonmarine volcanoclastic sedimentary strata with minor lavas and pyroclastic units; the Miocene Trapa-Trapa formation formed by mafic-to-andesitic lavas,

pyroclastic deposits and volcanogenic sedimentary strata; Miocene-to-Pliocene intermediate-to-silicic volcanic rocks of the Campanario formation; and the Pliocene-to-Pleistocene Cola de Zorro formation which consists of mafic-to-intermediate lavas.

The *rdm* and *rle* vents (Fig. 2.1) are mostly surrounded by the partially welded tuff of the ignimbrite of Bobadilla Caldera (*igcb*, Hildreth et al., 2010), the most voluminous eruption of LdM which formed a caldera-collapse north of the current lake. The deposits associated with the Bobadilla caldera were formed 950 ky BP and consist of rhyodacitic (66-72 wt.% SiO_2) juvenile clasts, fiamme and andesitic lithics. Both juvenile clasts and fiamme have 10-20% plagioclase, 2-5% biotite and sparse quartz, ortho- and clinopyroxene, and Fe-Ti oxides. In general, the welded tuff is white but may have a gray-brown surface due to hydrothermal alteration (Hildreth et al., 2010). Overlying *igcb*, the andesitic lavas and breccias (56-64 wt.% SiO_2) of the Volcán Atravesado crop out northeast the Los Espejos vent. The lavas are gray-green and have phenocrysts of plagioclase and two-pyroxenes, while the breccias are brownish-yellow due to weathering (Hildreth et al., 2010). The Los Espejos lava flow is underlain by one rhyolitic and two rhyodacitic lava flows (*rep*, *rdno*, *rdne* in Hildreth et al., 2010) which have phenocrysts of plagioclase, biotite and hornblende in decreasing order.

2.2.2. Summary of the postglacial silicic eruptive units of LdM

After the *rdm* eruption at least nine rhyodacitic (68-72 wt.% SiO_2) units and eleven rhyolitic (72-76 wt.% SiO_2) units were erupted in LdM (Fierstein, 2018; Hildreth et al., 2010). The rhyodacites are lava flows and domes carrying mafic blobs (Table 2.1), have 5-25 vol.% phenocrysts of plagioclase, biotite and hornblende in decreasing order. The least crystalline rhyodacites have sparse biotites and no hornblende. Most rhyodacites overlie and/or come from the same vent as andesitic lava and scoria. Only one rhyodacite, *rdcd*, started with an explosive phase that formed a rhyodacitic pumice ring. By contrast, most rhyolites are sequences of fall

deposits followed by lava flows with no mafic juvenile clasts or blobs (Table 2.2). The fall-lava flow sequences are continuous except for *rcb,* which was formed by several explosive-effusive stages (Fierstein, 2018; Hildreth et al., 2010). Both pumice clasts and lavas are crystal-poor (<5 vol.%) and have phenocrysts of plagioclase and biotite in decreasing order. Only one rhyolite (*ram*, 73.2-73.3 wt.% SiO_2) has mafic blobs, hornblende phenocrysts and is associated with andesitic scoria. The most relevant volcanic units surrounding *rdm* and *rle* are listed in Table 2.3.

Table 2.1: Postglacial rhyodacites (68-72 wt.% SiO_2) of LdM. The table shows the volcanic sequence, the main phenocrysts and other characteristics. The name codes are from Hildreth et al. (2010). For the complete name of the units, refer to Table 2.3 or Hildreth et al. (2010). Pl = plagioclase; bt = biotite; hbl = hornblende.

Eruptive unit	Eruptive sequence	Main phenocrysts	Description
rdac	Dome	Pl – Bt - Hbl	
rdep	Domes	Pl – Bt - Hbl	Dike-formed
rdnp	Lavas and domes with mafic blobs	Pl – Bt	Associated with mafic scoria
rdcd	Pumice ring + lavas and domes with mafic blobs	Pl – Bt - Hbl	Overlying andesitic lavas and pyroclastic deposits
rdam	Lava flow with minor mafic blobs	Pl – Bt - Hbl	Overlying andesitic lavas and pyroclastic deposits
rdne	Lava flow with mafic blobs	Pl – Bt - Hbl	
rdno	Lava flow with mafic blobs	Pl – Bt - Hbl	
rdcn	Lava flow with mafic blobs	Pl – Bt - Hbl	Associated with mafic scoria
rdsp	Dome with mafic blobs	Pl – Bt	Associated with mafic scoria

Los Espejos, the first and most silicic eruption after *rdm,* shows the most typical eruption sequence (fall deposit + lava flow) and mineralogy (plagioclase + biotite) of the postglacial

rhyolites of LdM. For this reason, I selected Los Espejos to analyze the potential indicators in the pyroclastic deposits preceding the formation of a lava flow. In order to obtain insights of the factors governing a silicic explosive eruption with no lava flow, I also study some physical characteristics of the rhyolite of Laguna del Maule.

Table 2.2: Postglacial rhyolites (72-76 wt.% SiO_2) of LdM. References, names of eruptive sequences and names of main phenocrysts are like in Table 2.1.

Eruptive unit	Eruptive sequence	Main phenocrysts	Description
ras	Lava	Pl – Bt	Associated with a rhyodacitic lava flow
rcd	Fall deposit + lava	Pl – Bt	
rle	Fall deposit + lava	Pl – Bt	
rap	Fall deposit + lava	Aphyric	
rln	Fall deposit + lava	Pl – Bt	
ram	Dome with mafic blobs	Pl – Bt - Hbl	Associated with mafic scoria
rsl	Fall deposit + lava	Aphyric	With inclusions of Hbl-Bt rhyolites
rcl	Fall deposit + lava	Pl – Bt	
rpp	Dome	Bt	
rng	Fall deposit + lava	Aphyric	
rcb	Multiple fall deposit + lavas	Pl – Bt	
rdm	Fall deposit + PDCs	Pl - Hbl	Associated with mafic juveniles, granitoids and no obsidians.

2.2.3. Background of the rhyolites of Laguna del Maule and Los Espejos

Some insights related to the tephra stratigraphy, and physical and textural parameters of silicic deposits have been presented in scientific meetings and shared by oral and written communication (e.g., Fierstein, 2018). Initially, the *rdm* deposits were described as an early

explosive stage of the *rle* eruption (Hildreth et al., 2010); however, soil between *rdm* and *rle* deposits and distinctive componentry indicate that they belong to separate eruptions (Fierstein, 2018). The Laguna del Maule eruption (*rdm*) is the only postglacial rhyolite of the LdM complex containing mafic juveniles and granitoid lithics (Fierstein, 2018; Hildreth et al., 2010). The mafic juveniles are olivine-bearing mafic andesites and hornblende-bearing andesites (Fierstein, 2018), and the granitoid lithics range from andesite to rhyolite compositions (62-73 wt.% SiO_2; Juliet Ryan-Davis, written communication). Based on isopach analysis, the *rdm* eruptive vent is inferred to be below the current lake (Fierstein, 2018). The *rdm* deposits are exposed >80 km east of the possible vent and crop out around most of the lake, always below other silicic postglacial deposits (Gho et al., in review).

The vent of the *rle* deposit is exposed in the northwest of the LdM volcanic complex, ~3 km north of the lake shoreline. The most distal *rle* fall deposits crop out ESE from the vent (Fig. 2.1a; Fierstein, 2018); however, little is known about the stratigraphy and componentry of the Los Espejos pyroclastic deposits. Because of the similarities in the location, pumices morphologies and whole-rock composition between *rdm* and *rle*, here I describe the stratigraphy and some physical parameters of *rdm* for geological context and comparison with *rle*. As the tephrostratigraphy of silicic units has not been published in scientific journals, and the interpretation of the eruption styles and transitions of Los Espejos and the other LdM rhyolites has not been investigated, this chapter offers new insights about the silicic explosive eruptions and their transitions to effusive phase in the LdM volcanic system.

Table 2.3: List of the LdM eruptive units studied and mentioned in this chapter for geographic reference. The name codes are from Hildreth et al. (2010). Ages are from Hildreth et al. (2010)[a], Andersen et al. (2017)[b], and Fierstein (2018)[c]

Name	Name code	Age (ky)	Description
Ignimbrite of Cajones de Bobadilla	*igcb*	990 ± 13[b]	North of *rle*; some lithics of *rle* come from *igcb*
Volcán Atravesado	*ava*	--	Northeast of *rle*; some lithics of *rle* come from *ava*
Rhyolite of Laguna del Maule	*rdm*	>23[b]	Studied in this chapter
Rhyodacite Northwest of Los Espejos	*rdno*	>19.0[b]	Around the *rle* lava flow
Rhyodacite Northeast of Los Espejos	*rdne*	>19.0[b]	Around the *rle* lava flow
Rhyolite of Los Espejos	*rle*	19.0 ± 0.7[b]	Studied in this chapter
Rhyodacite of Colada Dendriforme	*rdcd*	8.0 ± 0.8[b]	In the west of LdM
Rhyodacite of Colada Noroeste	*rdcn*	3.5 ± 2.3[b]	In the west of LdM
Andesite of Laguna Sin Puerto	*asp*	<3.5[b]	In the west of LdM
Rhyodacite of Laguna Sin Puerto	*rdsp*	<3.5[b]	In the west of LdM
Rhyolite of Cari Launa	*rcl*	<3.3[b]	In the northeast of LdM; north of *rcd*
Rhyolite of Colada Divisoria	*rcd*	2.1 ± 1.3[b]	In the east of LdM; near *rdm* and *rle* deposits
Rhyolite of Las Nieblas	*rln*	<2.0[c]	In the southwest of LdM; south of the current local inflation

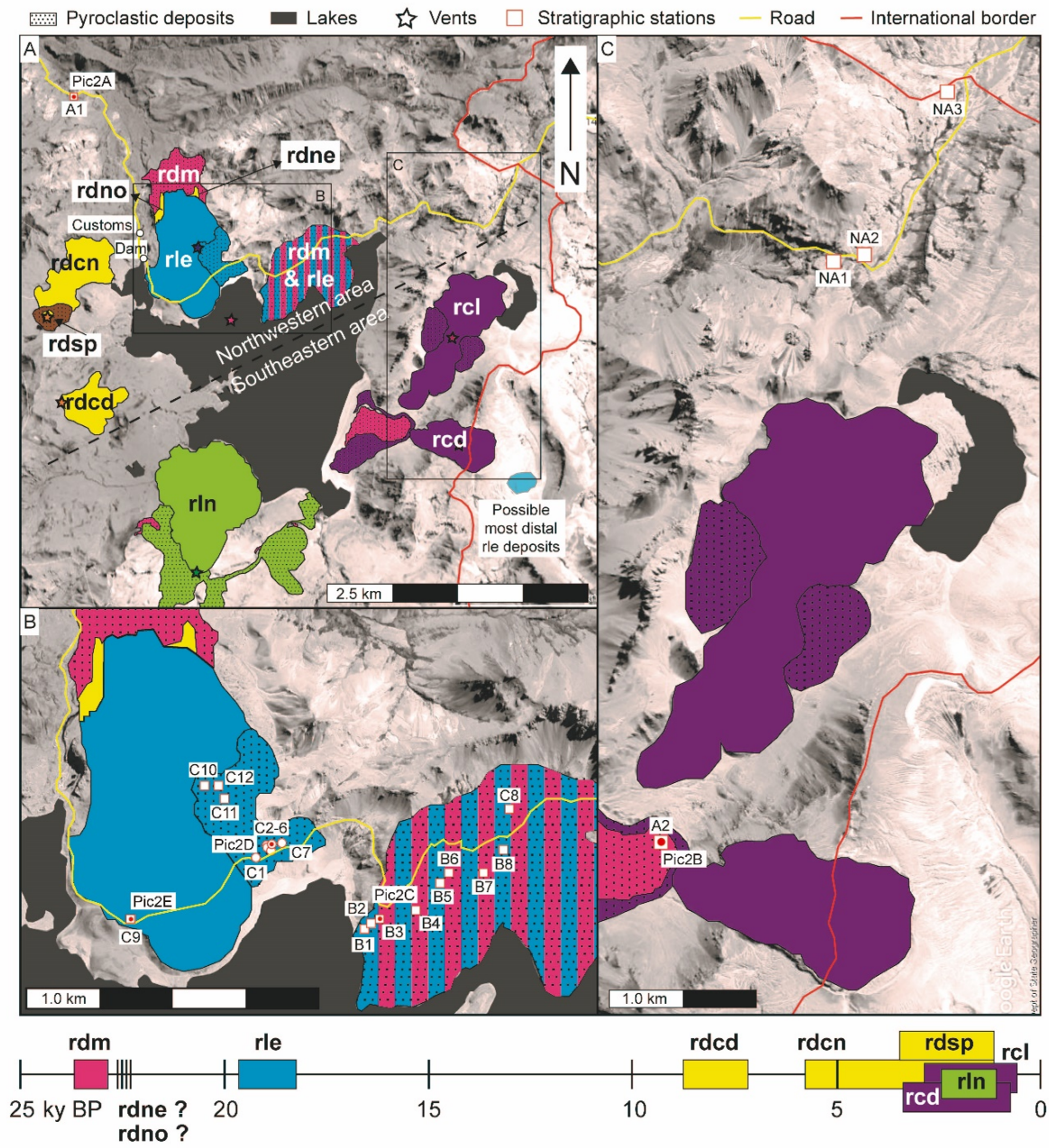

Fig. 2.1: Map of the Laguna del Maule volcanic complex. The deposits of the studied rhyolites and the stratigraphic stations are highlighted together with other eruptive units, the international road and other landmarks for geographical reference. **A** General view. **B** Stratigraphic stations of *rdm* and *rle*. **C** Stratigraphic stations of *rdm* and other eruptive units. The locations of eruptive units are based on field observations of this work, Fierstein (2018) and Hildreth et al. (2010). Ages are from Andersen et al. (2017)[1], Hildreth et al. (2010)[1,2] and Singer et al. (2000)[1]. Descriptions of the eruptive units are in Table 2.1 and geographic locations of the stratigraphic stations in UTM are in Supplementary Material. Red points show the location of photographs in Fig. 2.2.

[1] $^{40}Ar/^{39}Ar$
[2] K-Ar

2.2.4. Sedimentological and physical analyses applied on recent rhyolite eruptions

As no LdM eruption has been monitored, there are no insights about the duration of eruptions or explosive-effusive transitions. Here I review the analyses of sedimentological and physical features on recent rhyolite eruptions for comparison with the studied LdM postglacial rhyolites. In the climactic phase (layer-β) of the 2008 Chaitén eruption, the pumice clasts show a unimodal density distribution with a mode of 800 kg m^{-3} and a bubble connectivity of 0.70-0.85 (Alfano et al., 2012). These results are consistent with a high-intense and sustained silicic explosive eruption during which the outgassing was efficient (e.g., Colombier et al., 2017; Mueller et al., 2011). Bubble number densities (BND) of seven pumice clasts are low (~10^5 mm^{-3}) and overlap those from subplinian pumices; the bubble size show similar distributions among clasts with small size modes suggesting a short time for vesiculation due to a fast magma ascent.

Grain size distributions (GSD) of the climactic phase of the 2011 Cordón Caulle eruption show that the coarser layers correspond to the eruptive pulses with the highest eruption column, while the grain sorting mainly depends on the proximity to the eruption vent (Pistolesi et al., 2015). Componentry analyses reveal that layers formed during the climactic phase have a high fraction of silicic lithics, while the number fraction of pumice and obsidian clasts increase with decreasing the eruption intensity. The pumice morphologies and bubble textures are heterogeneous, consistent with the pulsatory explosive style. The juvenile clasts show internal heterogeneities and shear and strain localizations which would facilitate the magma degassing. Densities were measured only in the "white pumice clasts", the most vesiculated and homogeneous juvenile clasts, showing a unimodal distribution with mode of 400 kg m^{-3}.

For both rhyolite eruptions, the analyzed juvenile clasts are the most vesiculated (pumice) and come from deposits corresponding to the climactic phase of the explosive eruptions. Consequently, insights from less intense eruptive pulses or denser juvenile clasts are not provided.

2.3. Tephra stratigraphy

Our observations of the early postglacial deposits were made during two campaigns in February – March of 2016 and 2017 based on the description and sampling of 25 stratigraphic stations from proximal deposits (<12 km from vent; Fig. 2.1). Sampling location was guided by the map of Hildreth et al. (2010), information about tephra deposits along the north lake shoreline from Judy Fierstein, and our own exploration. The analysis of stratigraphic stations of the *rle* deposits presents some difficulties because they are not continuously exposed due to erosion by rivers, paleorivers and the action of rain and snow 6-9 months per year (Fierstein, 2018; Hildreth et al., 2010). Furthermore, at the time of the initial fieldwork, the rhyolite of Laguna del Maule was still considered as a first stage of the Los Espejos eruptive unit (see description of the northwest pyroclastic flow of Los Espejos in Hildreth et al., 2010), so the *rdm* deposits were described and sampled exclusively in two stratigraphic stations (A1 and A2). The most distal outcrop of the *rle* ash fall deposit has been found southeast of the SE lava flow of the Rhyolite of Divisoria (*rcd*, Fierstein, 2018; Hildreth et al., 2010). In this way, the *rle* ash fall deposit is ESE oriented and most of the deposit is covered by the current lake (Fig. 2.1a).

The tephra sequences of *rdm* and *rle* were correlated among the stratigraphic stations by both field observations and groundmass glass compositions. Detailed stratigraphic descriptions, definition of layers, and measurements of grain size were made at stratigraphic stations distributed among four areas: 1. an outcrop of *rdm* pyroclastic deposits was described on the

side of the Talca-Paso Pehuenche international road, NW of the lake (Area A, Station A1; Fig. 2.1a); 2. the characterization and sampling of the Los Espejos pyroclastic deposit and the lava flow were done at 1-2 km SE of the vent (Area C, Stations C1-12; Fig. 2.1b); 3. *rdm* pyroclastic deposits and the *rle* fall deposit were described in a SW-NE 3 km-long traverse of 4-km ESE of the *rle* vent (Area B, Stations B1-8; Fig. 2.1b); 4. *rdm* pyroclastic deposits were described and sampled in front of the *rcd* coulee in the east shoreline of the lake (Station A2; Fig. 2.1c). Three stratigraphic stations examined near the Chile-Argentina border contain deposits that do not correspond to *rdm* or *rle* (Stations NA1-3; Fig. 2.1c; Table 2.4) and are not discussed further in this chapter.

The layers were defined by variations of sedimentological and physical features such as the layer and clast orientation, color, grain size, sorting and componentry. They were organized into stratigraphic units based on unconformities or abrupt changes of the sedimentological and physical features, and thus represent different eruption phases. In the case of *rdm*, the deposits are split into two stratigraphic units (*rdm* units 1-2) according to the whole-rock composition and componentry: the *rdm* unit 1 is slightly more silicic and alkaline and the *rdm* unit 2 contains mafic juvenile clasts and granitoid lithics. The base of the Los Espejos sequence is identified by the contact with lake sediments or *rdm* tephra. In Los Espejos, four stratigraphic units (*rle* units 1-4) are identified and correlated among the stratigraphic stations (Table 2.5). The sequence of pumice-rich and lithic-rich layers (*rle* unit 1) and the minor PDCs (*rle* unit 2a) only crop out at 1-2 km from vent. Layers of the fall deposit (*rle* units 2b – 3) are exposed further to the SE and are correlated according to key layers with a high fraction of one type of clast (e.g., obsidian or altered lava) or with remarkable bubble textures (e.g., large elongate pumices with elongate bubbles).

Table 2.4: Averages of groundmass glass composition data[3] from Chapter 5 (Section 5.5) of pumices, pyroclastic obsidians and lavas from *rdm* and *rle* measured by EMPA and data of groundmass glasses of pumices and pyroclastic obsidians from other eruptive units (NA).

	rdm		*rle*						NA	
	PF P	FD P	Pum.	Pum.	Pum.	Obs.	Obs.	Lava	Pum.	Obs.
SiO_2	77.22	76.91	76.42	76.28	76.21	76.33	76.43	76.42	74.90	74.85
TiO_2	0.11	0.13	0.14	0.15	0.15	0.15	0.14	0.15	0.21	0.21
Al_2O_3	12.90	13.08	13.21	13.28	13.31	13.21	13.20	13.14	13.88	13.96
FeO	0.57	0.70	0.74	0.76	0.73	0.78	0.75	0.76	1.00	0.91
MnO	0.04	0.04	0.07	0.06	0.06	0.06	0.06	0.07	0.08	0.08
MgO	0.10	0.11	0.08	0.10	0.10	0.10	0.09	0.10	0.18	0.18
Cr_2O_3	0.00	0.00	-0.01	0.00	0.00	0.00	0.00	0.00	0.00	0.01
CaO	0.54	0.64	0.59	0.60	0.59	0.60	0.58	0.59	0.65	0.62
Na_2O	4.16	3.80	4.23	4.26	4.45	4.26	4.29	4.40	4.80	4.81
K_2O	4.20	4.39	4.35	4.33	4.30	4.35	4.30	4.33	4.07	4.20
P_2O_5	0.02	0.03	0.02	0.01	0.02	0.01	0.01	0.02	0.03	0.03
SO_2	0.01	0.02	0.00	0.00	0.00	0.00	0.00	0.00	0.01	0.00
Cl	0.13	0.13	0.15	0.16	0.15	0.14	0.14	0.13	0.17	0.14

This section summarizes the stratigraphy and sedimentological features observed in the field. Grain size, sorting, componentry, and pyroclast density are characterized according to fieldwork observations, while the detailed quantification of physical parameters such as grain size distribution, mean, median and maximum grain size, sorting, volume fraction of components and juvenile densities are presented below in the "Results of physical parameters" section.

Table 2.5: Summary of the eruptive subunits of the rhyolite of Laguna del Maule (*rdm*) and the rhyolite of Los Espejos (*rle*) and their main features.

Eruptive Subunit	Deposits	Main features
rdm 1	Fall and PDC deposits	Low-density pumices without mafic lithics
rdm 2	Fall and PDC deposits	Mid-density pumices with mafic lithics
rle 1	Interbedding layers of phreatomagmatic origin	Interbedding of brown and gray layers
rle 2	Fall and PDC deposits	Mid-to-high density pumices with lithics
rle 3	Fall deposit	Increasing fraction of vesicular obsidians
rle 4	Lava flow	Various textures from pumiceous to tuffsites

[3] The groundmass glass composition data was normalised to 100% anhydrous composition. The averages correspond to 37-55 points per sample.

2.3.1. The *rdm* pyroclastic deposits

I described and sampled the *rdm* pyroclastic deposits in area B where they are overlain by Los Espejos tephra, as well as at two stratigraphic stations (A1-A2) for comparison with the Los Espejos pyroclastic deposits. In particular, I visited the station A1 because it is described as an early pyroclastic flow of Los Espejos by Hildreth et al. (2010). These deposits are now identified as part of the *rdm* sequence and contain pumices less dense than those from the *rle* pyroclastic deposits (Section 2.5.3). The pumices are aphyric and have different textures to those from *rle*; importantly, there are no pyroclastic obsidians in this unit. Station A1 crops out as a 7 m-thick sequence of several fine layers with multiple sedimentary structures such as laminar strata, crossbedding and lenses with coarser grains (Fig. 2.3a). The pyroclastic deposit is white to yellowish, very poorly sorted and matrix-supported, with a matrix of ash; lapilli are pumices and lithics. Most of the clasts are fragile low-density pumices with equant to elongated shapes and a broad range of bubble textures, including frothy, banded and tubular. Above lies a more competent sequence comprising a massive matrix-supported ash pyroclastic deposit that contains similar componentry as the underlying sequence. Here I collected some of the biggest pumices with frothy and banded textures for textural analysis in the laboratory. For a more detailed description of the *rdm* deposits at station A1, see Appendix A.

A different *rdm* eruptive unit was described in the area B (stations B1-7) and at station A2. In these areas the deposits have thicknesses of tens of meters, the pumices are denser than those from the station A1 (Section 2.5.3), some pumices contain mafic enclaves, and there are mafic vesicular juveniles and granitoid lithics. Several layers are defined by variations of grain size and componentry; these layers are described in detail in the Appendix A and illustrated in Fig. 2.4. At station A2, a 2.6 m-thick sequence was described and three layers (rdm2S1-3) were sampled for laboratory analyses.

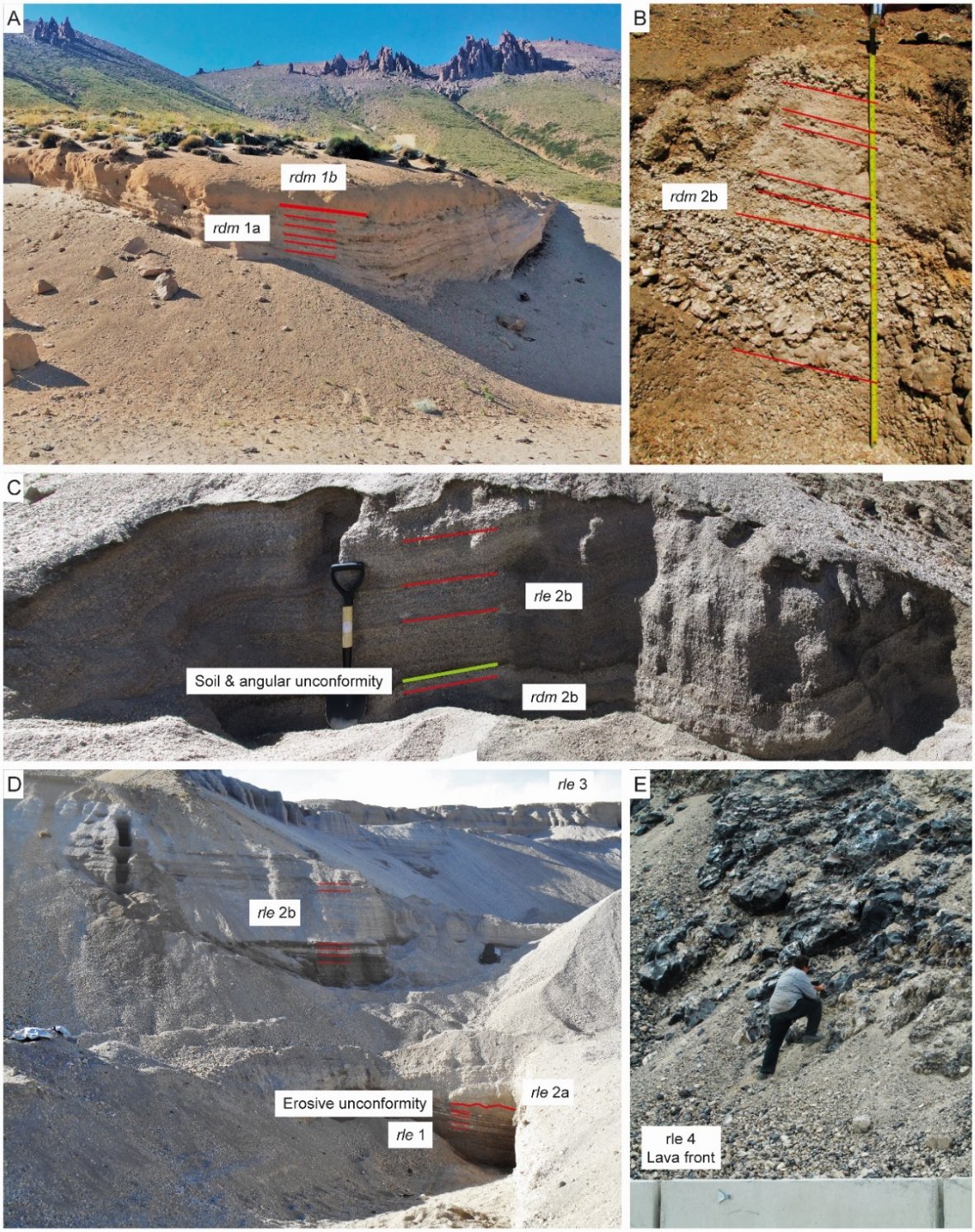

Fig. 2.2: General views of some stratigraphic stations. A The contact between the *rdm* 1a and the *rdm* 1b (station A1). Notice that the *rdm* 1b unit is more competent. **B** One stepped log showing the *rdm* 2b (station A2). **C** Panoramic of the contact between *rdm* and *rle* deposits separated by oxidized soil and angular unconformity (Green line). *rdm* is recognized by lapilli of mafic compositions and less dense pumices, while *rle* is recognized by the obsidian clasts and denser pumices (station B3). **D** General view of the *rle* pyroclastic deposits (stations C2-5). **E** The front of *rle* lava flow (station C9). Thicker red lines represent contacts between stratigraphic units of the same event, while thinner red lines represent some layers.

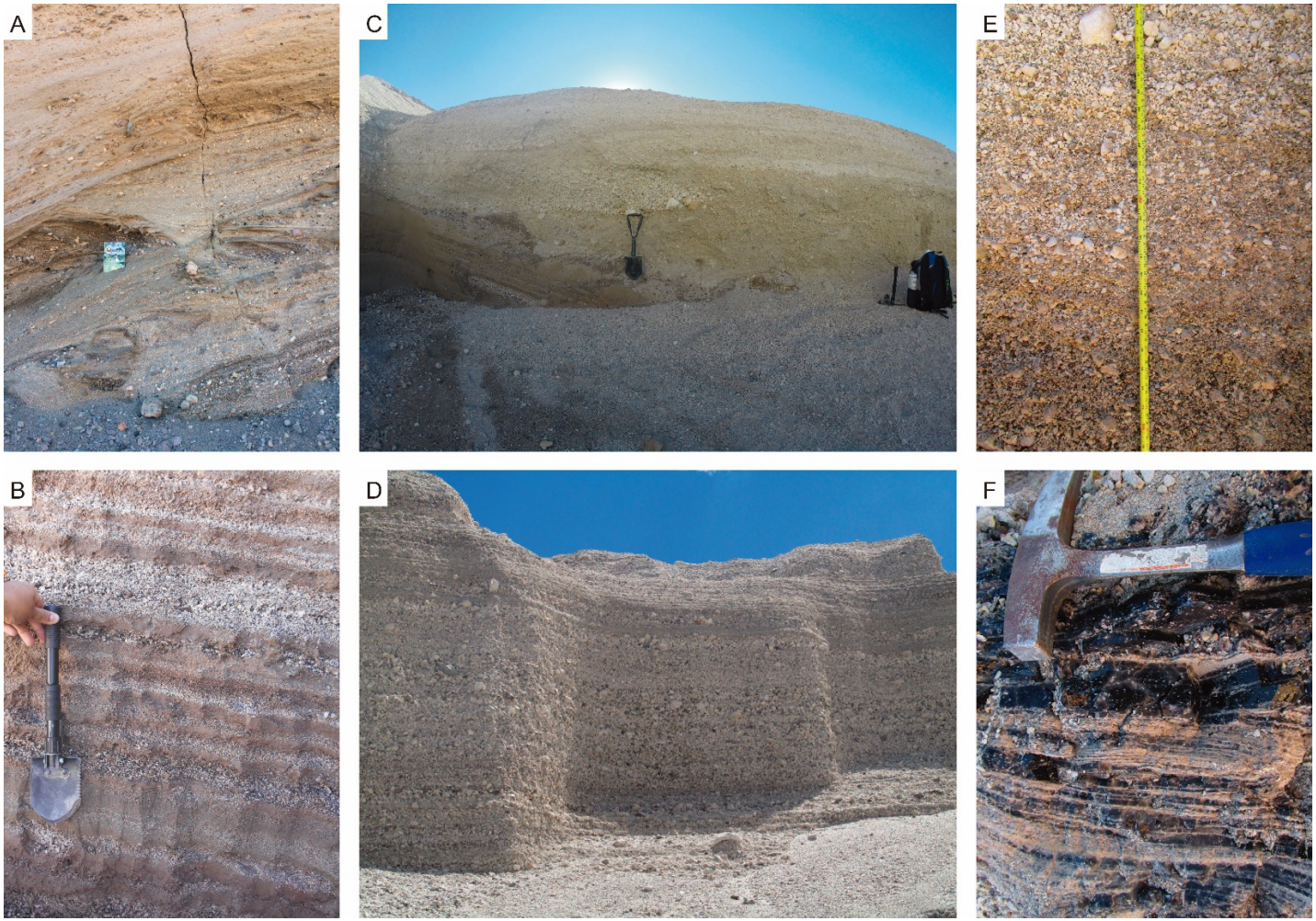

Fig. 2.3: Field pictures of sedimentological features of the LdM rhyolite subunits. A Sedimentary structures of a *rdm* pyroclastic flow observed in station A1. **B** The planar interbedding of the *rle* unit 1 showing the coarse-ash rich brown layers and the lapilli-rich white layers. **C** Sedimentary structures of a minor pyroclastic flow of the *rle* unit 2a. Notice the discordance with the *rle* unit 1. **D** An outcrop of the laminar pumice-rich layers of the *rle* unit 2b. **E** Upper part of the *rle* unit 3. Obsidian-rich layers are visible at the bottom. **F** A tuffsite block from the *rle* obsidian lava flow.

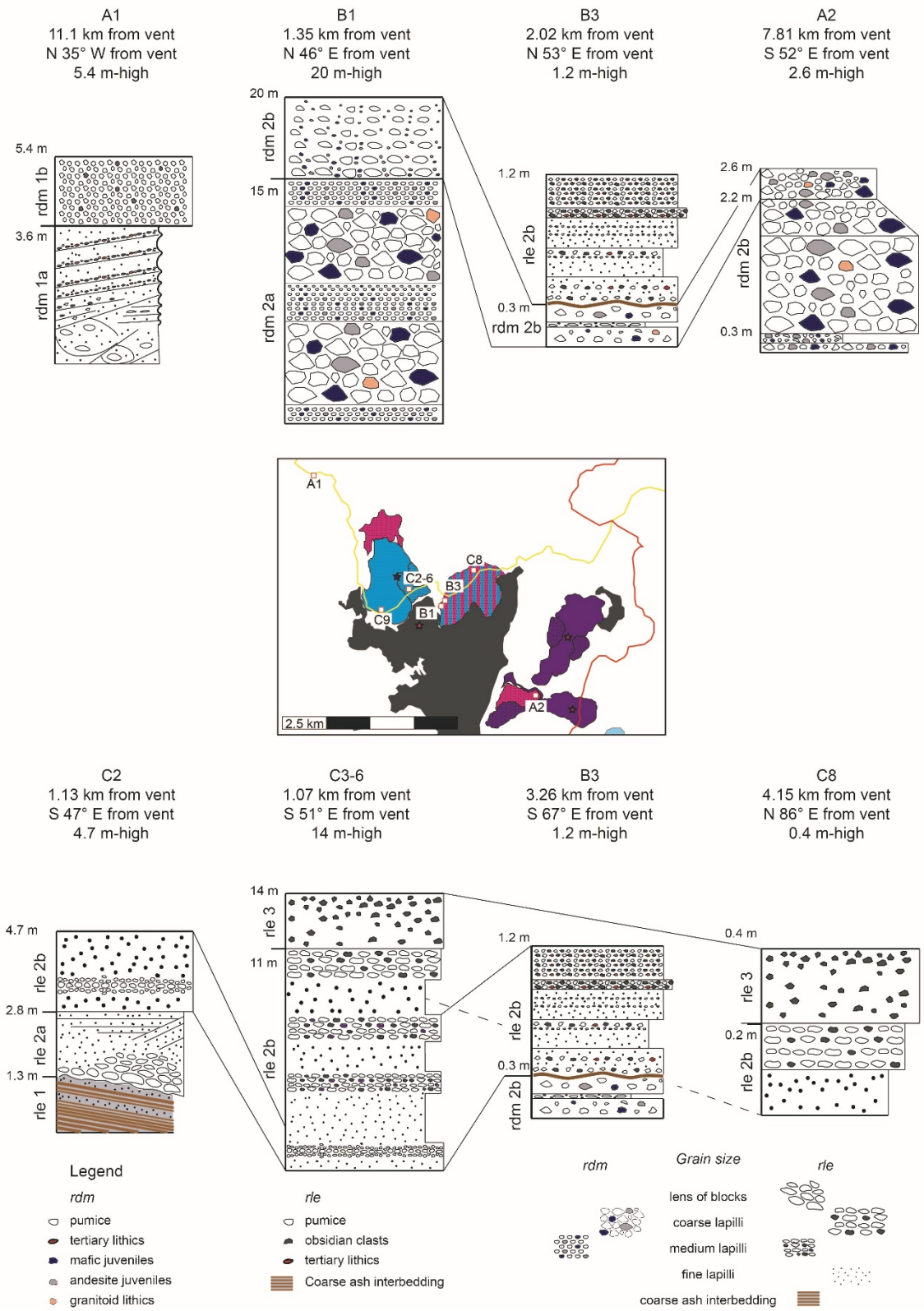

Fig. 2.4: Stratigraphic columns and correlations among stratigraphic stations. The distance and orientation from vent, and the deposit height are indicated in each stratigraphic column. The height of deposits is not proportional to allow a better visualization.

2.3.2. *rle* unit 1: An interbedded gray and brown multilayered fall deposit

rle unit 1 is only found in the proximal deposits (<2 km from the *rle* vent; Fig. 2.1a and b), overlies clay-to-silt lake deposits, and is mostly composed of mid-density subequant lapilli pumices and altered and oxidized lithics (Sections 2.5.2 and 2.5.3). The outcrops are fresh and can be easily accessed via a perlite mine that extracts layers from the *rle* unit 3 (Fig. 2.2d). The *rle* unit 1 can be recognized by the planar interbedding of two types of layers separated by sharp contacts: brown lithic-rich fine-grained and gray pumice-rich coarse-grained (Fig. 2.3b). The brown layers are mostly matrix-supported (except at the top) with a matrix composed of clay and silt (which retain water) and subequant and rounded clasts. The sequence is 1.3 m-thick and begins with a 21 cm-thick brown layer (Fig. 2.4) that is matrix-supported and contains clasts of <1 mm composed by altered and oxidized lithics and few pumices; no obsidian clasts were found. Brown layer *rle*1S1 was sampled for laboratory analyses. The thickness of the brown layers generally decreases upwards up to <1 cm-thick, and they have a higher content of coarser (<5 mm) pumices with increasing stratigraphic height. At the bottom (first 50 cm of the sequence), the brown layers are >10 cm-thick and have sedimentological features similar to *rle*1S1 but with a reddish alteration at the top. In the middle (50-80 cm), the brown layers are 6-10 cm-thick and have inverse and normal grading with a higher fraction of coarser pumices in the center. At the top (80-130 cm) the layers are thinner (<10 cm-thick) and have a higher fraction of coarse pumices.

The gray layers are clast-supported and contain subequant pumices, altered and oxidized lithics and minor obsidian clasts. These layers do not have the clay-to-silt matrix described in the brown layers and are commonly dry in field. The thickness (3-12 cm) and volume fraction of lithics slightly increase with stratigraphic height; as a whole, the pumices are >50% of the clasts. In the bottom 50 cm of the sequence, the gray layers are 3-5 cm-thick and have pumices of <2.0 cm, the lithics are subequant and angular, and include a few obsidians that are black

without vesicles. In the middle of the sequence (50-80 cm), the gray layers are 4-8 cm-thick and have the smallest maximum pumice size (<0.4 cm); the volume fraction of obsidians is higher than at the bottom and they are gray, less opaque and have some spherical bubbles. At the top, the gray layers are 7-12 cm-thick and contain coarser pumices (<1.6 cm) than in the middle, and a higher fraction of lithics. Two samples were collected from the gray layers for laboratory analyses, one from the bottom (*rle*1S2) and one from the top (*rle*1S3).

2.3.3. *rle* unit 2: A coarse-grain pumice-rich fall deposit with minor PDCs

The *rle* unit 1 is overlain in angular and erosive discordance by minor pyroclastic density currents (*rle* unit 2a) and a coarse-grained fall deposit (*rle* unit 2b), which at the bottom has the same components and grain size as the gray layers of the *rle* unit 1. The *rle* unit 2a is recognized in deposits <1.5 km from the vent as a sequence of layers forming sedimentary structures such as crossbedding and lenses with coarse mid-density pumices (Section 2.5.3). The layers of *rle* unit 2a are defined by changes of grain size, clast orientation and layer dip; changes of clast orientation and layer dip are abrupt, whilst changes of grain size are gradational except in pumice-rich lenses (Fig. 2.3c).

The *rle* unit 2a was analyzed at the same stratigraphic station as *rle* unit 1 (Fig. 2.2d). The thickness of unit 2a is irregular with an average of 1.1 m. At the base lie 20 cm-thick laminar strata with slight inverse grading and a maximum clast size of 1-4 cm. Clasts comprise ~70% pumices, ~25% lithics, and 5% obsidians. Above, showing angular and erosive unconformity in the contact, there is a 60-100 cm-thick section with sedimentary structures including crossbedding, lenses and inverse grading. These layers are very poorly sorted, clast supported with elongate and subangular clasts mostly oriented and parallel to layer orientation. The clasts are mostly (>90 vol.%) mid-to-high density pumices up to 20 cm; others are lithics from various sources (Sections 2.5.2 and 2.5.3). From this 60-100 cm-thick section with sedimentary

structures one sample was collected for laboratory analyses (*rle*2aS1). Above, it is a set of laminar layers, with crossbedding in some areas, poorly sorted and matrix supported with equant and subrounded clasts up to 4 cm showing reverse grading (Fig. 2.4). In this set of layers, two samples were collected, one from the bottom (*rle*2aS2) and the other from the top (*rle*2aS3).

The *rle* unit 2b is a sequence of several laminar pumice-rich layers in concordance with the *rle* unit 2a, and is more exposed to the east. The layers of *rle* unit 2b are defined by gradational changes of grain size and no important variations in the componentry as observed in field (Fig. 2.3d). The *rle* unit 2b is analyzed in areas B and C at eighteen stratigraphic stations (B1-8 and C3-12; Fig. 2.1b). In area C, the outcrops were mostly exposed by mining terraces (Fig. 2.2d), while in area B, some stepped sampling trenches (<3 m-high) were dug to the underlying clays from lake sediments or *rdm* tephra. The upper parts of the outcrops show reworking by gravity, while the two northern stations in this area showed reworking by fluvial and lake activity, as recognized by the good sorting and some rounding of the grains. Here I present a summary of the stratigraphic and sedimentological descriptions made in field for each area. The overall sequence presented at the end of this section was established through correlations based on distinctive variations of grain size and componentry among the layers.

In area C, *rle* unit 2b is ~12 m-thick and characterized by a sequence of multiple clast-supported layers that can be defined by transitional changes of grain size (Fig. 2.4). As a whole, there is a subtle normal grading at the bottom (≤1 m) followed by subtle reverse grading in the rest of the sequence; maximum clast sizes are 0.2-10 cm, and clasts are angular and subequant. The componentry shows ~70% dense pumices, ~15% obsidians, and ~15% lithics in the whole *rle* unit 2b; however, there is a higher fraction of lithics in the base, more noticeable in the coarser-grain layers, and the fraction of dense pumices and vesicular obsidian clasts increases with

stratigraphic height (Section 2.5.2). The clasts are angular and subequant. The top of this stratigraphic unit is defined by a <50 cm-thick pumice-rich and clast-supported layer that has the biggest pumices (<20 cm) of the entire fall deposit. These pumices are subelongate with elongated and oriented bubbles parallel to their long axes. Pumice comprises >90% of the clasts, while the others are vesicular obsidians. Six layers were sampled for laboratory analyses, one from a coarse-grained lithic-rich layer at the base (*rle*2bS1), one from the finest grained layer at 1 m (*rle*2bS2), three samples from three equidistant layers to represent the subtle inverse grading of *rle* unit 2 (*rle*2bS3-5) and one sample from the coarsest layer at the top (*rle*2bS6).

Correlation of the stratigraphic sequences in area B is not straightforward due to fluvial erosion and contact with pyroclastic deposits from other rhyolitic eruptions (both older and younger than Los Espejos). Five layers are defined by changes of grain size and componentry (Fig. 2.4). The entire *rle* sequence (~1 m-thick) here overlies a 3 cm-thick oxidized soil that separates the *rle* deposits from those of *rdm*. The first layer (~29 cm) show pulses of normal grading with a higher fraction of lithics at the base and is composed of dense pumices and lithics of different colors. The second layer (~20 cm) shows a similar componentry to the first and is inversely graded with a higher fraction of mid-density pumices of <2 cm diameter at the top. The third layer (~23 cm) is not graded and has a higher fraction of dense pumices and vesicular obsidians of <1.5 cm and <0.5 cm, respectively. Based on the variations of grain size and componentry, I determine that these three layers correspond to *rle* unit 2b. The fourth layer (~5 cm) has the coarsest grains (<5 cm) and the least dense pumice clasts of the sequence, which are subelongated with elongated bubbles; this layer corresponds to the top of the *rle* unit 2b (Section 2.5.3). Based on the defined stratigraphic sequence and the higher fraction of vesicular obsidians, the fifth layer (~18 cm) corresponds to *rle* unit 3 (Fig. 2.4).

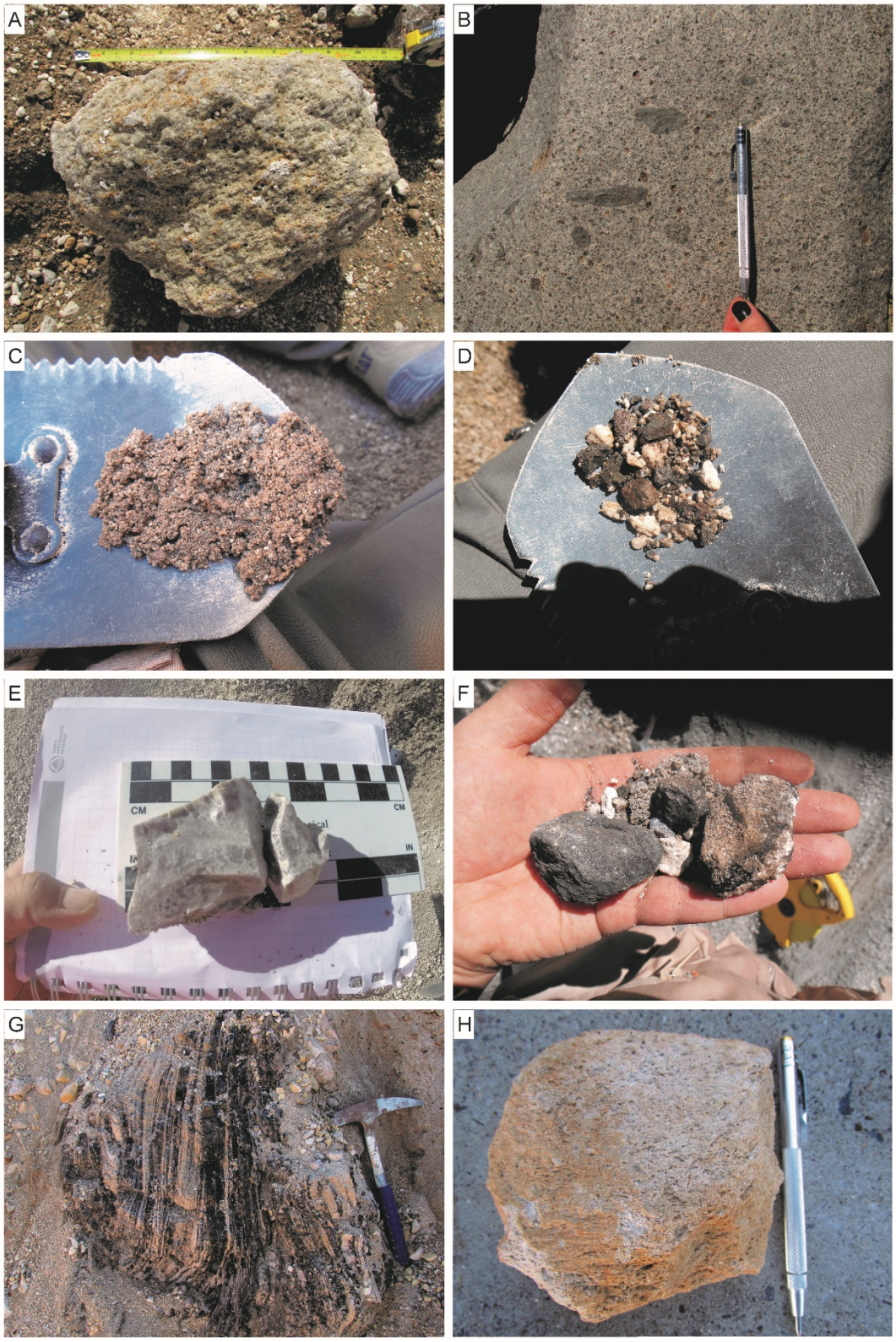

Fig. 2.5: Representative componentry found in field. A A big pumice of ~30 cm with tubular bubbles from the *rdm* 2b. **B** A granitoid lithic associated with the *rdm* 2. **C** Ash to lapilli from a brown layer of the *rle* 1. **D** Altered and oxidized lava lithics from the *rle* 2b. **E** Dense pumices of the *rle* fall deposit. **F** Examples of the vesicular obsidians from the *rle* fall deposit. **G** Banded obsidians from the *rle* lava flow. **H** Pumiceous obsidian from the *rle* lava flow.

2.3.4. *rle* unit 3: An obsidian-rich fall deposit

The *rle* unit 3 overlies the coarse-grained pumice-rich layer and is recognized by a higher vesicular obsidian content than the layers of the *rle* unit 2 (Fig. 2.3e). The *rle* unit 3 is formed by several planar layers defined by gradational changes of componentry and grain size. In the area C, a ~3 m-thick sequence is characterized by two subunits: the lower subunit is ~0.8 m-thick with multiple clast-supported layers, and the upper subunit is 2.2 m-thick, clast-supported and carries dense pumices of <8 cm. (Fig. 2.4). The layers of the lower subunit are defined by transitional changes of grain size and have a similar componentry to the top of the *rle* unit 2 but with smaller pumices (<3 cm), which are subequant and denser than those of *rle* unit 2b. The upper subunit is characterized by an increasing volume fraction of obsidians with stratigraphic height (Fig. 2.4). The pyroclastic obsidians can be vesicular or dense (bubble-free); vesicular obsidians have spherical bubbles distributed homogeneously or slightly elongated and oriented. The fraction of lithics also increases with stratigraphic height. No grading is observed in *rle* unit 3 except for some coarser grained layers at the top. In this area four layers were sampled, three equidistant from the base to the top to represent the increase of pyroclastic obsidian with height (*rle*3S1-2, *rle*3S4) and one from a coarser-grained layer (*rle*3S3).

The *rle* unit 3 is also found in area B as a ~18 cm-thick layer carrying <1 cm grains, overlying a layer with the biggest and most porous pumices (the top of the *rle* unit 2), and showing a higher fraction of vesicular obsidians.

2.3.5. *rle* unit 4: A lava flow

The *rle* eruptive sequence finishes with a 0.82 km^3 bi-lobate lava flow from the same vent as the pyroclastic deposits (Fig. 2.1a). One lobe went to the northwest and the other to the southwest; both are 2-3 km long and increase in thickness toward their front, up to 100 m,

which is decreased in the southern flow because of erosion by the lake. I collected samples and photographed the southern lobe ~2.2 km S30°W of the vent (Fig. 2.1b and 2.2e). The *rle* lava flow is crystal-poor with phenocrysts of plagioclase and biotite (as in the pyroclastic obsidians) and shows a wide variety of textures such as massive, amygdaloid massive filled by secondary minerals, pumice-banded, pumiceous, and tuffisite of millimetric to metric scale bands (Fig. 2.3f, 2.5g and h).

2.3.6. Summary of the tephra stratigraphy of Los Espejos

The Los Espejos fall deposit travelled to the ESE from a vent located in the NW of the LdM volcanic complex. The most distal outcrops are tens centimeters thick and are found at ~15 km from vent (Judy Fierstein and Patricia Sruoga, oral communication), while the thickness is ~17 m at 1 km from vent. The thicknesses of the *rle* outcrops are much less than observed in the *rdm* deposits at similar distances from the *rdm* vent. Both the thickness of layers and grain size within them decreases with distance from vent. The fall deposits are mostly pumice-rich and clast-supported, except for the brown layers of the *rle* unit 1, which are lithic-rich and matrix-supported. Most pumices are angular, subequant, dense and have vesicles that are difficult to see with naked eye, except for those from the top of the *rle* unit 2b, which are subelongate, less dense and have elongate bubbles oriented parallel to the main axis of the pumices. The pyroclastic obsidians are dark-gray, vesicular and have phenocrysts of plagioclase and biotite, as do the co-erupted pumice clasts and the obsidian lava flow. Pyroclastic obsidians are almost absent in the *rle* unit 1 and their abundance gradually increases with stratigraphic height in *rle* units 2 and 3. Neither dense microvesicular pumices nor pyroclastic obsidians are found in *rdm* deposits, which instead have low-density pumices and mafic vesicular juveniles.

In summary, four stratigraphic units of Los Espejos are defined (Table 2.5) from the older to the younger:

- The *rle* unit 1 is a planar interbedding of lithic-rich fine-grained matrix-supported layers with pumice-rich coarse-grained clast-supported layers. This sequence is in angular and erosive discordance with the *rle* unit 2.

- The *rle* unit 2 is a sequence of planar pumice-rich coarse-grained clast-supported layers that show coarser grains with the stratigraphic height and, at the top, a pumice-rich layer with subelongate and tubular pumices.

- The rle unit 3 is a sequence of planar coarse-grained clast-supported layers that show a higher fraction of vesicular obsidians with stratigraphic height.

- The *rle* unit 4 is a bi-lobate ~0.82 km^3 obsidian lava with variable bubble textures.

The sampled layers from the three tephra stratigraphic units were selected to quantify the variations of grain size, componentry and juvenile density with stratigraphic height (see sample descriptions in Supplementary Material). Those data are used to reconstruct the eruption styles of the different phases of Los Espejos event and to interpret the factors governing the transition to the lava flow formation.

2.4. Analytical methods

Nineteen samples of pyroclastic deposits (3 of *rdm*, 3 of *rle* unit 1, 3 of *rle* unit 2a, 6 of *rle* unit 2b, 4 of *rle* unit 3) were dried, sieved and weighed based on grain sizes between -5φ and ≥3φ with 1φ intervals for grain size distributions (GSDs). As the ≥3φ population is ≤10 wt.% in all the sieved samples, a finer separation was not carried out. The median, mean, sorting and skewness of the GSDs were estimated by Folk and Ward (1957). ~100 clasts from each unit in the -4φ to -2φ size range were selected for density measurements by Archimedes' method. The juveniles (pumices and obsidians) were weighed in air, covered by parafilm, weighed in air

with the parafilm and weighed in water with the parafilm to avoid water infiltration, following the procedure of Houghton and Wilson (1989). The pyroclasts were classified and counted by number and grain size population for componentry analysis.

Pumice clasts representative of the average density, and the average density ± the standard deviation, were selected for textural analysis. A matrix of ~100X magnification BSE images of 1024 x 768 pixels (1 pixel ~ 0.8 μm) with 10% overlap was run with scanning electron microscopy (Hitachi S3500) at the University of Bristol. The images were stitched in ImageJ (Preibisch et al., 2009). Three image layers were created to run textural analysis: background, bubbles and glass. The sample border was hand-marked to separate the bubbles from the background. Bubbles were selected by gray-scale thresholding and compared with the measured porosity. To calculate the porosity from the measured clast density, the matrix density is estimated from the glass composition according to Fluegel (2007). Further operations to separate bubbles were not applied. Bubble textures of 3 to 10 images of 200X-1000X magnification (1 pixel ~ 0.4-0.08 μm) were analyzed using the same procedure. Bubble number densities (BNDs) were estimated by counting the number of bubbles per unit of area of groundmass glass (N_A, mm^{-2}); thus, the area covered by crystals and bubbles is not considered for number density calculations. We plot bubble size distributions (BSDs) as the decreasing cumulative bubble number density with the equivalent diameter (N_A [mm^{-2}] > L) to interpret patterns of bubble nucleation during eruption, and as the decreasing cumulative bubble area fraction (or porosity) with the equivalent diameter to obtain insights into bubble growth during the eruption; both diagrams are also used to infer bubble coalescence (e.g., Shea et al., 2010). The interpretations of the vesiculation from BSD analyses in the *rle* juveniles are supported by visual descriptions from the 2D BSEM images. BSEM images of 50X-300X are used to describe qualitatively bubble textures in pyroclastic obsidians. Due to the low bubble number density, stitched BSE images were not constructed.

2.5. Results of physical parameters

Here I integrate the field observations with the analysis and measurements of physical parameters such as grain size distributions (GSDs), componentry analysis, density measurements, descriptions of bubble textures, bubble number density (N_A) and bubble size distributions (BSD). The physical parameters are presented in a stratigraphic context to give a temporal perspective of the eruption processes. In particular, the volume fraction of obsidian clasts and the bubble textures within juveniles are used to speculate about the origin of the pyroclastic obsidians and their potential link with the obsidian lava flow formation. The data of *rdm* deposits is presented for comparison with *rle*.

2.5.1. Grain size distributions

The calculated median and average grain size, standard deviation (sorting) and skewness of grain size distributions are presented in Table 2.6 and Fig. 2.6 (See the complete datasets in Supplementary Material). The pyroclastic deposit of the *rdm* 2 (*rdm*2S1-3) has reverse grading and similar median and average sizes, sorting and skewness as those from the intermediate-upper part (*rle*2bS4-5) of the *rle* unit 2b.

Sample *rle*1S1 from the brown layer at the bottom is the only sample of the *rle* suite with a positive φ mode, median and average and a small tail of bigger grains. The GSDs of the gray layers (*rle*1S2-3) are coarser than *rle*1S1, with a slightly coarser median size, poorer sorting and more positive skewness at the top (*rle*1S3).

GSDs of unit 2a show the difference of grain sizes between the lenses of bigger clasts and the upper part with sedimentary structures and reverse grading. Sample *rle*2aS1, a lens of coarse clasts, is well-sorted, comparable with the sorting of the *rle* 1 layers but coarser, with a median and average grain size of ~-4φ. We note, however, that this size is underestimated because

there were bigger clasts in the deposit that could not be sampled. On the other hand, both *rle*2aS2 and the *rle*2aS3 samples are poorly sorted with a slightly increasing median and average grain size with the stratigraphic height.

Table 2.6: Median and average grain size, standard deviation (sorting) and skewness of grain size distributions calculated by Folk and Ward (1957).

Unit	Sample	Median [φ]	Average [φ]	Std. Dev. [φ]	Skewness [φ]
rdm 2	S1	-1.71	-1.64	1.27	0.31
rdm 2	S2	-3.53	-3.36	1.34	0.30
rdm 2	S3	-4.32	-3.82	1.54	0.69
rle 1	S1	0.65	0.60	1.49	-0.05
rle 1	S2	-2.23	-2.14	1.20	0.16
rle 1	S3	-2.80	-2.55	1.47	0.32
rle 2a	S1	-4.04	-3.99	1.20	0.25
rle 2a	S2	-0.94	-1.10	2.41	-0.05
rle 2a	S3	-1.88	-1.70	2.09	0.18
rle 2b	S1	-2.13	-2.08	1.38	0.08
rle 2b	S2	-0.54	-0.41	2.12	0.05
rle 2b	S3	-2.00	-1.95	1.80	0.10
rle 2b	S4	-3.03	-2.70	1.50	0.39
rle 2b	S5	-3.72	-3.45	1.66	0.31
rle 2b	S6	-5.26	-4.97	0.69	0.72
rle 3	S1	-1.03	-0.92	2.15	0.09
rle 3	S2	-1.36	-1.14	1.98	0.16
rle 3	S3	-2.70	-2.62	2.16	0.15
rle 3	S4	-1.32	-1.25	2.27	0.04

The samples in the lower part of the *rle* unit 2b (*rle*2bS1-2) record normal grading at the bottom of the sequence and have a symmetric (log-normal) grain size distribution. The *rle*2bS2 sample has the finest grains and the poorest sorting of *rle* unit 2b. With increasing stratigraphic height, samples (*rle*2bS3-6) are coarser, better-sorted, and have longer tails to the smaller grains. In particular, *rle*2bS6 (the layer at the top of the *rle* 2b unit) is the coarsest, best-sorted and has the most positive skewness of the whole *rle* fall deposit.

Most of the layers from *rle* unit 3 (*rle*3S1-2 and *rle*3S4) have symmetric grain size distributions and are finer and more poorly sorted than those from *rle* unit 2b. The sample representative of the coarsest grained layer (*rle*3S3) has a larger median and average grain sizes, but with similar sorting and skewness to the other layers of the *rle* unit 3.

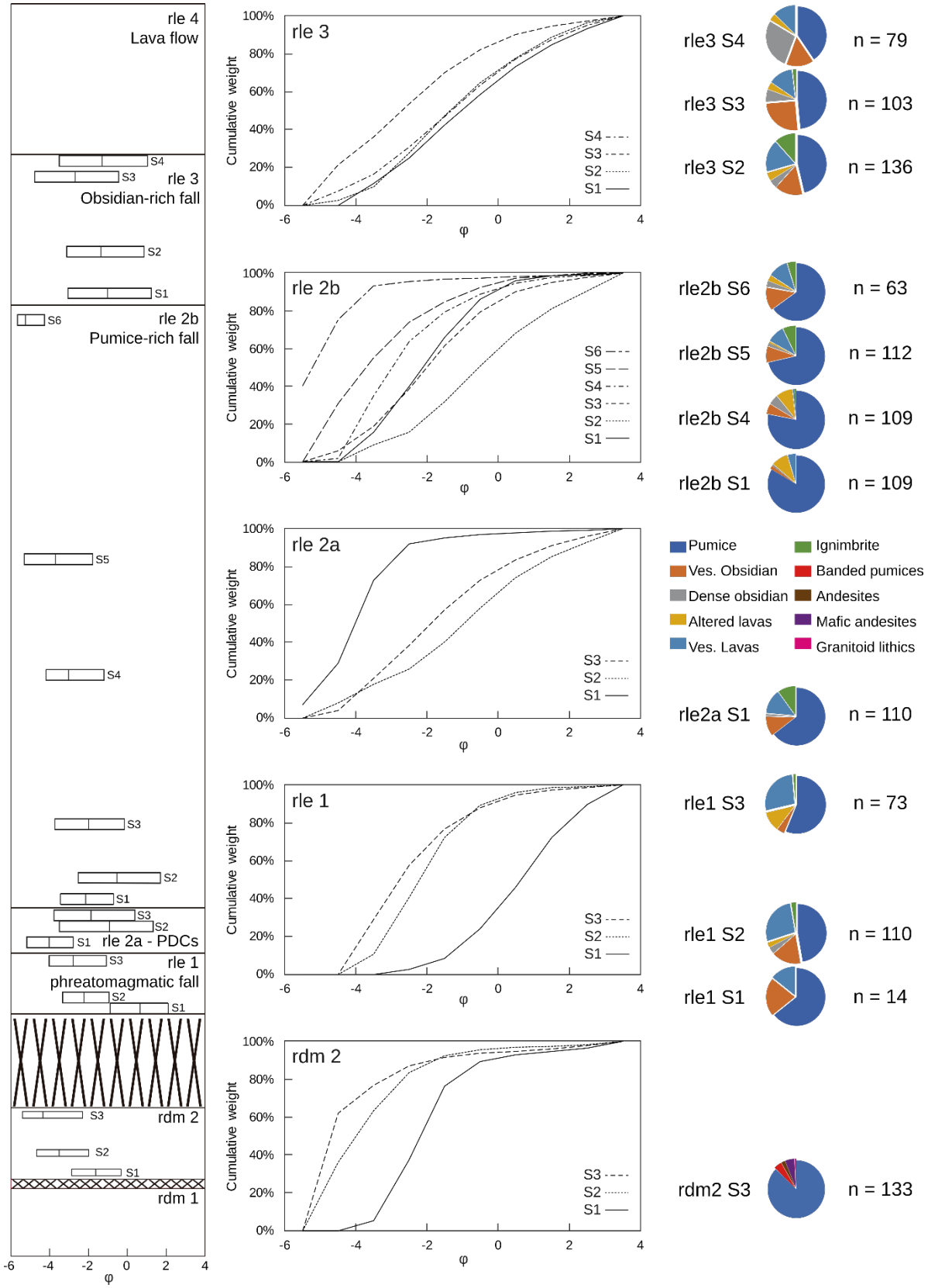

Fig. 2.6: Grain size distributions and componentry of *rdm* and *rle*. The bars represent the median size and the average ± the standard deviation and are located in stratigraphic order but the stratigraphic heights between *rdm* and *rle* deposits are not proportional. The full grain size data are plotted cumulatively in the central column. The componentry analysis (pie charts) was made by hand-picking in -4φ to -2φ populations.

2.5.2. Componentry analysis

2.5.2.1. Description of components

The components of the <-1φ population from both *rle* and *rdm* deposits are classified according to morphology, textures, color, and vesicularity to give insights about the origin of the clasts. All pumice types are included in a single group; pyroclastic obsidians are separated into dense and vesicular clasts due to the possibility that the former group could be lithics derived from older flows and the latter could be juveniles. The lithics are separated in three groups and related to underlying units to approximate the depth of lithic excavation during the magma ascent. The same rationale is applied to the *rdm* components in which the pumices with mafic enclaves are separated from the other pumices (regardless of bubble textures) in order to quantify the interaction with mafic magmas. Mafic juveniles are separated by color (blue or gray) to show the interaction of the rhyolites with mafic magmas of various compositions. The following ten components are classified: (1) pumices, (2) pumices with mafic blobs, (3) vesicular obsidians, (4) dense obsidians, (5) andesitic juveniles, (6) mafic andesitic juveniles, (7) altered angular mafic lavas and tuffs, (8) altered rounded mafic volcanic clasts, (9) granitoid lithics, (10) ignimbrites.

Pumices are the major components in both *rdm* and *rle* deposits and they show a wide variety of morphologies and textures (Fig. 2.5a and 2.5e). In the *rdm* deposits, the most common pumice type is elongated to subelongated (Fig. 2.7a) and has an intermediate density with tubular bubbles of some millimeters width (Fig. 2.5a). This type of pumice is aphyric in the deposits at station A1 and is crystal poor with phenocrysts of plagioclase, hornblende and minor pyroxene in the deposits at station A2. The *rdm* deposits also include foamy, banded and mid-to-high density aphyric pumices. The foamy pumices are low-density, very fragile, and have spherical bubbles of <1 cm (Fig. 2.7b); the banded pumices have parallel planes that separate

different textural domains of elongated bubbles; and the mid-to-high density pumices have flattened elongate bubbles. In the *rle* deposits, the most common pumices are mid-to-high density and contain small bubbles (Fig. 2.5e and 2.7c). In the field, it is difficult to define these as pumices because the bubbles are so small that they appear similar to the pieces of tertiary ignimbrites (see below); however, the pumices are less dense, have plagioclase and biotite phenocrysts and do not have argillic alteration. The *rle* deposits also have intermediate densities and elongate pumices with subelongated bubbles (Fig. 2.7d) which are mostly in the top part of the *rle* unit 2 (*rle*2bS6).

Pumices with mafic enclaves are exclusive to the *rdm* deposits. They have the same bubble textures and crystallinities of the elongate pumices with tubular bubbles described above but with millimetric to centimetric blue and/or gray enclaves with the same petrographic and textural features of the mafic juveniles described below. Each pumice has a few enclaves that are typically deformed in the orientation of the bubbles.

Vesicular obsidians are found in the *rle* pyroclastic deposits (Fig. 2.5f). They are gray to black and have spherical to elongated millimetric bubbles (Fig. 2.7e). The elongated bubbles form bands together with plagioclase, biotite and oxide microcrysts. The obsidians are crystal poor and contain the same mineralogy as the pumices.

Dense obsidians are mostly found in the *rle* units 1 and 3. These clasts are black and a few bubbles which are small and elongate (Fig. 2.7f). They have the same mineralogy as the co-erupted pumices and vesicular obsidians of the *rle* pyroclastic deposits.

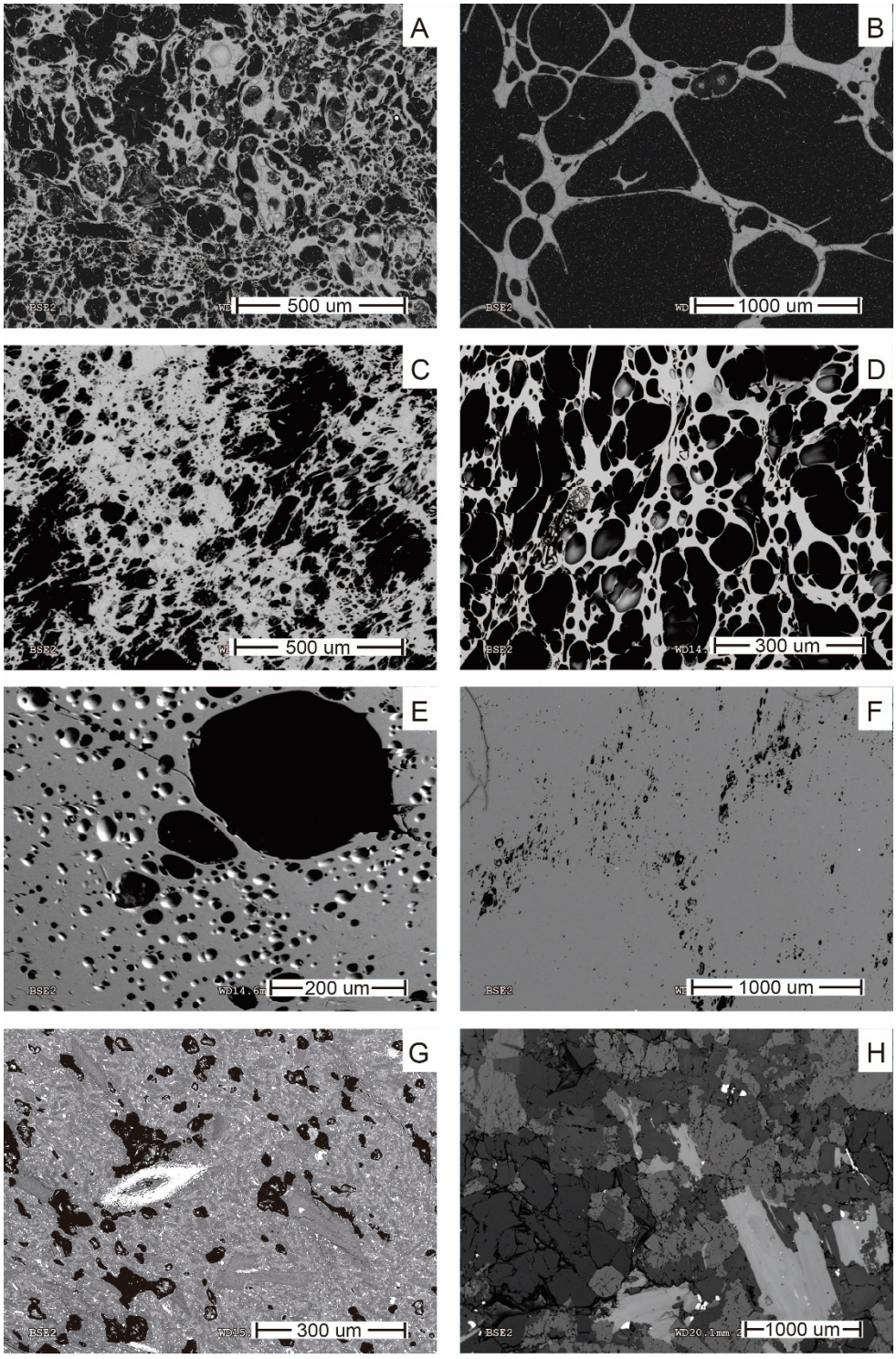

Fig. 2.7: BSE images of the most representative *rdm* and *rle* clasts. A A mid-density pumice from *rdm*. **B** A foamy pumice from *rdm*. **C** A mid-to-high density pumice from *rle*. Note the heterogeneities of porosity, bubble size and number density within the pumice clasts. **D** A mid-density pumice with subelongated bubbles from *rle*. **E** A vesicular obsidian clast showing two size populations of bubbles from *rle*. **F** A dense obsidian clast showing small elongate and oriented bubbles from *rle*. **G** Mafic andesitic juvenile clasts from *rdm*. The scoriaceous clasts have phenocrysts of plagioclase, olivine and hornblende; the latter show strong disequilibrium textures. **H** A granitoid lithic from *rdm* which contains k-feldspar phenocrysts.

Andesitic juveniles are found in the *rdm* deposits. They are fresh and have millimetric subelongated bubbles. The andesitic juveniles are gray and have phenocrysts of plagioclase and elongated to acicular hornblende.

Mafic andesitic juveniles are found in the *rdm* deposits and where studied are more abundant than the andesitic juveniles. They are almost fresh showing a white alteration in the clast surfaces and have millimetric subelongated bubbles. The mafic andesitic juveniles are blue and have phenocrysts of plagioclase and olivine with porphyritic to glomeroporphyritic textures (Fig. 2.7g).

Angular vesicular mafic lavas and tuffs are mostly found in the *rle* units 2 and 3 (Fig. 2.5d). They are angular, elongated to subelongated, gray-green and gray-blue. In the case of lavas, they have a low porosity formed by spherical millimetric bubbles; in the case of tuffs, they show clasts of red to green volcanic rocks. Based on the geographic proximity and similarities with the descriptions of Hildreth et al. (2010), these lithics likely come from lavas and tuffs from the Volcan Atravesado.

Ignimbrites comprise white to yellowish tuffs, mostly found in the *rle* units 1 and 2. They are angular and equant lithics of millimeters to centimeters in size. If they do not show argillic alteration, which gives them a yellow to brown color on the surface; instead they are white, similar but of a higher density than the *rle* pumices. Due to the geographic proximity and similarities of the petrographic features, I think that these lithics correspond to tuffs of the Pleistocene ignimbrite of Cajones de Bobadilla (Hildreth et al., 2010).

Altered rounded mafic volcanic clasts are mostly found in *rle* units 1 and 2. They are rounded and oblate, and show various colors such as black, gray, blue and red. They do not have bubbles and it is difficult to distinguish the type of phenocrysts because of the pervasive alteration or oxidation. Based on the color and mineral content they likely have intermediate to mafic compositions; considering their pervasive alteration and lack of bubbles, these lithics likely come from the Oligocene to Pliocene volcanic rocks of the LdM basement.

Granitoid lithics are associated with the *rdm* deposits and appear around the lake, mostly along the northern shoreline (Fig. 2.5b). They appear as blocks of millimetric to metric scale inside or near the *rdm* deposits despite the absence of exposed igneous bodies within the LdM volcanic complex. They are mostly gray and contain phenocrysts of plagioclase, quartz, biotite and hornblende; in the case of some pink granitoids, they contain k-feldspar phenocrysts (Fig. 2.7h). Based on the similar mineralogy to the LdM postglacial rhyolites and the absence of igneous bodies on surface, Singer et al. (2014) and Fierstein (2018) suggest that these granitoid are pieces of the silicic crystal mush below LdM, which were entrained during the *rdm* eruption.

2.5.2.2. Componentry in the stratigraphic context

The number fraction of components is quantified for each sampled layer and placed in the context of the stratigraphy described above (Fig. 2.6). In the grain size range of -4φ – -2φ, the proportion of clast types is nearly independent of the clast size. >85% of clasts of the *rdm* fall deposit are pumices. If pumices with mafic enclaves are considered, pumices are >90%. The number of mafic lithics is too small to distinguish relative fractions between mafic andesites and andesites (7 vs 3 of a total number of grains = 133). I just counted one granitoid of -2φ size.

The componentry analysis of the *rle*1S1 sample is not representative because only 14 clasts of the -2φ population were counted, consisting of >50% of pumices, altered rounded mafic lithics, and vesicular obsidians; however, our field observations suggest that the number fraction of pumices is lower and the number fraction of lithics is higher than was quantified. The number fraction of angular mafic lithics is similar (>25%) in both *rle*1S2-3 samples, but the number fraction of pumices (~50-60%) and altered rounded mafic lithics (~1-16%) increases, and the number fraction of obsidians decreases (20-3%) with the stratigraphic height.

The *rle*2aS1 sample consists of ~65% of pumices and ~10-12% of each vesicular obsidian, altered rounded mafic lithics and tertiary ignimbrites. The componentry of the *rle*2aS2-3 samples was not quantified.

Pumices are the most important component in *rle* unit 2b; pumice abundance slightly decreases with stratigraphic height (from 85 to 70%). The altered rounded mafic lithics are ~10% in the *rle*2bS1-4 but are almost absent in the *rle*2bS5-6. Both vesicular obsidians and angular vesicular mafic lithics are minor components that increase with stratigraphic height (1-15%).

The number fraction of pumices is similar in *rle*3S1-3 (50%) and slightly decreases at the top (40% in *rle*3S4). The number fraction of dense obsidians is marginal in *rle*3S1-3 (5%) and sharply increases in *rle*3S4 (25%); vesicular obsidians are nearly constant in the whole *rle* unit 3 (20-25%). The proportion of both angular vesicular mafic lithics and tertiary ignimbrites decreases with stratigraphic height.

2.5.3. Juvenile densities

Pumice is the most abundant component in both *rdm* and *rle* deposits; however, they show a range of textures and densities. In particular, the *rle* deposits include dense pumices and vesicular obsidian clasts which may be confused with each other. To determine numerically

the diversity of juvenile densities and variations of the density clasts with stratigraphic height, I measure the density of 70-120 juvenile clasts from layers of units *rdm* 2, *rle* 1, *rle* 2, and *rle* 3 (Supplementary Material). Therefore, I measure the density from two pumice cylinders of *rdm* 1.

The density of two 15 mm-diameter cylinders of one frothy pumice and one banded pumice from the *rdm* deposits of the station A1 are 0.27 g cm^{-3} and 0.67 g cm^{-3} respectively. The density histogram of pumices from the *rdm* deposits in the station A2 shows a narrow unimodal distribution with a mode of 0.85 g cm^{-3} and a small tail of higher densities (Fig. 2.8). Pumice density is not correlated with the pumice size.

The densities of pumices, vesicular obsidians and dense obsidians of *rle* are presented together in Fig. 2.8, although the biggest juvenile clasts (-4φ) are slightly less dense than the smallest juvenile clasts for most of the sampled layers. As for other physical parameters, the density data are presented in the context of the stratigraphy described above.

As in the componentry analysis, the number of juvenile clasts in *rle*1S1 is not sufficient to be representative, but the density distribution shows two peaks of 1.2 and 2.1 g cm^{-3} corresponding to the pumices and obsidians. Samples *rle*1S2-3 also show a bimodal density distribution, documenting the presence of both pumice and obsidian clasts. Pumice density decreases with pumice size and stratigraphic height, and the density distribution is narrower with increasing stratigraphic height (an average of 1.03±0.17 g cm^{-3} in the *rle*1S2 versus an average of 0.86±0.07 g cm^{-3} in *rle*1S3). The difference between the modes of pumice and obsidian densities is also greater in *rle*1S3.

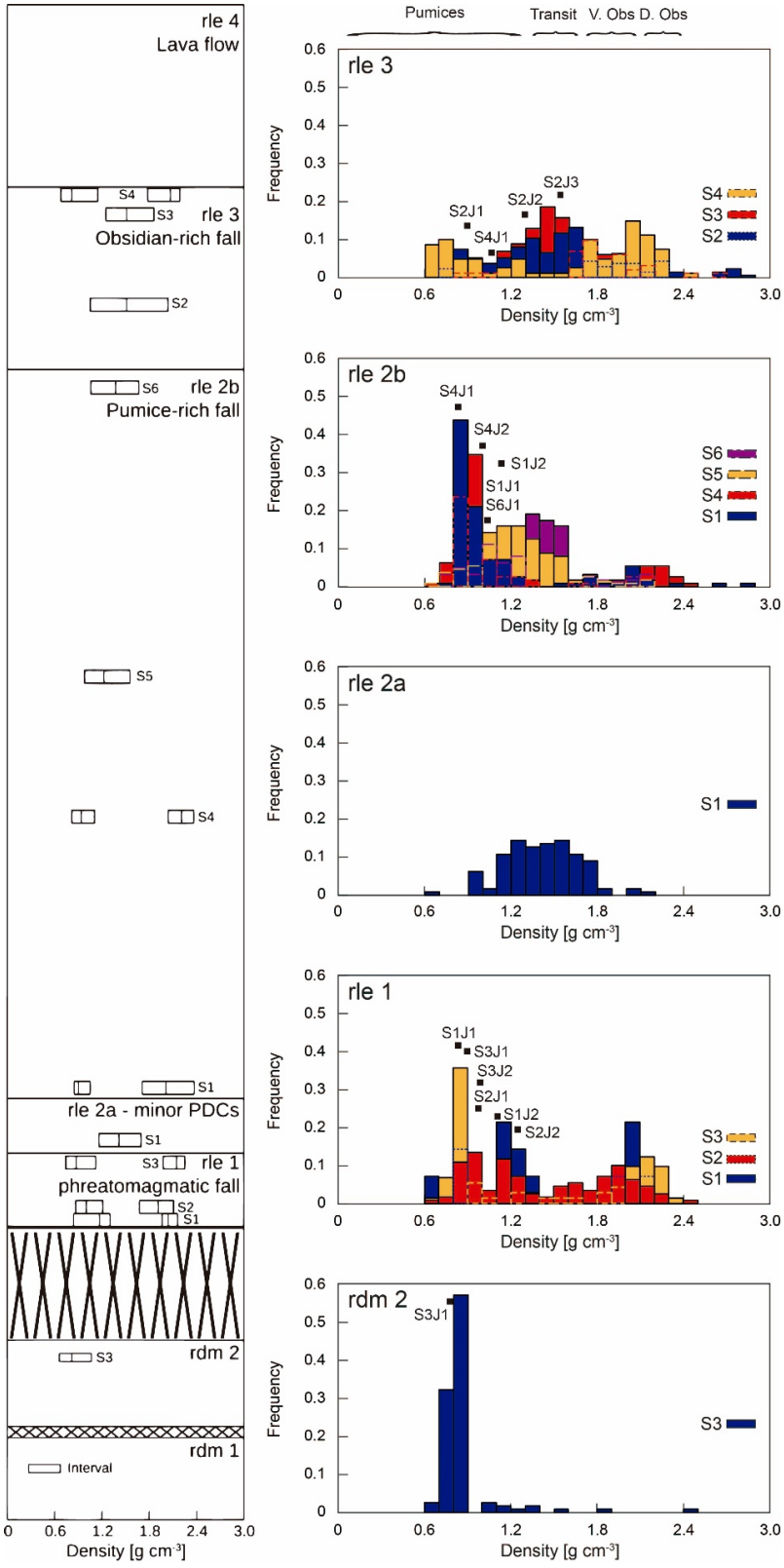

Fig. 2.8: Density distributions of juvenile pyroclasts. The bars indicate the median density and the average density ± the standard deviation. The bimodal distributions are represented by two bars corresponding to each mode. The density histograms were done for juveniles of -4φ – -2φ size showing decreasing densities with juvenile size. Black squares represent the samples used for bubble textural analysis. Above density histograms, ranges show the type of juvenile clasts, where "transit" is a transition between pumice and obsidian, "V. Obs" is vesiculated obsidian, and "D. Obs" is dense obsidians.

The juveniles of *rle*2aS1 show a broad unimodal density distribution (average of 1.42±0.26 g cm^{-3}), with a mode markedly higher than the modes of the pumices in the *rle* unit 1 (Fig. 2.8). Pumice density does not depend on the pumice size.

The density histograms of samples *rle*2bS1-4 show bimodal distributions with pumice modes of 0.85 and 0.95 g cm^{-3} and modes of obsidian clasts between 1.8 and 2.0 g cm^{-3}. By contrast, the density distributions of *rle*2bS5-6 are unimodal and show wide density ranges; the average densities increase with stratigraphic height (from 0.95±0.12 g cm^{-3} to 1.29±0.23 g cm^{-3}).

The density distributions of *rle*3S1-3 are unimodal with dense modes (~1.5 g cm^{-3}) and have the widest ranges of the whole *rle* fall deposit (averages of ~1.55±0.50 g cm^{-3}). The *rle*3S4 samples have a bimodal distribution with less dense pumices (average of 0.91 g cm^{-3}) and low-density obsidian clasts (average of 1.99 g cm^{-3}).

In general, average densities and density ranges of the *rle* pumices are higher and wider, respectively, than those of the *rdm* pyroclastic deposits.

2.5.4. Bubble textural analysis

The most representative pumices of each sampled layer according to the density distributions were selected for bubble textural analysis (see the BSEM images in Supplementary Material). The segmented area fraction of bubbles from 2D BSEM images is well correlated to the porosity calculated from the measured clast density (Fig. 2.9). Herein I describe sizes, shapes and elongation of bubbles (Fig. 2.10 and 2.11) and present quantitative analyses (see the complete datasets in Supplementary Material) such as bubble size distributions (BSD; Fig. 2.12) and bubble number density (BND; Fig. 2.13). The 2D textural data are not numerically corrected to 3D to avoid assumptions of the rock fabric, bubble shapes, projected areas and cutting probabilities (e.g., Higgins, 2002; Sahagian and Proussevitch, 1998). Additionally,

some obsidian clasts from different sectors and layers were selected for the description of sizes, shapes and elongation of bubbles (Fig. 2.14). Textural analyses are presented in a stratigraphic context to show the evolution of the vesiculation during the Los Espejos eruption. The pumices are named based on the bulk sample that they are from (e.g., *rle*1S1) and an index that increases with the pumice density (e.g., J1...JN; Table 2.7). The dependence of the bubble textures on pumice density is analyzed for each layer. In particular, pumices from unit *rle* 2a are not analyzed so the name *rle*2SXJY refers to pumices from the *rle* 2b by default. The bubble textures of one frothy pumice from *rdm* and one perpendicular section to the main orientation of an elongate tube pumice with a density corresponding to the mode of the *rdm* density distribution are analyzed for comparison with the Los Espejos sample suite.

Table 2.7: Summary of the main physical and textural parameters. The porosity is estimated from the clast density considering a matrix density of 2.34 g cm^{-3} calculated by Fluegel (2007).

Unit	Station	Juvenile clast	Density [g cm^{-3}]	Porosity	Total number of bubbles analysed	Area of rock [mm^2]	Area of groundmass [mm^2]	N_A [x 10^3 mm^{-2}]	Max. bubble size - equivalent diameter [mm]
*rdm*1	A1	S1J1	0.27	0.88	17,068	426.01	41.63	0.41	2.149
*rdm*2	A2	S3J1	0.77	0.67	263,507	146.57	55.01	4.79	2.991
*rle*1	C2-6	S1J1	0.83	0.65	47,341	49.67	16.21	2.92	0.773
*rle*1	C2-6	S1J2	1.10	0.53	48,976	46.82	22.99	2.13	0.560
*rle*1	C2-6	S2J1	0.97	0.59	113,737	179.14	70.21	1.62	2.585
*rle*1	C2-6	S2J2	1.24	0.47	125,121	190.50	106.03	1.18	2.510
*rle*1	C2-6	S3J1	0.89	0.62	70,815	59.83	20.65	3.43	1.337
*rle*1	C2-6	S3J2	0.98	0.58	90,730	66.46	29.62	3.30	1.564
*rle*2b	C2-6	S1J1	1.03	0.56	73,685	77.90	36.12	2.04	0.533
*rle*2b	C2-6	S1J2	1.09	0.53	83,378	110.83	54.14	1.54	1.025
*rle*2b	C2-6	S4J1	0.83	0.65	80,342	90.82	34.78	2.31	0.920
*rle*2b	C2-6	S4J2	1.00	0.57	38,913	41.03	17.85	2.18	0.591
*rle*2b	C2-6	S6J1	1.03	0.56	187,924	243.20	116.72	1.61	2.143
*rle*3	C2-6	S2J1	0.89	0.62	46,065	86.62	29.91	1.54	1.572
*rle*3	C2-6	S2J2	1.29	0.45	128,604	141.32	77.47	1.66	0.590
*rle*3	C2-6	S2J3	1.54	0.34	80,741	102.27	71.45	1.13	0.564
*rle*3	C2-6	S4J1	1.06	0.55	33,034	32.67	14,24	2.32	0.452

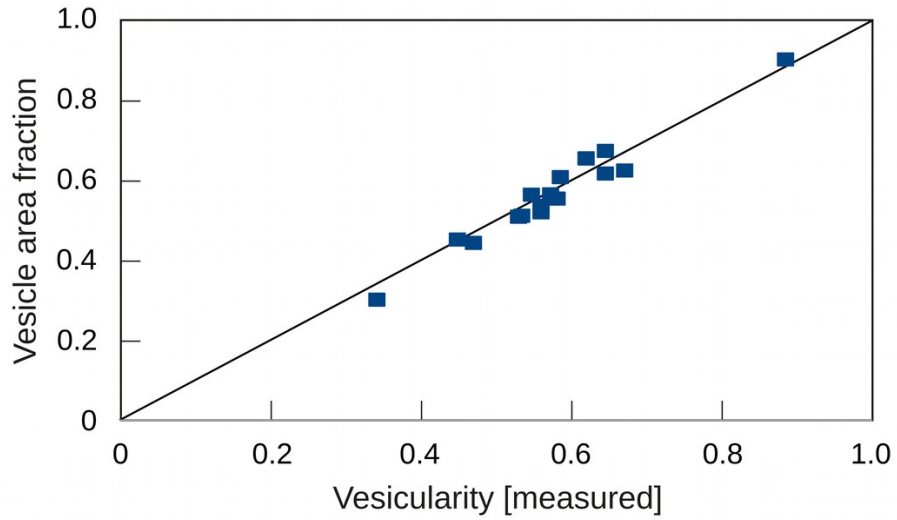

Fig. 2.9: Comparison between the vesicularity calculated from the measured density clast and the area fraction of vesicles in the segmented 2D BSEM images. The difference between both parameters is lower than 0.1 for all the pumice clasts.

2.5.4.1. Rhyolite of Laguna del Maule (rdm 1 and 2)

The frothy pumice (rdm1S1J1) shows big (>200 µm) nearly equant bubbles separated by thin (<50 µm) bubble walls (Fig. 2.10a) that may be coalesced and have colloform shapes (Fig. 2.11a). A few smaller bubbles (<30 µm) are spherical and occur within the thickest bubble walls (Fig. 2.11b). The tubular pumice (rdm1S3J1) have elongate bubbles with straight rims (Fig. 2.10b) which may coalesce and form irregular to colloform shapes (Fig. 2.11c). The smallest bubbles (<150 µm-long) are very elongated (>10 µm-wide) and parallel the biggest bubbles (Fig. 2.11d). The cumulative bubble number density of the tubular pumice (rdm1S3J1) increases more rapidly (with decreasing bubble size) than in the frothy pumice (rdm1S1J1). The frothy pumice also has larger bubbles (> ~60 µm) than the tubular pumice, which has numerous smaller bubbles (Fig. 2.12a). The cumulative area fraction of the frothy pumice is higher than the tubular pumice for all bubble sizes; in particular, the *rdm* frothy pumice has a very high cumulative area fraction (~0.8) for the bubbles >200 µm (Fig. 2.12b). By contrast, the tubular pumice has a sigmoidal cumulative area fraction with kinks at 10 and 1000 µm. The very low density (0.27 g cm^{-3}) frothy pumice has the lowest (total) bubble number density analyzed (Fig. 2.13) while the tubular pumice of more typical density (0.77 g cm^{-3}) has the

highest N_A and the greatest maximum bubble size (circle-equivalent diameter of 3 mm; Table 2.7).

2.5.4.2. Rhyolite of Los Espejos unit 1

Pumice samples from both *rle*1S1J1 and *rle*1S1J2 samples have big bubbles with irregular angular to spherical colloform shapes and nearly spherical small bubbles with rounded rims. The bubbles of *rle*1S1J1 pumice are bigger than those from the *rle*1S1J2 (maximum sizes of 0.8 and 0.5 mm respectively) and the cumulative number density and the cumulative area fraction are higher in the *rle*1S1J1 pumice for all bubble sizes (Fig. 2.12c and 2.12d). The cumulative area distributions of both *rle*1S1 pumices are nearly sigmoidal but show kinks for bubble sizes of tens of microns (*rle*1S1J1 ~ 30 μm and *rle*1S1J2 ~ 10 μm) and for the biggest bubbles (*rle*1S1J1 ~ 500 μm and *rle*1S1J2 ~ 300 μm). In the *rle*1S1 pumices the bubble number density per unit of area (N_A) increases with decreasing pumice density (Fig. 2.13).

Both *rle*1S2J1 and *rle*1S2J2 pumices have small subelongated and oriented bubbles with rounded rims (Fig. 2.11f) and big bubbles with colloform shapes and rounded rims (Fig. 2.11e) that are the largest of the whole Los Espejos sample suite (Table 2.7). The *rle*1S2J1 have higher cumulative number density and cumulative area fraction than from *rle*1S2J2 for all bubble sizes (Fig. 2.12c and 2.12d). Both *rle*1S2 pumices have a sigmoidal cumulative area fraction (Fig. 2.12d) with kinks at bubble sizes of tens of microns (*rle*1S2J1 ~ 20 μm and *rle*1S2J2 ~ 40 μm) and a second one for the biggest bubbles (*rle*1S2J1 ~ 300 μm and *rle*1S2J2 ~ 700 μm). These two pumices have the lowest N_A of the *rle* 1 samples and show a subtle increase in N_A with decreasing pumice density (Fig. 2.13). The biggest bubbles (<1.6 mm) of the *rle*1S3J1 have complex and rounded shapes, whilst the smallest bubbles are equant (Fig. 2.10c). The *rle*1S3J2 pumice have similar bubble shapes as the *rle*1S3J1 but contain smaller bubbles that are homogeneously distributed even around plagioclase phenocrysts (Fig. 2.10d). Both *rle*1S3

pumices have a sigmoidal cumulative area fraction with kinks at 20 μm and 200 μm, and have the same bubble area fraction for the bubbles >100 μm that diverge for the smallest bubbles (Fig. 2.12d). The *rle*1S3 pumices have the highest N_A of the Los Espejos suite (Table 2.7), and N_A increases slightly with decreasing the pumice density as in the other *rle* 1 layers (Fig. 2.13). In summary, in the gray layers (*rle*1S2-3) the pumices show sigmoidal cumulative area fractions which decrease with the stratigraphic height (*rle*1S3); in both layers N_A increases with decreasing the pumice density, and N_A is higher in the *rle*1S3 pumices.

2.5.4.3. Rhyolite of Los Espejos unit 2

Pumices from *rle* unit 2 have the narrowest ranges of density and N_A of the Los Espejos suite (Table 2.7). N_A increases only slightly with decreasing pumice density, in contrast to the strong trend in *rle* 1 pumices (Fig. 2.13). The *rle*2S1-4 pumices have big subelongated bubbles with colloform rounded shapes and their smallest bubbles are mostly spherical to subelongated and oriented. These pumices have heterogeneous bubble number density, size, shape and aspect ratio (Fig. 2.10e). For instance, a low number density of big and spherical bubbles surround plagioclase phenocrysts (Fig. 2.10f) and areas of stretched and oriented bubbles surround domains that encircle the biggest bubbles together with the smallest equant bubbles. In general, the domains of higher porosities show both a higher number density and bigger bubbles than domains of lower porosities (Fig. 2.11g). Pumice samples *rle*2S1-4 have similar cumulative number densities that merge at 100-200 μm (Fig. 2.12e), and have similar cumulative area fraction that have one kink at ~20-30 μm (Fig. 2.12f). The rle2S4J1 (the least dense of the *rle*2S1-4 pumices) has the highest cumulative area fraction of the *rle*2S1-4 pumices for any bubble size (Fig. 2.12f).

Sample *rle*2S6J1 has a cumulative number density similar to other *rle*2 pumices (Fig. 2.12e and 2.13), but different bubble shapes. Here the biggest bubbles (>0.2 mm) are subelongated

with complex and irregular shapes, while the smallest bubbles are flattened and oriented forming trends of deformation. In the extremes of the trends of deformation, there are small equant bubbles with angular rims (Fig. 2.11h). Pumice *rle*2S6J1 is the only of the *rle*2 pumice showing a sigmoidal cumulative area fraction with kinks at 40 and 1000 μm (Fig. 2.12f).

2.5.4.4. Rhyolite of Los Espejos unit 3

Bubble heterogeneities are clearer in the *rle* 3 pumices than in the *rle* 2 pumices (Fig. 2.10g). The big bubbles occur in clusters or surrounding plagioclase phenocrysts (Fig. 2.11i), and the contrast between domains of low number density and high number density is stronger (Fig. 2.10h). Shear localization and deformation of oriented bubbles isolates domains without deformation. In the *rle*3S2J1 pumice (the least dense of the *rle* 3 pumices), the biggest bubbles (~1.6 mm) have irregular to colloform shapes and are distributed in clusters, while some of the smallest bubbles are flattened (Fig. 2.11j). The other *rle* 3 pumices show similar bubble shapes, but with a lower number density and smaller bubbles (maximum sizes = 0.4-0.6 mm). The *rle* 3 pumices show two trends of N_A with pumice density (Fig. 2.13): N_A increases (1.5-2.3 x 10^3 mm^{-2}) with the pumice density for 0.8-1.0 g cm^{-3}, but decreases (2.3-1.1 x 10^3 mm^{-2}) for densities of 1.0-1.6 g cm^{-3}. These pumices show a kink at ~20 μm in the cumulative area fraction plot (Fig. 2.12h). By contrast, the *rle*3S2J1 (0.89 g cm^{-3}) has the highest N_A of the *rle* unit 3 samples for bubbles > 100 μm (Fig. 2.12g) and has a sigmoidal cumulative area fraction with kinks at 50 and 600 μm (Fig. 2.12h).

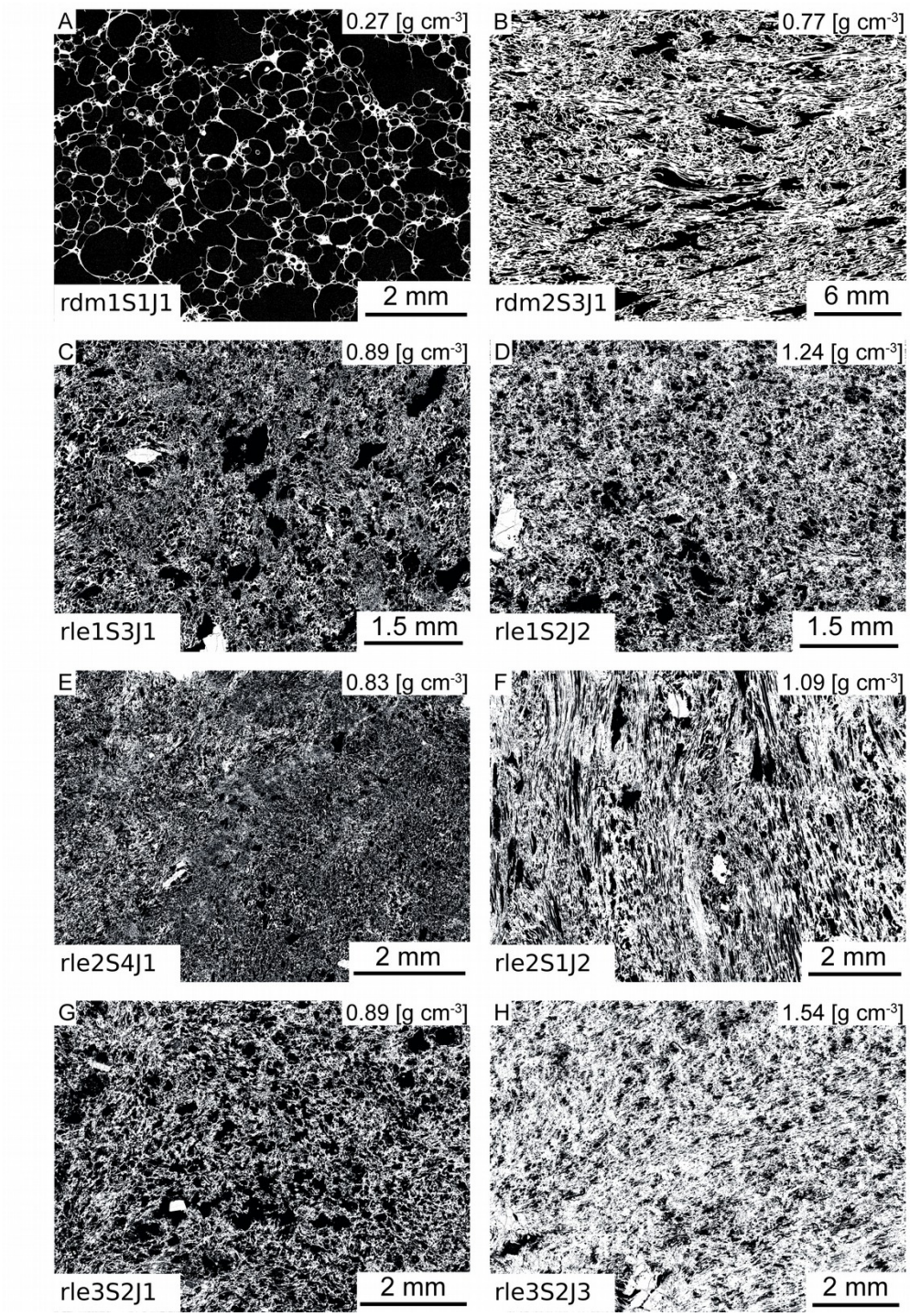

Fig. 2.10: Binary images from pumices of the *rdm* and *rle* deposits. Vesicles are black and glass and crystals are white. The binary images are obtained from BSE stitched images of 100X magnification. **A** A frothy low-density pumice from the *rdm* 1 showing spherical to colloform shaped bubbles, **B** An elongate tubular-bubble pumice from the *rdm* 2. **C-D** Pumices from the *rle* 1 showing two populations of bubbles. **E** A pumice from the *rle* 2 showing a heterogeneous distribution of bubble number densities and sizes. **F** A denser pumice from the *rle* 2 showing higher heterogeneities and strain localizations. **G-H** In the *rle* 3 pumices the heterogeneities increase and the big bubbles have flattened rims.

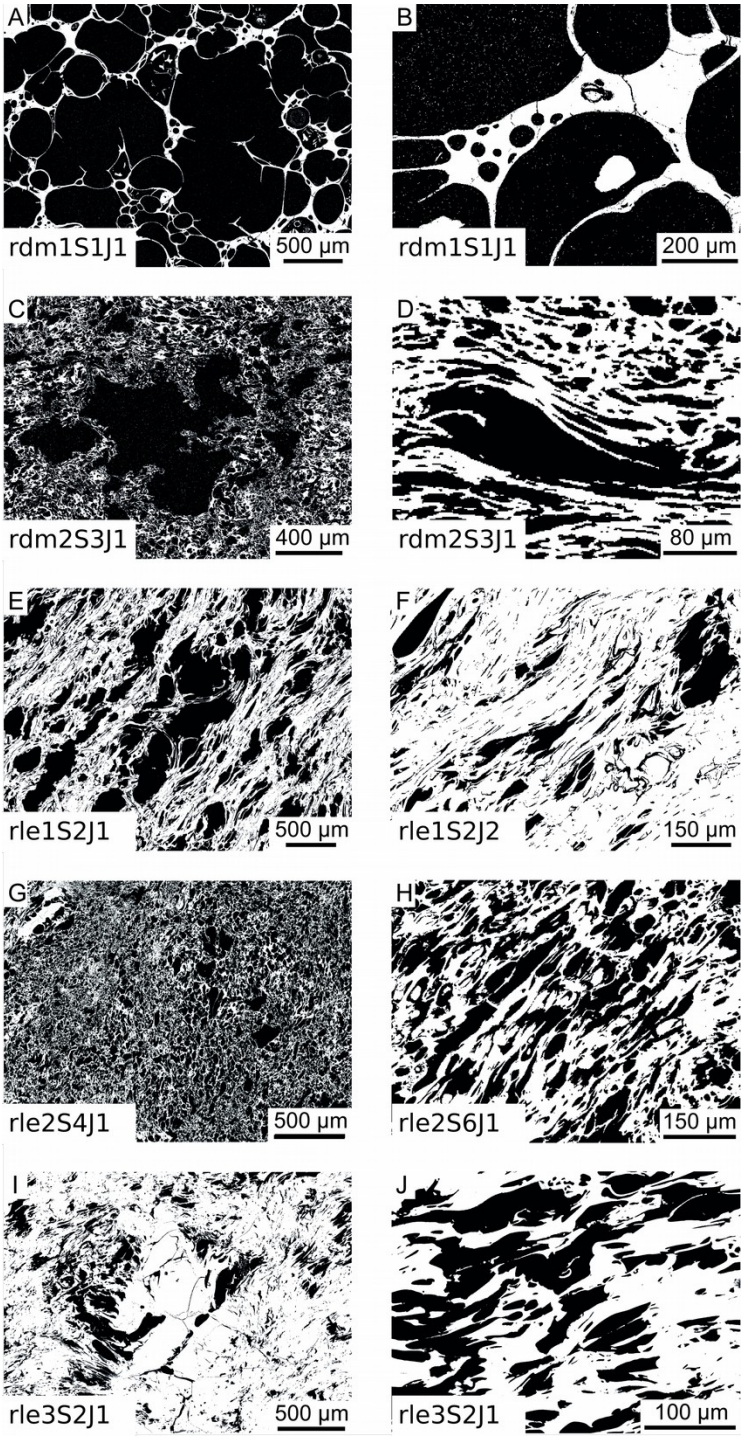

Fig. 2.11: Shapes, strain localizations and heterogeneities of bubbles. Vesicles are black and glass and crystals are white. **A-B** Images from pumices of the *rdm* 1. **A** The spherical to colloform bubbles may have bubble walls of <10 µm. **B** Small spherical bubbles are formed inside the thickest bubble walls. **C-D** Images from pumices of the *rdm* 2. **C** Coalesced bubbles are flattened in the orthogonal view to elongation. **D** Bubbles are elongated with pointed rims. **E-F** Images from pumices of the *rle* 1. The bubbles are elongated and rounded but show strain localizations in zones of low vesiculation. **G-H** Heterogeneities and strain localizations highlight in pumices of the *rle* 2. **I-J** Images from pumices of the *rle* 3. **I** Plagioclases are local domains of a higher vesiculation. **J** Bubbles are elongated with straight borders due to bubble collapse.

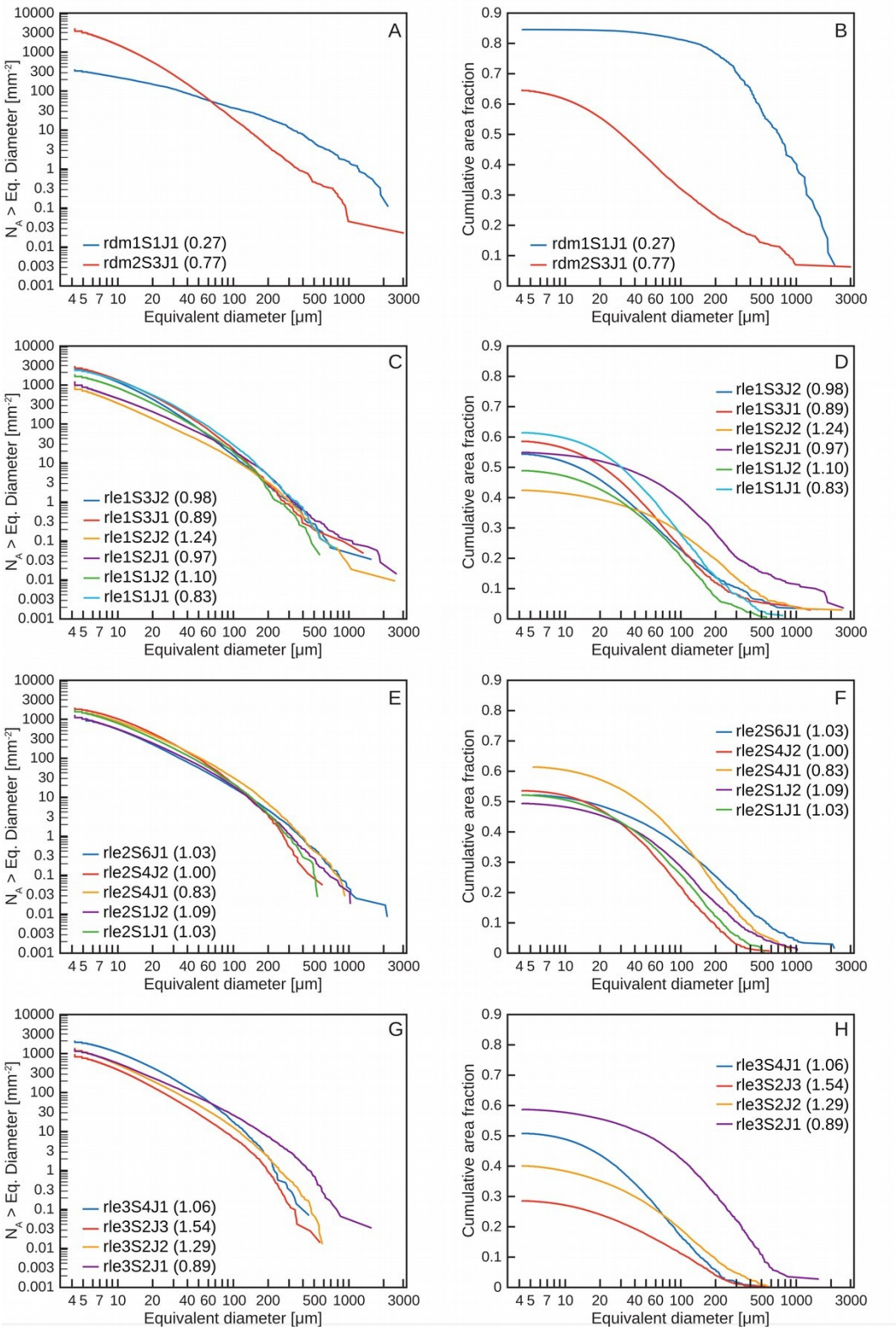

Fig. 2.12: Bubble size distributions. The results are plotted in the form of decreasing cumulative number of bubbles per unit of area of glass (number density, left) and decreasing cumulative area fraction of bubbles (right). The axes for the cumulative number density and equivalent diameter are logarithmic. **A-B** BSDs of the *rdm* pumices. **C-D** BSDs of the *rle* 1 pumices. **E-F** BSDs of the *rle* 2 pumices. **G-H** BSDs of the *rle* 3 pumices. In the legend, the numbers are the pumice density in g cm^{-3}.

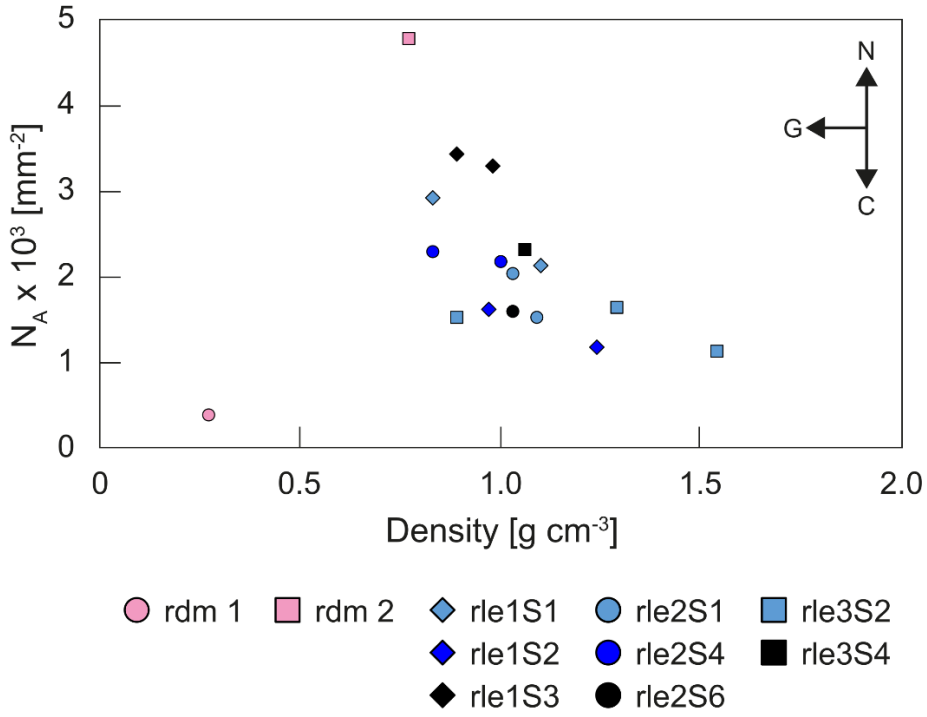

Fig. 2.13: Pumice density versus 2D bubble number density. Analysis were made on modal pumices of the pyroclast density distribution for each stratigraphic unit. The arrows show trends when vesiculation is controlled by nucleation (N), growth (G) and coalescence (C) (e.g., Rotella et al., 2014). The distribution of bubble number densities from *rdm* and *rle* pumices would be mostly controlled by nucleation and growth; however, based on the bubble collapse and strain localizations, the trend direction should be seen inversely to indicate the the decrease of number density and the contraction of bubbles. The frothy pumice of the *rdm* 1 does not follow the whole N_A – juvenile density trend.

2.5.4.5. Pyroclastic obsidians of Los Espejos

Pyroclastic obsidians of *rle* units 2 and 3 (obsidian clasts from the *rle* unit 1 were not analyzed) show a low number density of <100 μm bubbles. The bubbles may be equant, spherical or having straight rims, mostly isolated or with subtle coalescence (Fig. 2.14a). Some bubbles are slighly elongate and oriented, showing a heterogeneous distribution within the obsidian pyroclast (Fig. 2.14b); the main orientation of bubbles may coincide with the orientation of phenocrysts and microphenocrysts which commonly preserve fractures at an angle, or perpendicular, to the main orientation of bubbles and crystals (Fig. 2.14c and d). The fractures may be extended to the rest of the obsidian clasts until reaching the rock borders (Fig. 2.14e); and usually show a darker halo (~10 μm) in the BSE images, perhaps due to secondary hydration (e.g., Castro et al., 2014). I used Raman to measure water, but a high fluorescence

(probably because of the low iron content of the juvenile clasts) produced a high and broad peak that covered the range of the expected water measurement. I also did thermogravimetric analysis (TGA) in seven pyroclasts of *rdm* and *rle* which show that secondary water is <0.2 wt.% (higher in pumices than in the obsidians). TGA show that the retained magmatic water in groundmass glass is <0.3 wt.% in pumices and <0.1 wt.% in obsidian clasts (Supplementary Material). The pyroclastic obsidians also show oriented microcrysts of plagioclase, biotite and oxides (Fig. 2.14f).

2.6. Discussion

In this section, the styles and transitions of the Los Espejos eruption are reconstructed. The grain size distributions (GSDs), componentry analysis and juvenile densities are used to interpret the type of volcanic activity and associated eruption intensity, changes of the fragmentation level, and the homogeneity of magma vesiculation. In particular, variations with stratigraphic height (eruption time) of the abundance of lithics and pyroclastic obsidian, the juvenile densities, and the bubble textures are used to assess the factors governing the formation of dense juvenile clasts before the formation of the Los Espejos lava flow. The interpretations from physical parameters are then analyzed in a stratigraphic context together with the sedimentological features observed in the field in order to reconstruct the eruption history of the Los Espejos eruption. The physical characteristics of the rhyolite of Laguna del Maule deposit are also analyzed for comparison with the Los Espejos event.

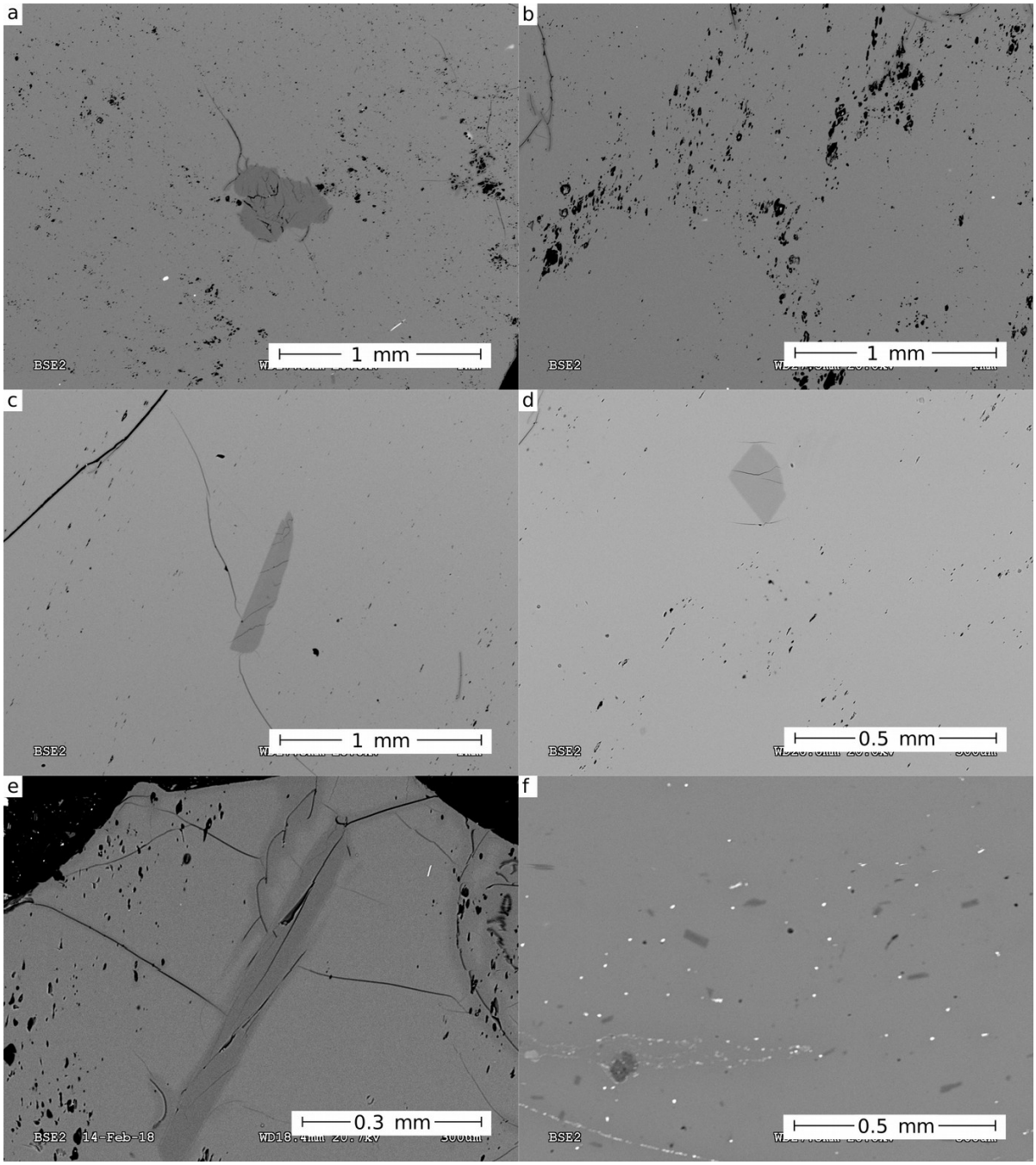

Fig. 2.14: Textures of pyroclastic obsidians of Los Espejos. The 50-300X of magnification BSE images comes from obsidian clasts from the *rle* units 2 and 3. **A** Near equant bubbles. **B** Slightly elongate and oriented bubbles. **C** Slightly elongate and oriented bubbles showing a lower number density than **B**. **D** Bubbles elongated and oriented in the same direction to the phenocrysts. **E** Fractures in the pyroclastic obsidians. **F** Oriented elongate microcrysts of plagioclase, biotite and oxides within the obsidian groundmass.

2.6.1. Interpretations of physical parameters

The analysis of physical parameters is presented in a stratigraphic context from the base to the top of the Los Espejos pyroclastic deposits to show the temporal evolution of the volcanic processes.

In general, the analyzed layers of Los Espejos are coarse as they come from proximal deposits (e.g., Carey and Sparks, 1986), except for *rle*1S1 which is the only sample showing a positive φ median grain size and a tail of bigger clasts (Fig. 2.6). Despite the proximity to the vent, the brown layers of this basal unit (including rle1S1) have a high abundance of lithics, oxidation at the top, and the sharp contacts with the pumice-rich layers; these characteristics are consistent with pulses of phreatomagmatic activity (e.g., Barberi et al., 1989; Yang et al., 2019). Although the measured juvenile densities of *rle*1S1 are not representative due to the small number of clasts <-1φ, my observations are consistent with the density distribution of juveniles from other phreatomagmatic deposits, which usually have the widest density ranges (e.g., Houghton et al., 2010; Rotella et al., 2013).

Due to the high fraction of pumice and the common whole-rock composition and mineralogy between the pumice and obsidian clasts, I infer that the other layers analyzed were formed during magmatic activity. In these stages, the total strain is related to the ratio between the conduit radius and the magma-flow distance in the conduit, and to the radial position within the conduit (Okumura et al., 2009). A narrower conduit, a larger magma-flow distance, and a radial position closer to the conduit margin produces a higher total strain (Fig. 2.15a). Assuming that the juvenile textures are mostly associated with the total strain (Gonnermann et al., 2017; Okumura et al., 2009), and that magmas come from a static reservoir, the magma flow distance is controlled by the fragmentation level. In Los Espejos, a higher fraction of

vesicular mafic lithics is related to a shallower fragmentation level which produces a higher content of obsidian clasts and high-permeability juveniles (Fig. 2.15b).

I interpret the pumice-rich *rle*1S2 and *rle*1S3 layers to represent pulses with a greater magmatic component than the *rle*1S1 layer (e.g., Barberi et al., 1989). The larger median grain size (Fig. 2.6), the lower average and narrower range of density with stratigraphic height (Fig. 2.8) suggest an increase in eruption intensity with time (Carey and Sparks, 1986; Houghton et al., 2010). The high relative abundance of mafic lithics in sample rle1S2, interpreted to be from from Volcan Atravesado, suggest a shallow fragmentation level (Hildreth et al., 2010); the high relative abundance of lithics, including the high content in *rle* 1 brown layers, suggests the widening of the eruption conduit by the excavation of the host rock (e.g., Rust and Cashman, 2007; Stasiuk et al., 1996; Fig. 2.15c). As the mafic lithics occur with obsidian clasts, I suggest that the ascending magma also excavated vanguard silicic melt within fractures in the host rock and/or that obsidians were formed by the high strain in the conduit margins (e.g., Rust and Cashman, 2007). By contrast, the higher contents of tertiary mafic lava lithics and pumice in sample *rle1*S3 suggest that an increase of the eruption intensity was accompanied by a downward propagation of the fragmentation level (e.g., Macedonio et al., 1994; Fig. 2.15c).

The *rle* unit 1 is overlain by minor PDCs which comprise coarse grained lenses (*rle*2aS1) and finer layers with sedimentary structures (*rle*2aS2-3). The high average density and the wide density range of the pumices of sample *rle* unit 2a are consistent with the partial column collapse forming the minor PDCs (e.g., Shea et al., 2011). The well sorted coarse grains of layer *rle*2aS1 suggest formation of lenses at the base of a pyroclastic density current by fluid drag (e.g., Sulpizio et al., 2014). By contrast, the finer grain size, poorer sorting and reverse grading in *rle*2aS2-3 represent the fluid lift, particle transportation and kinetic sieving in the upper turbulent part of the PDC (Sulpizio et al., 2007).

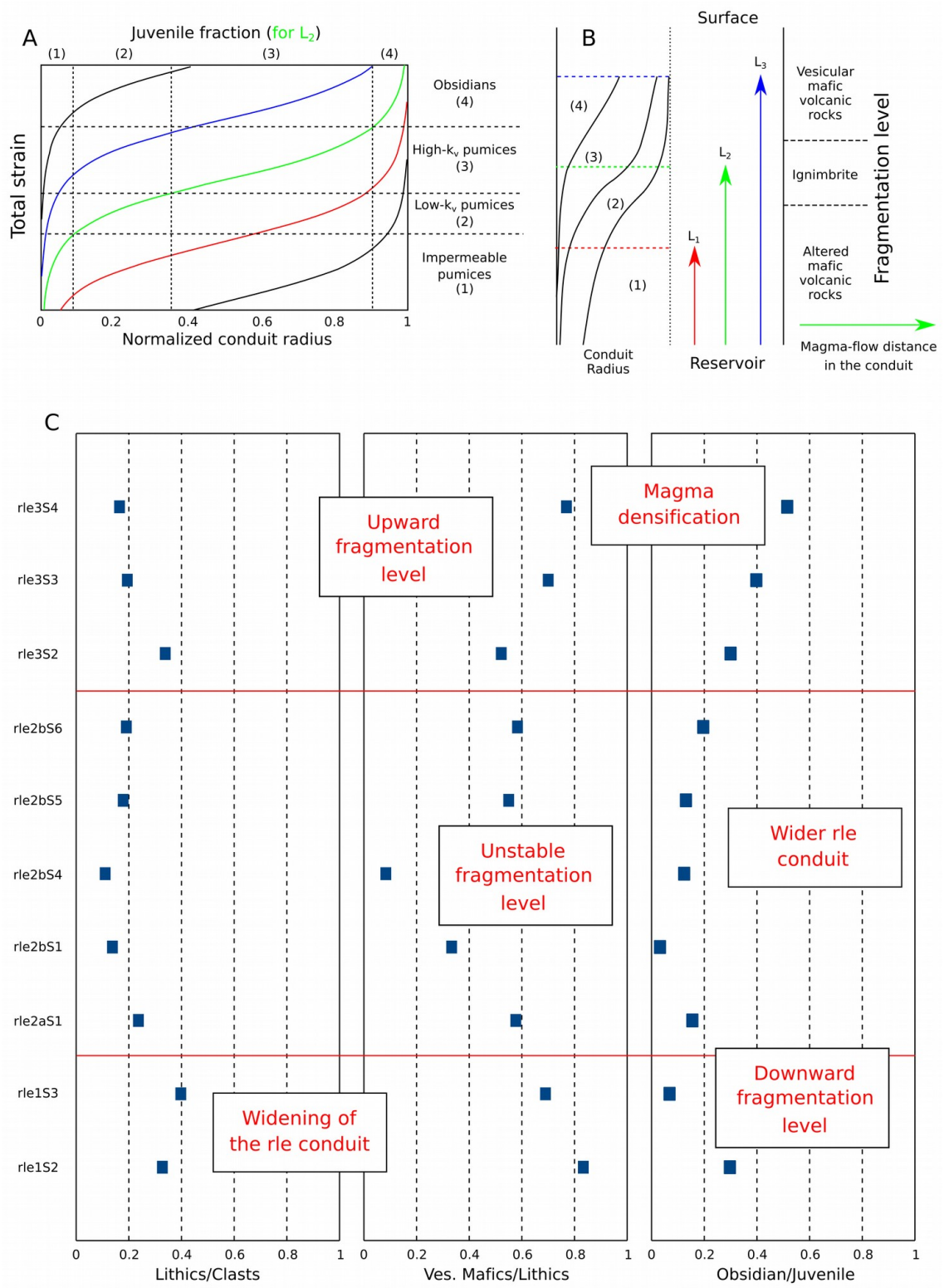

Fig. 2.15: Relationship of the fragmentation level with the lithic and obsidian content. A Relative total strain versus normalized conduit radius. The curves in color are different ratios of conduit radius and the magma-flow distance in the conduit. The fraction of pumices with a range of permeabilities and juvenile obsidian clasts is associated with the total strain. Modified from Okumura et al. (2009). **B** Juvenile fraction according to the fragmentation level. In the *rle* fall deposit, the fragmentation level is related to the type of lithics. **C** Variations of the lithic-clast ratio, vesicular mafic lithics (the shallowest host rock) compared with the abundance of lithics, and the abundance of obsidian clasts compared with the juvenile clasts.

The fluctuations in the median grain size, pumice content, and tertiary mafic lithic content at the bottom (*rle*2bS1-4) of the coarse-grained unit *rle* 2b suggest a pulsatory magmatic explosive phase of the Los Espejos eruption (e.g., Pistolesi et al., 2015). The narrow ranges of juvenile densities and the high content of tertiary mafic lithics suggest that each discrete eruption was intense and fed by magmas which fragmented at deep levels (Fig. 2.15c). By contrast, the reverse grading at the top suggests an increasing eruption intensity with time. The *rle*2bS5-6 samples, in contrast, have a high average juvenile density, a wide density range and a higher fraction of vesicular obsidian, which suggests heterogeneities associated with a partial densification of the silicic magma. As the *rle*2bS6 contains the elongate tube pumices, I suggest that this partial densification is related to a more efficient magma degassing associated with a high total strain and strain rate (e.g., Okumura et al., 2009; Schipper et al., 2013). Based on the increase of vesicular mafic lithics, I suggest that the high total strain is related to a subtle upward propagation of the fragmentation level, which enlarged the magma-flow distance through the volcanic conduit (Okumura et al., 2009; Fig. 2.15c). Thus, the combination of high magma ascent and strain rates governed the paroxysm of the Los Espejos explosive eruption and produced both the elongate pumice and vesicular obsidian clasts.

As the density distributions of *rle*3S2-3 are similar to those from *rle2*S5-6 (Fig. 2.8), it appears that the control of the shallow fragmentation level and high total strain in the eruptive dynamics persisted in this stage (Fig. 2.15c). However, the finer grains and the greater abundance of dense obsidian clasts suggest a slower magma ascent rate which allowed sufficient time for magma outgassing and a more efficient densification of magma. The bimodal density distribution together with the lower fraction of pumices in *rle*3S4 (the top of the pyroclastic sequence; Fig. 2.6) suggests a localized vesicular silicic melt co-erupted with a low-porosity silicic magma in the end of the explosive phase of Los Espejos.

In order to determine the key factors that controlled the increasing eruption intensity during the phreatomagmatic phase and the magma densification before the transition to the obsidian lava formation of the Los Espejos eruption, the analyses of bubble textures within the silicic juvenile clasts are presented below.

2.6.2. Insights from bubble textural analyses

The bubble number densities of Los Espejos pumices are comparable with those of pumices from the 2008 Chaiten (Chile) pulsatory subplinian rhyolite eruption, and are lower than those of Plinian eruptions such as that of Pinatubo, Philippines, in 1991 (e.g., Alfano et al., 2012; Polacci et al., 2001; Fig. 2.16). A trend of increasing N_A with decreasing pumice density could be explained by the kinetics of vesiculation: higher eruption rates lead to a delayed burst of bubble nucleation (e.g. Mangan and Sisson, 2000) and rapid bubble growth before the magma is too permeable to hinder further expansion (Rust and Cashman, 2011). However, a different explanation is required for the LdM samples because many have bubble textures indicating partial bubble collapse (e.g. Fig. 2.10 and 2.11). I hypothesize that the trend of decreasing N_A with increasing pumice density is due to complete collapse of large bubbles (connected channels) during compaction. Most of the pumices show an inflection around tens of microns in the cumulative area fraction diagrams (Fig. 2.12), which suggests a decreasing number density of the smallest bubbles due to collapse (Shea et al., 2010), consistent with the hypothesis from the N_A-pumice density diagrams. Pumice clasts corresponding to *rle* unit 1 and *rle*2bS6 (the top of unit 2) show two inflections (one around tens of microns, the other near to 1 mm) in the cumulative area fraction diagrams that indicate depletion of the smallest bubbles in favor of the biggest bubbles; I interpret this signal to reflect bubble coalescence (Shea et al., 2010).

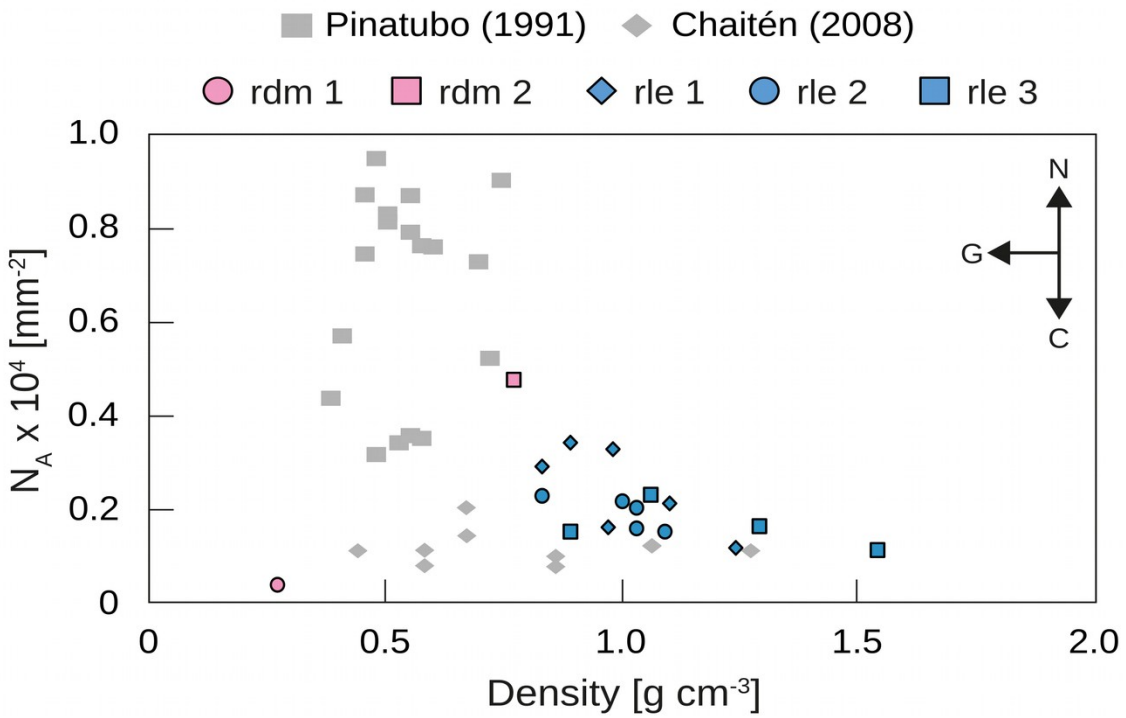

Fig. 2.16: Comparison of the *rle* bubble textural data with other rhyolitic deposits. The N_A of *rle* pumices is slightly higher than those from the pumices of the 2008 Chaitén eruption (Alfano et al., 2012); by contrast, the *rle* pumices have a higher density and lower N_A than the pumices from the 1991 Pinatubo eruption (Polacci et al., 2001).

The colloform and irregular shapes of the biggest bubbles (Fig. 2.11e) and the two kinks for the smallest and biggest bubbles in the cumulative area fraction diagrams (Fig. 2.12d) in pumices from *rle* 1 suggest that the smallest bubbles coalesce with the biggest bubbles during the *rle* 1 eruptive phase (Shea et al., 2010). The decreasing N_A with increasing pumice density suggests that the vesiculation and the bubble coalescence are controlled by the increase of nucleation and growth (e.g., Rotella et al., 2014). The increase of N_A with stratigraphic height is consistent with an increase of the eruption intensity and the magmatic component during this eruption phase (e.g., Alfano et al., 2012).

Pumice clasts from *rle* 2 have elongate small bubbles with straight borders and are heterogeneous in porosity, bubble number density, size and shape. Most pumices have one inflection for the smallest bubbles in the cumulative area fraction diagrams suggesting bubble collapse (Shea et al., 2010; Section 1.1.3), which is consistent with the elongate bubbles with

straight borders; bubble collapse is localized in some magma domains (e.g., Wright and Weinberg, 2009). As the pumice density and the fraction of vesicular obsidians increase with stratigraphic height, a protracted bubble collapse within the ascending silicic melt may be the origin of obsidian clasts. The colloform shapes of the biggest bubbles and the sigmoidal cumulative area fraction of the subelongate pumice of the *rle*2bS6 suggest bubble coalescence (Shea et al., 2010; Section 1.1.3), consistent with the high total strain in the end of the *rle* 2 phase proposed above (Gonnermann et al., 2017; Okumura et al., 2009).

The *rle* 3 pumices have flattened bubbles and more heterogeneous bubble textures that suggest more pervasive bubble collapse within the silicic magma in this phase. As the *rle* 2 pumices, the rle 3 pumices show one inflection for the smallest bubble sizes in the cumulative area fraction diagram, consistent with bubble collapse (Shea et al., 2010; Section 1.1.3). The bubble collapse and the higher fraction of dense pumice (Fig. 2.6, 2.8) are related to the formation of obsidian clasts (Fig. 2.15). The densification of magma related to a higher total strain and an upward propagation of the fragmentation level was possibly facilitated by the multiple strain localizations within the *rle* 3 pumices (Fig. 2.10h and Fig. 2.11j). The strain localizations together with shear heating have a weakening effect in silicic melts (Wright and Weinberg, 2009), which may overcome the glass transition in the localized bands of high shearing to facilitate the magma outgassing (Papale, 1999). The efficient outgassing aided by the high total strain, the decreasing magma ascent rate and the strain localizations promoted the formation of obsidian clasts and preluded the transition to the effusive stage.

In the following section I analyze the factors governing the formation of the pyroclastic obsidians and dense pumices during the last phases of the Los Espejos eruption, and, in contrast, which factors prevented the development of obsidian clasts and the formation of obsidian lava in the rhyolite of Laguna del Maule event.

2.6.3. The formation of dense juvenile clasts and the transition to the effusive stage

The late stage of the *rle* 2 phase and unit *rle* 3 are characterized by the increasing development of pyroclastic obsidians, dense pumices, and subelongate tube pumices. I infer that the pyroclastic obsidians are juvenile clasts due to the similar glass composition and mineralogy as the co-erupted pumices (Table 2.4). The obsidian clasts could be formed during ascent in the conduit margins due to a localized high strain (e.g., Rust and Cashman, 2007). The total strain of magma increases with a longer distance through the conduit and towards the conduit margins because of the higher strain rate and the lower ascent velocity (e.g., Gonnermann and Manga, 2003; Okumura et al., 2009; Rust and Cashman, 2007). As the magma ascends the cross-sectional area of high total strain widens radially from the conduit margins to the center (Okumura et al., 2009; Fig. 2.15b). The high strain deforms the bubbles creating flattened, oriented and banded textures and promotes bubble coalescence. Coalescence increases the bubble connectivity within magma, even for a low magma vesicularity, allowing the magma outgassing (e.g., Stasiuk et al., 1996). Effective outgassing decreases the volatile pressurization, facilitating bubble collapse and magma densification. Consequently, high and protracted strain rates may create radial bubble heterogeneities in the conduit during ascent, with poorly connected spherical bubbles in the center, well-connected elongated bubbles towards the conduit margin and obsidians (low-vesicularity magmas) near the conduit margins. Assuming that the magma reservoir depth did not vary during the Los Espejos eruption, the magma-flow distance depended on the fragmentation level. The upward propagation of the fragmentation level during the late stages of the *rle* eruption, inferred from the type and fraction of lithics, increased the magma flow distance in the conduit, as well as the total strain at the top of the conduit, and widened the sectional area of large strain (e.g., Okumura et al., 2009; Rust and Cashman, 2007). As the obsidians and dense tube pumices are produced (among

others) by high total strain, the upward migration of the fragmentation level explains both the formation and increasing fraction of pyroclastic obsidians and dense tube pumices during the late explosive eruption of Los Espejos. Based on the variations of GSDs, the formation of dense tube pumices and obsidians was also facilitated by a lower magma ascent rate which allowed a longer available time to produce a more effective outgassing.

In this conceptual model (Fig. 2.17), the lava flow formed by a pervasive bubble collapse and densification of magma within the conduit due to the increasing strain, strain rate and outgassing, and the decreasing magma ascent rate. A higher strain rate at the conduit margins would also allow the magma to overcome the glass transition and develop brittle fractures (e.g., Gonnermann and Manga, 2003). Brittle fragmentation along the conduit margins would allow more effective gas escape from magma, producing a positive-feedback with the formation of the obsidian lava (e.g., Schipper et al., 2013). The broken silicic melt can be annealed into the ascending magma and deformed by the viscous flow to form flow banding (Gonnermann and Manga, 2003). Tuffsites in the obsidian lava flow of Los Espejos are testimonies of degassing, brittle fragmentation, annealing and flow deformation (Fig. 2.5g). Because of the long time since the Los Espejos eruption, and the protracted annual season of rain and snow which may erode the volcanic deposits, I cannot determine if there were minor explosive eruptive pulses during the formation of the lava flow, as seen in recent obsidian eruptions (e.g., Carn et al., 2009; Pistolesi et al., 2015).

By contrast, the higher vesicularity and higher bubble number density of the pumices from the rhyolite of Laguna del Maule suggest a higher eruption intensity and a higher magma ascent rate than Los Espejos event (e.g., Alfano et al., 2012; Houghton et al., 2010). This high magma ascent rate precluded the magma outgassing and promoted the volatile overpressurization of magma during ascent (Rust and Cashman, 2011). The near absence of crystals in the *rdm*

pumices suggest that the silicic magmas ascended near the liquidus temperature. Both the high temperature and low crystallinity produced a relative low magma viscosity which aided the acceleration of the magma ascent rate by buoyancy (Gonnermann and Manga, 2007). This closed-system magma degassing avoided the bubble collapse and densification of the silicic magma, consistent with the lack of pyroclastic obsidian clasts. It is possible that strain rates at the conduit margins was just sufficient to form the elongate and wide bubbles of the *rdm* pumices, but not enough to aid an efficient magma outgassing. The granitoid lithics in the upper sequence of the *rdm* deposits suggest, conversely to Los Espejos, a downward propagation of the fragmentation level, which could produce or, at least, facilitate, the extraction of hotter and mafic magmas from below, as evidenced by the vesicular mafic juveniles. Considering the same rationale applied to the Los Espejos eruption, downward propagation of the fragmentation level during the *rdm* eruption prevented the formation of pyroclastic obsidians and subsequent formation of a lava flow. By contrast, the interaction of the silicic melt with the hotter and deeper mafic magma promoted the high intensity of the *rdm* eruption by heating, massive vesiculation and/or magma overpressure within the silicic reservoir (Cassidy et al., 2018). The final result was efficient evacuation of the magma reservoir and accompanying caldera collapse.

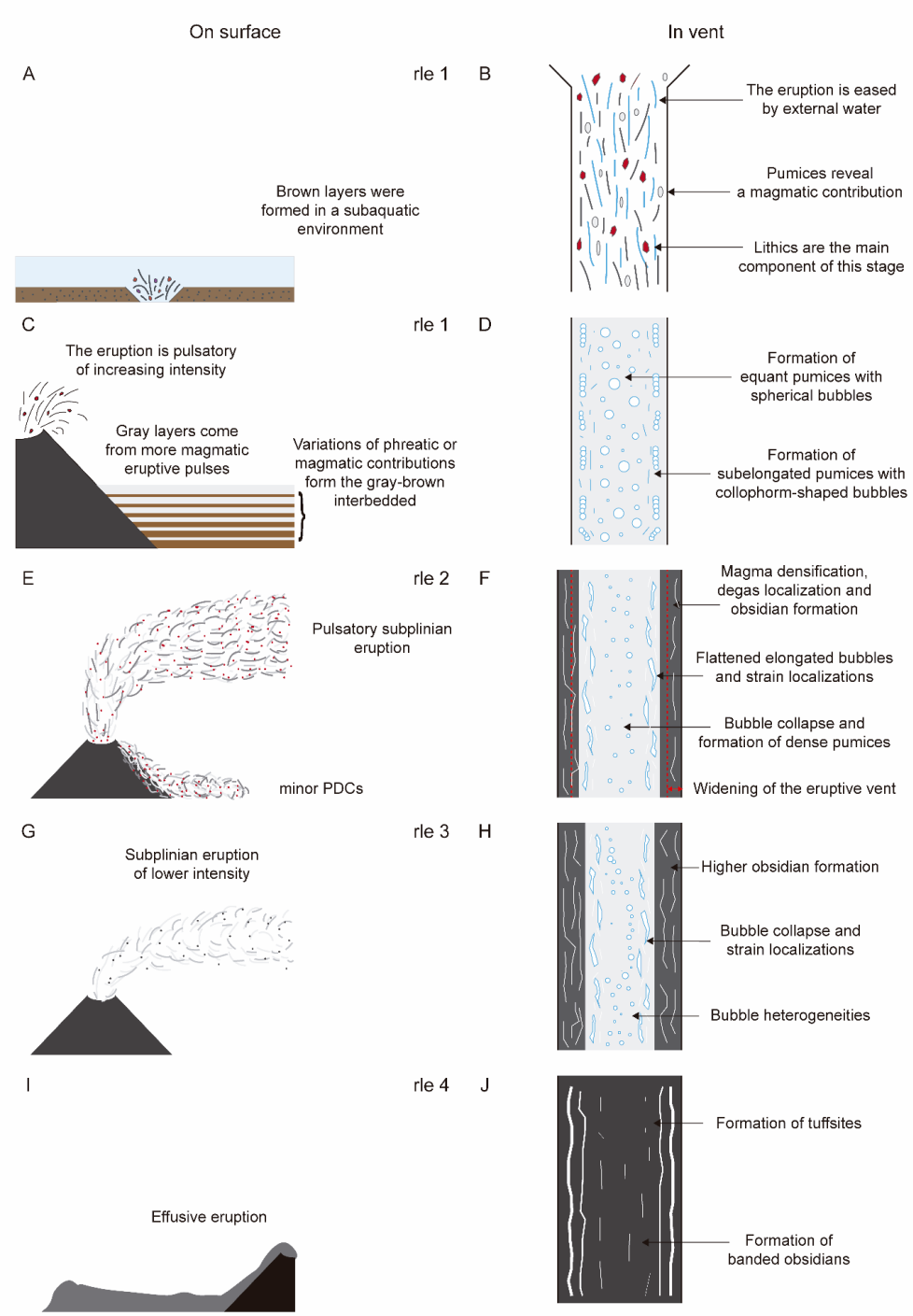

Fig. 2.17: Interpretation of the history of the *rle* eruption. A-B The eruption begins with a pulsatory phreatomagmatic eruption that is eased by external water forming the lithic-rich ash-to-lapilli matrix brown layers of the *rle* 1 stage. **C-D** The pumice-rich gray layers represent eruptive pulses with a higher magmatic contribution. Both the thickness of the gray layers and the pumice porosity increase with the deposit height suggesting an increasing eruption intensity. **E-F** The pulsatory phreatomagmatic stage develops into a subplinian magmatic eruption forming a multi-layered fall deposit and minor PDCs. **G-H** A decrease of the eruption intensity promotes the outgassing and bubble heterogeneities, promoting the bubble collapse and degas and strain localizations, and resulting in a higher fraction of obsidian clasts and dense pumices. **I** The magma densification develops the transition to an effusive phase forming the lava flow. **J** The bands of elongate bubbles in a millimetric to metric scale represents heterogeneities of the degas localization during the magma ascent.

2.7. Conclusion

In this chapter, I studied the two first postglacial rhyolite eruptions of LdM which show great differences of volume, eruption sequences, clasts and juvenile textures. The large erupted volume of the rhyolite of Laguna del Maule is associated with the interaction of the silicic magma with hotter and deeper mafic magmas. Los Espejos, the first and most silicic eruption of LdM after the rhyolite of the Laguna del Maule event, is much smaller and consisted of four eruption phases (Fig. 2.17): 1. A phreatomagmatic forming an interbedding planar layered sequence; 2. A subplinian magmatic eruption forming a pumice-rich fall deposit; 3. A subplinian magmatic eruption forming an obsidian-rich fall deposit; 4. An effusive phase forming an obsidian lava flow. Each eruption phase was mostly controlled by the fragmentation level, the total strain and strain rate, and the efficiency of outgassing. In particular, an upward propagation of the fragmentation level, a higher total strain and a more efficient outgassing promoted the bubble collapse, magma densification and formation of vesicular obsidians. The paroxysm of the Los Espejos eruption occurred by coupled high magma ascent rate and a high strain rate, which produced a radial density zonation within the volcanic conduit. A subsequent decrease in magma ascent rate accelerated the magma densification to aid the transition to the effusive phase. I propose a gradual explosive-effusive transition of the Los Espejos event according to the increasing fraction of pyroclastic obsidians in the pyroclastic deposits and the common magmatic and volcanic origin of the pyroclastic and lava obsidians. This hypothesis is consistent with the eruption histories of recent subplinian silicic eruptions in which the explosive-effusive transition occurred over weeks to months (e.g., Alfano et al., 2011; Schipper et al., 2013). The styles and transitions of a potential future rhyolitic eruption may show similar features as Los Espejos sequence; however, comparison with the *rdm* rhyolite eruption suggest that if there is interaction with a hotter and deeper mafic magma from below then a more explosive eruption without an effusive phase would be expected.

2.8. Highlights

- Eruption intensity controlled the fragmentation level and/or the depth of magma extraction during the two first rhyolite postglacial eruptions in LdM.
- The high intensity of the *rdm* eruption allowed the extraction of hotter and deeper mafic magmas and the consequent mixing with rhyolitic magma. The rhyolite-mafic magma interaction had a positive feedback with the eruption intensity and triggered the Plinian-ignimbrite forming eruptive transition of *rdm*. No obsidian pyroclasts or lavas were formed.
- By contrast, during the *rle* eruption, an upward propagation of the fragmentation level increased the total strain and the outgassing efficiency of the rhyolitic magma. The high total strain and outgassing favored the formation of high-density pumice and obsidian juvenile clasts. The increasing formation of dense juveniles is related to a gradual decrease of the eruption intensity and preludes the formation of a lava flow.

Acknowledgments

This work was supported by Becas Chile PhD scholarship [grant number 72160339 CC]. Thanks go to Luis Torres, local authority of Laguna del Maule, for his assistance on logistics and boat trips; to Barbara Buono-Core, Marcelo Cortés, Carolina Geoffroy, Rayen Gho, Christian Pizarro and Florencia Rosas, students of University of Chile, for their assistance in field; and to Judy Fierstein for her fruitful comments about the volcanic field.

References

Alfano, F., Bonadonna, C., Gurioli, L., 2012. Insights into eruption dynamics from textural analysis: the case of the May, 2008, Chaiten eruption. Bulletin of Volcanology 74, 2095-2108.

Alfano, F., Bonadonna, C., Volentik, A. C., Connor, C. B., Watt, S. F., Pyle, D. M., Connor, L. J., 2011. Tephra stratigraphy and eruptive volume of the May, 2008, Chaitén eruption, Chile. Bulletin of Volcanology, 73(5), 613-630.

Alidibirov, M., Dingwell, D. B., 1996. Magma fragmentation by rapid decompression. Nature 380, 146–148.

Andersen, N.L., Singer, B.S., Jicha, B.R., Beard, B.L., Johnson, C.M., Licciardi, J.M., 2017. Pleistocene to Holocene growth of a large upper crustal rhyolitic magma reservoir beneath the active Laguna del Maule volcanic field, central Chile. Journal of Petrology, 58, 85–114.

Barberi, F., Cioni, R., Rosi, M., Santacroce, R., Sbrana, A., Vecci, R., 1989. Magmatic and phreatomagmatic phases in explosive eruptions of Vesuvius as deduced by grain-size and component analysis of the pyroclastic deposits. Journal of Volcanology and Geothermal Research, 38(3-4), 287-307.

Cáceres, F., Castruccio, Á., Parada, M. A., 2018. Morphology, Effusion Rates, and Petrology of Postglacial Lavas of Laguna del Maule Volcanic Field, Chilean Andes, and Implications for Their Plumbing System. Geochemistry, Geophysics, Geosystems, 19(12), 4925-4944.

Carey, S., Sparks, R. S. J., 1986. Quantitative models of the fallout and dispersal of tephra from volcanic eruption columns. Bulletin of volcanology, 48(2-3), 109-125.

Carn, S. A., Pallister, J. S., Lara, L., Ewert, J. W., Watt, S., Prata, A. J., Thomas, R. J., Villarosa, G., 2009. The unexpected awakening of Chaitén volcano, Chile. Eos, Transactions American Geophysical Union, 90(24), 205-206.

Cassidy, M., Manga, M., Cashman, K., Bachmann, O., 2018. Controls on explosive-effusive volcanic eruption styles. Nature communications, 9(1), 2839.

Castro, J. M., Bindeman, I. N., Tuffen, H., Schipper, C. I., 2014. Explosive origin of silicic lava: textural and δD–H2O evidence for pyroclastic degassing during rhyolite effusion. Earth and Planetary Science Letters, 405, 52-61.

Castro, J. M., Dingwell, D. B., 2009. Rapid ascent of rhyolitic magma at Chaitén volcano, Chile. Nature, 461(7265), 780.

Cembrano, J., Lara, L., 2009. The link between volcanism and tectonics in the southern volcanic zone of the Chilean Andes: a review. Tectonophysics, 471(1-2), 96-113.

Colombier, M., Wadsworth, F. B., Gurioli, L., Scheu, B., Kueppers, U., Di Muro, A., Dingwell, D. B., 2017. The evolution of pore connectivity in volcanic rocks. Earth and planetary science letters, 462, 99-109.

Degruyter, W., Huber, C., Bachmann, O., Cooper, K. M., Kent, A. J. R., 2016. Magma reservoir response to transient recharge events: the case of Santorini volcano (Greece). Geology 44, 23–26.

Feigl, K.L., Le Mével, H., Ali, S.T., Cordova, L., Andersen, N.L., DeMets, C., and Singer, B.S., 2014. Rapid uplift in Laguna del Maule volcanic field of the Andean Southern Volcanic Zone (Chile) 2007–2012. Geophysical Journal International, 196, 885–901, doi: 10.1093/gji/ggt438.

Fierstein, J., Postglacial eruptive history established by mapping and tephra stratigraphy provides perspectives on magmatic system beneath Laguna del Maule, Chile, Presented at: AGU Chapman Conference on Merging Geophysical, Petrochronologic, and Modeling Perspectives of Large Silicic Magma Systems, Quinamavida, Chile, 2018.

Fluegel, A., 2007. Global model for calculating room-temperature glass density from the composition. Journal of the American Ceramic Society, 90(8), 2622-2625.

Folk, R. L., Ward, W. C., 1957. Brazos River bar [Texas]; a study in the significance of grain size parameters. Journal of Sedimentary Research, 27(1), 3-26.
Gonnermann, H. M., Manga, M., 2003. Explosive volcanism may not be an inevitable consequence of magma fragmentation. Nature, 426(6965), 432.
Gonnermann, H. M., Manga, M., 2007. The fluid mechanics inside a volcano. Annual Reviews of Fluid Mechanics, 39, 321-356.
Higgins, M. D., 2002. Closure in crystal size distributions (CSD), verification of CSD calculations, and the significance of CSD fans. American Mineralogist, 87(1), 171-175.
Hildreth, W., Godoy, E., Fierstein, J., Singer, B.S., 2010. Laguna del Maule volcanic field: eruptive history of a Quaternary basalt to rhyolite distributed volcanic field on the Andean range crest in central Chile. Servicio Nacional de Geología y Minería, Boletin 63.
Houghton, B. F., Carey, R. J., Cashman, K. V., Wilson, C. J., Hobden, B. J., Hammer, J. E., 2010. Diverse patterns of ascent, degassing, and eruption of rhyolite magma during the 1.8 ka Taupo eruption, New Zealand: evidence from clast vesicularity. Journal of Volcanology and Geothermal Research, 195(1), 31-47.
Houghton, B. F., Wilson, C. J. N., 1989. A vesicularity index for pyroclastic deposits. Bulletin of volcanology, 51(6), 451-462.
Macedonio, G., Dobran, F., Neri, A., 1994. Erosion processes in volcanic conduits and application to the AD 79 eruption of Vesuvius. Earth and planetary science letters, 121(1-2), 137-152.
Mangan, M., Sisson, T., 2000. Delayed, disequilibrium degassing in rhyolite magma: decompression experiments and implications for explosive volcanism. Earth and Planetary Science Letters, 183(3-4), 441-455.
Mueller, S., Scheu, B., Kueppers, U., Spieler, O., Richard, D., Dingwell, D. B., 2011. The porosity of pyroclasts as an indicator of volcanic explosivity. Journal of Volcanology and Geothermal Research, 203(3-4), 168-174.
Okumura, S., Nakamura, M., Takeuchi, S., Tsuchiyama, A., Nakano, T., Uesugi, K., 2009. Magma deformation may induce non-explosive volcanism via degassing through bubble networks. Earth and Planetary Science Letters, 281(3-4), 267-274.
Pallister, J. S., Hoblitt, R. P., Reyes, A. G., 1992. A basalt trigger for the 1991 eruptions of Pinatubo volcano?. Nature, 356(6368), 426.
Papale, P., 1999. Strain-induced magma fragmentation in explosive eruptions. Nature, 397(6718), 425.
Pistolesi, M., Cioni, R., Bonadonna, C., Elissondo, M., Baumann, V., Bertagnini, A., Chiari, L., Gonzales, R., Rosi, M., Francalanci, L., 2015. Complex dynamics of small-moderate volcanic events: the example of the 2011 rhyolitic Cordón Caulle eruption, Chile. Bulletin of Volcanology, 77(1), 3.
Polacci, M., Papale, P., Rosi, M., 2001. Textural heterogeneities in pumices from the climactic eruption of Mount Pinatubo, 15 June 1991, and implications for magma ascent dynamics. Bulletin of Volcanology 63, 83-97.
Preibisch, S., Saalfeld, S., Tomancak, P., 2009. Globally optimal stitching of tiled 3D microscopic image acquisitions. Bioinformatics, 25(11), 1463-1465.
Pyle, D. M., 2015. Sizes of volcanic eruptions. In The encyclopedia of volcanoes, pp. 257-264. Academic Press.
Rotella, M.D., Wilson, C.J.N., Barker, S.J., Cashman, K.V., Houghton, B.F., Wright, I.C., 2014. Bubble development in explosive silicic eruptions: insights from pyroclast vesicularity textures from Raoul volcano (Kermadec arc). Bulletin of Volcanology 76.
Rotella, M. D., Wilson, C. J., Barker, S. J., Wright, I. C., 2013. Highly vesicular pumice generated by buoyant detachment of magma in subaqueous volcanism. Nature Geoscience, 6(2), 129.

Rust, A. C., Cashman, K. V., 2007. Multiple origins of obsidian pyroclasts and implications for changes in the dynamics of the 1300 BP eruption of Newberry Volcano, USA. Bulletin of Volcanology, 69(8), 825-845.
Rust, A. C., Cashman, K. V., 2011. Permeability controls on expansion and size distributions of pyroclasts. Journal of Geophysical Research: Solid Earth, 116(B11).
Sahagian, D. L., Proussevitch, A. A., 1998. 3D particle size distributions from 2D observations: stereology for natural applications. Journal of Volcanology and Geothermal Research, 84(3-4), 173-196.
Schipper, C. I., Castro, J. M., Tuffen, H., James, M. R., How, P., 2013. Shallow vent architecture during hybrid explosive–effusive activity at Cordón Caulle (Chile, 2011–12): evidence from direct observations and pyroclast textures. Journal of Volcanology and Geothermal Research, 262, 25-37.
Self, S., Zhao, J. X., Holasek, R. E., Torres, R. C., King, A. J., 1993. The atmospheric impact of the 1991 Mount Pinatubo eruption.
Shea, T., Gurioli, L., Houghton, B. F., Cioni, R., Cashman, K. V., 2011. Column collapse and generation of pyroclastic density currents during the AD 79 eruption of Vesuvius: the role of pyroclast density. Geology, 39(7), 695-698.
Shea, T., Houghton, B.F., Gurioli, L., Cashman, K.V., Hammer, J.E., Hobden, B.J., 2010. Textural studies of vesicles in volcanic rocks: An integrated methodology. Journal of Volcanology and Geothermal Research 190, 271-289.
Singer, B. S., Andersen, N. L., Le Mevel, H. et al., 2014. Dynamics of a large, restless, rhyolitic magma system at Laguna del Maule, southern Andes, Chile. GSA Today 24, 4–10.
Singer, B., Hildreth, W., Vincze, Y., 2000. 40Ar/39Ar evidence for early deglaciation of the central Chilean Andes. Geophysical Research Letters, 27(11), 1663-1666.
Sulpizio, R., Dellino, P., Doronzo, D. M., Sarocchi, D., 2014. Pyroclastic density currents: state of the art and perspectives. Journal of Volcanology and Geothermal Research, 283, 36-65.
Sulpizio, R., Mele, D., Dellino, P., La Volpe, L., 2007. Deposits and physical properties of pyroclastic density currents during complex Subplinian eruptions: the AD 472 (Pollena) eruption of Somma-Vesuvius, Italy. Sedimentology, 54(3), 607-635.
Stasiuk, M. V., Barclay, J., Carroll, M. R., Jaupart, C., Ratté, J. C., Sparks, R. S. J., Tait, S. R., 1996. Degassing during magma ascent in the Mule Creek vent (USA). Bulletin of Volcanology, 58(2-3), 117-130.
Tarasewicz, J., Brandsdóttir, B., White, R. S., Hensch, M., Thorbjarnardóttir, B., 2012. Using microearthquakes to track repeated magma intrusions beneath the Eyjafjallajökull stratovolcano, Iceland. Journal of Geophysical Research: Solid Earth, 117(B9).
Tuffen, H., James, M. R., Castro, J. M., Schipper, C. I., 2013. Exceptional mobility of an advancing rhyolitic obsidian flow at Cordón Caulle volcano in Chile. Nature communications, 4, 2709.
Wright, H. M., Weinberg, R. F., 2009. Strain localization in vesicular magma: Implications for rheology and fragmentation. Geology, 37(11), 1023-1026.
Yang, Q., Bursik, M., Pouget, S., 2019. Stratigraphic and sedimentologic framework for tephras in the Wilson Creek Formation, Mono Basin, California, USA. Journal of Volcanology and Geothermal Research, 374, 197-225.

3. Optimizing the X-ray microtomography conditions for the application to silicic pumices

Abstract

Silicic pumices are testimonies of bubble networks within magma at the fragmentation level and their bubble textures reflect the dynamics of the eruptions that formed them. Vesicularity, bubble number density, bubble size distributions and bubble shape factors are textural parameters that can be analyzed from 3D images (tomograms) acquired from X-ray microtomography systems; however, the quality of the obtained tomograms depends on the applied X-ray microtomography conditions. I test the role of six X-ray microtomography conditions on the image contrast, the signal-to-noise ratio and the edge sharpening. The tomogram quality improves by applying low energies and virtual beam hardening filters of second-degree polynomials. Variations in the tomogram quality affect the capability of constraining small bubbles around big bubbles. I analyze bubble textures in silicic pumices from several volcanic complexes. By improving the tomogram quality, the resulting bubble number density (BND) increases and the bubble size log-normal distributions are steeper. Thus, interpretations about eruptive dynamics and degassing mechanisms may be biased because of the applied X-ray tomography conditions. To ensure confident estimations of eruptive numerical parameters, I recommend the optimum settings to apply for the analysis of silicic pumices.

Keywords

X-ray microtomography; Silicic pumices; Eruptive dynamics; Bubble Number Density; Bubble Size Distribution.

3.1. Introduction

Silicic eruptions can be catastrophic volcanic events for society because of their high explosivity and unpredictable nature (e.g., Alfano et al., 2012; Preece et al., 2016). Their associated deposits consist of lithics (from basement, volcanic structure or surface), crystals, juvenile obsidians and pumices. Due to the high-viscosity of the magmas, silicic pumice juvenile clasts are testimonies of bubble networks within magma at the fragmentation level (Degruyter et al., 2010b). Fragmentation is the process by which magma is transformed from a liquid phase that contains solids and gas bubbles to a gas phase that transports solids and melt pockets (Cashman and Scheu, 2015). That expanded gas phase is the result of a series of volcanic processes that affects gas bubbles: when magma reaches a critical water-oversaturation, bubbles can start to nucleate. Bubble nucleation decreases magma density and drives magma ascent. During ascent, the lithostatic pressure surrounding magma decreases, allowing bubble growth (Gonnermann and Manga, 2007). When bubbles reach a critical volume, they overcome the melt-gas surface tension and begin to coalesce (e.g., Castro et al., 2012). That bubble connectivity allows gas flow through the magma and promotes the outgassing. Because of the positive feedback between decreasing magma density and increasing magma ascent rate, a high strain rate begins to elongate the coalesced bubbles and forms gas channels that increase the degassing efficiency (Degruyter et al., 2010b). In this way, the analysis of size and textures of bubbles within pumices permits inversion of volcanic processes that affected gas bubbles.

Some examples of inversion of the volcanic processes by bubble textural analysis from 2D images are the magma decompression rate of the Chaiten eruption as determined from the bubble number density (BND) of several pumices (Alfano et al., 2012); different eruptive styles of Campi Flegrei and Somma-Vesubio deciphered by analysing bubble size distributions (Mastrolorenzo and Pappalardo, 2006); and the origin and role of textural heterogeneities on

eruptive dynamics determined by quantifying bubble shapes (Polacci et al., 2001). However, the analysis of 2D images usually requires the stereological correction of objects to 3D by considering some textural assumptions (e.g., Shea et al., 2010). X-ray tomography systems permit acquisition of a 3D volume from a set of several radiograms (2D images) which are reconstructed using specialized algorithms (Cnudde and Boone, 2013; Rivers et al., 1999).

X-ray tomography is a non-destructive technique that applies an X-ray beam to the object to be imaged to obtain a 3D gray-scale image (tomogram) based on the linear attenuation coefficient, a function of the atomic number and the density of the material (Ketcham and Carlson, 2001; Rivers et al., 1999; Sutton et al., 2002). There are two types of X-ray tomography systems that perform analysis at the microscopic scale: synchrotron X-ray tomography and conventional (tube) X-ray tomography. The former acquires tomograms of low signal-to-noise ratio by the application of a dual beam with monochromatic spectra from a source with plane geometry (Baker et al., 2012); the latter acquires tomograms with some associated artifacts by the application of a single beam with polychromatic spectra from a source with tube geometry (Ketcham and Carlson, 2001). However, synchrotron technology can be difficult to access, and the artifacts from conventional X-ray tomography can be easily minimized by the application of physical and virtual filters (Cnudde and Boone, 2013). Thus, conventional X-ray tomography results a good cost-efficient option by which to analyze object sizes and shapes within silicic rocks.

Baker et al. (2012) and Cnudde and Boone (2013) offer excellent reviews about the basis of X-ray tomography systems, its advantages and disadvantages regarding other imaging techniques, and applications in earth sciences. However, despite its increasing usage (e.g., Polacci et al., 2018), there are no published guidelines about how to set up applied X-ray tomography conditions to optimize tomogram acquisition for volcanic materials. Herein I present a review

of applied X-ray tomography conditions in works mainly focused on vesiculated volcanic rocks and I test different energies, frames per radiogram, exposure times and the usage of metal filters and virtual artifact arrangements on pumices from several volcanic complexes. I analyze the effect of the applied X-ray tomography conditions on tomogram quality and resulting bubble textural analyses. I end by analyzing how analytical conditions can alter interpretations about volcanic processes and which X-ray tomography conditions should be applied to optimize the analysis of silicic pumices.

3.2. Compilation of X-ray tomography conditions in literature

To evaluate the acquisition conditions of past studies I have compiled the sample diameter, obtained voxel size, number of radiograms, energy applied, current applied, frames per radiogram, exposure time, application of metal filter, application of ring artifact filter, type of rock and objects to study of 54 analyses done in synchrotron and conventional systems from 36 studies published in the last 20 years (Supplementary material). Most of the selected studies are focused on intermediate-to-silicic vesiculated rocks (Baker et al., 2011; Berg et al., 2016; Degruyter et al., 2010a; 2010b; Dioguardi et al., 2017; Ersoy et al., 2010; Giachetti et al., 2011; Gualda and Rivers, 2006; Le Gall and Pichavant, 2016; Pamukcu and Gualda, 2010; Pardo et al., 2014; Schipper et al., 2013; Voltolini et al., 2011; Zandomeneghi et al., 2010), but the compilation also includes diamonds and kimberlites (Jerram et al., 2009; 2010; Nimis et al., 2016; Rivers et al., 1999), ultramafic rocks (Godel et al., 2013; Jöns et al., 2017), basalts (Pankhurst et al., 2014; Polacci et al., 2006; 2009; 2012; Song et al., 2001), magma-mingling pyroclasts (Morgavi et al., 2016), trachytes (Arzilli et al., 2015) and granitoids (Álvarez-Valero et al., 2016; Boone et al., 2011; Holwell et al., 2016).

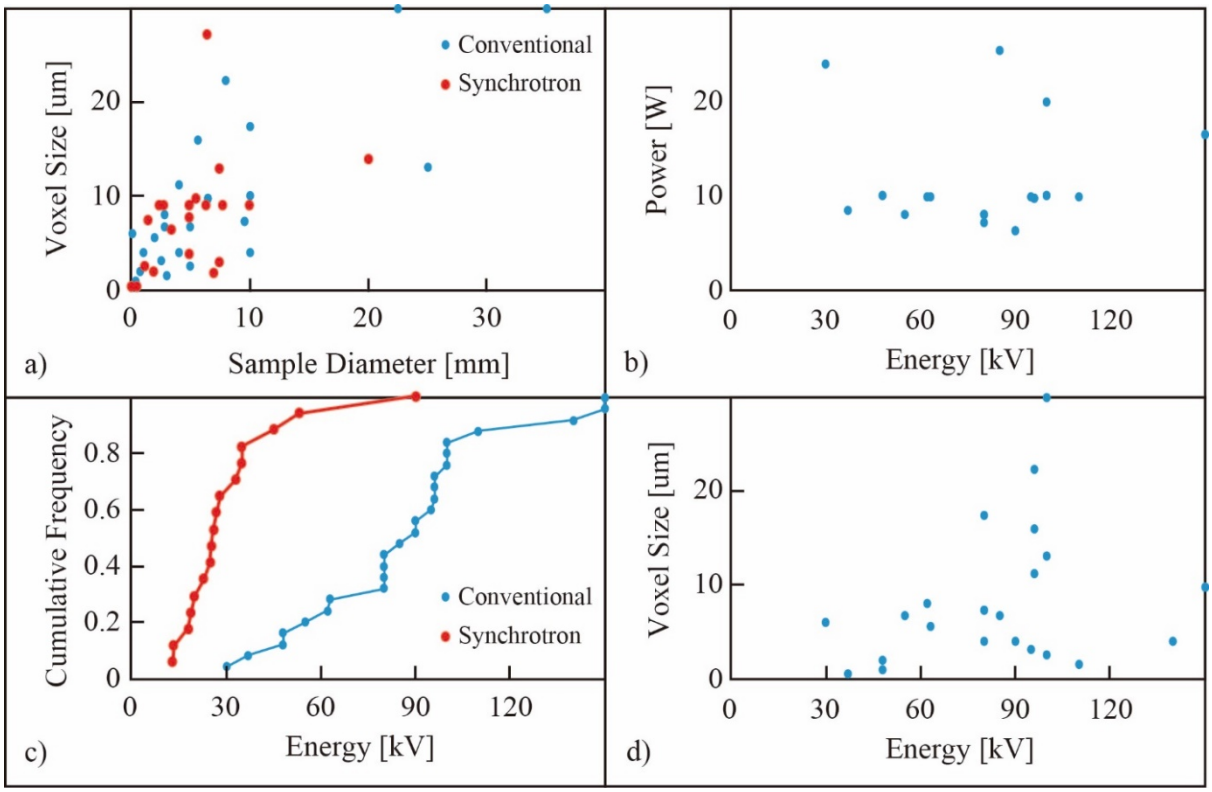

Fig. 3.1: Compilation of X-ray tomography conditions in literature[4]. A Sample diameter versus voxel size for both X-ray tomography systems. **B** Applied energy versus power for conventional X-ray tomography. **C** Cumulative frequency of applied energy for both X-ray tomography systems. **D** Applied energy versus voxel size for conventional X-ray tomography.

In most cases, the analyzed sample diameter is <10 mm. The obtained voxel size is <10 µm regardless of the X-ray tomography system. There is no empirical relationship between the sample diameter and the obtained voxel size (Fig. 3.1a) despite theoretical dependence (Cnudde et al., 2011). This could be explained by the different settings (spot size, target resolution, source-target distance) applied to the different instruments. Each X-ray tomography instrument has an optimum applicable power (where power is the product of the applied current and the applied energy). Most of them present an optimum power of ~10 W (Fig. 3.1b). Because synchrotron systems can apply very high current regarding to conventional systems, the applied energy is highly dependent on the X-ray tomography system: all the analyses using a conventional X-ray tomography system applied >30 kV, whilst most analyses using a

[4] The compilation considers analyses from 54 works which are mostly focused on the study of silicic pumices.

synchrotron X-ray tomography system applied <30 kV (Fig. 3.1c). Coherent with theoretical expressions (Attix, 1986; Cnudde et al., 2011), there is no relationship between the applied energy and either the obtained voxel size or the sample diameter (Fig. 3.1d). The rest of the compiled X-ray tomography conditions are not specified in most considered studies: the number of frames per radiogram is specified in 43%, the exposure time per radiogram is only presented in 13%, the application of metal filter in 57% and application of ring artifact filter in 53% of works.

3.3. Methodology

3.3.1. Analyzed samples

Four pumices from four volcanic complexes were selected to test the effect of X-ray tomography conditions on the tomogram quality: one pumice from Los Espejos unit of the Laguna del Maule volcanic complex (Hildreth et al., 2010), one pumice from the Aluto volcano (Fontijn et al., 2018), one pumice from fall deposits of the Mount Mazama (Bacon and Lanphere, 2006) and one pumiceous needle from the Katla volcanic system (Larsen et al., 2001). These samples were selected because they have silicic compositions, but with differences in major elements (see details in Table 3.1): the Los Espejos pumice is the most silicic sample (>75 wt.% SiO_2) and has high alkalis (~8.5 wt.% $Na_2O + K_2O$); the Aluto pumice is also rhyolitic (>73 wt.% SiO_2) and it is the richest in alkalis (> 11 wt.% $Na_2O + K_2O$); the Mazama pumice has a rhyodacitic composition with lower silica and alkalis content than the previous ones (~70 wt.% SiO_2; ~7.9 wt.% $Na_2O + K_2O$); and the Katla needles are dacitic pumices (>65 wt.% SiO_2) of relatively high alkali content (>7.2 wt.% $Na_2O + K_2O$). The different compositions could affect the optimum acquisition conditions because the linear attenuation coefficient depends on the material density and the atomic number of components (Attix, 1986; Knoll, 2000; McCullough, 1975). Thus, I theoretically expect different visual and

numerical tomogram features among the analyzed samples. All the pumices are crystal-poor: Mazama pumice contains ~ 5% crystals, Los Espejos and Aluto pumices contain ~3 % crystals whilst Katla needles is almost aphyric. The pumices, except the Katla needle, were cut as 15-mm diameter cylinders of 20-30 mm-long. The Katla needle is ~8 mm long and has irregular cross section of 1-3 mm. The density of each pumice was measured by weighing the cylinder and estimating an ideal volume of cylinder shape by considering the diameter and length. The porosity was measured by considering a solid rock density of 2.4 g cm^{-3} in order to estimate the porosity for image segmentation.

Table 3.1: Major element compositions (wt.% oxides) of the four selected silicic pumices. The analyses correspond to averages of whole-rock composition measured by XRF in the cases of Los Espejos pumice[5] (Hildreth et al., 2010) and Mazama pumice[6] (Bruggman et al., 1987), and to averages of point analyses in groundmass glass measured by EMPA in the cases of Aluto pumice[7] (Fontijn et al., 2018) and Katla needle[8] (Larsen et al., 2001).

	Los Espejos	Mazama	Aluto	Katla
SiO_2	75.68	70.65	73.40	65.31
TiO_2	0.17	0.47	0.18	1.18
Al_2O_3	13.32	15.29	8.13	14.15
FeO*	0.84	2.54	6.65	6.04
MnO	0.06	0.05	0.32	0.19
MgO	0.15	0.80	0.01	1.06
CaO	0.65	2.24	0.20	2.94
Na_2O	4.31	5.17	6.70	4.55
K_2O	4.45	2.69	4.39	2.70
P_2O_5	0.05	0.10	0.01	
LOI	0.65	2.92		
Total	100.23	99.76	95.48	98.12

[5] Average of five samples normalized to 100% anhydrous composition in the original work.
[6] Average of nineteen samples from the CIP dataset normalized to 100% anhydrous composition by me.
[7] Average of 153 points from seven samples. The percentages of each oxide were normalized to 100% anhydrous composition in the original work.
[8] Average from ten samples.

3.3.2. Instrument settings and X-ray tomography conditions

The tomograms were acquired with a conventional X-ray computed tomography instrument (Nikon XTH225ST) at the Life Science Building, University of Bristol. It applies a single beam of polychromatic spectra to the sample. The target is a planar 2,000 x 2,000 pixels pad, the optimum and applied number of radiograms is 3,141, and the power applied is 7 W. The analyses of the effect of the applied energy, number of frames per radiogram, exposure time, and virtual beam hardening filter were made by applying three different settings of the target parameter and fixing the others (See conditions of the tomogram quality tests in Table 3.2). The lowest energy applied was 55 kV because a lower energy would produce blurry radiograms. To test the effect of the metal filter, two analyses were made: one by analyzing with a 0.25 mm-width copper filter and another without the metal filter. Both analyses were done with the same other X-ray tomography conditions. To test the effect of the virtual ring artifact minimizer, two analyses were made: one by applying the ring artifact minimizer algorithm and another without the minimizer. The application of the ring artifact minimizer doubles the analysis duration. Both analyses were done with the same other X-ray tomography conditions.

3.3.3. Tests of tomogram quality

Tests of tomogram quality were performed with ImageJ by analyzing a selected centered 2D slice (corresponding to slice #1000 from 0 to 1999). To evaluate the quality of tomograms, three tests were applied: the resulting range of linear attenuation coefficient, the signal-to-noise ratio, and the edge sharpening. The resulting range of linear attenuation coefficient was directly recorded from Nikon CT Pro 3D XT4.4 (Fig. 3.2a). A wider coefficient interval defines a better tomogram because mid-grayscale values can be defined by more gray color tones, thus improving the image contrast. The signal-to-noise ratio was measured by marking areas inside bubbles, no touching bubble-glass boundaries. The histogram of the number of pixels with

grayscale index from marked areas are obtained to calculate the average, maximum and standard deviation of the grayscale indexes (Fig. 3.2b). Considering that pixels corresponding to bubbles should be black (0 in 16-bits grayscale index), a lower average, maximum and standard deviation of the grayscale indexes defines a better tomogram. The edge sharpening was measured by doing five perpendicular traverses across bubble-glass boundaries. In a biaxial plot, the resulting grayscale index is compared to the pixel-distance (Fig. 3.2c). The average, minimum and maximum of the grayscale-pixel ratio from the five bubble-glass boundary traverses were calculated. Considering that the boundary between bubbles and glass should be clear (the grayscale index should sharply change passing through different materials), a higher grayscale-pixel ratio defines a better tomogram.

Table 3.2: X-ray tomography conditions for tests of tomogram quality and bubble textural analysis. The column "Used for" refers to which X-ray tomography condition was evaluated by that setting. AE = applied energy; FPR = frames per radiogram; ET = exposure time; BH = virtual beam hardening filter; MF = metal filter; RA = ring artifact. The twelve settings were applied to Los Espejos pumice; whilst only settings used for AE and BH were applied to Mazama, Aluto and Katla pumices.

Energy	Frames per radiogram	Exposure time	Beam hardening filter	Metal filter	Ring artifact minimizer	Used for
150	1	1	3	no	no	AE ET MF
100	1	1	3	no	no	AE FPR
55	1	1	3	no	no	AE
100	4	1	3	no	no	FPR
100	2	1	3	no	no	FPR
150	1	0.5	3	no	no	ET
150	1	1.4	3	no	no	ET
100	1	2	3	no	no	BH RA
100	1	2	1	no	no	BH
100	1	2	2	no	no	BH
150	1	1	3	yes	no	MF
100	1	2	3	no	yes	RA

Specifically, to analyze the influence of the virtual filter to decrease the beam hardening effect, one traverse that completely passes through rim to rim from the centered XY-view slice was done for the three beam hardening filter conditions to measure the resulting linear attenuation coefficient with sample radius. Therefore, to observe the effect of ring artifact on tomograms, the centered area where rings are viewable (2-mm view) were cut to apply bubble textural analysis. The 2D tomogram slice segmentation was applied with the "Threshold" tool of ImageJ, using a similar procedure used with Avizo Lite 9.4 presented below. Number, sizes and shape factors were analyzed with "Object Measurements" tool of JMicrovision.

3.3.4. Image reconstruction and segmentation

The set of radiograms were reconstructed (converted to a tomogram) with Nikon CT Pro 3D XT4.4 software. A center of rotation of the sinograms (mid-step of the reconstruction) was created by applying a dual method. In this panel, the resulting linear attenuation coefficient interval is recorded for image quality tests (see above). CT Pro 3D offers six pre-set virtual beam hardening filters (Table 3.3) which arrange the obtained linear attenuation coefficient as a function of cylinder radius by applying a fourth order polynomial. I tested the three weakest options because the three strongest decrease the whole image contrast (not only modify the rims). Other virtual filters such as noise reduction and median vicinity filters were not applied to avoid biasing the test analyses. To visually compare the effect of the X-ray tomography conditions on the resulting images, I convert the same linear attenuation coefficient range to grayscale index for all the analyses made. Thus, a pixel with a linear attenuation coefficient $\leq$ 0 appears black (0 in grayscale index of 16-bits images) and a pixel with a linear attenuation coefficient $\geq$ 400 appears white (65535 in grayscale index of 16-bits images). The reconstructed tomogram is opened with VGStudio Max 3.0 software to export a XY view slice from the cylinder center. The XY view slice is used for image quality tests and 2D bubble shape analysis. Videos of scanning in Z and Y direction (XY and XZ views, respectively) were

also obtained from this software (see Supplementary Material). The set of 2000 XY view slices was exported for 3D bubble textural analysis.

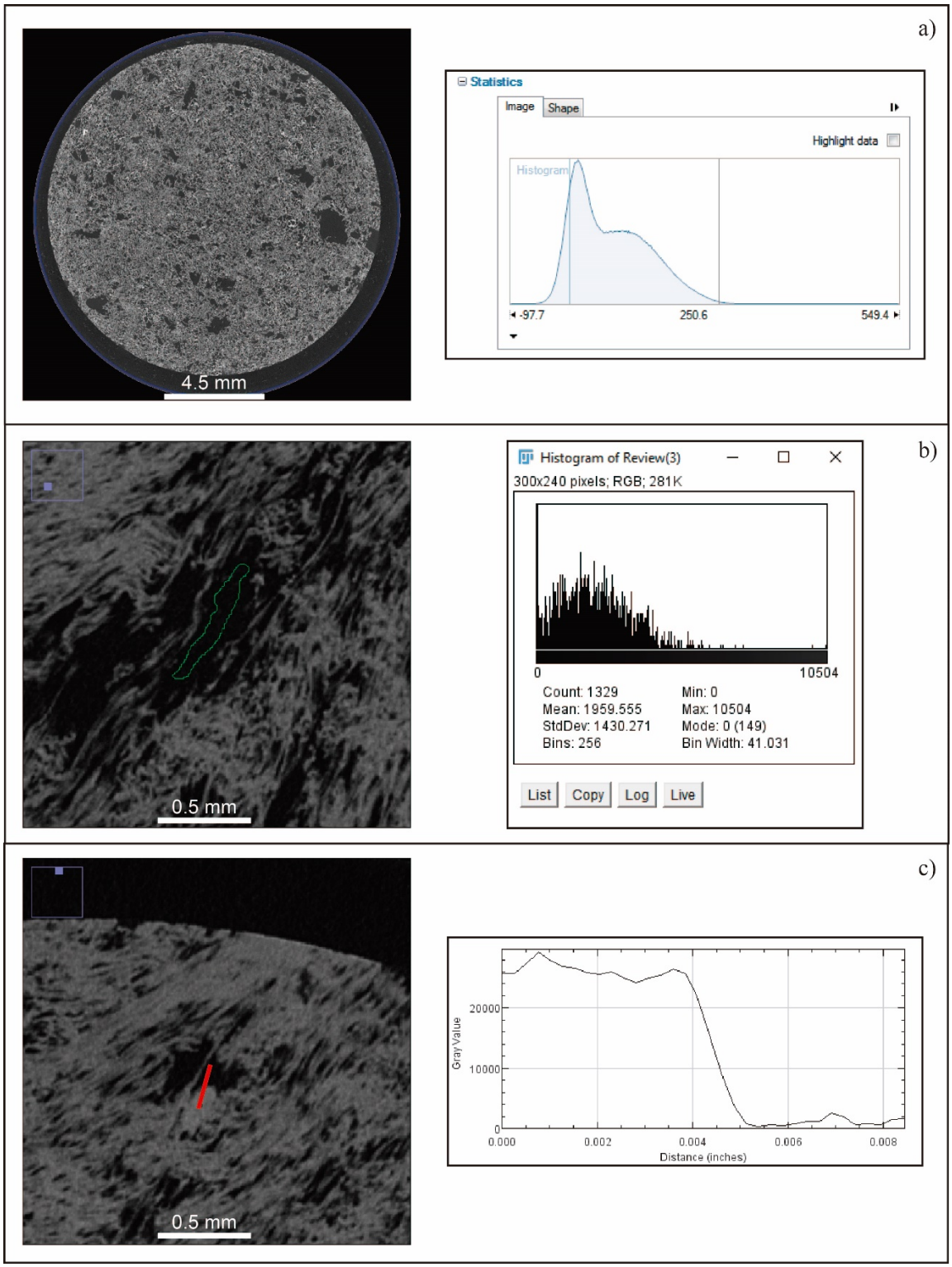

Fig. 3.2: The three quantitative tests applied to analyze tomogram quality. A The linear attenuation coefficient range. **B** Histogram of grayscale values within bubbles. **C** Grayscale-pixel ratio of traverses orthogonal to bubble-glass boundaries. Caption of **A** comes from Nikon CT Pro 3D XT4.4 software; whilst captions of **B** and **C** come from ImageJ.

The resulting reconstructed tomographic slices were opened with Avizo Lite 9.4 software for 3D bubble textural analysis. First, a volume of interest (VOI) was selected in order to avoid the external background, and to avoid the Z-axis sample extremes which present failures of sinogram-tomogram reconstruction (the image turns blurry and sample rims are darker). The image is segmented by the "Interactive Threshold" tool by which a grayscale interval beginning at 0 is selected such that the bubble volume fraction corresponds to the calculated porosity of the cylinder. Quantitative bubble textural analyses are performed by the "Porosities Analysis Wizard" tool which is designed to analyze voids inside solid materials. Here, crystals and glass are recognized as the solid materials and the bubbles as the voids. No denoising or median filter are applied to avoid biasing the control of X-ray tomography conditions on the tomogram quality. Bubbles are selected with two methods: selection of "strong" voids by the application of the previously selected grayscale interval and the selection of "weak" voids by defining the tolerance of selected objects. No limits of bubble size or object separation (Watershed filters) are applied to avoid biasing the obtained textural distributions.

Table 3.3: Coefficients of the polynomial functions with sample radius of the pre-set virtual beam hardening filters offered by Nikon CT Pro 3D XT4.4 software. In this study, I applied the options 1, 2 and 3.

	Scale	X^0	X^1	X^2	X^3	X^4
Option 1	1	0	1	0	0	0
Option 2	1.32	0	0.75	0.25	0	0
Option 3	1.94	0	0.5	0.5	0	0
Option 4	4.44	0	0.2	0.8	0	0
Option 5	10	0	0	0.8	0.2	0
Option 6	139	0	0	0.2	0.8	0

3.3.5. Principles of bubble textural analysis

3.3.5.1. Bubble number density

The bubble number density (BND) is the measure of the number of bubbles per unit of volume of silicic melt. The silicic melt is considered as the current groundmass glass, and neither considering the volume of the crystal phenocrysts (formed before the ascent) nor the bubbles (bubbles cannot nucleate or grow within other bubbles). By assuming some ideal conditions (e.g., magma is homogeneous during ascent, bubbles are spheres and coalescence does not occur), BND has been used to estimate the magma decompression rate, and so intensity, of explosive eruptions (Toramaru, 2006). Silicic-to-intermediate pumices usually have higher BNDs than mafic scoriae; whilst silicic-to-intermediate pumices from Plinian eruptions usually have higher BNDs than ones from subplinian eruptions (e.g., Alfano et al., 2012). If the duration of magma ascent is known, BND can be also used to estimate average nucleation rates.

3.3.5.2. Bubble size distributions

The size distribution of objects within volcanic rocks is probably the most applied quantitative textural analysis for deciphering magmatic processes. The technique was originally designed to determine the kinetics of feldspar crystallization within a lava fountain by comparing the population density (the number of crystals of a certain size per unit of volume) with the crystal size in a log-normal diagram (Cashman and Marsh, 1988; Marsh, 1988). By assuming a steady-state magmatic process, the Y-axis intercept is used as a proxy for crystal nucleation rate and the diagram slope is used as a proxy for crystal growth rate or residence time (Marsh, 1988). The same numerical structure was started to use for bubble size distributions. In some of the pioneer studies, bubbles were treated like crystals to obtain quantitative parameters of bubble dynamics (e.g., Mastrolorenzo and Pappalardo, 2006). Later, bubble size distributions were used to semi-quantitatively compare among deposits and to decipher processes like multiple

stages of bubble nucleation and growth (e.g., Mastrolorenzo and Pappalardo, 2006), bubble coalescence (e.g., Gurioli et al., 2008), bubble ripening (e.g., Mangan and Cashman, 1996) and bubble collapse (e.g., Burgisser and Gardner, 2005). Bubble size distributions can be also plotted in histograms of the bubble volume fraction per bubble size and in decreasing cumulative distribution with size (Shea et al., 2010). The advantage of the first method is that it clearly shows the number of stages of magma conditions (according to the number of modes in the histograms), bubble coalescence (when a low second peak occurs at largest sizes), ripening (with a unimodal distribution of negative skewness) and collapse (with a unimodal distribution of positive skewness; Section 1.1.3). The advantages of the second method are that it does not depend on the selected number of bins of bubble size to plot the distributions and that log-log cumulative distributions are straight when coalescence occur. A good summary of the different ways to plot BSDs and the type of information that can be retrieved from them can be found in Shea et al. (2010).

3.3.5.3. Bubble shape factors

Shape factors are parameters that numerically describe the shape of objects. The most used shape factor is probably the aspect ratio or elongation, which is the ratio between the object length and width (or conversely) by considering the object like an ideal ellipse or rectangle (e.g., Polacci et al., 2001). In the case of bubbles, elongation is a fundamental parameter by which to understand the local and general control of strain in magmatic processes by considering that bubbles ideally nucleate and grow with a spherical shape (e.g., Wright and Weinberg, 2009). Together with bubble orientation, the elongation of several bubbles can be used to constrain flux diagrams that represent trends of deformation or flow (e.g., Cai et al., 2014). More locally, they can define strain localizations. An excellent review of shape factors and their application to volcanic processes can be seen in Liu et al. (2015).

3.4. Tests of tomogram quality

3.4.1. Energy

For all analyzed samples, the linear attenuation coefficient range is broadened by decreasing the applied energy (Fig. 3.3). For example, for the Los Espejos and Mazama samples (from now on, silicic samples) present a ~1.2 orders of magnitude broader range in linear attenuation coefficient for and applied energy of 55 kV compared to 150 kV; in the Aluto sample the difference is ~1.4 orders of magnitude and in the Katla sample (from now on, both together called alkaline samples) it is ~1.5 orders of magnitude (See details in Table 3.4). A consequence of this is that the frequency of pixels corresponding to the minimum and maximum grayscale values, after reconstructing the tomogram, increases by decreasing the applied energy. The signal-to-noise ratio is slightly better with higher energy (Table 3.5); however, these variations are lower than 1% with respect to the maximum grayscale values. Consequently, I consider that this tomogram quality parameter is not highly affected by the applied energy. The edge sharpening considerably improves by decreasing the applied energy: in the most silicic samples, the attenuation coefficient-pixel ratio when applying 55 kV is 4.3 times higher than when applying 150 kV and 2.7 times higher than when applying 100 kV; in the most alkaline samples, the resulting attenuation coefficient-pixel ratios are even higher (Table 3.6).

3.4.2. Number of frames per radiogram

The maximum linear attenuation coefficient range occurs by applying 2 frames per radiogram: the resulting coefficient range with 2 frames per radiogram is 1.7 and 2.2 times higher than applying 1 and 4 frames per radiogram, respectively (Table 3.4). The signal-to-noise ratio improves by increasing the number of frames per radiogram: although the average grayscale value within bubbles does not vary significantly by changing this parameter, the resulting maximum grayscale value and the standard deviation of the grayscale values within bubbles

are three and two times higher by applying 4 frames per radiogram, respectively, with regard to the other applied conditions (Table 3.5). The edge sharpening slightly improves by applying 2 frames per radiogram: the attenuation coefficient-pixel ratio by applying 2 frames per radiogram is 1.3 times higher than applying 1 frame per radiogram and 1.5 times higher than applying 4 frames per radiogram. Also, the variation of this parameter is lower with 2 frames per radiogram (Table 3.6).

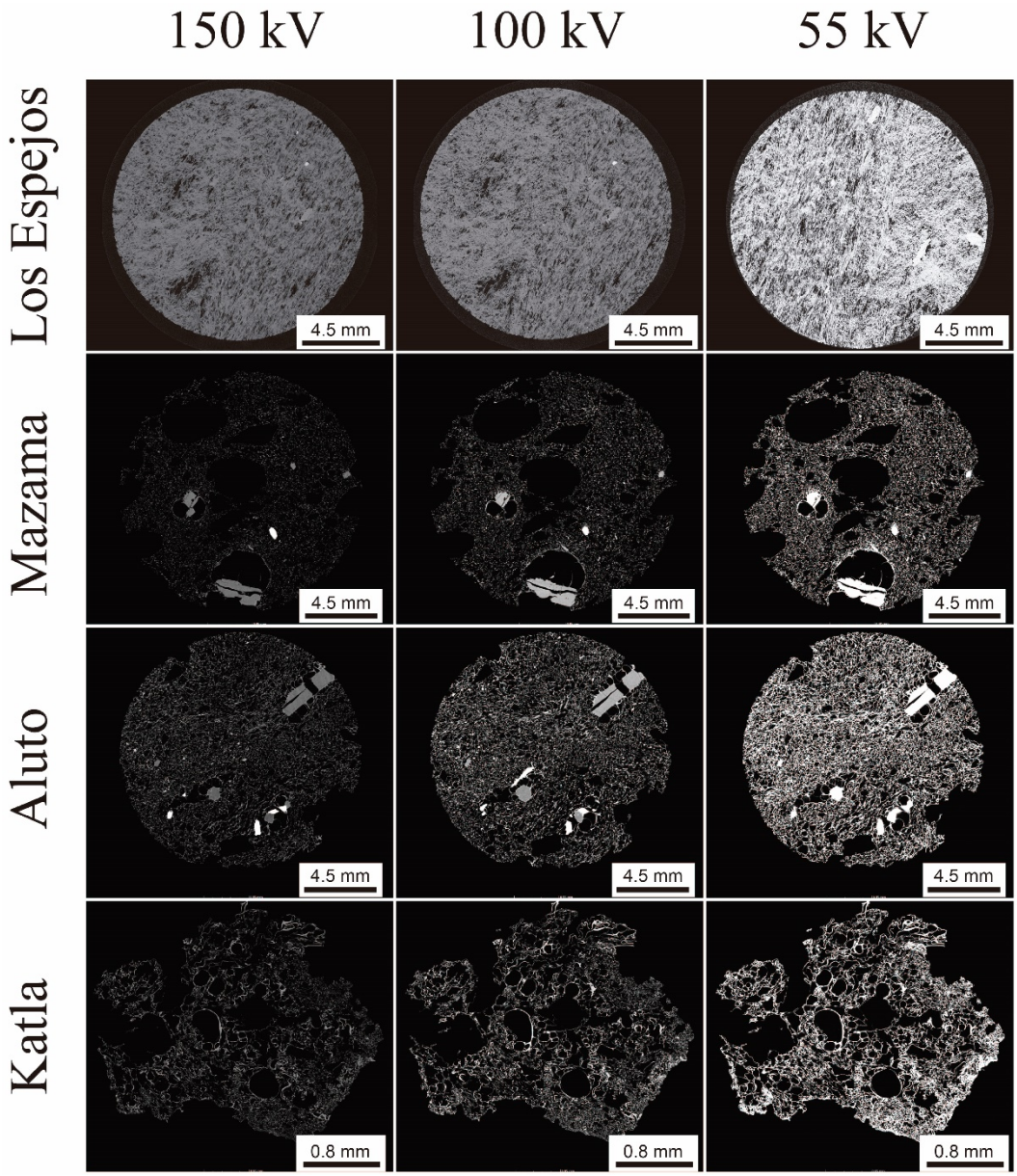

Fig. 3.3. Variations of acquired tomograms with applied energy. The 16-bits grayscale values represent a linear coefficient attenuation range between 0 and 400. The images are the #1000 slice in XY view.

Table 3.4: Linear attenuation coefficient ranges for the applied tests of tomogram quality. For conditions where the sample is not specified, it refers to Los Espejos pumice. The values are in m^{-1}.

Voltage								
	Los Espejos		Mazama		Aluto		Katla	
150 kV	-47.8	380.9	-32.8	453	-42.8	357	-32.6	298
100 kV	-110	2360	-89	2862	-142	3156	-84.6	3260
55 kV	-340	6049	-302	6253	-522	8670	-509	11207
Frames per radiogram								
4 fpi	-81	1867						
2 fpi	-125	4169						
1 fpi	-110	2360						
Exposure time								
0.5 s	-121.8	533.2						
1.0 s	-47.8	380.9						
1.4 s	-96	2340						
Beam Hardening								
	Los Espejos		Mazama		Aluto		Katla	
Op 1	-42	1001	-54	1164	-59	1247	-72	1299
Op 2	-62	1576	-84	1836	-107	2005	-81	2361
Op 3	-120	2689	-147	3061	-162	3589	-206	3782
Metal Filter								
With	-88.5	270.4						
Without	-47.8	380.9						
Ring Artifact								
With	-98	2248						
Without	-120	2689						

3.4.3. Exposure time

The resulting linear attenuation coefficient range is broadened by increasing the exposure time: while the resulting coefficient range is quite similar between 0.5 and 1.0 seconds per radiogram, the range considerably widens by applying 1.4 seconds per radiogram being 3.7 and 5.7 times broader than 0.5 and 1.0 seconds per radiogram, respectively (Table 3.4). The signal-to-noise

ratio is slightly better when increasing the exposure time; however, these variations are lower than 1% with respect to the maximum grayscale values (Table 3.5). Consequently, I consider that this tomogram quality parameter is not highly affected by the exposure time of radiograms. The edge sharpening slightly improves by increasing the exposure time: the attenuation coefficient-pixel ratio when applying 1.4 seconds per radiogram is 1.6 times higher than when applying 1 second per radiogram. I do not consider the 0.5 seconds per radiogram application in this analysis because of the high variability of results (Table 3.6).

3.4.4. Virtual beam hardening filter

The radial traverse of gray-scale values in the XY-view center slice suggests that the softest virtual beam hardening setting, which applies a linear correction with sample radius, is not enough to arrange the beam hardening (Fig. 3.4): from rim to core, the highest resulting grayscale value (corresponding to glass or silicates) varies from 22,000 to 14,000. On the other hand, the intermediate and strongest virtual beam hardening settings (both corresponding to second order polynomials as functions of sample radius) do correct the beam hardening artifact. However, the application of a very-strong virtual beam hardening filter may bias the whole linear attenuation coefficient range as this is broader for any sample composition. By comparing the application of the strongest beam hardening filter with the application of the weakest one, Los Espejos and Mazama (silicic) samples present a ~2.7 times broader range; whilst in Aluto and Katla (alkaline) samples is ~2.9 times (Table 3.4). A consequence of this is that the frequency of pixels corresponding to the minimum and maximum grayscale values, after reconstructing the tomogram, increases by applying a stronger beam-hardening filter. The signal-to-noise ratio is slightly better with a stronger beam hardening filter; however, these variations are lower than 1% with respect to the maximum grayscale values (Table 3.5). Consequently, I consider that this tomogram quality parameter is not highly affected by the virtual beam-hardening filter. The edge sharpening is similar for both second order polynomial

filters, whilst it is worse for the weakest one (Table 3.6): in the most silicic samples, the attenuation coefficient-pixel ratio is 2.0-2.3 times higher when applying the strongest filters than when applying the weakest one; in the most alkaline samples, the resulting attenuation coefficient-pixel ratios are even higher.

3.4.5. Metal filter

The application of the 0.25-mm Cu-Al filter does not strongly impact the tomogram quality. For instance, the linear attenuation coefficient range is 1.2 times broader when not applying the filter (Table 3.4). The signal-to-noise ratio is slightly better by not applying the metal filter; however, the variation is lower than 1% with respect to the maximum grayscale values (Table 3.5). Consequently, I consider that this tomogram quality parameter is not highly affected by the application of the metal filter. The edge sharpening slightly improves not applying the metal filter: the obtained attenuation coefficient-pixel ratio without metal filter is 1.2 times higher than applying the metal filter (Table 3.6).

3.4.6. Ring artifact minimizer

The application of the ring artifact minimizer also does not strongly affect the tomogram quality (Fig. 3.5). For instance, the linear attenuation coefficient range is 1.2 times broader when not applying the ring artifact minimizer (Table 3.4). The resulting signal-to-noise ratio is similar in both conditions (Table 3.5). The edge sharpening slightly improves by applying the ring artifact minimizer: the obtained attenuation coefficient-pixel ratio with ring artifact minimizer is 1.2 times higher than when not using the virtual filter (Table 3.6).

Table 3.5: Signal-to-noise ratio (values correspond to grayscale within an interval of 0 – 65535) for the applied tests of tomogram quality. For conditions where the sample is not specified, it refers to Los Espejos pumice.

Voltage												
	Los Espejos			Mazama			Aluto			Katla		
	Mean	Max	StdDev	Mean	Max	StdDev	Mean	Max	StdDev	Mean	Max	StdDev
150 kV	2328	21860	2274	2108	15203	1360	2564	25164	2543	2832	28476	2632
100 kV	2886	23853	2869	2456	18637	1842	2630	29402	2837	3086	32496	3018
55 kV	2889	21742	3556	2817	16244	2311	2896	26197	3408	3321	28912	3634
Frames per radiogram												
	Mean	Max	StdDev									
4 fpi	1915	6245	1222									
2 fpi	1736	19229	2174									
1 fpi	2507	21579	2224									
Exposure time												
	Mean	Max	StdDev									
0.5 s	2471	11062	2272									
1.0 s	1669	7024	1296									
1.4 s	1102	6493	1243									

Beam Hardening												
	Los Espejos			Mazama			Aluto			Katla		
	Mean	Max	StdDev	Mean	Max	StdDev	Mean	Max	StdDev	Mean	Max	StdDev
Op 1	3137	7223	1150	3712	7526	1286	4319	9054	1424	4622	10257	1544
Op 2	2479	8577	1594	2933	10265	1785	3408	12547	2054	3589	11853	1965
Op 3	1754	11199	2012	2126	13276	2546	2677	16947	3046	2738	17660	3108
Metal Filter												
	Mean	Max	StdDev									
With	1022	8622	1326									
Without	1897	6251	1328									
Ring Artifact												
	Mean	Max	StdDev									
With	1636	8137	1797									
Without	1759	11199	2015									

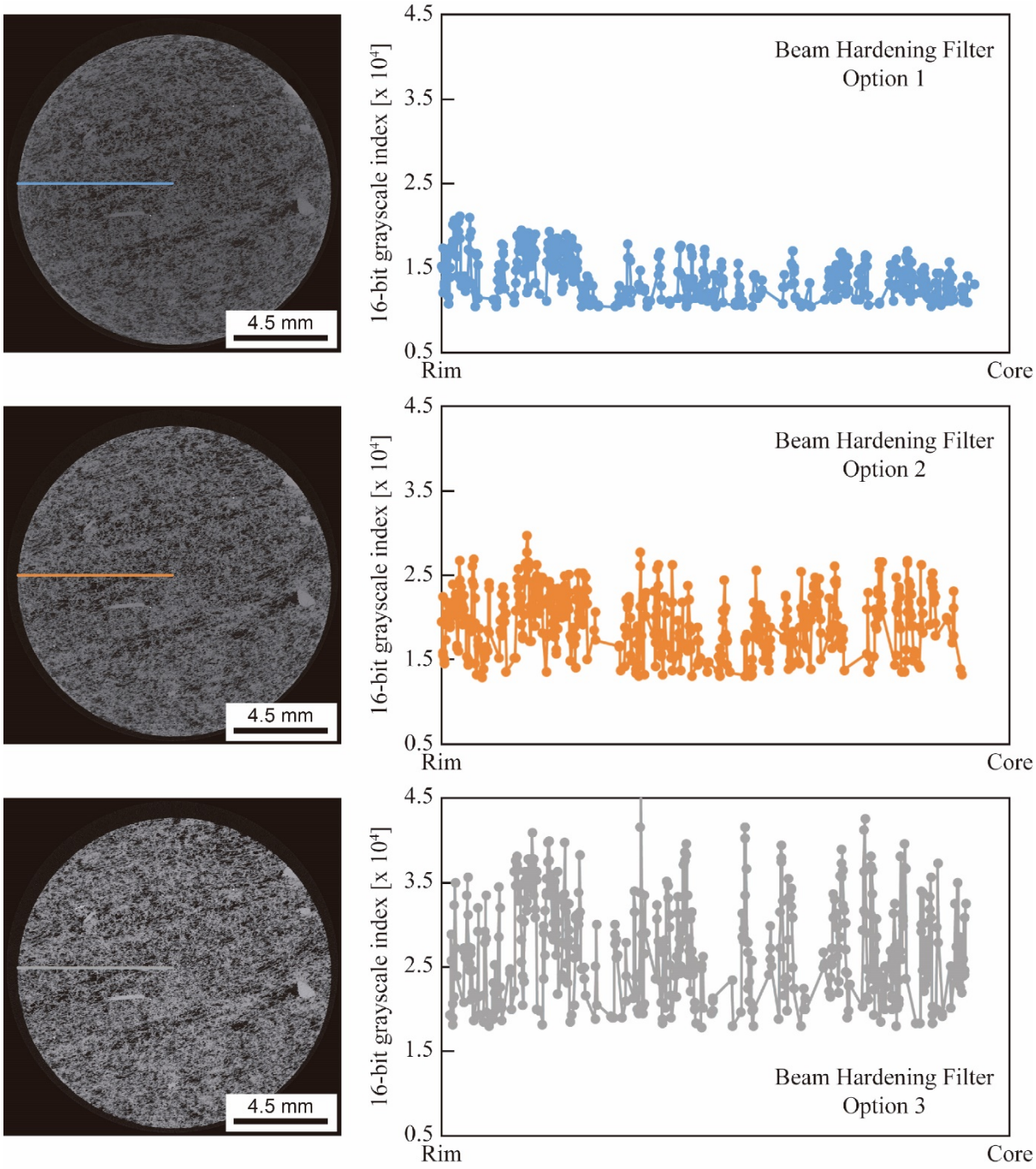

Fig. 3.4. Application of three settings of beam hardening filter. At the right are indicated the 16-bits grayscale values corresponding to the rim-to-core traverses. The three grayscale images correspond to the #1000 slice in XY-view of Los Espejos sample.

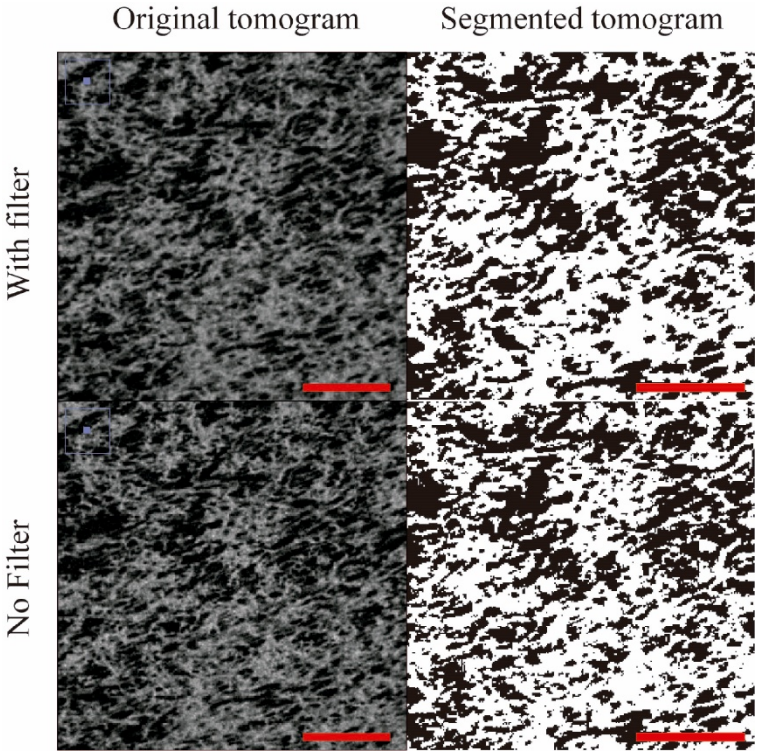

Fig. 3.5. The effect of the application of ring artifact minimizer. The ring artifact minimizer does not produce significant changes to acquired tomograms. Although blurry rings are observable at the center, they do not affect the image segmentation. The images correspond to Los Espejos sample and the red bar = 0.5 mm.

Table 3.6: Edge sharpening (grayscale value / pixel) for the applied tests of tomogram quality. For conditions where the sample is not specified, it refers to Los Espejos pumice.

Voltage (Los Espejos)							
	P1	P2	P3	P4	P5	Average	Std. Dev.
150 kV	3800	3241	5001	2141	1788	3194.2	1296.2
100 kV	5130	6701	3855	6577	5532	5559	1165.0
55 kV	10627	17402	16342	10056	14438	13773	3313.8
Voltage (Aluto)							
	P1	P2	P3	P4	P5	Average	Std. Dev.
150 kV	3629	3176	4627	2236	2043	3142.2	1057.4
100 kV	7364	8467	5603	8940	7364	7547.6	1287.7
55 kV	14653	24817	22689	16507	19632	19659.6	4206.6
Frames per radiogram							
	P1	P2	P3	P4	P5	Average	Std. Dev.
4 fpi	4244	5427	6106	5773	2181	4746.2	1596.8
2 fpi	6776	7521	8670	6537	6542	7209.2	910.5
1 fpi	5130	6701	3855	6577	5532	5559	1165.0

Exposure time							
	P1	P2	P3	P4	P5	Average	Std. Dev.
0.5 s	3523	2610	5266	7353	8598	5470	2517.0
1.0 s	3800	3241	5001	2141	1788	3194.2	1296.2
1.4 s	5127	6490	6299	3939	4404	5251.8	1127.8
Beam hardening (Los Espejos)							
	P1	P2	P3	P4	P5	Average	Std. Dev.
Op 1	3383	2901	3072	1782	1876	2602.8	728.0
Op 2	4972	5565	3757	5395	6629	5263.6	1040.1
Op 3	8619	5820	3103	7631	4944	6023.4	2182.7
Beam hardening (Aluto)							
	P1	P2	P3	P4	P5	Average	Std. Dev.
Op 1	2946	3154	3347	2048	2164	2731.8	590.0
Op 2	6749	7348	4997	7144	8863	7020.2	1386.1
Op 3	12846	8846	5078	11475	7487	9146.4	3102.6
Metal Filter							
	P1	P2	P3	P4	P5	Average	Std. Dev.
With	2026	2668	2479	4243	1782	2639.6	963.0
Without	3800	3241	5001	2141	1788	3194.2	1296.2
Ring Artifact							
	P1	P2	P3	P4	P5	Average	Std. Dev.
With	6010	7559	8299	9291	6111	7454	1413.2
Without	8619	5820	7631	4944	3103	6023.4	2182.7

3.5. Bubble textural analysis

In this section I determine the sensitivity of bubble number densities, bubble size distributions and bubble aspect ratios to tomogram acquisition conditions. The bubble textural analyses are more focused on the applied energy and the virtual beam hardening filters as they are the two X-ray tomography conditions that strongly affect the tomogram quality. I also analyze bubble

textures for the application of metal filters, that is the X-ray tomography condition with lowest impact on the tomogram quality tests. The analysis of bubble textures by applying the ring artifact minimizer was done to determine how the existence of blurry rings can affect the results of bubble textural analysis.

3.5.1. Bubble number densities

Around 1 million low-density objects are recognized in each tomogram. However, just ~25% of them are objects suitable for textural analysis according to their volume (objects comprised of >4 voxels). The groundmass glass volume was initially estimated as the sample volume minus the bubbles volume. As the samples analyzed are crystal poor, crystals were segmented by hand in order to subtract their volume. The estimated bubble number density increases by decreasing the applied energy regardless of the sample composition (see a compilation of BND results in Table 3.7). In the silicic samples, the BND obtained from the lowest applied energy is ~1.5 times higher than for the highest applied energy; whilst, in the case of the alkaline samples, the BND is ~1.9 higher for the lowest applied energy versus the highest applied energy. However, the virtual beam hardening has almost no effect on the calculated BND: although the obtained BND is slightly higher when applying a stronger virtual beam hardening, the variations between the strongest and the weakest ones are <10% regardless of the sample composition. Surprisingly, the BND is significantly affected by application of the metal filter: the BND calculated from the analysis with metal filter is ~1.3 times higher than that calculated from the analysis without metal filter. The application of ring artifact minimizer almost does not affect the calculated BND: although the obtained BND is slightly higher when not applying the ring artifact minimizer, the variation between both X-ray tomography conditions is <6% for the entire sample and <1% when considering only the center where rings are observable.

Table 3.7: Calculated bubble number densities (in number of bubbles per cubic millimeter) for the applied X-ray tomography conditions. For conditions where the sample is not specified, it refers to Los Espejos pumice.

Voltage				
	Los Espejos	Mazama	Aluto	Katla
150 kV	184180	1593645	613933	452893
100 kV	239434	2007993	920900	724629
55 kV	276270	2294849	1166473	928431
Beam Hardening				
	Los Espejos	Mazama	Aluto	Katla
Option 1	216068	1828454	792147	596030
Option 2	224913	1891041	804697	612764
Option 3	234942	1965421	845276	652794
Metal Filter				
With	179742			
Without	138903			
Ring Artifact				
	Complete	Center		
With	213919	307272		
Without	234942	324937		

3.5.2. Bubble size distributions

I plot the bubble size distributions by using pointed log-normal diagrams in order to make quantitative descriptions. I do not observe significant variations in BSDs by varying the applied energy, regardless of the sample composition (Fig. 3.6). One slight difference, clearer with the silicic samples, is that the maximum bubble size is larger when increasing the applied energy. A similar trend is observed by varying the virtual beam hardening filter: the intercept and slopes of BSD are similar among the three X-ray tomography conditions, but the maximum bubble size is increased by applying a weaker beam hardening filter. Like the observed variations in BNDs, the metal filter does affect the BSDs: the resulting BSD from the application of metal filter present higher population densities for the smallest bubble sizes, lower population

densities for the largest bubble sizes; hence, sharper BSD slopes, and larger maximum bubble size. The application of the ring artifact minimizer does not affect the calculated BSD, even at the center of the tomogram.

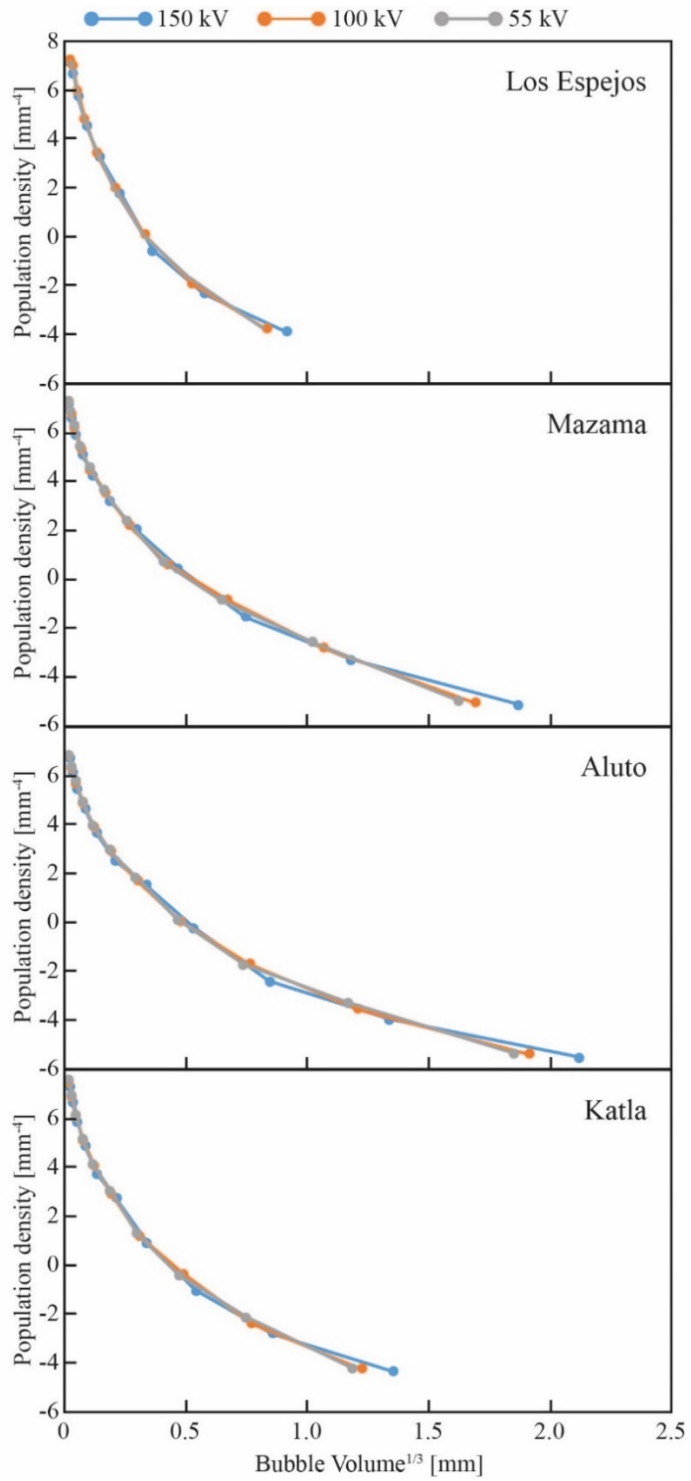

Fig. 3.6. Variations of bubble size distributions with applied energy. Because of the different bubble aspect ratios among samples, the bubble size is expressed as the cubic root of the bubble volume. Data is plotted in log-normal diagrams (Section 1.1.3).

3.5.3. Bubble aspect ratios

Considering that Aluto, Mazama and Katla samples are affected by high strain resulting in tubular bubble arrangements, the analyzed aspect ratio is calculated in 2D slices, orthogonal to the direction of preferable orientation (i.e. I analyze the cross-sectional shapes of the elongate bubbles). To use the same procedure for all the analyzed samples, I also use 2D slices for analyzing bubble aspect ratios of the Los Espejos sample. The resulting aspect ratios are not affected by variations for any of the analyzed X-ray tomography conditions (Fig. 3.7).

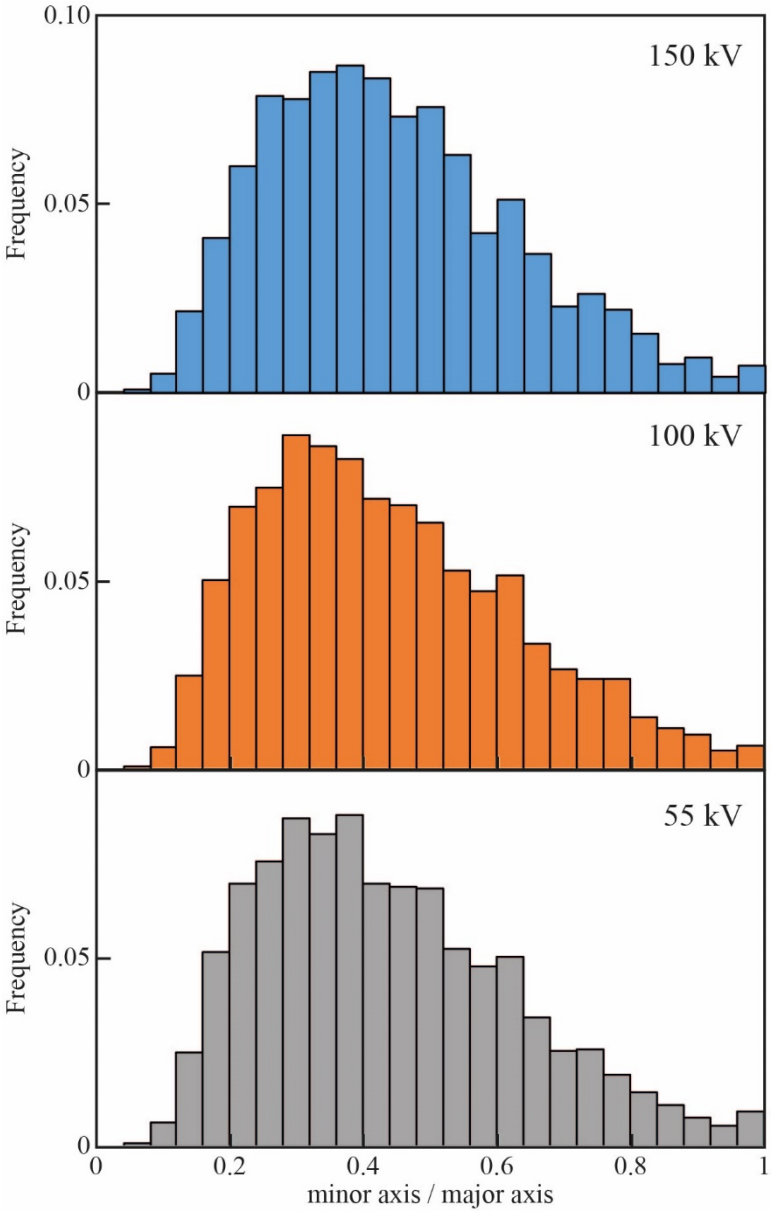

Fig. 3.7. Histograms of bubble aspect ratios. The bubble aspect ratio is not controlled by the applied energy. The three histograms correspond to aspect ratios measured in XY-view slices of Aluto sample.

3.6. Interpretations

This section presents the direct interpretations from the effect of X-ray tomography conditions on the tomogram quality and how the variations of the resulting tomograms may affect the analysis of bubble textures.

3.6.1. The role of X-ray tomography conditions on the tomogram quality

I observe that X-ray tomography conditions do affect the quality of tomograms. The obtained linear attenuation coefficient range is highly dependent on the applied energy: a variation of 100 kV can broaden the resulting coefficient range by more than one order of magnitude. The application of an exposure time longer than 1 s can also significantly increase the linear attenuation coefficient range, but with the obvious cost of a longer acquisition time for each analysis. The application of virtual beam hardening filters may also improve the image contrast: my analyses show that the application of a second order polynomial with sample radius may broaden by three times the attenuation coefficient range with regard to the application of a linear arrangement with sample radius. The number of frames per radiogram, the application of metal filters and the ring artifact minimizer do not control the obtained linear attenuation coefficient range. The signal-to-noise ratio, measured by obtaining grayscale histograms of voxels within bubbles, is not affected by most of the conditions considered, but increasing the number of frames per radiogram does decrease the number of gray pixels inside bubbles. However, it is important to highlight that the increment of frames per radiogram results in long-duration analysis. The edge sharpening, that is the definition of boundaries between different materials, is also affected by the applied X-ray tomography conditions. It seems that the edge sharpening is closely related to the obtained linear attenuation coefficient range because both depend on the applied energy and the virtual beam hardening filter: the resulting edge sharpening can be improved up to 5 times by decreasing the applied energy in 100 kV. Therefore, the application of second order polynomial (with sample radius) virtual

beam hardening filters can improve the resulting edge sharpening by up to 2.5 times relative to the application of a filter that linearly depends on sample radius. The number of frames per radiogram and the exposure time play a secondary role in controlling edge sharpening: the attenuation coefficient-pixel ratio slightly increases with 2 frames per radiogram and an exposure time shorter than 1 s is not recommended to constrain object boundaries. The application of metal filters and ring artifact minimizer do not play an important role on the edge sharpening.

3.6.2. The role of the tomogram quality on bubble textural analysis

The tomogram quality does affect the analysis of bubble textures. A broader linear attenuation coefficient range and higher attenuation coefficient-pixel ratios allow to determine the boundary between different objects; for example, a decrease of 100 kV permits recognition of up to 1.5 times more bubbles in the same sample. Consequently, the variation of the applied energy highly controls the resulting bubble number density. Despite its importance for improving the attenuation coefficient range and the edge sharpening, the application of virtual beam hardening filters does not significantly affect the bubble number density. Conversely, the application of metal filters, which did not quantitatively improve the tomogram quality, does increase the recognition of bubbles.

What kind of bubbles are better recognized by improving the tomogram quality? By analyzing bubble size distributions, I observe that a smaller maximum bubble size is obtained by decreasing the applied energy and by applying a stronger virtual beam hardening filter. Consequently, the improvement of the tomogram quality results in the recognition of more bubbles and the reduction of the bubble sizes. I interpret this as the existence of small bubbles around big bubbles that are increasingly recognized by improving the tomogram quality. This is not a matter of the image resolution (all the applied analyses have voxel size of ~7 μm in

linear dimension), else of the capability of recognizing narrow bubble walls (high edge sharpening) by using grayscale values (broader linear attenuation coefficient range) (Fig. 3.8). A special situation is occurring with the application of metal filters: I obtained steeper (higher population density of small bubbles and lower population density of large bubbles) BSDs by using a metal filter.

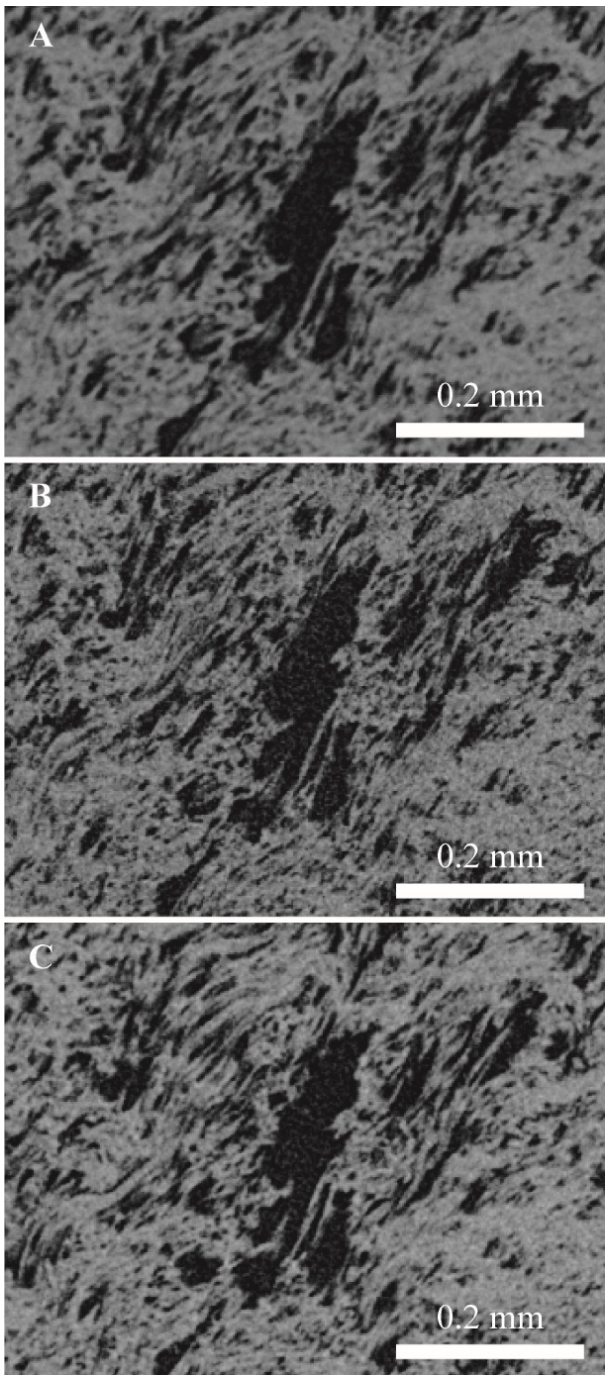

Fig. 3.8. Same view of Los Espejos sample for different applied energies. Bubble-glass boundaries are clearer by decreasing the energy resulting in higher amount of small bubbles recognized. **A**, **B** and **C** correspond to 150 kV, 100 kV and 55 kV respectively.

3.7. Discussion

In this section I give further consideration to the parameters that control the resulting linear attenuation coefficient from a physical perspective, why the analyzed X-ray tomography conditions control the tomogram quality and resulting textural analysis in the way that they do, and what geological implications come from the observed variations on bubble textural analysis.

3.7.1. Controlling factors on the linear attenuation coefficient

With applied energies lower than 200 kV, the photoelectric absorption controls the resulting linear attenuation coefficient (Ketcham, 2005; McCullough, 1975). In this condition, the linear attenuation coefficient has a linear dependence on the material density, a power-law dependence on the atomic number and an inverse power-law dependence on the applied energy (Attix, 1986; Knoll, 2000; McCullough, 1975). Silicic pumices may present wide variations in vesicularities, and those vesicularities can be represented by bubbles or voids of different sizes. The population of bubbles with sizes smaller than the voxel size of the acquired tomogram will not be visible in the resulting grayscale images but can decrease the obtained linear attenuation coefficient by decreasing the apparent glass density of pumices. Thus, the existence of submicrovesicles may darken the analyzed glass of pumices in X-ray tomograms.

X-ray tomograms are the result of the reconstruction of a set of radiograms that vary according to the angular position from which they were taken. Radiograms are squared pixel maps that represent the resulting linear attenuation coefficient passing through the object. Each pixel is the result of the integral of the attenuation corresponding to each position along the X-ray path in the source-target direction (Feldkamp et al., 1984; Kak and Slaney, 1988; Quinto, 2005). As pumices are multi-phase and multi-component materials, the obtained linear attenuation coefficient in each pixel within radiograms is the average of the atomic number of all the

components that were crossed by the incident X-rays. The higher the atomic number, the higher the linear attenuation coefficient. This explains why in tomograms Fe-Ti-Cr oxides appear white (high linear attenuation coefficient), while mafic minerals like olivine, pyroxene, hornblende and biotite appear light-gray (medium-high linear attenuation coefficient), felsic minerals like plagioclase, k-feldspar and quartz appear dark-gray (medium-low linear attenuation coefficient), and voids and background appear black (low linear attenuation coefficient). The role of the atomic number on the linear attenuation coefficient also explains why zoning within minerals can be recognized in tomograms. For instance, the zoning in plagioclase can be recognized because the high relative content of Ca (higher atomic number, higher linear attenuation coefficient, lighter color) versus a high relative content of Na (lower atomic number, lower linear attenuation coefficient, darker color; Boone et al., 2011). In the same way, variations in glass composition will be represented by variations in the obtained linear attenuation coefficient. The higher content of Fe, Ca and K should imply acquisition of higher linear attenuation coefficients; hence, lighter colors of glass. That implication may explain that the alkaline samples present higher variations on the resulting attenuation coefficient ranges, the edge sharpening and the calculated bubble number densities than the silicic samples by varying the applied energy.

The analyzed X-ray tomography parameter that most highly impacts the tomogram quality and the bubble textures is the applied energy. The tomogram quality improves by decreasing the applied energy because the linear attenuation coefficient is inversely proportional to almost the fourth power of the applied energy. In this way, the attenuation coefficient of different material diverges with decreasing applied energy (Gualda and Rivers, 2006; Ketcham and Carlson, 2001).

The rest of the considered X-ray tomography conditions do not substantially affect the linear attenuation coefficient but can also be analyzed from a theoretical point of view. The virtual beam hardening filter used by the CT Pro 3D software modifies the original linear attenuation coefficient according to the radial position of the voxel to be transformed by applying a fourth order polynomial function. Thus, objects with the same composition and density but different radial positions may appear to have different linear attenuation coefficients in the acquired tomogram if the applied virtual beam hardening filter is inadequate (Van de Casteele et al., 2002). I observe that as the beam hardening filter increases the obtained linear attenuation coefficient of all the analyzed voxels (except the ones located exactly at the center of the view), the whole tomogram quality is improved. In this way, a broader linear attenuation coefficient range, a better edge sharpening, and a better recognition of small objects around the biggest ones were obtained by applying a stronger virtual beam hardening filter. A physical condition that has not been deeply analyzed in this work is the applied current. Applying a higher current (or the same for a longer time) would perturb more electrons of the sample that would be received by the target (Rivers et al., 1999). As each X-ray tomography instrument has an optimum applied power, when the applied energy is decreased, the applied current is increased. That increment on the applied current also improves the obtained tomogram quality. The effect of the applied current on the tomogram quality may explain why a longer exposure time broadens the resulting attenuation coefficient range and improves the edge sharpening.

Another function that increases the total duration of the analysis is application of several frames per radiogram. In this way, the resulting linear attenuation coefficient of each pixel is the average of the different acquired radiograms of the same angular position. This improves the signal-to-noise ratio because the possibility of obtaining extreme linear attenuation coefficient is diminished by averaging several values. A similar result can be obtained by applying Kernel or median filters, which reduce noise using the values in surrounding voxels; however, these

tend to worsen the delimitation of boundaries between objects. I observe that both the attenuation coefficient range and the edge sharpening improve by increasing the number of frames per radiogram until an optimum value is reached (probably because the improvement of the signal-to-noise ratio), but later both tomogram quality parameters worsen by still increasing the number of frames (probably because of the decrease of the maximum linear attenuation coefficient and the decrease of the attenuation coefficient-pixel ratio).

3.7.2. Implications on the analysis of eruptive processes

I apply the model of Toramaru (2006) to estimate how the variations of applied X-ray tomography conditions could affect calculations of magma decompression rate of an eruption (Fig. 3.9). In the case of silicic pumices, the variation in the calculated magma decompression rate is proportional to estimated variations of BNDs. For instance, the estimated magma decompression rate of Los Espejos pumice decreases from 18 to 27 MPa s^{-1} by decreasing by 100 kV the applied energy, and from 18 to 14 MPa s^{-1} by removing the metal filter. In the case of alkaline pumices, the variation in the calculated magma decompression rate is lower than estimated variations of BNDs. Thus, the estimated magma decompression rate of Aluto pumice varies from 73 to 97 MPa s^{-1} decreasing by 100 kV the applied energy, and from 73 to 65 MPa s^{-1} by removing the metal filter. Although these variations in the calculated magma decompression rate are not enough to change the classification of the eruptive behavior (which usually is ranked in orders of magnitude), they are significant to distinguish among volcanic pulses or to classify eruptive stages of the same eruptive event (e.g., Alfano et al., 2012; Shea et al., 2010). Moreover, I realize that the propagated error resulting from the variations in the tomogram quality are comparable to the resulting variations from different vesicularities and/or population densities from the same eruption. Thus, the application of different X-ray tomography conditions in the analysis of silicic pumices may lead to misinterpretations on the degassing mechanisms and eruptive dynamics of eruptive events.

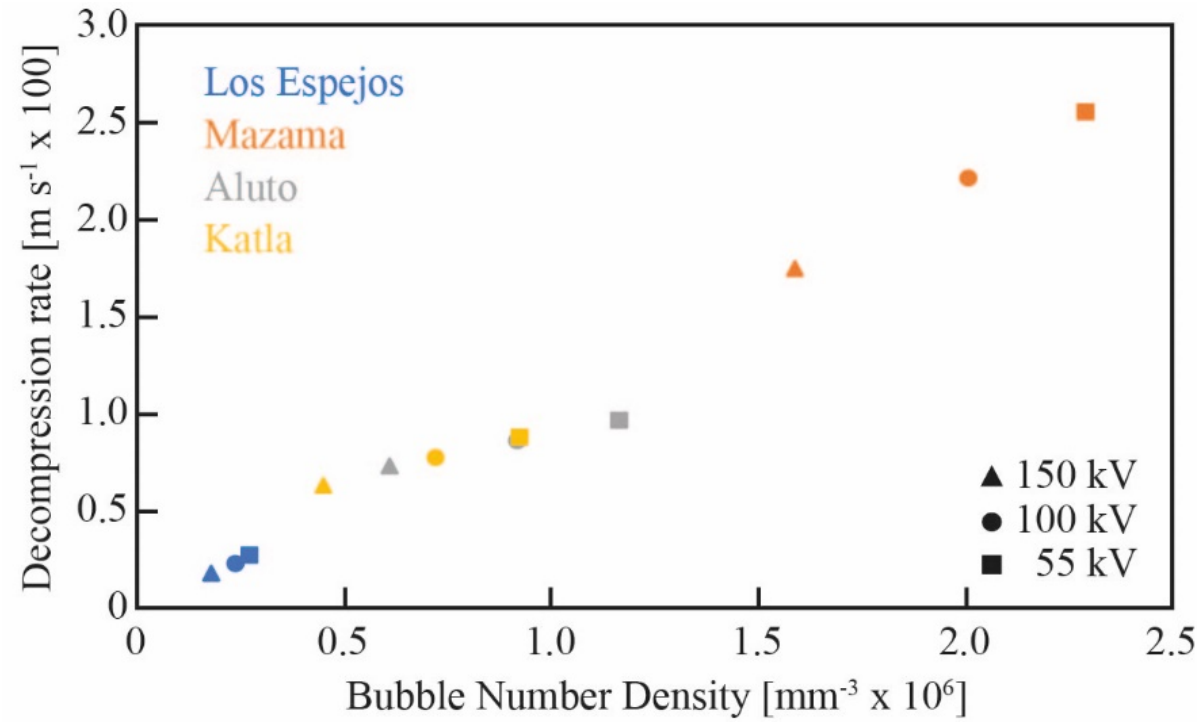

Fig. 3.9. Estimated magma decompression rate with Bubble Number Density. The three values per sample correspond to the three applied energies. The decompression rate was estimated by applying Toramaru model (2006).

Inaccurate bubble size distributions may lead to errors in estimates of nucleation and growth rates. The Y-intercept of a standard BSD plot is related to the bubble nucleation rate and the BSD slope is related to the bubble growth rate or to the duration of vesiculation. Thus, not resolving all of the smallest bubbles would lead to lower apparent nucleation rate and a higher bubble growth rate or longer duration of vesiculation. From a qualitative perspective, the improvement of edge sharpening permits recognition of small bubbles from borders of big bubbles; thus, lower degree of coalescence would be interpreted by improving the tomogram quality. Bubble coalescence is directly related with connectivity within volcanic rocks (Mancini et al., 2016). The connectivity, i.e., the ratio of open porosity with total porosity, is closely related to viscous permeability of magmas during ascent (Colombier et al., 2017). Without an optimum separation of the different bubbles within a porous media, numerical simulations of flow through the pore network imaged by tomography (e.g. Chapter 4) would

overestimate the permeability. Consequently, worse tomogram quality may lead to the interpretation of more efficient degassing.

3.8. Conclusion

Variations in applied X-ray tomography conditions do affect the quality of the acquired tomogram. I show that the applied energy, the applied current, the number of frames per radiogram, the exposure time, the application of virtual and metal beam hardening filters, and the application of ring artifact minimizer control directly or indirectly the resulting linear attenuation coefficient and the differential of attenuation coefficient between different materials within volcanic rocks. The variations of linear attenuation coefficients affect the whole image contrast, the signal-to-noise ratio and the edge sharpening. The improvement of these imaging parameters results in a better recognition of small objects (bubbles, voids, minerals, zoning). This affects the analysis of bubble textures. For instance, I show that the bubble number density increases almost one order of magnitude by decreasing the applied energy 100 kV or by applying a stronger virtual beam hardening filter. Moreover, I show that bubble size distributions are steeper by applying a metal filter or by decreasing the applied energy. Consequently, the quality of the acquired tomogram may affect the interpretation of volcanic processes: estimated magma decompression rate, bubble nucleation and growth rates, connectivity indexes and viscous permeabilities vary proportionally to the applied conditions.

According to the set of applied X-ray tomography conditions for silicic pumices of different anhydrous compositions and from several volcanic complexes, I recommend the following:

- Apply the lowest possible energy and the optimum power for the used instrument (hence, the highest possible current). In this way, the resulting linear attenuation coefficient range will be broadened and the differential of attenuation coefficient among

different materials will be higher. Consequently, the image contrast, the signal-to-noise ratio and the edge sharpening will be improved.

- Acquire two frames per radiogram. This is the most effective way to improve the signal-to-noise ratio and to decrease the possibility of pixel saturation. Do not apply a higher number of frames will result in a long analysis duration.
- One second per radiogram is enough. I do not observe significant improvements with longer durations. Therefore, the total analysis duration would be extended.
- Apply an intermediate virtual beam hardening filter. The application of a linear beam hardening filter with sample radius is insufficient to correct the beam hardening artifact. On the other hand, a very strong beam hardening filter may tighten the linear attenuation coefficient range, and then worsen the image contrast as a function of the radial location within samples. Even the application of a second order polynomial correction is useful to broaden the linear attenuation coefficient range and to improve the edge sharpening.
- Apply metal filters to improve the recognition of small objects around the biggest ones. However, I could not decipher what imaging parameter was controlled by the application of metal filters.
- Only apply a ring artifact minimizer in case of bad conditions of the X-ray tomography target. I show that although blurry rings can be visible at the center of tomograms, they do not affect the analysis of bubble textures. Moreover, the application of the ring artifact minimizer doubles the duration of tomogram acquisition.

Acknowledgments

This work was supported by Becas Chile PhD scholarship [grant number 72160339 CC]. To Barbara Buono-Core Marcelo Cortés, Carolina Geoffroy, Rayen Gho, Christian Pizarro and Florencia Rosas, students of University of Chile for their assistance in field. To Hannah

Buckland, Keri McNamara and Jen Saxby for contributing samples from Mazama eruption, Aluto eruption and Katla needles to this work. To Charles Clapham for his careful sample preparation. To Ailsa Naismith and Jen Saxby for language checking and fruitful discussions.

References

Alfano, F., Bonadonna, C., Gurioli, L., 2012. Insights into eruption dynamics from textural analysis: the case of the May, 2008, Chaiten eruption. Bulletin of Volcanology 74, 2095-2108.

Alvarez-Valero, A.M., Okumura, S., Arzilli, F., Borrajo, J., Recio, C., Ban, M., Gonzalo, J.C., Benítez, J.M., Douglas, M., Sasaki, O., Franco, P., Gómez-Barreiro, J., Carnicero, A., 2016. Tracking bubble evolution inside a silicic dike. Lithos, 262, 668-676.

Arzilli, F., Mancini, L., Voltolini, M., Cicconi, M.R., Mohammadi, S., Giuli, G., Mainprice, D., Paris, E., Barou, F., Carroll, M.R., 2015. Near-liquidus growth of feldspar spherulites in trachytic melts: 3D morphologies and implications in crystallization mechanisms. Lithos, 216, 93-105.

Attix, F.H., 1986. Introduction to Radiological Physics and Radiation Dosimetry. Wiley-VCH.

Bacon, C.R., and Lanphere, M.A., 2006. Eruptive history and geochronology of Mount Mazama and the Crater Lake region, Oregon. Geological Society of America Bulletin, 118(11-12), 1331-1359.

Baker, D.R., Mancini, L., Polacci, M., Higgins, M.D., Gualda, G.A.R., Hill, R.J., Rivers, M.L., 2012. An introduction to the application of X-ray microtomography to the three-dimensional study of igneous rocks. Lithos 148, 262-276.

Baker, D.R., Polacci, M., LaRue, A., 2011. A study on the reproducibility of counting vesicles in volcanic rocks. Geosphere, 7(1), 70-78.

Berg, S.E., Troll, V.R., Deegan, F.M., Burchardt, S., Krumbholz, M., Mancini, L., Polacci, M., Carracedo, J.C., Soler, V., Arzilli, F., Brun, F. (2016). Heterogeneous vesiculation of 2011 El Hierro xeno-pumice revealed by X-ray computed microtomography. Bulletin of Volcanology, 78(12), 85.

Boone, M., Dewanckele, J., Boone, M., Cnudde, V., Silversmit, G., Van Ranst, E., Jacobs, P., Vincze, L., Van Hoorebeke, L., 2011. Three-dimensional phase separation and identification in granite. Geosphere, 7(1), 79-86.

Bruggman, P.E., Bacon, C.R., Aruscavage, P.J., Lerner, R.W., Schwarz, L.J., and Stewart, K.C., 1987. Chemical analyses of rocks and glass separates from Crater Lake National Park and vicinity, Oregon: U.S. Geological Survey Open-File Report, 87-57, 36 p.

Burgisser, A., Gardner, J.E., 2004. Experimental constraints on degassing and permeability in volcanic conduit flow. Bulletin of volcanology, 67(1), 42-56.

Cai, B., Karagadde, S., Yuan, L., Marrow, T.J., Connolley, T., Lee, P.D., 2014. In situ synchrotron tomographic quantification of granular and intragranular deformation during semi-solid compression of an equiaxed dendritic Al–Cu alloy. Acta Materialia, 76, 371-380.

Cashman, K.V., Marsh, B.D., 1988. Crystal size distribution (CSD) in rocks and the kinetics and dynamics of crystallization II: Makaopuhi lava lake. Contributions to Mineralogy and Petrology, 99(3), 292-305.

Cashman, K.V., Scheu, B., 2015. Magmatic fragmentation. In The Encyclopedia of Volcanoes (Second Edition) 459-471.

Castro, J.M., Burgisser, A., Schipper, C.I., Mancini, S., 2012. Mechanisms of bubble coalescence in silicic magmas. Bulletin of Volcanology, 74(10), 2339-2352.

Cnudde, V., Boone, M.N., 2013. High-resolution X-ray computed tomography in geosciences: A review of the current technology and applications. Earth-Science Reviews 123, 1-17.

Cnudde, V., Boone, M., Dewanckele, J., Dierick, M., Van Hoorebeke, L., Jacobs, P., 2011. 3D characterization of sandstone by means of X-ray computed tomography. Geosphere 7, 54-61.

Colombier, M., Wadsworth, F.B., Gurioli, L., Scheu, B., Kueppers, U., Di Muro, A., Dingwell, D.B., 2017. The evolution of pore connectivity in volcanic rocks. Earth and Planetary Science Letters, 462, 99-109.

Degruyter, W., Bachmann, O., Burgisser, A., 2010a. Controls on magma permeability in the volcanic conduit during the climactic phase of the Kos Plateau Tuff eruption (Aegean Arc). Bulletin of Volcanology 72, 63-74.
Degruyter, W., Burgisser, A., Bachmann, O., Malaspinas, O., 2010b. Synchrotron X-ray microtomography and lattice Boltzmann simulations of gas flow through volcanic pumices. Geosphere 6, 470-481.
Dioguardi, F., Mele, D., Dellino, P., Dürig, T., 2017. The terminal velocity of volcanic particles with shape obtained from 3D X-ray microtomography. Journal of Volcanology and Geothermal Research, 329, 41-53.
Ersoy, O., Şen, E., Aydar, E., Tatar, İ., Çelik, H.H., 2010. Surface area and volume measurements of volcanic ash particles using micro-computed tomography (micro-CT): a comparison with scanning electron microscope (SEM) stereoscopic imaging and geometric considerations. Journal of Volcanology and Geothermal Research, 196(3-4), 281-286.
Feldkamp, L.A., Davis, L.C., Kress, J.W., 1984. Practical cone-beam algorithm. Journal of the Optical Society of America a-Optics Image Science and Vision 1, 612-619.
Fontijn, K., McNamara, K., Tadesse, A.Z., Pyle, D.M., Dessalegn, F., Hutchison, W., Mather, T.A., Yirgu, G., 2018. Contrasting styles of post-caldera volcanism along the Main Ethiopian Rift: Implications for contemporary volcanic hazards. Journal of Volcanology and Geothermal Research, 356, 90-113.
Giachetti, T., Burgisser, A., Arbaret, L., Druitt, T.H., Kelfoun, K., 2011. Quantitative textural analysis of Vulcanian pyroclasts (Montserrat) using multi-scale X-ray computed microtomography: comparison with results from 2D image analysis. Bulletin of Volcanology, 73(9), 1295-1309.
Godel, B.M., Barnes, S.J., Barnes, S.J., 2013. Deposition mechanisms of magmatic sulphide liquids: Evidence from high-resolution X-ray computed tomography and trace element chemistry of komatiite-hosted disseminated sulphides. Journal of Petrology, 54(7), 1455-1481.
Gonnermann, H.M., Manga, M., 2007. The fluid mechanics inside a volcano. Annual Review of Fluid Mechanics 39, 321-356.
Gualda, G.A.R., Rivers, M., 2006. Quantitative 3D petrography using X-ray tomography: Application to Bishop Tuff pumice clasts. Journal of Volcanology and Geothermal Research 154, 48-62.
Gurioli, L., Harris, A.J.L., Houghton, B.F., Polacci, M., Ripepe, M., 2008. Textural and geophysical characterization of explosive basaltic activity at Villarrica volcano. Journal of Geophysical Research: Solid Earth, 113(B8).
Hildreth, W., Godoy, E., Fierstein, J., Singer, B., 2010. Laguna del Maule Volcanic Field: Eruptive history of a Quaternary basalt-to-rhyolite distributed volcanic field on the Andean rangecrest in central Chile. Servicio Nacional de Geología y Minería, Boletín, 63: 145 pp. Santiago.
Holwell, D.A., Barnes, S.J., Le Vaillant, M., Keays, R.R., Fisher, L.A., Prasser, R., 2016. 3D textural evidence for the formation of ultra-high tenor precious metal bearing sulphide microdroplets in offset reefs: an extreme example from the Platinova Reef, Skaergaard Intrusion, Greenland. Lithos, 256, 55-74.
Jerram, D.A., Davis, G.R., Mock, A., Charrier, A., Marsh, B.D., 2010. Quantifying 3D crystal populations, packing and layering in shallow intrusions: a case study from the Basement Sill, Dry Valleys, Antarctica. Geosphere, 6(5), 537-548.
Jerram, D.A., Mock, A., Davis, G.R., Field, M., Brown, R.J., 2009. 3D crystal size distributions: A case study on quantifying olivine populations in kimberlites. Lithos 112, 223-235.

Jöns, N., Kahl, W.A., Bach, W., 2017. Reaction-induced porosity and onset of low-temperature carbonation in abyssal peridotites: insights from 3D high-resolution microtomography. Lithos, 268, 274-284.
Kak, A.C., Slaney, M., 1988. Principles of Computerized Tomographic Imaging. IEEE Press, New York (329 pp.).
Ketcham, R.A., 2005. Three-dimensional grain fabric measurements using high-resolution X-ray computed tomography. Journal of Structural Geology 27, 1217-1228.
Ketcham, R.A., Carlson, W.D., 2001. Acquisition, optimization and interpretation of X-ray computed tomographic imagery: applications to the geosciences. Computers & Geosciences 27, 381-400.
Knoll, G.F., 2000. Radiation Detection and Measurement. J. Wiley & Sons.
Larsen, G., Newton, A.J., Dugmore, A.J., Vilmundardóttir, E.G., 2001. Geochemistry, dispersal, volumes and chronology of Holocene silicic tephra layers from the Katla volcanic system, Iceland. Journal of Quaternary Science: Published for the Quaternary Research Association, 16(2), 119-132.
Le Gall, N., Pichavant, M., 2016. Homogeneous bubble nucleation in H2O-and H2O-CO2-bearing basaltic melts: results of high temperature decompression experiments. Journal of Volcanology and Geothermal Research, 327, 604-621.
Liu, E.J., Cashman, K.V., Rust, A.C., 2015. Optimising shape analysis to quantify volcanic ash morphology. GeoResJ, 8, 14-30.
Mancini, S., Forestier-Coste, L., Burgisser, A., James, F., Castro, J., 2016. An expansion–coalescence model to track gas bubble populations in magmas. Journal of Volcanology and Geothermal Research, 313, 44-58.
Mangan, M.T., Cashman, K.V., 1996. The structure of basaltic scoria and reticulite and inferences for vesiculation, foam formation, and fragmentation in lava fountains. Journal of Volcanology and Geothermal Research, 73(1-2), 1-18.
Marsh, B.D. (1988). Crystal size distribution (CSD) in rocks and the kinetics and dynamics of crystallization. Contributions to Mineralogy and Petrology, 99(3), 277-291.
Mastrolorenzo, G., Pappalardo, L., 2006. Magma degassing and crystallization processes during eruptions of high-risk Neapolitan-volcanoes: evidence of common equilibrium rising processes in alkaline magmas. Earth and Planetary Science Letters, 250(1), 164-181.
McCullough, E.C., 1975. Photon attenuation in computed tomography. Medical Physics 2, 307-320.
Morgavi, D., Arzilli, F., Pritchard, C., Perugini, D., Mancini, L., Larson, P., Dingwell, D.B., 2016. The Grizzly Lake complex (Yellowstone Volcano, USA): Mixing between basalt and rhyolite unraveled by microanalysis and X-ray microtomography. Lithos, 260, 457-474.
Nimis, P., Alvaro, M., Nestola, F., Angel, R.J., Marquardt, K., Rustioni, G., Harris, J.W., Marone, F., 2016. First evidence of hydrous silicic fluid films around solid inclusions in gem-quality diamonds. Lithos, 260, 384-389.
Pamukcu, A.S., Gualda, G.A.R., 2010. Quantitative 3D petrography using X-ray tomography 2: Combining information at various resolutions. Geosphere 6, 775-781.
Pankhurst, M.J., Dobson, K.J., Morgan, D.J., Loughlin, S.C., Thordarson, T., Lee, P.D., Courtois, L., 2014. Monitoring the magmas fuelling volcanic eruptions in near-real-time using X-ray micro-computed tomography. Journal of Petrology, 55(3), 671-684.
Pardo, N., Cronin, S.J., Wright, H.M., Schipper, C.I., Smith, I., Stewart, B., 2014. Pyroclast textural variation as an indicator of eruption column steadiness in andesitic Plinian eruptions at Mt. Ruapehu. Bulletin of Volcanology, 76(5), 822.
Polacci, M., Arzilli, F., La Spina, G., Le Gall, N., Cai, B., Hartley, M.E., Di Genova, D., Vo, N.T., Nonni, S., Atwood, R.C., Llewellin, E.W., Lee, P.D., Burton, M.R., 2018. Crystallisation

in basaltic magmas revealed via in situ 4D synchrotron X-ray microtomography. Scientific reports, 8.
Polacci, M., Baker, D.R., La Rue, A., Mancini, L., Allard, P., 2012. Degassing behaviour of vesiculated basaltic magmas: an example from Ambrym volcano, Vanuatu Arc. Journal of volcanology and geothermal research, 233, 55-64.
Polacci, M., Baker, D.R., Mancini, L., Tromba, G., Zanini, F., 2006. Three-dimensional investigation of volcanic textures by X-ray microtomography and implications for conduit processes. Geophysical Research Letters, 33(13).
Polacci, M., Burton, M.R., La Spina, A., Murè, F., Favretto, S., Zanini, F., 2009. The role of syn-eruptive vesiculation on explosive basaltic activity at Mt. Etna, Italy. Journal of Volcanology and Geothermal Research, 179(3-4), 265-269.
Polacci, M., Papale, P., Rosi, M., 2001. Textural heterogeneities in pumices from the climactic eruption of Mount Pinatubo, 15 June 1991, and implications for magma ascent dynamics. Bulletin of Volcanology 63, 83-97.
Preece, K., Gertisser, R., Barclay, J., Charbonnier, S.J., Komorowski, J.C., Herd, R.A., 2016. Transitions between explosive and effusive phases during the cataclysmic 2010 eruption of Merapi volcano, Java, Indonesia. Bulletin of Volcanology 78.
Quinto, E.T., 2005. An introduction to X-ray tomography and radon transforms, American-Mathematical-Society Short Course on the Radon Transform and Applications to Inverse Problems, Atlanta, GA, pp. 1-23.
Rivers, M.L., Sutton, S.R., Eng, P., 1999. Geoscience applications of x-ray computed microtomography, Conference on Developments in X-Ray Tomography II, Denver, Co, pp. 78-86.
Schipper, C.I., Castro, J.M., Tuffen, H., James, M.R., How, P., 2013. Shallow vent architecture during hybrid explosive–effusive activity at Cordón Caulle (Chile, 2011–12): evidence from direct observations and pyroclast textures. Journal of Volcanology and Geothermal Research, 262, 25-37.
Schipper, C.I., Castro, J.M., Tuffen, H., Wadsworth, F.B., Chappell, D., Pantoja, A.E., Simpson, M.P., Le Ru, E.C., 2015. Cristobalite in the 2011–2012 Cordón Caulle eruption (Chile). Bulletin of Volcanology, 77(5), 34.
Shea, T., Houghton, B.F., Gurioli, L., Cashman, K.V., Hammer, J.E., Hobden, B.J., 2010. Textural studies of vesicles in volcanic rocks: An integrated methodology. Journal of Volcanology and Geothermal Research 190, 271-289.
Song, S.R., Jones, K.W., Lindquist, B.W., Dowd, B.A., Sahagian, D.L., 2001. Synchrotron X-ray computed microtomography: studies on vesiculated basaltic rocks. Bulletin of Volcanology, 63(4), 252-263.
Sutton, S.R., Bertsch, P.M., Newville, M., Rivers, M., Lanzirotti, A., Eng, P., 2002. Microfluorescence and microtomography analyses of heterogeneous earth and environmental materials. Applications of Synchrotron Radiation in Low-Temperature Geochemistry and Environmental Sciences 49, 429-483.
Toramaru, A., 2006. BND (bubble number density) decompression rate meter for explosive volcanic eruptions. Journal of Volcanology and Geothermal Research 154, 303-316.
Van de Casteele, E., Van Dyck, D., Sijbers, J., Raman, E., 2002. An energy-based beam hardening model in tomography. Physics in Medicine and Biology 47, 4181-4190.
Voltolini, M., Zandomeneghi, D., Mancini, L., Polacci, M., 2011. Texture analysis of volcanic rock samples: Quantitative study of crystals and vesicles shape preferred orientation from X-ray microtomography data. Journal of Volcanology and Geothermal Research 202, 83-95.
Wright, H.M.N., Weinberg, R.F., 2009. Strain localization in vesicular magma: Implications for rheology and fragmentation. Geology 37, 1023-1026.

Zandomeneghi, D., Voltolini, M., Mancini, L., Brun, F., Dreossi, D., Polacci, M., 2010. Quantitative analysis of X-ray microtomography images of geomaterials: Application to volcanic rocks. Geosphere, 6(6), 793-804.

4. The role of magma permeability on the styles and transitions of the early postglacial rhyolitic eruptions of Laguna del Maule

Abstract

The magma degassing is one of the key factors controlling the styles and transitions of silicic eruptions. The magma permeability measures the capability of the exsolved volatiles to flow through the available pore space within the ascending magma and its evolution is intrinsically related to the eruption histories. Herein I address how the magma permeability controlled the styles and transitions in the early postglacial silicic eruptions of the Laguna del Maule volcanic complex (LdM). To do this I measure pyroclast porosities and permeabilities and perform X-ray tomography simulations in pumices of the rhyolite of Laguna del Maule *(rdm),* the largest of the postglacial rhyolite eruptions with no lava flow phase, and Los Espejos (*rle*), a subplinian eruption which made the transition to a lava flow. Most of the analyzed pumice clasts of *rdm* have high viscous permeabilities ($>10^{-11}$ m^2), consistent with their high total porosities and high bubble connectivities; the *rle* pumice also have high viscous permeabilities ($>10^{-11}$ m^2) despite of their wide porosity range. Simulated velocity and pressure fields for gas flow through pore spaces imaged by X-ray tomography show that the high permeabilities are explained by the samples are anisotropic and the gas flows preferentially through the widest and least tortuous bubble pathways and is more localized for lower pumice porosity. I propose that the anisotropic tube pumices of *rdm* were formed by a high strain rate due to a decrease of the eruption intensity towards the end of the large explosive eruption. The dense pumices with elongate bubbles of *rle* were formed by a high total strain due to a shallow fragmentation level which may also explain the formation of the vesicular obsidians. The densification of magma

continued until flow pathways collapsed sufficiently to promote the complete transition to the effusive phase.

Keywords

Laguna del Maule volcanic complex; magma porosities; bubble connectivities; viscous and inertial permeabilities; X-ray tomography; permeability simulation; eruptive styles and transitions.

4.1. Introduction

The early postglacial rhyolitic eruptions of the Laguna del Maule volcanic complex (LdM) had a range of styles and intra-eruptive transitions controlled by different governing factors (Chapter 2; Fierstein, 2018). The first, rhyolite of Laguna del Maule (*rdm*; 23 ky in Andersen et al., 2017), began as a Plinian eruption (*rdm* 1) and developed into an ignimbrite-forming eruption (*rdm* 2), producing fall and pyroclastic density deposits but no lava flows (Section 2.3). The increase of the eruption intensity with time was likely controlled by a downward propagation of the fragmentation level which extracted deeper and hotter mafic magmas and mixed them with the silicic magmas. In contrast, the rhyolite of Los Espejos (*rle*; 19 ky in Singer et al., 2000) began as a pulsatory phreatomagmatic eruption (*rle* 1) that developed into a subplinian magmatic phase (*rle* 2 and 3) and ended with a lava flow (*rle* 4; Section 2.3). The high fraction of dense pumices and vesicular obsidian clasts in the top of the *rle* fall deposit suggest that the explosive-effusive eruption was aided by a high total strain and a decrease of the magma ascent rate. This slower ascent rate allowed sufficient time for open-system degassing and the densification of magma during ascent (Chapter 2).

The different eruptive styles of *rdm* and *rle* are reflected in the porosities of the juvenile pyroclasts. In Figure 4.1 I show that most *rdm* pumices have an open (connected) porosity (φ_C) of 0.6-0.7; the complete range is wider (φ_C = 0.3-0.9) due to a few pumices from the lower sequence that have high open porosities (φ_C = 0.8-0.9) and a few pumice clasts coming from the top of the *rdm* sequence that have low open porosities (φ_C = 0.3-0.5). In contrast, most clasts of *rle* have φ_C = 0.25-0.45 and a few have φ_C = 0.5-0.6 coming from the top of the fall deposit. The porosities are related to the bubble textures within the pumice clasts. The dominant 0.6-0.7 porosity *rdm* pumices have elongate bubbles with subtle features of collapse; the denser pumices have flattened elongate bubbles and the more porous pumice have nearly spherical bubbles. In the case of *rle*, the low porosity clasts contain flattened bubbles with straight rims and/or strain localization; the most porous have flattened elongate bubbles. Here I relate the bubble textures and the fabric anisotropy to the histories of degassing of both rhyolitic eruptions.

Magma degassing is controlled in part by permeability, which is a measure of how readily exsolved volatiles flow through the available pore space (Rust and Cashman, 2004). Permeability is usually measured by two components because fluids flowing through a porous media can lose energy by both viscous and inertial effects (Forchheimer, 1901; Rust and Cashman, 2004). At sufficiently low flow rates, the (total) permeability is equal to the viscous permeability (k_v) because the flow is laminar with negligible inertia. The inertial permeability (k_i) records the resistance to flow due to turbulence and other inertial effects. Both permeability components (k_v and k_i) depend on the porosity and the bubble connectivity (Colombier et al., 2017). They are properties of the porous media that, together with the density and viscosity of the pore-filling fluid, determine how quickly the fluid flows through the porous medium in response to a pressure gradient.

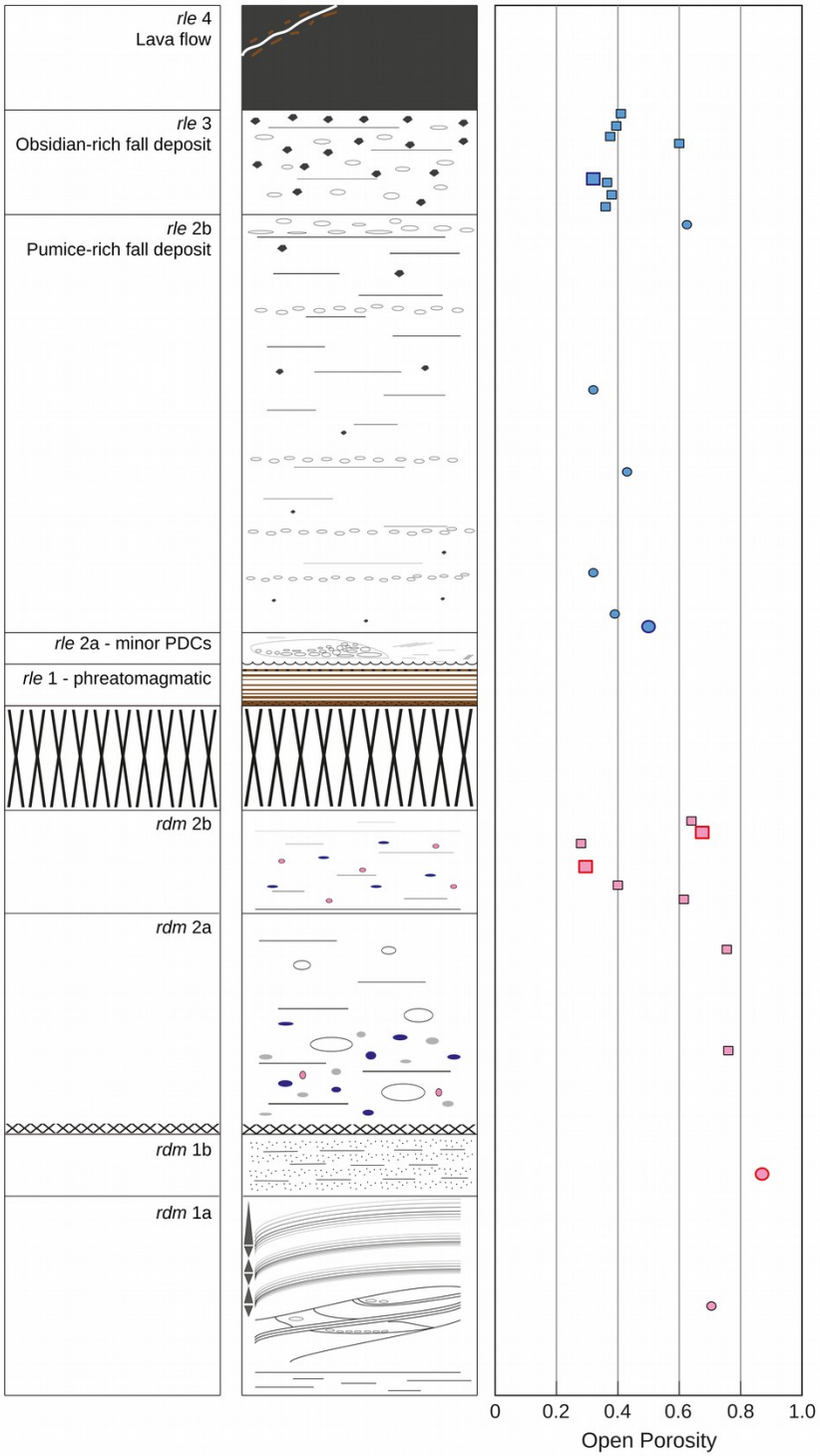

Fig. 4.1: Stratigraphic column and location, and open porosity of the studied pumices. The height of some sample position has been shifted slightly to avoid overlap of symbols. The bigger and highlighted symbols are samples used for X-ray tomography analysis.

The porous media properties, in turn, change with the conditions and extent of vesiculation. At early stages of vesiculation, bubbles nucleate and grow but cannot form a connected network that would allow outgassing. After overcoming a porosity threshold, the magma permeability

sharply increases with magma porosity (Eichelberger et al., 1986; Rust and Cashman, 2004; Takeuchi et al., 2008; Lindoo et al., 2016). If the volatile phase flows out of the magma slowly relative to the generation of vapor by decompression-induced volatile exsolution, then the porosity will increase and degassing during ascent can be approximated as a closed-system. If the magma is sufficiently permeable and magma ascent is sufficiently slow, then there is open-system degassing, and the flow of exsolved volatiles (out the top of the volcano or into conduit wall rocks) decouples from the silicic melt ascent. With efficient outgassing, the bubbles begin to collapse, decreasing the magma porosity (Cassidy et al., 2018; Gonnermann and Manga, 2007) but only slightly decreasing the magma permeability because the network of flow pathways remains largely connected (Colombier et al., 2017; Rust and Cashman, 2004). At some lower porosity, the collapsing bubble framework reaches a densification threshold where the magma permeability drops sharply due to closing of flow pathways (e.g., Melnik and Sparks, 2002). In this way, bubble textures govern degassing during magma ascent. Importantly, there is a hysteresis in the porosity-permeability paths: for the same porosity, the connectivity and permeability of the magma are less during initial vesiculation than during densification (e.g, Degruyter et al., 2010a; Rust and Cashman, 2004). I therefore expect that the degassing history and evolution in eruption styles are inextricably linked.

In this chapter I consider the role of both viscous and inertial permeabilities on eruption transitions. In order to reconstruct the history of degassing during the *rdm* and *rle* explosive eruptions, I measured the porosities and permeabilities of 24 pyroclast pumice clasts from both pyroclastic deposits and compared the results with information from other silicic explosive eruptions. I also selected five representative pumices to describe the 3D bubble textures by X-ray tomography. After segmentation of bubbles and groundmass, I simulated the laminar flow of fluid through the imaged 3D pore space using AVIZO Lite. These simulations of the velocity and pressure fields were used to assess the role of bubble textures on the viscous permeability

(k_v). Based on the hysteresis theory applied to the pumice connectivity and magma permeability, I propose a link between the evolution of magmas permeabilities and the histories of the early postglacial rhyolitic eruptions of LdM.

4.2. Background: Governing equations for porosity and permeability

The bulk density (ρ) of a volcanic rock is the ratio between its mass (m) and its convex hull volume (V_c). The matrix density (ρ_m) may be estimated based on the composition (e.g., Fluegel, 2007) or calculated by pycnometer (e.g., Alfano et al., 2012; Rust and Cashman, 2004). The total porosity of the sample (φ_T) is calculated from ρ and ρ_m as:

$$\varphi_T = \frac{\rho_m - \rho}{\rho_m} \quad (1)$$

The open porosity (φ_c) refers to the voids connected to the outer margin of a sample. For the X-ray tomography simulations, I define φ_c as the voids connected both ends of the sample in the flow direction (i.e. the inlet side and the outlet side); the bubble connectivity (c) is defined as:

$$c = \frac{\varphi_c}{\varphi_T} \quad (2)$$

Permeability is the capability of a material to allow fluids to flow through its pore space and is governed by Darcy's law (1856):

$$\frac{\Delta P}{L} = \frac{\mu}{k_a} v \quad (3)$$

where ΔP is the pressure drop, L is the sample length, μ is the dynamic viscosity of the fluid, k_a is the measured permeability and v is the filter velocity that is the volumetric flow rate passing through a cross sectional area orthogonal to the flow direction. Darcy's law (Eq. 1) is

based on low Re flow for which v is proportional to the average pressure gradient ($\Delta P/L$); if it is applied to conditions where inertia is significant then the measured (or 'apparent') permeability (k_a in Eq. 3) decreases with increasing pressure gradient (and flow rate) because at high Re, $v^2 \propto \Delta P/L$. To characterize the permeability of a porous media with constants that do not vary with flow conditions therefore requires two parameters: the viscous permeability k_v, and the inertial permeability k_i. These are related to v and $\Delta P/L$ through the Forchheimer equation (Forchheimer, 1901; Reynolds, 1900):

$$\frac{\Delta P}{L} = \frac{\mu}{k_v} v + \frac{\rho_f}{k_i} v^2 \quad (4)$$

where ρ_f is the density of the fluid. If the fluid is compressible, it will expand as it flows through the sample, which is taken into account by:

$$\frac{P_i^2 - P_o^2}{2PL} = \frac{\mu}{k_v} v + \frac{\rho_f}{k_i} v^2 \quad (5)$$

where P_i and P_o correspond to the inlet and outlet pressure of the fluid. Herein, we consider P_o as atmospheric and $P = P_o$, thus μ and ρ_f are estimated for atmospheric conditions (Rust and Cashman, 2004).

The viscous permeability can be estimated from bubble textures by applying the channel-based Kozeny-Carman equation (e.g., Degruyter et al., 2010a; Klug and Cashman, 1996; Saar and Manga, 1999; Wright et al., 2006):

$$k_v = \frac{\varphi_c d^2}{16 \chi \tau^2} \quad (6)$$

where d is the cross-sectional diameter of the pore apertures which make up the pore space of the porous medium, χ is a cross section shape factor (for circles $\chi = 2$), and τ is the tortuosity,

which is the ratio of the actual fluid path length to the straight distance between the ends of the path. k_i, can be estimated from the inertia-dominated version of Eq. (6):

$$k_i = \frac{d\varphi_c^2}{2f_0\tau^3} \quad (7)$$

which includes a surface roughness factor (f_0) and depends on the tortuosity cubed.

4.3. Methodology

4.3.1. Configuration of the permeameter

I used a new permeameter designed, developed and tested in the University of Bristol for the analysis of volcanic rocks. The permeameter uses low-cost industrial components and was developed to measure permeabilities in a range of 10^{-15}-10^{-9} m^2 by flowing air through the samples of 15 mm-diameter and a range of lengths. The permeameter is composed of an air compressor, a pressure regulator, an analog pressure gauge, rotameter-type flow meters, an air flow conditioner to reduce turbulence before the air goes into the sample, a 16 mm-diameter copper pipe, a 4-digit pressure manometer and a sample holder (Fig. 4.2a).

The pressure meter is connected to the permeameter with a 22-mm equal tee brass compression fitting, which is followed downstream by a 3 cm-length 22 mm- diameter pipe which is connected with a 22 x 15mm straight coupler brass compression fitting. The compression fitting reducer was widened 1 mm in the outer end (from 15 to 16 mm-diameter) to introduce the sample holder. The sample holder is a 15-mm diameter copper pipe surrounded by a 15-mm diameter compression olive to avoid air leak. The 15-mm diameter sample is put in one end of the sample holder and the three pieces (the sample holder pipe, the compression olive and the sample) are wrapped in a 0.95 mm-wall thickness polyolefin heat shrink tubing sleeve.

The heat shrink is incorporated to avoid air flowing in the space between the sample and the gas flow line. The sample is inserted, and the sample holder is fixed in the permeameter by a compression nut which is screwed at the compression fitting reducer (Fig. 4.2b).

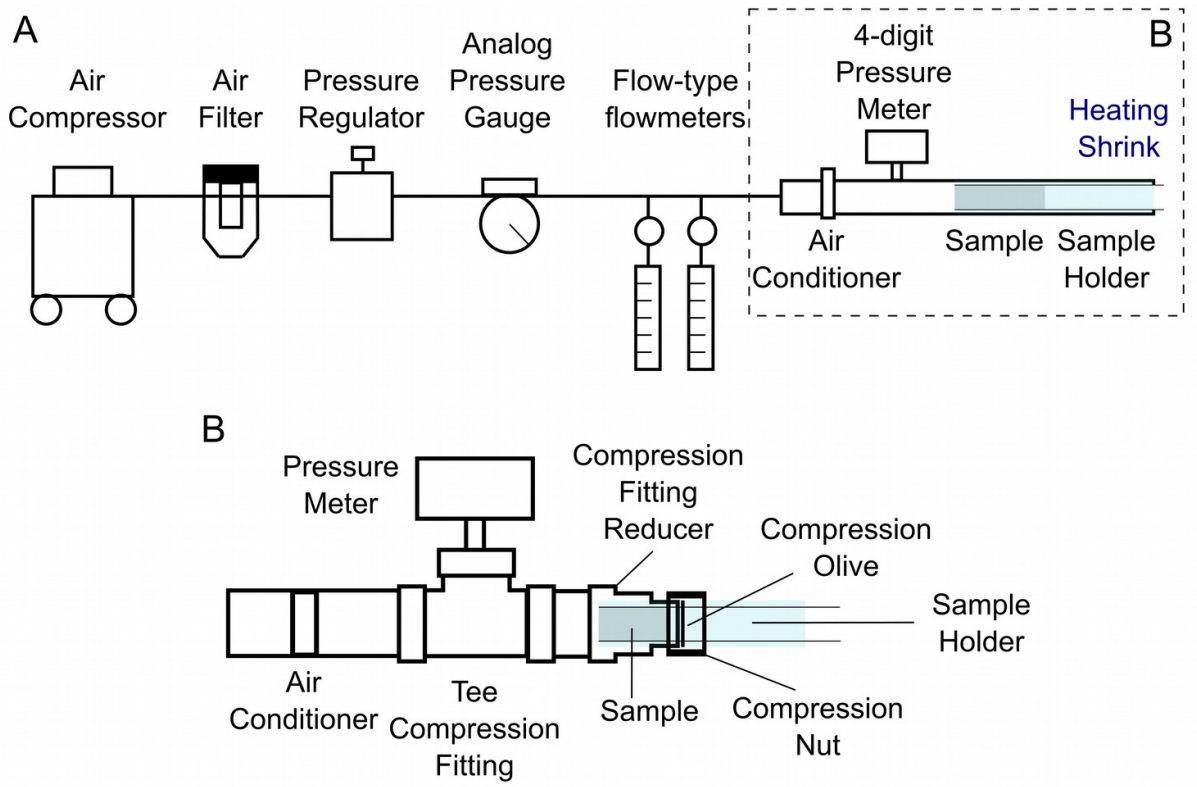

Fig. 4.2: Schematic configuration of the permeameter. A The main components including the artefacts upstream the instruments are illustrated not to scale. **B** Detailed assemblage of the components highlighted by a dotted line in **A**.

The air flow through a rotameter-type flow meter (which measure the air flow in L/min) goes into the permeameter and passes through the air conditioner to decrease the air turbulence before going through the sample. The inlet pressure is measured by the pressure meter and the outlet pressure is considered as the atmospheric pressure to measure the pressure gradient. The air flow passes through the sample and out the permeameter.

4.3.2. Porosity and permeability measurements

Twenty-four pumices of <-4φ size, 10 from *rdm* and 14 from *rle*, were drilled to make 15 mm-diameter cylinders of 20-30 mm-length (Table 4.1). The long axis of the cylinders corresponds to the main orientation of bubbles when visible to the naked eye. In the case of microvesicular

samples, the cylinders were drilled parallel to the main elongation of the pumice clast. The macroscopic textures of the pumice clasts were described from observations to the cylinders. The cylinders were weighed, and their length and diameter were measured to calculate the pumice density. As the *rdm* and *rle* pumices are crystal-poor, the matrix density was estimated from the glass composition by Fluegel's (2007) model. The open porosity and bubble connectivity were calculated by analyzing the cylinders by He-pycnometry (Quantachrome Ultrapyc 1200e in SERNAGEOMIN, Santiago, Chile; complete data in Supplementary Material). Permeability measurements were made with the new permeameter at the University of Bristol. The samples were covered with a cylindrical heating wrap leaving the two circular ends uncovered to limit the flow to one direction. The inlet air flow was increased gradually from 0 to ~50 lpm (~8.3 x 10^{-4} m^3/s) and the pressure measured with a 4-digit barometer from 0 to ~1.4 bar. The filter velocity was obtained from the ratio of the volumetric flow rate and the cross-sectional area (Fig. 4.3a) and is plotted against the pressure gradient to obtain k_v and k_i using eq. (5) (Fig. 4.3b; Supplementary Material).

4.3.3. X-ray tomography and flow simulations

The tomograms of three *rdm* pumices and two *rle* pumices were acquired with a conventional X-ray computed tomography system (Nikon XTH225ST in University of Bristol) at 70 kV, 7 W and a voxel size of 3.5-7.0 μm; these conditions were found to optimize the image quality (Chapter 3). The tomograms were reconstructed by Nikon CT Pro 3D XT4.4 software to output 2,000 slices of 2000^2 pixel resolution. An initial volume of interest (VOI) of ~1300 x 1300 x 1700 voxels (4.5-9.0 x 4.5-9.0 x 6.0-12.0 mm^3) was selected in AVIZO Lite software to avoid background and sample regions affected by beam hardening and other artifacts (Ketcham and Carlson, 2001). After applying a median filter to improve the signal-to-noise ratio, a binary image was generated by segmenting the darkest gray-value interval using a multi-thresholding tool (Appendix B); this allowed me to separate the vesicles from glass and crystals. The total

porosity was calculated from this binary image as the ratio of the total volume of vesicles to the VOI. The connected bubbles, defined as the pore space in pathways connecting the two circular ends of the samples, were identified with the axis connectivity analysis tool in Avizo Lite and converted to a binary image, from which the open porosity and bubble connectivity were calculated (Appendix B). The pore aperture (*d*) of 100 to 200 bubbles from the connected pore space were measured by hand in a centered region of interest of a 2D slice perpendicular to the long axis of the sample. The region of interest has the same size (~100^2 pixels) for the 5 samples analyzed and all the bubbles >5 pixel-area within the region of interest were measured. The average of the pore apertures is calculated to give a characteristic *d* for each sample.

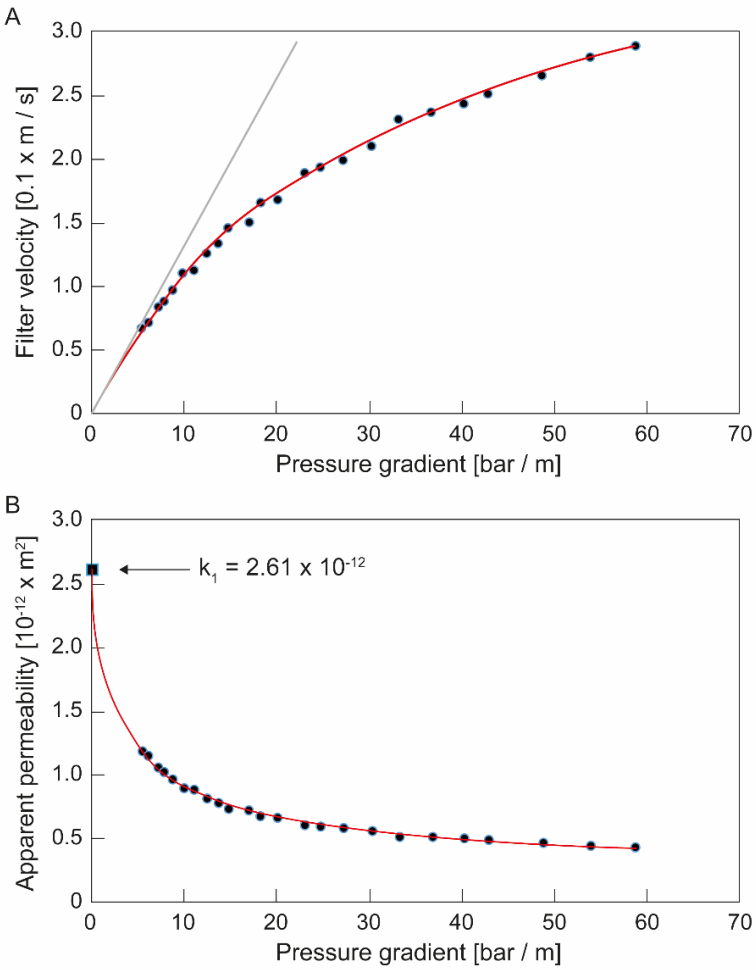

Fig. 4.3: Plots of increments of pressure gradient for the estimation of permeabilities. A Filter velocity versus pressure gradient. The data are fitted by a second order polynomial according to the expression for compressible gas (red line; Eq. 5). The viscous permeability is proportional to the slope as the filter velocity approaches zero (gray line). **B** Apparent permeability (Eq. 3) versus pressure gradient. The pumice LSM4BB1 from *rle* 4 was used for this example.

Table 4.1: Measured porosities, connectivities and permeabilities. The samples used for porosity and permeability simulations are in bold. The textures correspond to the macroscopic description of the pumice cylinders.

Sample	Unit	φ_T	φ_c	C	K_v [m^2]	K_i [m]	Textures
rdm 1 T1	*rdm* 1	0.89	0.87	0.98	2.2×10^{-10}	2.9×10^{-5}	Frothy
PF LE Banded	*rdm* 1	0.72	0.71	0.97	3.0×10^{-11}	1.7×10^{-7}	Banded
rdm 2 T2	*rdm* 2	0.30	0.30	0.98	7.7×10^{-12}	3.3×10^{-8}	Tube pumice
rdm 2 T1	*rdm* 2	0.68	0.64	0.94	1.1×10^{-11}	2.9×10^{-8}	Tube pumice
DivM6	*rdm* 2	0.28	0.28	0.99	8.3×10^{-12}	1.4×10^{-8}	Tube pumice
DivM1	*rdm* 2	0.77	0.76	0.98	2.2×10^{-11}	7.3×10^{-7}	Tube pumice
DivM7	*rdm* 2	0.71	0.67	0.95	1.5×10^{-11}	3.5×10^{-7}	Tube pumice
DivM2	*rdm* 2	0.78	0.76	0.97	9.6×10^{-11}	2.4×10^{-7}	Tube pumice
DivM3	*rdm* 2	0.66	0.62	0.93	1.0×10^{-11}	4.3×10^{-8}	Tube pumice
DivM4	*rdm* 2	0.42	0.40	0.95	5.7×10^{-11}	2.6×10^{-8}	Tube pumice
rle 2 T1	*rle* 2	0.55	0.50	0.91	8.5×10^{-12}	2.2×10^{-8}	Banded microvesicular
H9C	*rle* 2	0.68	0.63	0.91	8.5×10^{-12}	2.2×10^{-8}	Banded microvesicular
H1b	*rle* 2	0.42	0.39	0.93	7.8×10^{-12}	2.7×10^{-8}	Isotropic microvesicular
H9AA2	*rle* 2	0.42	0.42	1.00	8.3×10^{-12}	1.8×10^{-8}	Isotropic microvesicular
H9AB1	*rle* 2	0.39	0.32	0.82	5.7×10^{-12}	8.5×10^{-8}	Isotropic microvesicular
rle 3 T1	*rle* 3	0.41	0.32	0.77	5.2×10^{-12}	4.6×10^{-8}	Isotropic microvesicular
LSM4BB1	*rle* 3	0.39	0.36	0.92	2.6×10^{-12}	2.0×10^{-8}	Banded microvesicular
LSM4E	*rle* 3	0.65	0.60	0.92	6.5×10^{-11}	4.6×10^{-8}	Tube pumice
LSM4BC1	*rle* 3	0.34	0.32	0.95	9.0×10^{-12}	1.7×10^{-8}	Isotropic microvesicular
LSM4BA1	*rle* 3	0.38	0.36	0.94	7.3×10^{-11}	1.9×10^{-8}	Tube pumice
LSM4BA2	*rle* 3	0.41	0.38	0.92	1.6×10^{-11}	1.6×10^{-8}	Isotropic microvesicular
LSM6H1	*rle* 3	0.39	0.38	0.97	7.8×10^{-12}	2.5×10^{-8}	Isotropic microvesicular
LSM6H4	*rle* 3	0.43	0.41	0.96	1.1×10^{-11}	2.0×10^{-8}	Isotropic microvesicular

A second VOI of about the half-length of each axis of the first VOI was selected for permeability simulations because the modeling is computationally expensive. The permeability

simulations were performed with the "Absolute Permeability Experiment Simulation" (APES), a module of the X-Lab simulation platform in AVIZO Lite. It is based on Darcy's law (Eq. 3) applied through a finite volume scheme with no-slip conditions at fluid-solid boundaries. Flow is from one square face of the tomogram with a boundary condition of a constant pressure P_i, through the porous network, and out the opposite square face set to at lower constant pressure, P_o. A one-voxel-wide solid (impermeable) plane is added to the four rectangular faces of the tomogram perpendicular to the square faces parallel to the average flow direction, such that there is no flow in or out these sides of the system. The simulation assumes the fluid is incompressible (ρ_f is constant) and Newtonian (μ is constant) and that the flow is steady (v does not vary with time) and has a low Re (to avoid turbulence). The latter condition means that APES only allows determination of the viscous permeability. The simulations were run with P_i = 130 kPa, P_o = 101.3 kPa (atmospheric pressure), and $\mu = 1.81 \times 10^{-5}$ Pa s (the dynamic viscosity of the air) in order to emulate the conditions of the laboratory permeability measurements of the same samples. The APES module gives the permeability and a matrix with spatial coordinates of the fluid velocity and pressure to visualize their fields in AVIZO Lite. Herein the velocity fields are displayed by 500 pathlines where the color indicates the magnitude of the velocity (Supplementary Material). The tortuosity was calculated in AVIZO Lite from 5 randomly selected pathlines of the velocity field.

4.4. Results

In this section I present macroscopic textural descriptions of the pumice cylinders, and the data obtained from porosity and permeability measurements of samples from subunits of *rdm* and *rle* deposits defined in Chapter 2. I then characterize the porosities, pore apertures and tortuosities from the X-ray tomograms and compare these data with the characterization of bubble textures from 2D BSEM images (Section 2.5.4). I also present permeabilities derived

from numerical simulations of low Re flow through the pore space imaged by tomography and relate the simulated velocity and pressure fields to the bubble textures.

4.4.1. Macroscopic textural description

Most pumice clasts from the rhyolite of Laguna del Maule (*rdm*) are almost aphyric, elongate and have tubular bubbles oriented parallel to the main elongation of the clast. However, the two pumices clasts analyzed from the *rdm* unit 1 (the lower unit) show distinctive textures. One (*rdm* 1 T1) is a ~25 cm-long, subelongate frothy pumice which has nearly spherical bubbles of millimeters in diameter that can be easily seen to the naked eye; the other (PF LE Banded) is a <10 cm-long, oblate banded pumice with planes separating bubble domains, parallel to the elongation of the pumice clast. The eight analyzed samples of the *rdm* unit 2 (Table 4.1) are anisotropic tube pumices with bubbles visible to the naked eye (submillimetric to millimetric). A few denser pumices are mostly microvesicular but have a few (<20 observed in the cylinder ends) tubular bubbles nearly parallel to the main elongation of the pumice clasts.

The studied pumice clasts from the rhyolite of Los Espejos (*rle*) come exclusively from the *rle* units 2 and 3 as the *rle* unit 1 does not contain <-4φ clasts (Section 2.5.1). The *rle* pumice are crystal-poor with plagioclase and biotite phenocrysts visible to the naked eye. Most pumice clasts are nearly equant with straight faces and microvesicular, except two (LSM4BA1 and LSM4E) which are subelongate with tubular bubbles parallel to the main elongation of the pumice clasts. Once I drilled the *rle* pumice clasts, textures became more apparent. I classify two types of microvesicular pumice (Table 4.1): isotropic and banded. The isotropic microvesicular pumice clasts (9 clasts) have no clear fabric and may have a few spherical (or with circular cross-sectional area) bubbles visible to the naked eye. The banded microvesicular pumice clasts (3 clasts) show planar millimetric white and light-gray bands with no visible bubbles.

4.4.2. Porosity and permeability measurements

The total porosity range of the entire sample suite is 0.28-0.89; most pumices from *rdm* have φ_T = 0.65-0.90, except for two samples from *rdm* 2 (the upper unit) that have φ_T = 0.28 and 0.30. The *rle* pumices have a total porosity range of 0.33-0.69, but most have $\varphi_T \sim 0.4$; pumices from stratigraphic levels *rle* 2 and *rle* 3 have similar φ_T (Fig. 4.4a). Most of the *rdm* and *rle* pumices have a bubble connectivity *(c)* > 0.9, except for two isotropic microvesicular pumices of *rle* with *c* = 0.70-0.85 (Fig. 4.4b); thus, the open porosity is approximately the total porosity for most of the pumices.

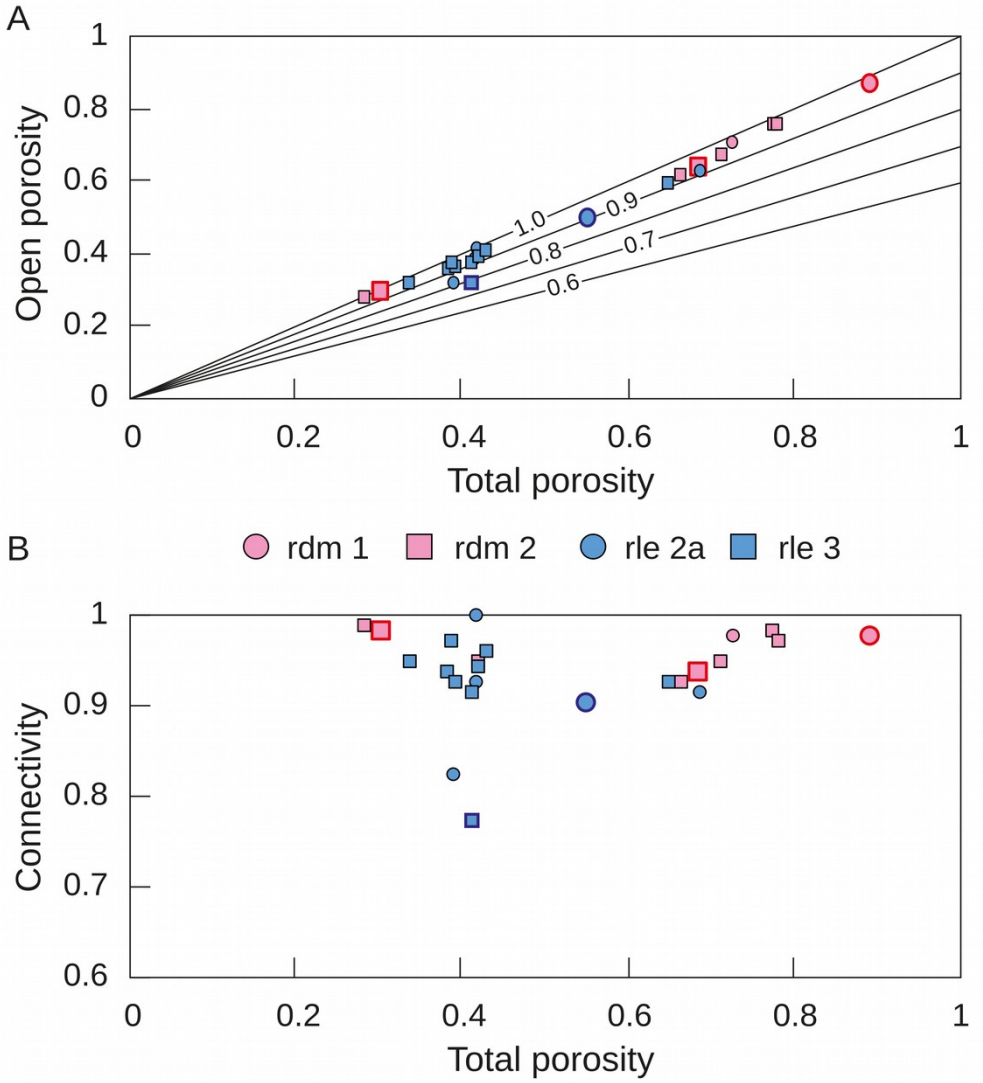

Fig. 4.4: Measured porosities in pumices of the early postglacial rhyolites. A Open porosity versus total porosity. The lines represent connectivity. **B** Connectivity versus total porosity. The bigger and highlighted symbols are pumices analyzed by X-ray tomography.

The viscous permeabilities for the entire sample suite range from 2.6 x 10^{-12} – 2.3 x 10^{-10} m^2. These values are relatively high compared with silicic rocks from other volcanic complexes (e.g., Colombier et al., 2017; Gonnermann et al., 2017). The maximum measured k_v is from a frothy pumice of *rdm* 1, while pumices of *rdm* 2 have a lower k_v and cover a range of one order of magnitude (Table 4.1). The pumices of the *rle* 2 (the subplinian magmatic stage) have the lowest k_v, while the pumices of *rle* 3 (the explosive stage before the transition to the effusive phase) have the widest range of viscous permeabilities (Table 4.1). The viscous permeability generally increases slightly with (open) porosity except in *rle* 2, where k_v is independent of φ_c (Fig. 4.5a). By contrast, the inertial permeability has two trends with the open porosity: pumice with $\varphi_c < 0.65$, most of them from *rle,* have a limited range of k_i (1.4-8.6 x 10^{-8} m), whilst for $\varphi_c > 0.65$, all from *rdm*, show an increase in k_i with φ_c (1.7 x 10^{-7} – 2.9 x 10^{-5} m; Fig. 4.5b). Unusually (cf., Rust and Cashman, 2004; Zhou et al., 2019), log k_v and log k_i are not correlated except for a limited number that define a correlation of log k_i = 1.63log k_v + 11.18, which defines an upper envelope for the data (Fig. 4.6a). The logarithm of k_v/k_i shows a maximum at a connected porosity of ~0.4-0.5 (Fig. 4.6b).

For 3D bubble textural analysis and permeability simulations, we selected five pumices (Table 4.2): the frothy pumice of *rdm* 1, which has the highest porosity and permeability of the sample suite (Fig. 4.4 and 4.5; sample *rdm* 1 T1), a tube pumice of *rdm* 2 that is at the inflection of the two trends in Figure 4.5 (sample *rdm* 2 T1), a low-porosity pumice of *rdm* 2 that has the lowest k_v/k_i (Fig. 4.6; sample *rdm* 2 T2), a banded microvesicular pumice of *rle* 2 that is at the inflection point of the two trends in the k_v/k_i - φ_c plot (Fig. 4.6; sample *rle* 2 T1), and an isotropic microvesicular pumice of *rle* 3 that has the lowest φ_c and k_v/k_i of the eruptive unit (Fig. 4.6; sample *rle* 3 T1).

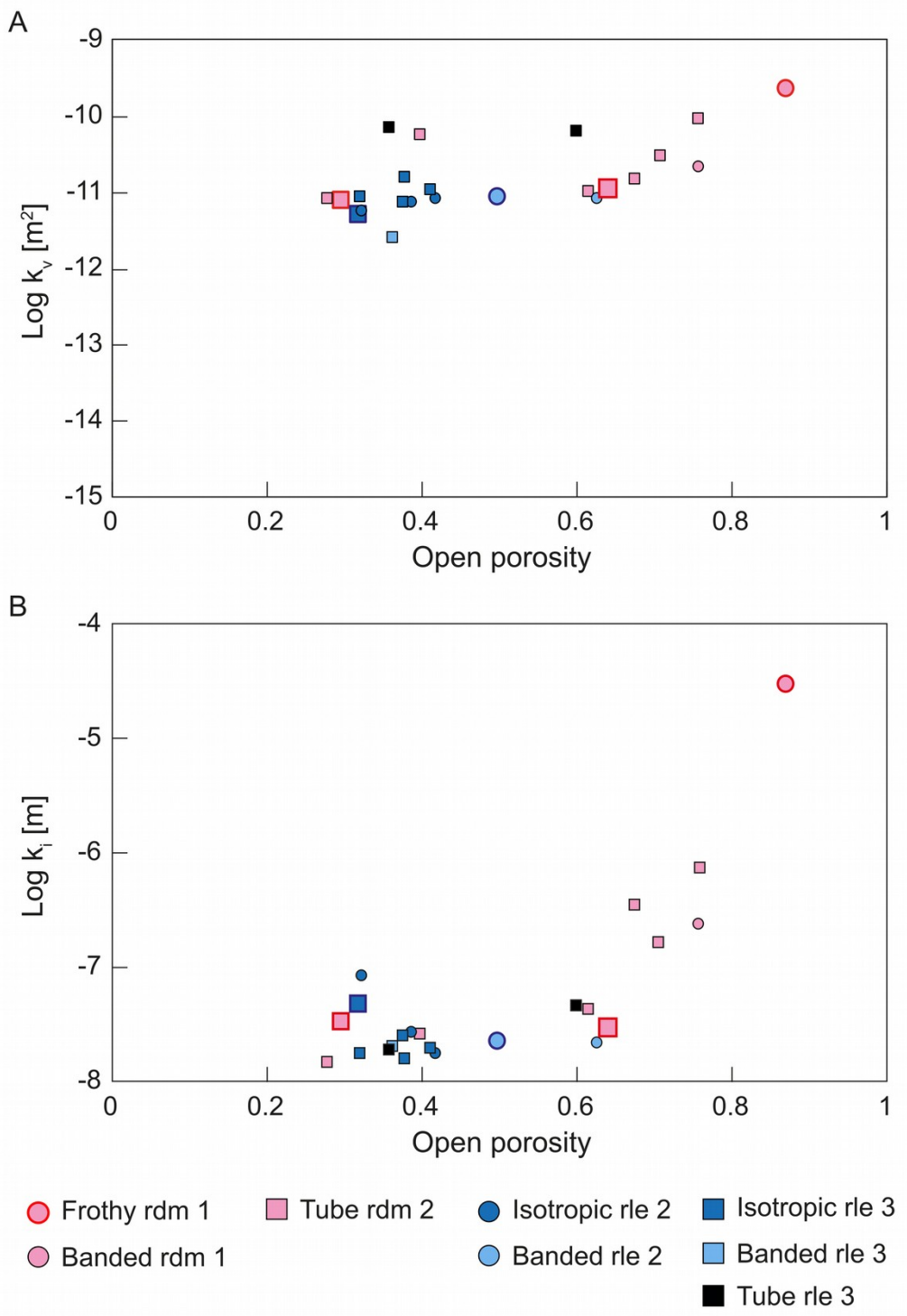

Fig. 4.5: Permeabilities versus the open porosity from laboratory measurements. A The viscous permeability slightly increases with the open porosity. The axis range covers typical permeability values in natural samples. **B** The inertial permeability shows two trends with the open porosity: it is independent of the open porosity for $\varphi_c = 0.25 – 0.60$ and increases with the open porosity for $\varphi_c = 0.6 – 0.9$. Larger symbols indicate samples that were also analysed by tomography.

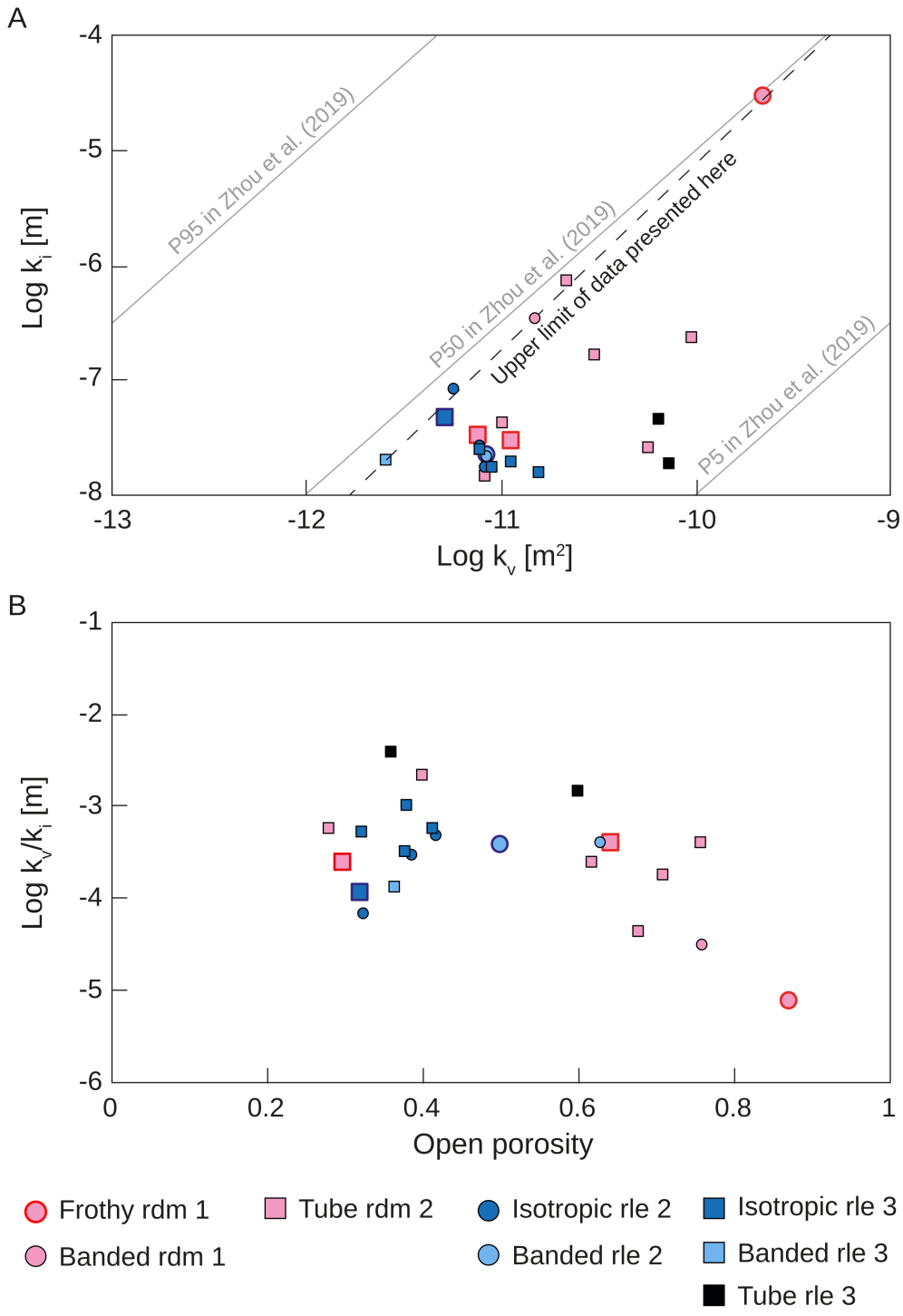

Fig. 4.6: Comparison between viscous and inertial permeabilities from laboratory measurements. A Measured inertial versus viscous permeability. The dashed line represents the upper limit mentioned in the main text. The whole *rdm-rle* sample suite is within the permeability trend proposed by Zhou et al. (2019). **B** Log k_v/k_i versus the open porosity. Larger symbols indicate samples that were also analysed by tomography.

Table 4.2: Physical parameters determined from X-ray tomography and simulations of flow through the derived pore geometry (connectivity, connected porosity, viscous and inertial permeabilities, average tube diameter, tortuosity) some of which are used to calculate theoretical permeabilities predicted by the capillary-based Kozeny-Carman expressions (Eqs. 6 and 7), and equivalent data from laboratory experiments. The superscripts "m", "s" and "kc" refer to measured in the laboratory, simulated using tomograms, and estimated by the Kozeny-Carman expression, respectively.

	rdm 1 T1	rdm 2 T1	rdm 2 T2	rle 2 T1	rle 3 T1
C^m	0.98	0.94	0.98	0.91	0.77
C^s	0.96	0.99	0.89	0.99	0.99
φ_c^m	0.87	0.64	0.30	0.50	0.32
φ_c^s	0.84	0.43	0.25	0.39	0.40
K_v^m [m^2]	2.2×10^{-10}	1.1×10^{-11}	7.7×10^{-12}	8.5×10^{-12}	5.2×10^{-12}
K_v^s [m^2]	6.7×10^{-11}	3.6×10^{-11}	3.5×10^{-13}	1.7×10^{-11}	1.1×10^{-11}
K_i^m [m]	2.9×10^{-5}	3.0×10^{-8}	3.3×10^{-8}	2.3×10^{-8}	4.7×10^{-8}
Tube diameter [μm]	450	70	28	49	57
Tortuosity	1.2	1.4	2.1	2.6	1.5
K_v^{kc} [m^2]	3.8×10^{-9}	4.0×10^{-11}	9.2×10^{-13}	2.4×10^{-12}	5.8×10^{-12}
K_i^{kc} [m]	2.0×10^{-4}	1.0×10^{-5}	3.2×10^{-7}	7.8×10^{-7}	1.7×10^{-6}

4.4.3. X-ray tomograms

4.4.3.1. Bubble textural description

In Chapter 2, I describe the vesicles of the frothy pumices from *rdm* as spherical to colloform with irregular curvilinear shapes based on observations from 2D BSEM images (Section 2.5.4). The X-ray tomogram of *rdm* 1 T1 shows, however, that the bubbles are connected, oriented and form bands of two types (Fig. 4.7a): elongated (centimetric in the long axis) individual vesicles and wide (1-3 mm in the intermediate axis) channels formed by one or more vesicles, with thinner sequences (0.2-1.5 mm intermediate axis) of several nearly spherical bubbles separated by discontinuous thin bubble walls of ~10 μm. Both types of connected bubble bands are separated by thick bubble walls (≤100 μm), which may contain spherical bubbles of ≤50

µm. The average pore aperture of the vesicles is 420 µm (Table 4.2). The pumice is completely aphyric.

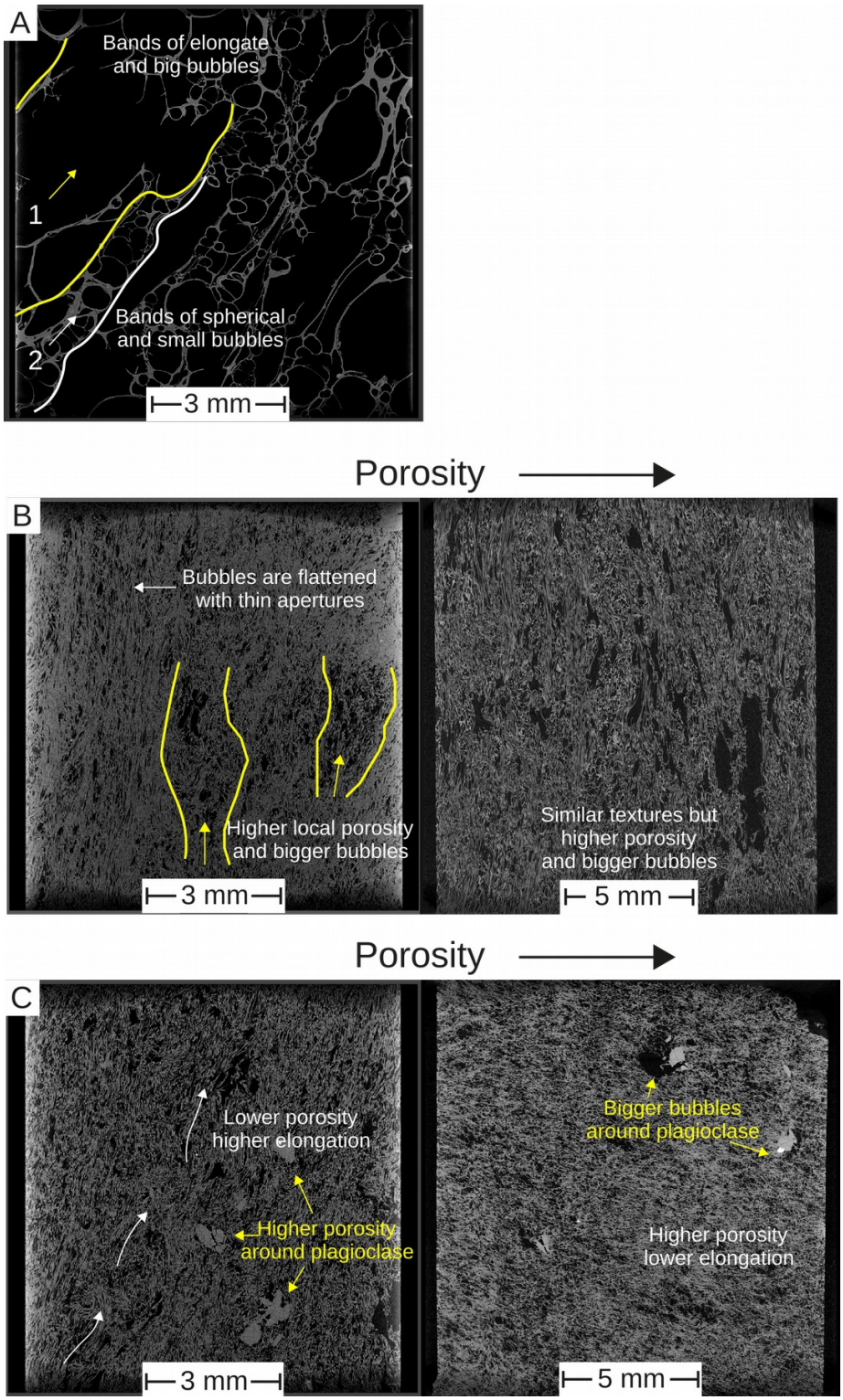

Fig. 4.7: Bubble textures within pumices. 2D slices through X-ray tomograms of ~1300 x 1300 x 1700 (voxel size = 3.5-7.0 µm). **A** Reticulated pumice of *rdm* 1. The two types of bubble bands are highlighted in the image. **B** Long-tube pumices of *rdm* 2. The differences in porosity are controlled by the width of gas channels and heterogeneities within pumices. **C** Pumices of *rle*. Orientation trends are less clear than in *rdm* 2 pumices.

The two pumices from *rdm* 2 (*rdm* 2 T1 and *rdm* 2 T2) are crystal-poor with glassy groundmass and elongate vesicles with straight and irregular boundaries in 2D sections (Fig. 4.7b). The lowest porosity pumice (*rdm* 2 T2) is heterogeneous in porosity, bubble number density, size and elongation. Zones of higher porosity show nearly equant bubbles with straight borders separated by bubble walls <40 μm. The other domains have flattened elongate bubbles with pore apertures of <100 μm; that can terminate with pointed tips or coalesce to form wider channels. The porosity is locally higher surrounding plagioclase phenocrysts due to the presence of large near-spherical bubbles of diameter <200 μm. The higher porosity pumice (*rdm* 2 T1) has bubbles with similar shapes as the *rdm* 2 T2, but with a higher number density of wider and elongate bubbles (<400 μm-wide) distributed more homogeneously. The average pore aperture of *rdm* 2 T1 and *rdm* 2 T2 are 68 and 26 μm, respectively (Table 4.2).

Both pumices from *rle* are crystal poor but contain phenocrysts of plagioclase and biotite; they have somewhat elongated and oriented bubbles with features of bubble collapse (Fig. 4.7c). As seen in *rdm* 2, the local porosity increases around plagioclase phenocrysts due to large (<150 μm) and nearly spherical bubbles. Although not clear in hand sample (see macroscopic description above), the low-porosity isotropic pumice (*rle* 3 T1) has elongate tubular bubbles; the anisotropy of this sample is clearer than in the banded microvesicular pumice (*rle* 2 T1). The lowest porosity pumice (*rle* 3 T1) shows clear heterogeneities of bubble elongation, shape, size and number density. The *rle* 3 T1 pumice is characterized by tortuous elongate bubbles of thin diameters (>10 μm) that may be discontinuous with pointed tips or may coalesce to form wider channels. Minor domains of nearly equant and larger bubbles (<100 μm) are surrounded by flattened small (<50 μm) bubbles. By contrast, the higher porosity pumice (*rle* 2 T1) shows subtle bubble heterogeneities and wider pore apertures with rhomboidal shapes. The average pore apertures of *rle* 2 T1 and *rle* 3 T1 are 75 and 57 μm, respectively (Table 4.2).

4.4.3.2. Porosity and permeability simulations

The total porosities measured by X-ray tomography are 0.28-0.88 and the connectivity range is 0.88-1.00 (Table 4.2). The high-porosity pumice of *rdm* 2 and both pumices of *rle* have a connectivity ~0.99. By contrast, the frothy pumice of *rdm* 1 has c = 0.96 due to two types of bubbles: some isolated spherical bubbles within the thinner bands of spherical bubbles, and some of the smallest spherical bubbles within the thickest bubble walls (Fig. 4.8). The low-porosity pumice of *rdm* 2 has c = 0.88 due to several flattened elongate isolated bubbles (Fig. 4.8).

In Figure 4.9, I show the pressure and velocity fields of the permeability simulations for the five pumices studied. The images of the air pressures (Fig. 4.9a) correspond to a 2D slice through the centre and parallel to the longest axis of the pumice core. As the dominant flow pathway for each sample is three-dimensional, it could not be entirely represented in the pressure image and does not even necessarily intersect it. The images of the velocity fields show 500 of the main pathways in a 3D volume captured in a view orthogonal to the longest axis of the pumice core (Fig. 4.9b). The regions with a higher density of pathways represent the bubbles that carry most of the flux.

The frothy pumice from *rdm* 1 has the highest simulated k_v of the sample suite (6.74 x 10^{-11} m^2), which can be explained by one <300µm gas channel that covers a big section of the VOI (Fig. 4.9b). The gas pressure changes sharply from one bubble to another in the pressure slice (i.e. there are discrete change of colors on each side of bubble walls) because not all bubbles in the slice are part of the same flow pathway and the intermediate pressures for those pathways are in the 3D volume, outside of the slice shown (Fig. 4.9a).

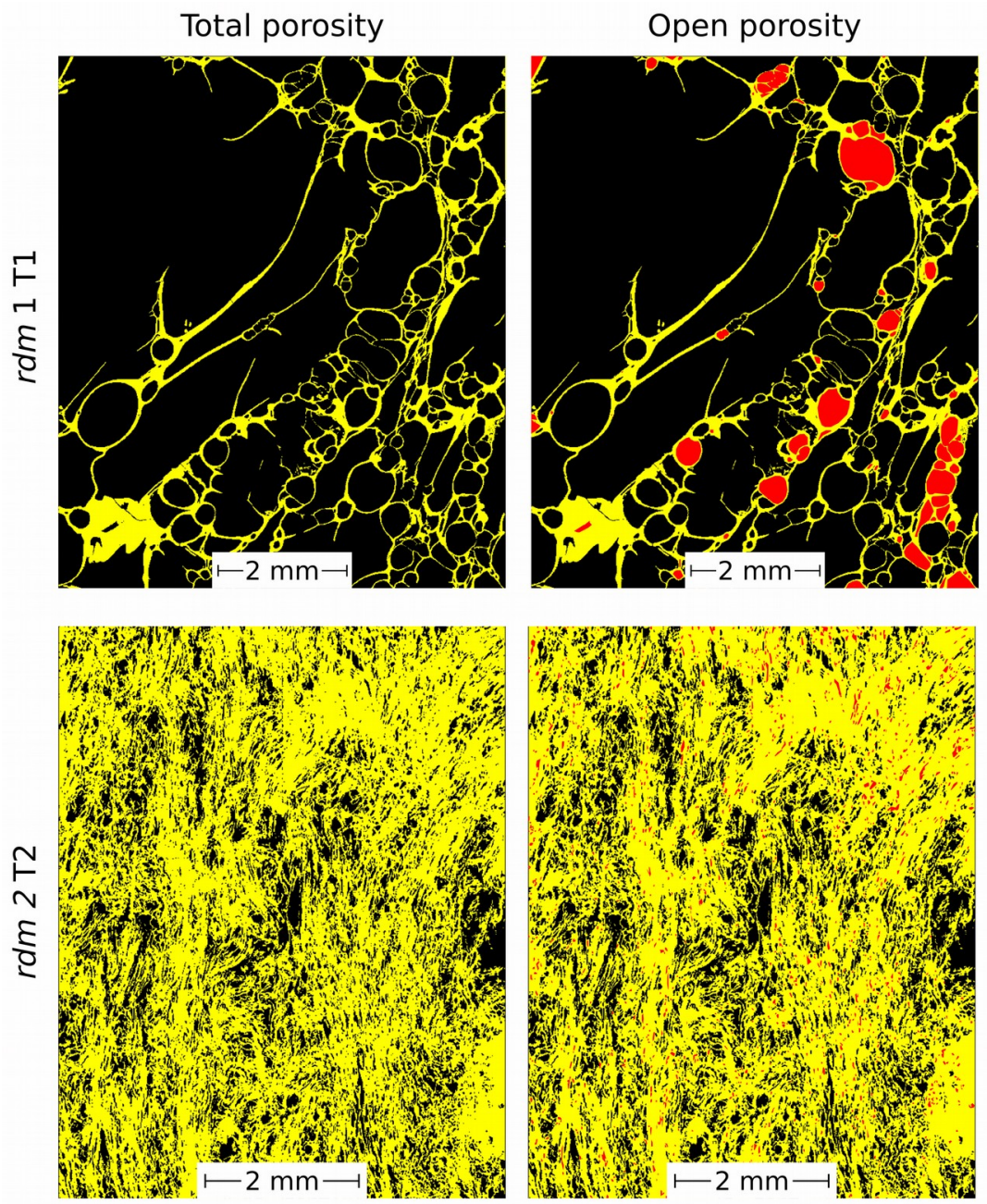

Fig. 4.8: Comparison of total and open porosity in X-ray tomograms. Examples of the least connected pumices. In the images to the left, glass and crystals are yellow and vesicles are black; in the images to the right, we use the same colors but isolated bubbles are red. In the reticulated pumice (*rdm* 1 T1), some of the big spherical bubbles and the smallest bubbles inside thick bubble walls are isolated. In the low-porosity long-tube pumice (*rdm* 2 T2), several small flattened bubbles are isolated.

The *rdm* 2 T2 pumice has by far the lowest simulated k_v of the sample suite ($k_v = 3.48 \times 10^{-13}$ m^2; Table 4.2). Figure 4.9b shows that in this sample, the gas travels primarily through the widest channel, which has a lower tortuosity ($\tau \sim 1.3$) than the minor flow pathways through some thinner bubbles (τ average ~ 2.3). This relatively low-tortuosity channel narrows down-

flow (towards to bottom of the figure) causing the flow velocity to decrease. Because of the homogeneous low gas velocity and permeability, the gas pressure drops gradually through the entire sample except near the gas inlet and outlet (Fig. 4.9a). The other pumice from *rdm* 2 (*rdm* 2 T1) has the second highest simulated viscous permeability of the sample suite (k_v = 3.64 x 10^{-11} m^2). Flow path imaging of this sample (Fig. 4.9b) shows four fairly straight and connected gas channels ($\tau \sim 1.4$) that are wider than the dominant channel of *rdm* 2 T2, as well as several narrower low-tortuosity channels ($\tau \sim 1.6$) associated with a lower velocity (Fig. 4.9b). In the bubbles where main flow pathways pass the gas pressure drop is low. In the rest of the sample (i.e., where the velocities are low), the gas pressure drops gradually between both flow ends (Fig. 4.9a).

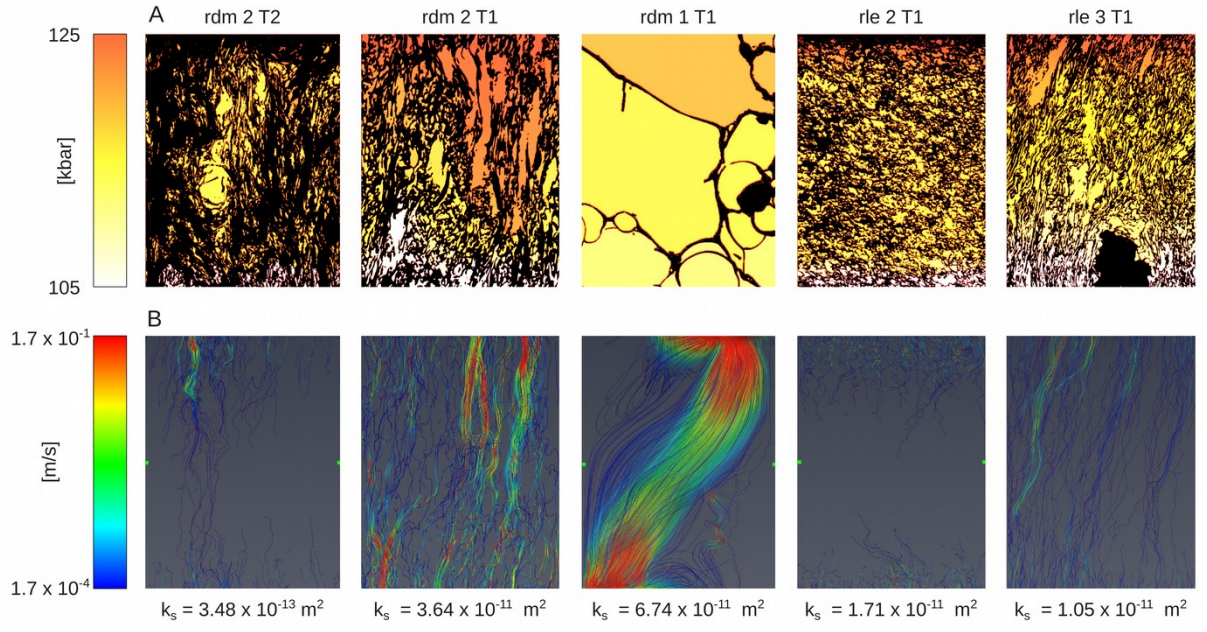

Fig. 4.9: Images from permeability simulations where air flows from top to bottom through a porosity structure determined by X-ray tomography. A A 2D slice of the pressure field in a slice through the centre of the simulated volume parallel to the average air flow direction. Black represents glass, crystals and isolated bubbles; the grading from white to dark orange represents a pressure interval of 105-125 kPa for all the images. **B** Image of the 3D velocity field acquired from the same perspective as the pressure field. The solid portion has been made transparent and for each sample the projection of 500 3D flow pathlines through the pore spaceare shown. Red represents high velocity and blue represents low velocity along the pathline. Velocities <1.7 x 10-4 m/s are not shown; this means that some pathlines with lower velocities appear discontinuous although they are not. The velocity range for visualization is the same in the five images. Note the velocity lines (3D projections) in **B** do not necessarily match with the pressure patterns in the images from **A** which are 2D slices.

Both pumices of *rle* have similar viscous permeability (k_v = 1.0-1.7 x 10^{-11} m^2) despite different flow pathway geometries (Fig. 4.9b). The high-porosity banded pumice (*rle* 2 T1) has the most homogeneous velocity field and a gas pressure that gradually drops in the direction of the flow (Fig. 4.9a). This is because there are no dominant flow paths; rather flow is distributed through thin complex channels of high tortuosity (e.g. $\tau \sim 2.6$). No complete flowpaths are shown for this sample in Fig 4.9b because the air flow velocity through the thin complex channels is mostly lower than the threshold I chose for visualizing flow. By contrast, in the low-porosity pumice (*rle* 3 T1) the flow pathways are mainly concentrated in the widest bubble, while the low-tortuousity thin gas channels (τ average ~ 1.5) show a lower velocity (Fig. 4.9b). As in *rdm* 2 T1, the gas pressure remains high (~120 kPa) or low (~105 kPa) in the bubbles if the high flow velocities are located near the inlet or the outlet, respectively. As there are tens of high-velocity flow pathways near the ends of the sample, the gas pressure is homogeneously high (~125 kPa) in the ~first quarter of the sample, and homogeneously low (~105 kPa) in the last quarter of the sample (Fig. 4.9a).

4.5. Discussion

In this section I analyze the source of variations between the measurements and simulations of the physical parameters and compare the 2D and 3D textural descriptions. I analyze the porosity-permeability patterns of the *rdm* and *rle* pumices and the role of the bubble textures on the calculated magma permeabilities. Based on the X-ray tomograms and the simulated velocity and pressure fields, the control of some textural parameters is quantified by the Kozeny-Carman expression for the viscous and inertial permeabilities. In the end, I discuss the relationship of the magma permeabilities with the eruption histories of the *rdm* and *rle* events, and compare them with information from other silicic eruptions.

4.5.1. A comparison of the X-ray tomography with other techniques

4.5.1.1. Measurements vs simulations of porosities and permeabilities

This is one of the few studies that analyzes both laboratory measurements and numerical simulations of permeabilities in the same rhyolitic samples (e.g., Bouvet de Maissoneuve et al., 2009; Degruyter et al., 2010b; Wright et al., 2006). The size of the domain in my flow simulations to assess permeability (2-5 mm in linear dimension) is larger than in these previous studies, which were about 1 mm in linear dimension. It was feasible for me to model a larger volume because I applied a finite-volume computation method limited to low Re flow (APES) which is less computationally expensive than the Lattice-Boltzmann schemes used previously. Computation efficiency was also aided by the relatively large voxel size (3.5-7.0 μm) which was a consequence of using conventional X-ray tomography rather than synchrotron X-ray tomography. However, some of the advantages of the simulations in previous studies are related to the quality of images and detail of the simulations as the synchrotron X-ray tomography acquires images of higher quality and resolution than this study, allowing a more detailed visualization of the pumice structure (Section 3.2; Baker et al., 2012).

I expect the simulated viscous permeabilities to be slightly higher than the measured permeabilities for the following reasons: 1. The segmented pumice 3D image does not consider the bubble walls thinner than the voxel size, creating an artificial and more connected pore structure (e.g., Degruyter et al., 2010b; Wright et al., 2006); 2. The image resolution and the segmentation processes soften the irregularities in the bubble walls and simplify the internal pumice structure. Heterogeneities in bubble textures may also cause discrepancies because the VOI selected for the simulation, which is much smaller than the core, may not be representative. Indeed, three samples (*rdm* 2 T1 and *rle* 2 T1 and 3 T1) yield simulated permeabilities that are slightly higher and well-correlated with the measured viscous

permeability (Fig. 4.10b). By contrast, the simulated permeability of *rdm* 1 T1 is ~3 times lower, and *rle* 3 T1 is one order of magnitude lower, than the measured permeability. The underestimation of permeability in the *rdm* 1 T1 pumice can be explained by the heterogeneities of bubble textures in this sample and the selection of VOI with a local lower permeability than the whole sample. The low permeability obtained in the simulation of the low-porosity pumice of *rdm* 2 could reflect the presence of bubbles below the tomogram resolution not being included in the calculation of the open porosity, or to a high fraction of artificially isolated bubbles due to lack of resolution of small pore apertures that connect adjacent bubbles (Fig. 4.9).

A representative textural analysis should consider objects formed by at least 3-5 pixels/voxels (e.g., Gualda and Rivers, 2006; Shea et al., 2010). As the voxel size of the acquired tomograms is 3.5 – 7.0 μm, the bubbles not recognized under the X-ray tomography are <30 μm. Comparisons of area fractions of pores in thin sections (Section 2.5.4) to volume fractions of pores in tomograms of different parts of the same clasts suggest that this fine bubble population represents <0.15 of the porosity of *rdm* and *rle* pumices. The open porosity from tomograms of core subvolumes is generally similar to, although slightly lower than, the measured open porosity determined by pycnometry on the entire core. An exception is the tubular bubble pumice of *rdm* 2, which has a tomogram open porosity 0.2 lower than that measured by pycnometry (Fig. 4.10a). This discrepancy could reflect the high number density of small flattened bubbles (that is, diameters below or near the tomogram resolution; see Section 2.5.4). One pumice (*rle* 3 T1) has a slightly higher tomogram open porosity than measured by pycnometry. In this case, the subvolume imaged by tomography may not be representative of the entire core. More generally, the densest pumices of *rle* have remarkably heterogeneous bubble populations, which makes it difficult to define a representative subsample.

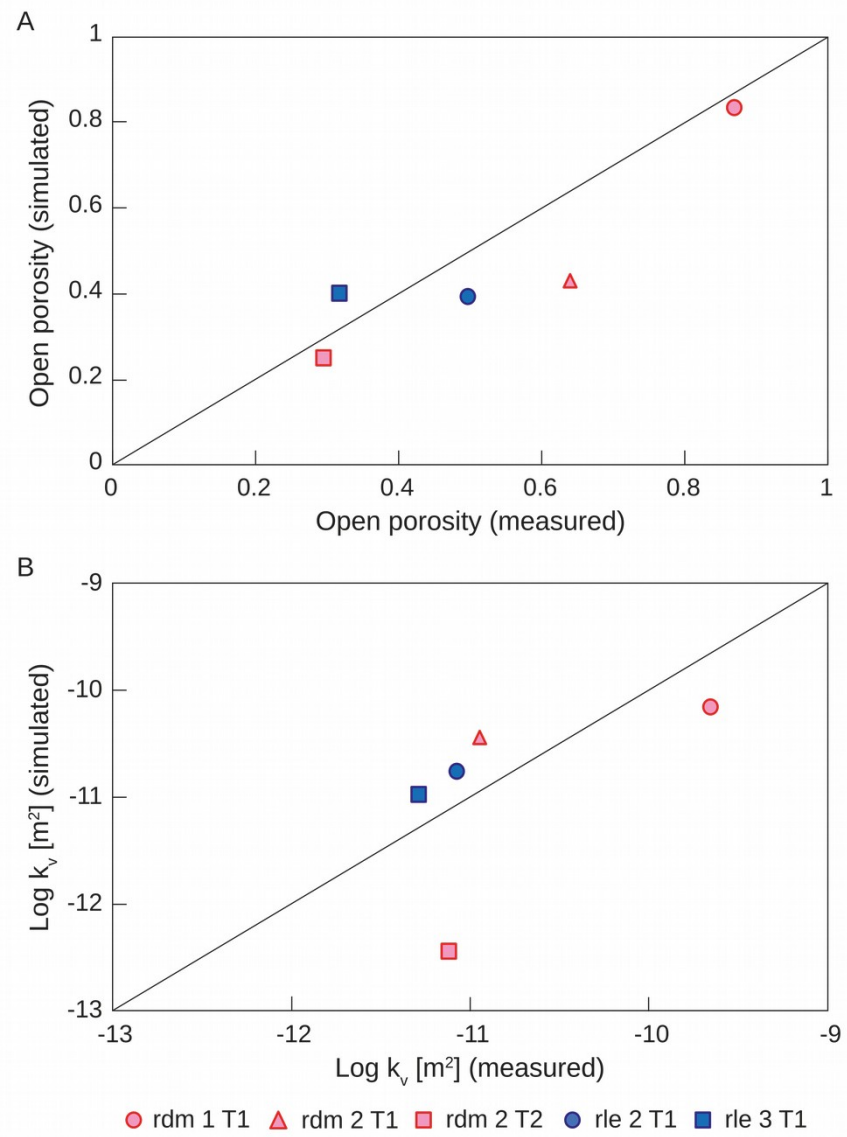

Fig. 4.10: Comparison of simulated with measured physical parameters. A Comparison of open porosities. The correlation of measurements and segmentation is good, except for two samples. A lower simulated open porosity can be explained by the presence of some vesicles smaller than the voxel size. **B** Comparison of viscous permeabilities. The correlation of measurements and simulations is good, except for the sample with the lowest porosity.

4.5.1.2. 2D vs 3D bubble textural analysis

2D images from thin sections can be sufficient to evaluate the fabric of pumices (Section 2.5.4); however, it is difficult to determine the orientation and degree of coalescence of the bubbles if they are not elongate (as the *rle* 2 T1) or if the tubes are too thin (as the *rdm* 2 T2). In this study of pumice from *rdm* and *rle* of Laguna del Maule, 3D imaging revealed that all pumices have interconnected and well-oriented bubbles, even those that did not seem to have a fabric in hand sample or 2D images. For instance, the low-mid porosity pumices of *rle* appeared isotropic in

hand sample and thin section but show a high connectivity of flattened oriented bubbles forming planar bands and tortuous gas channels (Fig. 4.9b) that, according to both laboratory permeability measurements and flow simulations, would allow effective degassing. Additionally in 3D, the frothy pumice of *rdm* 1, which appears isotropic in hand sample and thin section (Section 2.5.4), has oriented bands of coalesced spherical bubbles that form gas pathways through the sample (Fig. 4.7a).

In the following sections I analyze the porosities and permeabilities of the *rdm* and *rle* pumices to assess their evolution, including the role and origin of anisotropy, during the *rdm* and *rle* eruptions. I then compare the permeabilities determined by numerical simulation and laboratory measurements to those predicted by Kozeny-Carmen theory, interpreting discrepancies in the context of the assumptions of that theory.

4.5.2. Insights from porosity and permeability

Most *rdm* pumice clasts have a high total porosity (>0.65) consistent with coming from a sustained explosive eruption (Chapter 2; Mueller et al., 2011). The pumices were probably affected by a high total strain as they show a high anisotropy in the form of tubular bubbles and banded textures. A high total strain is related to an increase of the bubble coalescence, and then of the bubble connectivity (e.g., Rust and Cashman, 2011), and may explain the high bubble connectivity (>0.9) and viscous permeability ($>10^{-11}$ m^2) of the *rdm* pumice clasts.

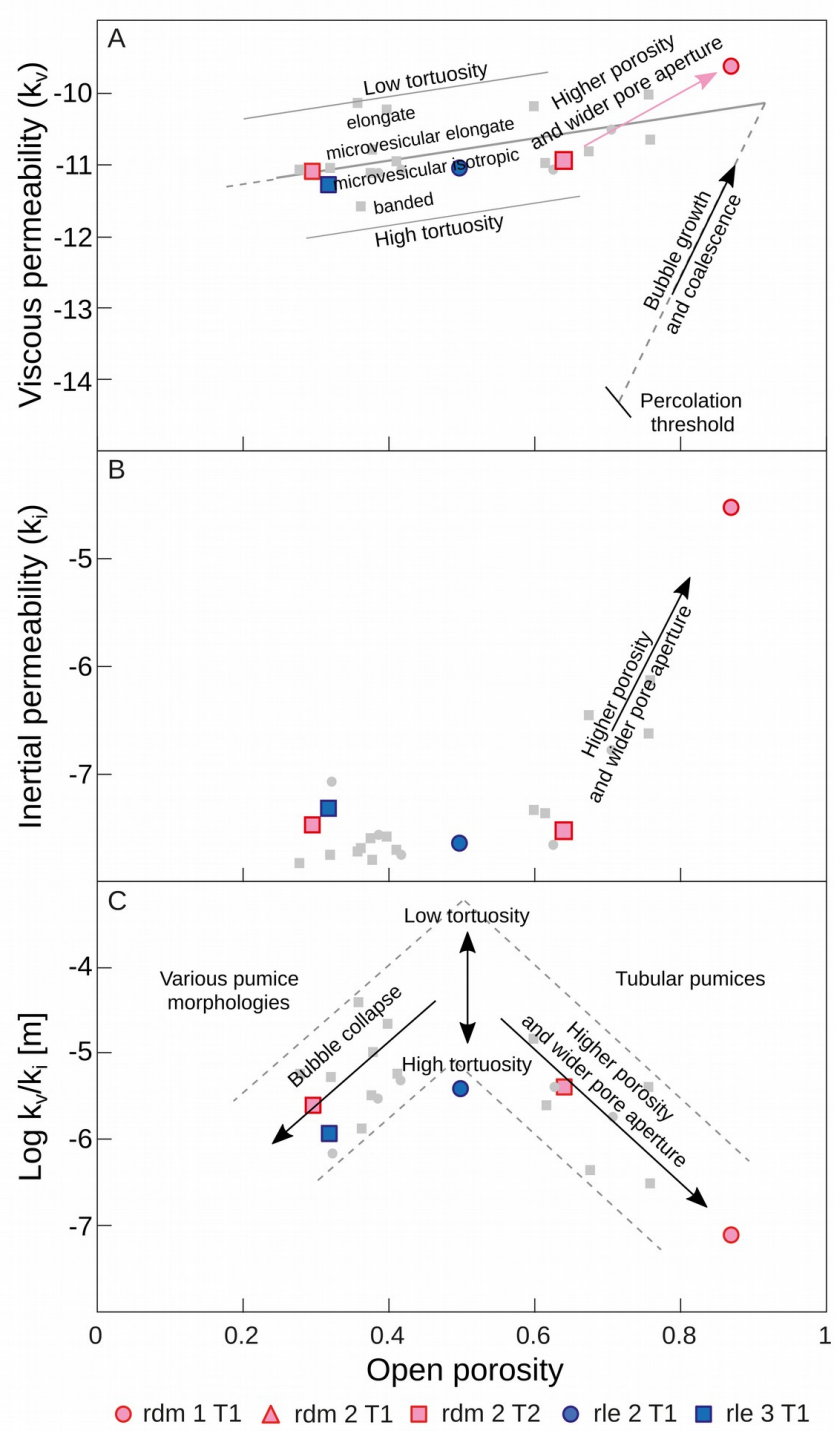

Fig. 4.11: Summary of the governing factors on the magma permeabilities. A Viscous permeability (k_v) versus open porosity. For the *rdm* pumices, k_v increases with the open porosity and the pore aperture. For the *rle* pumices, k_v depends on the pumice morphology and the average tortuosity of the flow pathways. We add other governing factors according to the hysteresis theory. **B** Inertial permeability (k_i) versus open porosity. Most of the *rdm* pumices show an increasing k_i with the open porosity; instead k_i is almost constant in the *rle* pumices regardless of having different porosities. **C** k_v/k_i versus the open porosity. For this sample suite k_v/k_i shows two trends with the open porosity controlled by the pumice morphology and tortuosity. Symbols in color are the samples scanned by X-ray tomography; symbols in grey are the others measured only in the laboratory.

Most *rdm* pumices of high porosity (>0.65) are tube pumices except for the frothy and the banded pumice clasts from the *rdm* unit 1 (Table 4.1; Fig. 4.5). This consistency in the type of bubble textures may explain the regular pattern of increasing viscous permeability with increasing porosity (Fig. 4.5a; Fig. 4.11a). Comparison of the X-ray tomography analyses of the *rdm* samples suggests that the increasing viscous permeability is in part related to wider pore apertures and straighter bubbles, in addition to increased open porosity. In the high-porosity *rdm* pumices, the inertial permeability also increases with increasing porosity (Fig. 4.5b; Fig. 4.11b) and k_v/k_i decreases with porosity (Fig. 4.6; Fig. 4.11c). In particular, the banded pumice of *rdm* 1 has 3-4 times lower viscous and inertial permeabilities than the tube pumices for the same porosity (Fig. 5). The trends in the permeabilities of relatively high *rdm* samples do not extend to $\varphi_c \leq 0.6$: both *rdm* and *rle* samples with $0.28 \leq \varphi_c \leq 0.62$ have fairly constant inertial permeabilities and have similar (but variable) viscous permeabilities that show a subtle increasing trend with porosity (Figs. 4.5, 4.11). I suggest that the high anisotropy (e.g., *rdm* 2 T2) and the occurrence of a few elongate bubbles with wide pore apertures visible to the naked eye (e.g., DivM4) allows higher permeabilities in these samples than predicted by extending the porosity-permeability trends of the high-porosity pumice clasts (Fig. 4.11a).

The *rle* pumice clasts have a wide porosity range consistent with coming from a pulsatory silicic explosive eruption (Chapter 2; Schipper et al., 2013). Like the *rdm* pumices, most *rle* pumices have high bubble connectivities (>0.9) and high viscous permeabilities ($>10^{-12}$ m^2). The X-ray tomograms (e.g., *rle* 3 T1) suggest that the high connectivities and permeabilities are controlled by the high anisotropy of the *rle* pumices in the form of elongate bubbles with wide pore apertures regardless of the pumice porosity. However, this is not a general pattern as isotropic microvesicular pumices from other rhyolite eruptions have lower bubble connectivities and viscous permeabilities (Fig. 4.11).

I suggest that the great scatter of the porosity-permeability trend of the *rle* pumices is due to the different rock fabric and various bubble textures (Fig. 4.11). In the "Macroscopic textural description" section (Table 4.1), I classified three types of *rle* pumices: elongate (2 samples), banded (3 samples) and isotropic (9 samples). The elongate pumices have some of the highest viscous permeabilities of *rle* but relatively low inertial permeabilities (Fig. 4.5). By contrast, the banded pumices have relatively low viscous permeabilities. As the isotropic microvesicular pumices show a relatively wide range of both viscous and inertial permeabilities, I suggest that the pumices with the highest permeabilities contain elongate micrometric tube bubbles as in *rle* 3 T1 (i.e., they are not isotropic); in contrast, the pumices with the lowest permeabilities are microvesicular and more isotropic. In this way, the occurrence of four classes of pumices (elongate, microvesicular elongate, microvesicular isotropic, and banded) precludes a log-log relationship between both permeabilities for the sample set as a whole; however, the samples with the highest relative k_i follow the typical trend of $\log(k_i)/\log(k_v) \sim 3/2$ in silicic pumices (e.g., Gonnermann et al., 2017; Rust and Cashman, 2004), and the others with lower k_i overlaps most of the measurements in volcanic rocks (Fig. 4.6a; Zhou et al., 2019).

In order to analyze quantitatively how the bubble textures control the measured permeabilities in both *rdm* and *rle* pumices, in the following section I estimate both the viscous and inertial permeabilities by the Kozeny-Carman expressions in the five pumices analyzed by the X-ray tomography.

4.5.3. A comparison with the Kozeny-Carman expressions

The Kozeny-Carman permeability-porosity relation (Eq. 6) predicts that the viscous permeability is proportional to the open porosity and to the square of the bubble diameter (or pore aperture; Burgisser et al., 2017), and is inversely proportional to the square of the tortuosity. In general, the viscous permeability estimated using the Kozeny-Carman expression

is similar to numerical simulations and laboratory measurements except for the *rdm* 1 T1 and *rle* 2 T1 samples (Fig. 4.12a,b; Table 4.2). For *rdm* 1 T1, either a reduction of the average pore aperture to ~50 μm or an increase of the average tortuosity to 8 could match k_v estimated by the Kozeny-Carman expression with the simulated numerically (Table 4.3). A reduction of the average pore aperture could be explained by a higher number density of bubbles <50 μm than the measured from X-ray tomograms based on the analysis of bubble number densities (Section 2.5.4); in contrast, a very high tortuosity is not feasible based on the velocity pathlines (Fig. 4.9). For *rle* 2 T1, either a variation of the average pore aperture (~90 μm) or tortuosity (variation of 1.5) could produce a higher k_v than estimated by the Kozeny-Carman expression (Fig. 4.12a). The measured viscous permeability generally increases slightly with porosity but there is substantial scatter which I infer is mainly controlled by the average pore aperture (the wider bubble diameter, the larger permeability) and tortuosity (the more tortuous the lower permeability) of the gas pathways. In this way, the difference in k_v can be explained by the pumices of higher permeabilities having gas pathways that are on average wider and/or straighter than those from the low-permeability pumices (Fig. 4.9b; 4.12b). In the case of the samples with the lowest porosities, gas flow through the magma is effectively localized in the widest bubbles with the least tortuous gas pathways (Fig. 4.9b). The high permeabilities of the LdM pumices in comparison with pumices from other rhyolitic eruptions may be explained by the high anisotropy of the bubble fabrics, which increases the bubble connectivity and reduces the tortuosities of the gas pathways (e.g., Wright et al., 2009).

The high Re version of the Kozeny-Carman expression (Eq. 7) predicts that the inertial permeability is proportional to the pore aperture and the square of the open porosity, and inversely proportional to the cube of the tortuosity. It predicts a k_i range of $7 \times 10^{-8} – 1 \times 10^{-4}$ m for my samples (Fig. 4.12; Table 4.2), however all scanned samples except *rdm* 1 T1 have an inertial permeability of $2 – 5 \times 10^{-8}$ m based on laboratory measurements of air flow through

the cores. The overestimate of k_i by the Kozeny-Carman expressions could be explained by an overestimate of the pore aperture and/or an underestimate of the tortuosity (determined from the tomograms); however, adjusting these parameters to match k_i calculated by Kozeny Carmen to laboratory measurements, would for most samples make the corresponding k_v calculated by the Kozeny-Carman further from that simulated numerically (Fig. 4.12c) and measured in the laboratory. I suggest that the discrepancies of k_i between measurements and those estimated by Kozeny-Carman occur because the Kozeny-Carman expressions are based on capillary tubes and fracture flow models (e.g., Mueller et al., 2008), not taking into account the inertial effects of along-path pore aperture variations (e.g., Rust and Cashman, 2004; Zhou et al., 2019). In fact, most of the tubular bubbles (e.g., the two of *rdm* 2 and the *rle* 3 T1) show variations in their pore apertures of tens of microns which should increase the turbulence around local expansions or constrictions (Zhou et al., 2019) and may change k_i around one order of magnitude as the average pore apertures of these samples is 20-60 μm.

The highly vesiculated pumices of *rdm* 1 are exceptional in the context of the early postglacial deposits of LdM (Fig. 4.12b). The high viscous and inertial permeabilities of sample *rdm* 1 T1 may be explained by the high porosity (0.85-0.90), the large bubble diameter (0.4-0.5 mm) and their circular pore apertures. However, as the pore geometry in *rdm* 1 T1 is formed by partially coalesced spherical bubbles, connected by apertures much smaller than the bubbles, the Kozeny-Carman expression overestimates both viscous and inertial permeabilities (Fig. 4.11).

In the following section I summarize the role of the magma permeabilities on the eruption histories of silicic explosive eruptions, and in particular, I analyze the factors governing the magma permeabilities and eruption styles and transitions of the rhyolites of Laguna del Maule and Los Espejos.

Table 4.3: Measured pore diameter (d) and tortuosity (τ) by X-ray tomography and the parameters input in the Kozeny-Carman expressions to match the simulated viscous permeability and both measured viscous and inertial permeabilities.

		Measured by X-ray	k_v simulated	k_v measured	k_i measured
rdm 1 T1	d [µm]	450	61	108	134
	τ	1.2	8.9	5	1.8
rdm 2 T1	d [µm]	70	81	37	0.5
	τ	1.4	1.2	2.6	7.3
rdm 2 T2	d [µm]	28	19	81	12
	τ	2	3	0.7	2.7
rle 2 T1	d [µm]	49	147	92	7
	τ	2.5	0.8	1.3	4.8
rle 2 T1	d [µm]	57	69	54	8
	τ	1.5	1.2	1.6	2.9

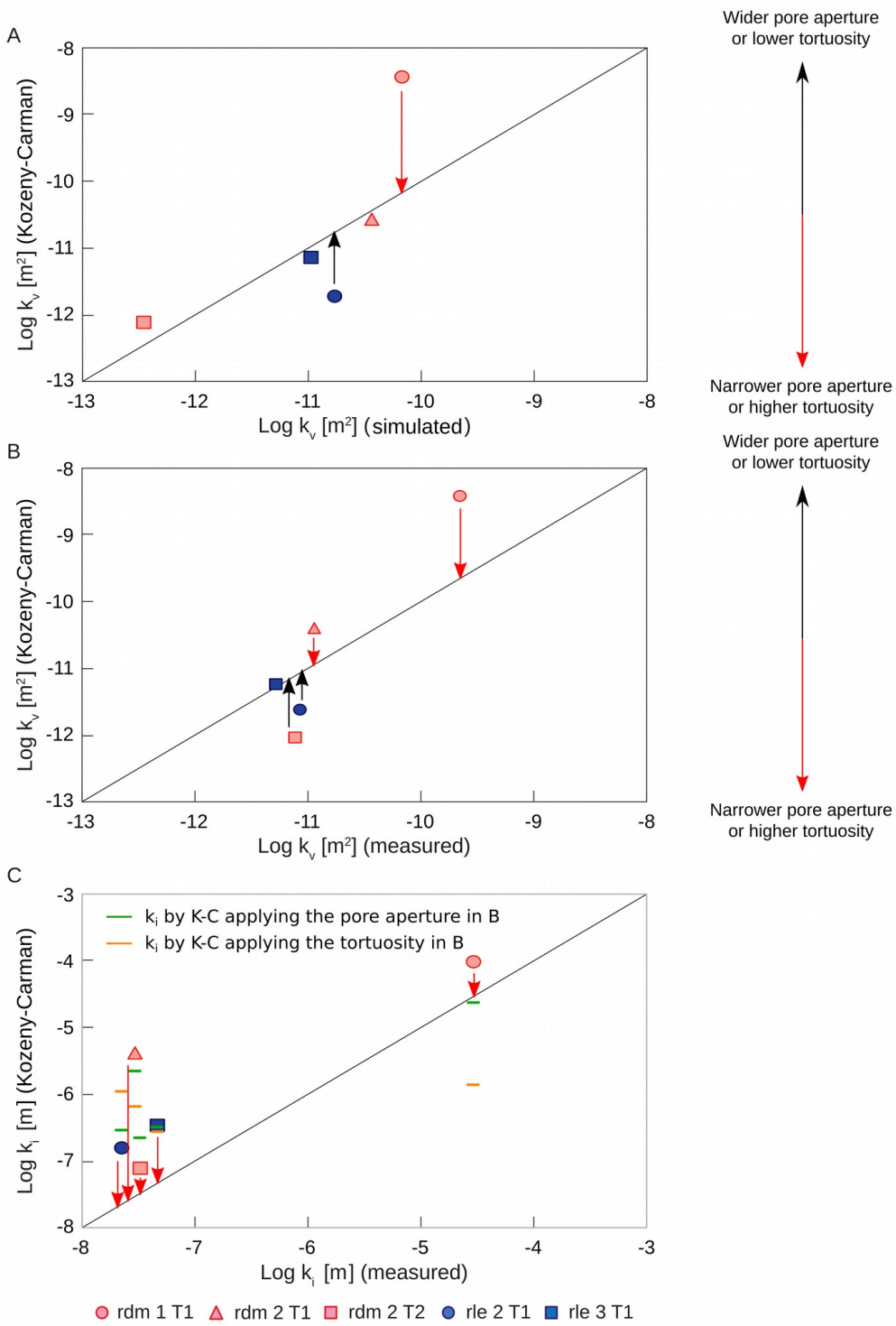

Fig. 4.12: A comparison of permeabilities simulated numerically and measured in the laboratory with estimated by Kozeny-Carman expressions for all samples scanned by X-ray tomography. The textural parameters used to estimate the permeabilities by the Kozeny-Carman expression were measured from the X-ray tomograms. The samples have different k_v and lower k_i than the estimations. **A** Comparison between viscous permeabilities simulated numerically and estimated by Kozeny-Carman. **B** Comparison between viscous permeabilities measured in the laboratory and estimated by Kozeny-Carman. **C** Comparison of inertial permeabilities. The estimated inertial permeabilities by Kozeny-Carman using the pore apertures applied in **B** are in green, and using the tortuosity applied in **B** are in orange.

4.5.4. The role of magma permeabilities on the eruption histories of LdM

The efficiency of outgassing is a key governing factor of the styles and transitions of silicic eruptions (Cassidy et al., 2018). As the products of an intense eruption are fed by magmas that retained their volatiles during ascent, the pumices formed during Plinian eruptions usually have narrow ranges of high porosities (0.7-0.9; e.g., Gonnermann et al., 2017; Klug et al., 2002). As the Plinian eruptions occurs because the gas overpressure cannot escape from magma by permeable flow (Rust and Cashman, 2011), their pumices have variable connectivities (0.4-1.0) and a range of viscous permeabilities (10^{-14}-10^{-11} m^2; e.g., Klug et al., 2002; Nguyen et al., 2014; Rust and Cashman, 2004; Fig. 4.13a). The variable connectivities and permeabilities are explained by an incipient and increasing bubble growth and coalescence and variable total strain (Bouvet de Maisonneuve et al., 2009). Higher bubble coalescence and total strain result in higher permeabilities because of the increase of the connected porosity and the simplification of the flow pathways (lower tortuosities; Bouvet de Maisonneuve et al., 2009; Wright et al., 2006). In this way, the anisotropic tube pumices are usually the juvenile clasts derived from sustained explosive eruptions with the highest permeabilities (e.g., Wright et al., 2006; 2009). The *rdm* pumices have these textural and physical characteristics as they have elongate bubbles of wide pore apertures distributed nearly homogeneouly within the pumices (Fig. 4.7b; Fig. 4.9b) resulting in high permeabilities. The *rdm* pumice anisotropy and their high porosity and permeabilities are consistent with a high magma ascent together with a high total strain and strain rate due to a downward propagation of the fragmentation level (Chapter 2). Unless magma ascent is extremely fast, those high permeabilities would promote outgassing which could produce densification of magma at different scales (e.g., Colombier et al., 2017; Gonnermann et al., 2017). I suggest that the few low-porosity *rdm* pumices (e.g., *rdm* 2 T2) and the irregular cross-sectional shapes of some elongate bubbles (Fig. 4.7b) are evidences of

an incipient densification of magma. In this way, the *rdm* pumices studied could represent a late stage of lower intensity during the Plinian phase of the Laguna del Maule eruption.

The juvenile clasts formed during pulsatory subplinian eruptions have a range of porosities (0.2-0.7) but high magma permeabilities (10^{-12}-10^{-10} m^2; Mueller et al., 2011; Schipper et al., 2013). The high magma permeabilities may be explained by shearing during ascent, which enhances bubble coalescence forming elongate and tubular bubbles which facilitate the outgassing during ascent. The effective outgassing may lead to bubble collapse without a major drop in magma permeability due to the gas flowing through the elongate bubbles. The *rle* pumices have elongate bubbles with variable and non-uniform pore apertures heterogeneously distributed within pumices (Fig. 4.7c) which concentrates the gas flow through the widest and straightest bubbles (Fig. 4.9b). In the lowest porosity pumice samples, that flow localization is more evident (Fig. 4.9b). A protracted efficient outgassing should hinder the generation of bubble overpressure and so delay or prevent bubble overpressure-driven fragmentation. In this way, the enhanced degassing from shearing and fracturing during the subplinian eruptive phases is a mechanism that facilitates the transition to an effusive phase (Schipper et al., 2013). The similarities of Los Espejos pumices with those from the Cordón Caulle 2011 eruption (Schipper et al., 2013) suggest that the increasing outgassing together with the decreasing magma ascent rate promoted the explosive-effusive transition. At the end, brittle fracturing may maintain effective outgassing during the effusive stage as it is revealed by the tuffsitic texture within the Los Espejos obsidian lava (e.g., Chaitén, 2008 in Castro et al., 2014).

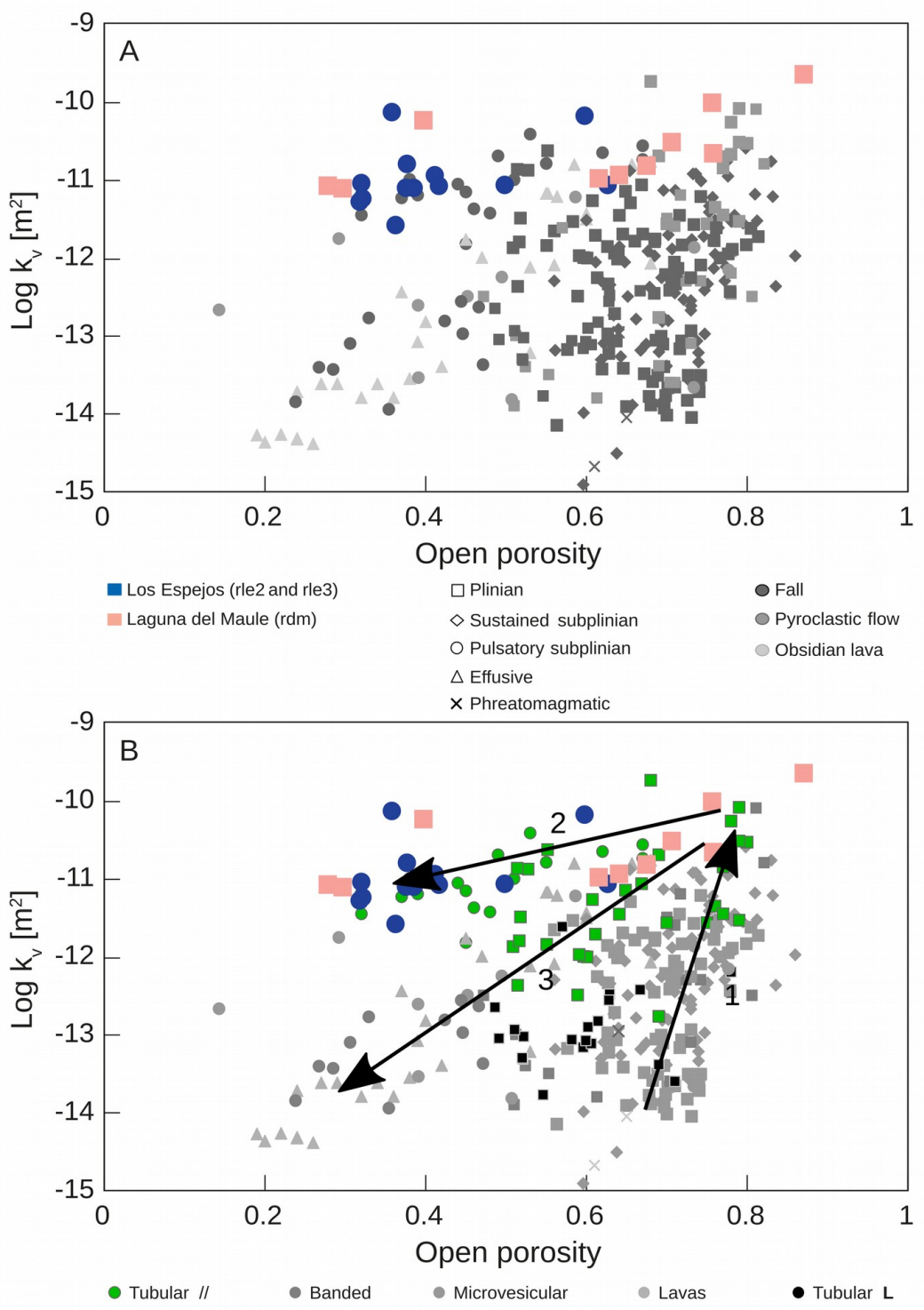

Fig. 4.13: Compilation of the viscous permeability data with open porosity from previous works. A Data of *rle* pumices match with data from pumices of pulsatory subplinian eruptions, while the data of *rdm* match with the highest viscous permeabilities of tube pumices from plinian eruptions. Data were obtained from Bouvet de Maisonneuve et al. (2009; fall deposits from Plinian and pulsatory subplinian eruptions), Gonnermann et al. (2017; covering the different classes of volcanic deposits and eruption styles), Nakamura et al. (2008; pyroclastic flow from Plinian eruptions), Rust and Cashman (2004; fall deposits and obsidian lavas from sustained subplinian and effusive eruptions), Schipper et al. (2013; fall deposits from pulsatory subplinian eruptions), Wright et al. (2006; fall and pyroclastic flow deposits from Plinian eruptions). **B** The three porosity-permeability trends. For details, see the main text.

In the following section I compare the porosities and permeabilities of the *rdm* and *rle* samples with those from other silicic explosive eruptions. I suggest relationships of the eruption styles and transitions with the physical parameters according to the main trends of porosity and permeability. Within those trends and consistent with the textures observed in the *rdm* and *rle* samples, a control of the juvenile anisotropy is proposed to explain the highest permeabilities.

4.5.5. A comparison with other silicic explosive eruptions

In Figure 4.13b I compare the open porosities and the viscous permeabilities of *rdm* and *rle* samples measured in the laboratory with rhyolitic juveniles (pumices and obsidians) from other volcanoes (Supplementary Material). The pumice clasts from sustained explosive eruptions show a wide range of viscous permeabilities (10^{-14} – 10^{-10} m^2). The pumice clasts from fall deposits usually have narrow ranges of permeability (1 to 2 orders of magnitude); the samples from Plinian eruptions tend to have lower permeability averages (e.g., Taupo 10^{-14} – 10^{-13} m^2 in Gonnermann and Manga, 2017; Mazama 10^{-14} – 10^{-12} m^2 in Klug et al., 2002) than those from smaller explosive eruptions (e.g., Little Glass Mountain 10^{-13} – 10^{-11} m^2 in Rust and Cashman, 2004). The lower permeabilities of pumices from the biggest eruptions are consistent with the expected low outgassing during sustained explosive eruptions (Cassidy et al., 2018). In contrast, the pumice clasts from pyroclastic flows tend to have wider ranges and higher average permeabilities (e.g., Wright et al., 2009). The juveniles of the highest permeabilities are usually anisotropic with tubular bubbles which facilitated magma outgassing (Wright et al., 2006). Juveniles from pulsatory subplinian phases tend to have higher permeabilities (>10^{-12} m^2) despite their variable porosity due to their high anisotropy (e.g., Bouvet de Maisonneuve et al., 2009; Schipper et al., 2013). Obsidians and isotropic clasts with microvesicularity show a wide range of permeability (10^{-15} – 10^{-11} m^2) which increases with porosity (e.g., Bouvet de Maisonneuve et al., 2009; Rust and Cashman, 2004).

In summary, three trends of porosity-permeability are suggested (Fig. 4.13b): 1. Pumices of high porosity and variable permeability coming from sustained explosive eruptions. In this trend, the pumices from the largest eruptions tend to have higher porosities and lower permeabilities; the pumices from pyroclastic flows usually have wider ranges of permeability which varies according to the anisotropy of the juvenile clasts. 2. Pumices of variable porosity and high permeability coming from pulsatory subplinian eruptions. In this trend, the pumices show high anisotropies regardless of the porosity. 3. Pumice and obsidian clasts of decreasing permeability with a decreasing porosity coming from pulsatory eruptions, lava flows and domes. This trend represents the compaction and total collapse of bubbles.

The wide range of viscous permeabilities of the first (sustained explosive) trend is explained by an incipient expansion of the silicic foam resulting in a range of connectivities, sample fabric, and bubble shapes (Gonnermann et al., 2017). The *rdm* pumices follow this trend and have higher viscous permeability than most of the silicic pumices from other volcanic complexes (e.g., Bouvet de Maisonneuve et al., 2009; Klug et al; 2002; Rust and Cashman, 2004). Their permeabilities match only the most permeable tube pumices measured parallel to the longest axis of the bubbles (e.g., Bouvet de Maisonneuve et al., 2009; Wright et al., 2006; 2009) and with some pumices from pyroclastic flows (e.g., Nakamura et al., 2008). In this way, the *rdm* pumices are similar to the most anisotropic juveniles which were formed in a region with high shear within the volcanic conduit (e.g., Dingwell et al., 2016) and/or during a less intense phase of the explosive eruption (e.g., Pistolesi et al., 2015). In particular, the total porosity and the viscous permeability of the frothy *rdm* pumice is greater than the typical range in silicic pumices, but matches with those from foams generated by metal, alumina, ceramic, and silicon carbide (Zhou et al., 2019 and references therein).

In the case of the pumices from deposits formed during pulsatory subplinian eruptions, the limited range of viscous permeabilities is explained by the compaction of the silicic foam resulting in the closure of some gas pathways but keeping the shape of the widest and least-tortuous bubbles (Gonnermann et al., 2017; Wright et al., 2009). In addition to pathways remaining open during magma compaction, strain localizations and melt fracturing can aid efficient outgassing at relatively low porosities (Okumura et al., 2009; Wright and Weinberg, 2009). The *rle* pumice permeabilities overlap with the trend from pumices of subplinian eruptions (trend 2 in Fig. 4.13; e.g., Bouvet de Maisonneuve et al., 2009; Schipper et al., 2013). Some of those subplinian eruptions also preluded the formation of lava flows suggesting that the studied pumices were formed during an effective outgassing and an increasing densification of magma during ascent (Chapter 2).

4.6. Final remarks on measurements, imaging and numerical simulations

The circular to elliptical bubbles observed in 2D images are crossed sections of various gas channels that may belong to one big complex-shape bubble. In simple words, most of the observed bubbles in 2D could be “branches of the same tree”. That complexity of the bubble framework may explain the high connectivity of most silicic pumices (this work; Colombier et al., 2017), but to analyse the bubble connectivity from 2D images is not possible. X-ray tomograms show that the high connectivity of the silicic pumices is explained by a structure of anastomosed gas channels that converge and diverge in several spots with each other. In this way, I recommend to re-evaluate the significance of the most typical 2D textural analysis. For instance, what the bubble number density represents, if they represent the density of pore apertures of a big complex bubble or if they are really linked to magma decompression rate (a model that assumes homogeneous bubble nucleation; Toramaru, 2006).

The segmentation and generation of 3D surfaces from tomograms allow to simulate numerically gas passing through the porous media of silicic pumices. The visualisation of the numerical simulations allows to locate the preferent pathways where the gas pass through and to calculate viscous permeability; thus, the permeabilities can be associated with the bubble textures within pumices. However, as the 3D imaging processing is time consuming, the gas flow simulations can be developed in just a few samples. Also, as both volume rendering of the surfaces and the numerical simulations are computationally expensive, the simulations can be only run in small volume of interests (VOIs), taking the risk that the selected VOI be not representative of the whole sample. The simulation of inertial permeabilities must consider a more complex flow (e.g., a high Reynolds number, a variable dynamic viscosity, compressible phases) becoming the simulation even less feasible.

Instead, the use of the permeameter allows the calculation of both viscous and inertial permeabilities in several samples (e.g., Gonnermann et al., 2017; Rust and Cashman, 2004). That robust dataset allows to compare both total and open porosities with both calculated permeabilities to constrain a history of the bubble formation (or collapse), and the efficiency of outgassing during the eruption (e.g., Rust and Cashman, 2004). Trends or clusters in the porosity-permeability diagram also allow the classification of eruption styles by comparison with data from other eruptions (e.g., Wright et al., 2006). However, the measurements do not allow by itself analysing the textural factors governing the permeabilities. In this way, I suggest that measurements, 3D imaging techniques and numerical simulations are complementary approaches to calculate magma permeabilities and to determine the governing factors of magma degassing during ascent.

4.7. Conclusion

The evolution of magma permeability controls the efficiency of outgassing and the styles and transitions of silicic eruptions. The pumices of the rhyolites of Laguna del Maule and Los Espejos reveal this dependence: one group of *rdm* pumices have high porosities and permeabilities due to a high connectivity and homogeneous degassing through wide pore apertures; and another group, comprised of a few *rdm* pumices, and all the *rle* pumices have low porosities, high viscous permeability and low inertial permeability due to the higher tortuosities, non-uniform shape and width of the gas channels, and the complex (non-circular) cross-sectional shapes of the bubble tubes. I propose that the first group represent a late stage of decreasing intensity of the *rdm* Plinian eruption, marked by a high magma strain which promoted an increase of the pore connectivity and a more efficient outgassing. In the case of *rle* pumices, the high and decreasing permeabilities with decreasing porosity represent a more effective outgassing during the eruption based on the features of bubble collapse and strain localization. In these pumices, the degassing was concentrated in the most uniform and widest bubble tubes. The degassing localization in some elongate bubbles allows the magma permeability to remain high with the porosity decreases because the collapse of the other bubbles only slightly affects gas flow through the magma. Once the bubble tubes that are the dominant gas flow pathways begin to collapse, the magma densification is more efficient, and the eruption can transition to an effusive stage.

4.8. Highlights

- Laboratory measurements of flow through cores, X-ray tomography imaging and numerical simulations of flow through pore spaces are complementary techniques to determine magma permeability and the bubble textures that govern permeability in silicic pumices.

- The styles and transitions of silicic eruptions are intrinsically related to the history of magma permeability.
- The high-explosive *rdm* eruption formed pumices of high porosity and moderate-to-high permeability, whereas the subplinian *rle* eruption formed juvenile clasts of a range of porosity but high permeabilities.
- The moderate permeability of the *rdm* pumices is consistent with an exsolved gas ascending with the silicic melt, promoting expansion and buoyancy of the rhyolitic magma and a high eruption intensity.
- The high permeability of the *rle* pumices is consistent with efficient outgassing and a decreasing eruption intensity that eased the transition to a lava flow.
- X-ray tomography images show that the moderate-to-high permeabilities in both *rdm* and *rle* upper-sequence pumices are related to their high anisotropy. Such high anisotropy suggests that the total strain was key to understanding a decreasing intensity during the last phase of both rhyolite eruptions.
- X-ray tomography images and permeability simulations show that a few elongate tube bubbles in the *rle* pumices explain the high permeability despite of the low porosity. These elongate tube bubbles have the widest pore apertures and show gas pathways with the lowest tortuosities within the pumice clasts.

Acknowledgments

This work was supported by Becas Chile PhD scholarship [grant number 72160339 CC]. Thanks go to Marcelo Cortés for the use of the He-pycnometer in SERNAGEOMIN; to Chris Pangalos and Charles Clapham for the design and fruitful conversations about the permeability measurements; and to Tom Davies for his helpful assistance in the use of the X-ray tomography and the softwares for imaging processing.

References

Alfano, F., Bonadonna, C., Gurioli, L., 2012. Insights into eruption dynamics from textural analysis: the case of the May, 2008, Chaiten eruption. Bulletin of Volcanology 74, 2095-2108.

Andersen, N.L., Singer, B.S., Jicha, B.R., Beard, B.L., Johnson, C.M., Licciardi, J.M., 2017. Pleistocene to Holocene growth of a large upper crustal rhyolitic magma reservoir beneath the active Laguna del Maule volcanic field, central Chile. Journal of Petrology, 58, 85–114.

Baker, D. R., Mancini, L., Polacci, M., Higgins, M. D., Gualda, G. A. R., Hill, R. J., Rivers, M. L., 2012. An introduction to the application of X-ray microtomography to the three-dimensional study of igneous rocks. Lithos, 148, 262-276.

Bouvet de Maisonneuve, C., Bachmann, O., Burgisser, A., 2009. Characterization of juvenile pyroclasts from the Kos Plateau Tuff (Aegean Arc): insights into the eruptive dynamics of a large rhyolitic eruption. Bulletin of volcanology, 71(6), 643.

Burgisser, A., Chevalier, L., Gardner, J. E., Castro, J. M., 2017. The percolation threshold and permeability evolution of ascending magmas. Earth and Planetary Science Letters, 470, 37-47.

Cassidy, M., Manga, M., Cashman, K., Bachmann, O., 2018. Controls on explosive-effusive volcanic eruption styles. Nature communications, 9(1), 2839.

Castro, J. M., Bindeman, I. N., Tuffen, H., Schipper, C. I., 2014. Explosive origin of silicic lava: textural and δD–H2O evidence for pyroclastic degassing during rhyolite effusion. Earth and Planetary Science Letters, 405, 52-61.

Cnudde, V., Boone, M.N., 2013. High-resolution X-ray computed tomography in geosciences: A review of the current technology and applications. Earth-Science Reviews 123, 1-17.

Colombier, M., Wadsworth, F.B., Gurioli, L., Scheu, B., Kueppers, U., Di Muro, A., Dingwell, D.B., 2017. The evolution of pore connectivity in volcanic rocks. Earth and Planetary Science Letters 462, 99-109.

Darcy, H. Les Fontaines Publiques de la Ville de Dijon, Dalmont, Paris, 1856.

Degruyter, W., Bachmann, O., Burgisser, A., 2010a. Controls on magma permeability in the volcanic conduit during the climactic phase of the Kos Plateau Tuff eruption (Aegean Arc). Bulletin of Volcanology, 72(1), 63.

Degruyter, W., Burgisser, A., Bachmann, O., Malaspinas, O., 2010b. Synchrotron X-ray microtomography and lattice Boltzmann simulations of gas flow through volcanic pumices. Geosphere, 6(5), 470-481.

Dingwell, D. B., Lavallée, Y., Hess, K. U., Flaws, A., Marti, J., Nichols, A. R., Gilg, H. A., Schillinger, B., 2016. Eruptive shearing of tube pumice: Pure and simple. Solid Earth Discussions, 7(4).

Eichelberger, J. C., Carrigan, C. R., Westrich, H. R., Price, R. H., 1986. Non-explosive silicic volcanism. Nature, 323(6089), 598.

Fierstein, J., Postglacial eruptive history established by mapping and tephra stratigraphy provides perspectives on magmatic system beneath Laguna del Maule, Chile, Presented at: AGU Chapman Conference on Merging Geophysical, Petrochronologic, and Modeling Perspectives of Large Silicic Magma Systems, Quinamavida, Chile, 2018.

Fluegel, A., 2007. Global model for calculating room-temperature glass density from the composition. Journal of the American Ceramic Society, 90(8), 2622-2625.

Forchheimer, P., 1901. Wasserbewegung durch boden. Z. Ver. Deutsch, Ing., 45, 1782-1788.

Gonnermann, H. M., Giachetti, T., Fliedner, C., Nguyen, C. T., Houghton, B. F., Crozier, J. A., Carey, R. J., 2017. Permeability during magma expansion and compaction. Journal of Geophysical Research: Solid Earth, 122(12), 9825-9848.

Gonnermann, H. M., Manga, M., 2007. The fluid mechanics inside a volcano. Annual Reviews of Fluid Mechanics, 39, 321-356.

Gualda, G. A., Rivers, M., 2006. Quantitative 3D petrography using X-ray tomography: Application to Bishop Tuff pumice clasts. Journal of Volcanology and Geothermal Research, 154(1-2), 48-62.
Ketcham, R. A., Carlson, W. D., 2001. Acquisition, optimization and interpretation of X-ray computed tomographic imagery: applications to the geosciences. Computers & Geosciences, 27(4), 381-400.
Klug, C., Cashman, K. V., 1996. Permeability development in vesiculating magmas: implications for fragmentation. Bulletin of Volcanology, 58(2-3), 87-100.
Klug, C., Cashman, K., Bacon, C., 2002. Structure and physical characteristics of pumice from the climactic eruption of Mount Mazama (Crater Lake), Oregon. Bulletin of Volcanology 64, 486–501. http://dx.doi.org/10.1007/s00445-002-0230-5.
Li, Q., Luo, K. H., Kang, Q. J., He, Y. L., Chen, Q., Liu, Q., 2016. Lattice Boltzmann methods for multiphase flow and phase-change heat transfer. Progress in Energy and Combustion Science, 52, 62-105.
Lindoo, A., Larsen, J. F., Cashman, K. V., Dunn, A. L., Neill, O. K., 2016. An experimental study of permeability development as a function of crystal-free melt viscosity. Earth and Planetary Science Letters, 435, 45-54.
Melnik, O., Sparks, R. S. J., 2002. Dynamics of magma ascent and lava extrusion at Soufrière Hills Volcano, Montserrat. Geological Society, London, Memoirs, 21(1), 153-171.
Mohamad, A. A., 2011. Lattice Boltzmann Method (Vol. 70). London: Springer.
Mueller, S., Scheu, B., Kueppers, U., Spieler, O., Richard, D., Dingwell, D. B., 2011. The porosity of pyroclasts as an indicator of volcanic explosivity. Journal of Volcanology and Geothermal Research, 203(3-4), 168-174.
Mueller, S., Scheu, B., Spieler, O., Dingwell, D. B., 2008. Permeability control on magma fragmentation. Geology, 36(5), 399-402.
Nakamura, M., Otaki, K., Takeuchi, S., 2008. Permeability and pore-connectivity variation of pumices from a single pyroclastic flow eruption: implications for partial fragmentation. Journal of Volcanology and Geothermal Research, 176, 302–314. http://dx.doi.org/10.1016/j.jvolgeores.2008.04.011.
Nguyen, C. T., Gonnermann, H. M., Houghton, B. F., 2014. Explosive to effusive transition during the largest volcanic eruption of the 20th century (Novarupta 1912, Alaska). Geology, 42(8), 703-706.
Okumura, S., Nakamura, M., Takeuchi, S., Tsuchiyama, A., Nakano, T., Uesugi, K., 2009. Magma deformation may induce non-explosive volcanism via degassing through bubble networks. Earth and Planetary Science Letters, 281(3-4), 267-274.
Pistolesi, M., Cioni, R., Bonadonna, C., Elissondo, M., Baumann, V., Bertagnini, A., Chiari, L., Gonzales, R., Rosi, M., Francalanci, L., 2015. Complex dynamics of small-moderate volcanic events: the example of the 2011 rhyolitic Cordón Caulle eruption, Chile. Bulletin of Volcanology, 77(1), 3.
Reynolds, O. Papers on Mechanical and Physical Subjects, Cambridge University Press, 1900.
Rust, A.C., Cashman, K.V., 2004. Permeability of vesicular silicic magma: inertial and hysteresis effects. Earth and Planetary Science Letters, 228, 93-107.
Rust, A. C., Cashman, K. V., 2011. Permeability controls on expansion and size distributions of pyroclasts. Journal of Geophysical Research: Solid Earth, 116(B11).
Saar, M. O., Manga, M., 1999. Permeability-porosity relationship in vesicular basalts. Geophysical Research Letters, 26(1), 111-114.
Safari, H., Rahimian, M. H., Krafczyk, M., 2013. Extended lattice Boltzmann method for numerical simulation of thermal phase change in two-phase fluid flow. Physical Review E, 88(1), 013304.

Schipper, C. I., Castro, J. M., Tuffen, H., James, M. R., How, P., 2013. Shallow vent architecture during hybrid explosive–effusive activity at Cordón Caulle (Chile, 2011–12): evidence from direct observations and pyroclast textures. Journal of Volcanology and Geothermal Research, 262, 25-37.
Shea, T., Houghton, B.F., Gurioli, L., Cashman, K.V., Hammer, J.E., Hobden, B.J., 2010. Textural studies of vesicles in volcanic rocks: An integrated methodology. Journal of Volcanology and Geothermal Research 190, 271-289.
Singer, B., Hildreth, W., Vincze, Y., 2000. 40Ar/39Ar evidence for early deglaciation of the central Chilean Andes. Geophysical Research Letters, 27(11), 1663-1666.
Takeuchi, S., Nakashima, S., Tomiya, A., 2008. Permeability measurements of natural and experimental volcanic materials with a simple permeameter: toward an understanding of magmatic degassing processes. Journal of Volcanology and Geothermal Research, 177(2), 329-339.
Toramaru, A., 2006. BND (bubble number density) decompression rate meter for explosive volcanic eruptions. Journal of Volcanology and Geothermal Research 154, 303-316.
Wright, H. M., Cashman, K. V., Gottesfeld, E. H., Roberts, J. J., 2009. Pore structure of volcanic clasts: measurements of permeability and electrical conductivity. Earth and Planetary Science Letters, 280(1-4), 93-104.
Wright, H. M., Roberts, J. J., Cashman, K. V,. 2006. Permeability of anisotropic tube pumice: Model calculations and measurements. Geophysical research letters, 33(17).
Wright, H.M.N., Weinberg, R.F., 2009. Strain localization in vesicular magma: Implications for rheology and fragmentation. Geology 37, 1023-1026.
Zhou, J. Q., Chen, Y. F., Wang, L., Cardenas, M. B., 2019. Universal Relationship Between Viscous and Inertial Permeability of Geologic Porous Media. Geophysical Research Letters, 46(3), 1441-1448.

5. The influence of magma storage and ascent conditions on variations in the styles and transitions of Laguna del Maule rhyolite eruptions

Abstract

For the last 25 ky, the Laguna del Maule volcanic complex (LdM) has erupted a wide and continuous range of bulk compositions, with predominance of rhyolites. The rhyolitic eruptions show a variety of styles and transitions despite of coming from a common silicic mush-type reservoir. Chapters 2 and 4 showed that the eruption histories in LdM were controlled by the fragmentation level, the efficiency of outgassing, and the magma ascent rate, but the role of the storage and ascent conditions is still unclear. Here I analyze the petrography and the storage and ascent conditions of the two first and the youngest rhyolites: Laguna del Maule (*rdm*), Los Espejos (*rle*) and Las Nieblas (*rln*). *rdm* is almost aphyric and is the only rhyolite with An_{40-60} plagioclase antecrysts, hornblende as the main mafic mineral, and mafic enclaves. *rle* and *rln* are crystal-poor and have plagioclase and biotite phenocrysts, but *rle* shows anhedral biotite phenocrysts and k-feldspar microcrysts while *rln* has euhedral biotite phenocrysts and only plagioclase microlites in the groundmass. Petrologic constraints indicate that the three studied rhyolites come from different sectors and stages of the silicic reservoir. *rdm* was formed in a deep (2.2-2.5 kbar) and hot (830-870 °C) magma pocket at the bottom of the crystal mush. Both *rle* and *rln* were formed in shallower magma pockets (1.7-2.3 and 1.5-2.0 kbar, respectively), although phase compositions suggest that the northwestern and older *rle* was fed by a homogeneous magma body, whilst the southern and younger *rln* erupted magma from a depth range. These subtle spatial variations in the silicic reservoir and the different P-T-H_2O paths during ascent were key to the diversity of eruptive styles and transitions in LdM. In particular, a >30 °C heating due to mafic and andesitic magma inputs become superliquidus

the silicic melt and triggered the *rdm* eruption. The superliquidus magma temperature and the low crystallinity allowed a fast ascent rate aided by the low magma viscosity. The *rle* eruption was triggered by external water into the magmatic system and the explosive-effusive transition may be explained by an effective water-loss and a ~30 °C cooling that produced the observed biotite breakdown and the syn-eruptive k-feldspar crystallization. The *rln* eruption was triggered by thermal mixing aided by a previous vertical grading of temperature and crystallization. The protracted and upward silicic melt accumulation within the crystal mush reservoir of LdM could have a surface expression in the current local inflation north of the *rln* lava flow. The current storage conditions are likely similar to those before the *rln* eruption; thus there is potential for a new rhyolitic subplinian eruption followed by an effusive stage.

Keywords

Laguna del Maule volcanic complex; Transcrustal magmatic systems; magma storage conditions; high-silica magmas; numerical thermodynamics; geothermobarometry methods; plagioclase composition.

5.1. Introduction

Laguna del Maule volcanic complex (LdM) is an intra-arc caldera-forming volcanic system straddling the Chile-Argentina border in the Transitional Southern Volcanic Zone (TSVZ) of the Andes (Cembrano and Lara, 2009). The LdM is underlain by a 450 km^3 crystal-rich (average 95%) silicic reservoir located at ~5 km depth (Le Mevel et al., 2016; Wespestad et al., 2019), which could contain smaller (≤30 km^3), lower crystallinity (35-50% crystals; Cáceres et al., 2018; Miller et al., 2017) magma bodies and explain the observed high uplift rates of the last ten years (Feigl et al., 2014; Singer et al., 2014). For the last 25 ky (a postglacial stage), the rhyolitic magmas from the silicic reservoir have fed ~20 subplinian-to-plinian

eruptions followed by an effusive stage. The exception is the first postglacial eruption which started with a Plinian phase followed by an ignimbrite-forming explosive eruption: the rhyolite of Laguna del Maule event (*rdm*) is the biggest (>20 km^3; Fierstein, 2018) and most silicic (76.4-76.7 wt.% SiO_2; "rle-ig" in Hildreth et al., 2010) rhyolitic eruption of the postglacial stage. The first rhyolitic eruption after *rdm*, the rhyolite of Los Espejos (*rle*; 75.5-75.7 wt.% of SiO_2) occurred with a time gap of ≤4 ka (19 ka by $^{39}Ar/^{40}Ar$; Singer et al., 2000) or 1 ky (15 ka by ^{14}C; Fierstein, 2018). *rle* comprises a smaller (>1 km^3; Gho et al, in review) pyroclastic deposit followed by the third most voluminous (~0.82 km^3) postglacial rhyolitic coulee of LdM (Fig. 5.1). The similarity of the *rle* and *rdm* zircon compositions suggests that *rle* was produced by a remnant rhyolitic magma from *rdm* (Andersen et al., 2019). The rhyolite of Las Nieblas (*rln*, 73.0-73.7 wt.% of SiO_2) is the youngest eruption of LdM (1.8 ka BP by ^{14}C; Fierstein, 2018) which erupted ≥1.5 km^3 in a sequence of pyroclastic flows, a synchronous fall deposit and lava flow, and a second lava flow which is the most voluminous (1.16 km^3) of the postglacial stage (Fig. 5.1; Cáceres et al., 2018).

The physical features of the first LdM postglacial rhyolites show the control of the magmatic processes during eruption on the eruptive styles and transitions. For instance, the *rdm* deposits have mafic to intermediate vesicular enclaves and clasts suggesting that this large, intense and sustained eruption was triggered by hot mafic magma inputs, which decreased the main silicic magma viscosity and could have induced volatile exsolution at depth (Chapter 2). The *rdm* pumices have high vesicularities (low densities of 0.25-0.85 g cm^{-3}) and high pore connectivity fractions (>0.95; Section 4.4.2). The *rdm* pumices are almost aphyric and so the vesiculation was probably facilitated by near- or super-liquidus temperature. By contrast, the *rle* sequence begins with an interbedding of lithic-rich finer grained and pumice-rich coarser grained layers formed during a phreatomagmatic phase that was triggered by both external water into the magmatic system (Chapter 2) and cryptic intermediate magma inputs (Andersen et al., 2018).

The *rle* pumices have heterogeneous bubble textures with strain and degassing localizations which allowed effective outgassing (Chapter 4), despite of the low pumice vesicularities (densities of 0.7-1.7 g cm^{-3}; Section 2.5.3). The variations of bubble textures and magma permeabilities during the eruptions can be linked to the histories of the eruptions, but ultimately the evolution of the storage conditions during the postglacial rhyolitic eruptions of the Laguna del Maule volcanic complex likely played a key role in controlling how the magma erupted.

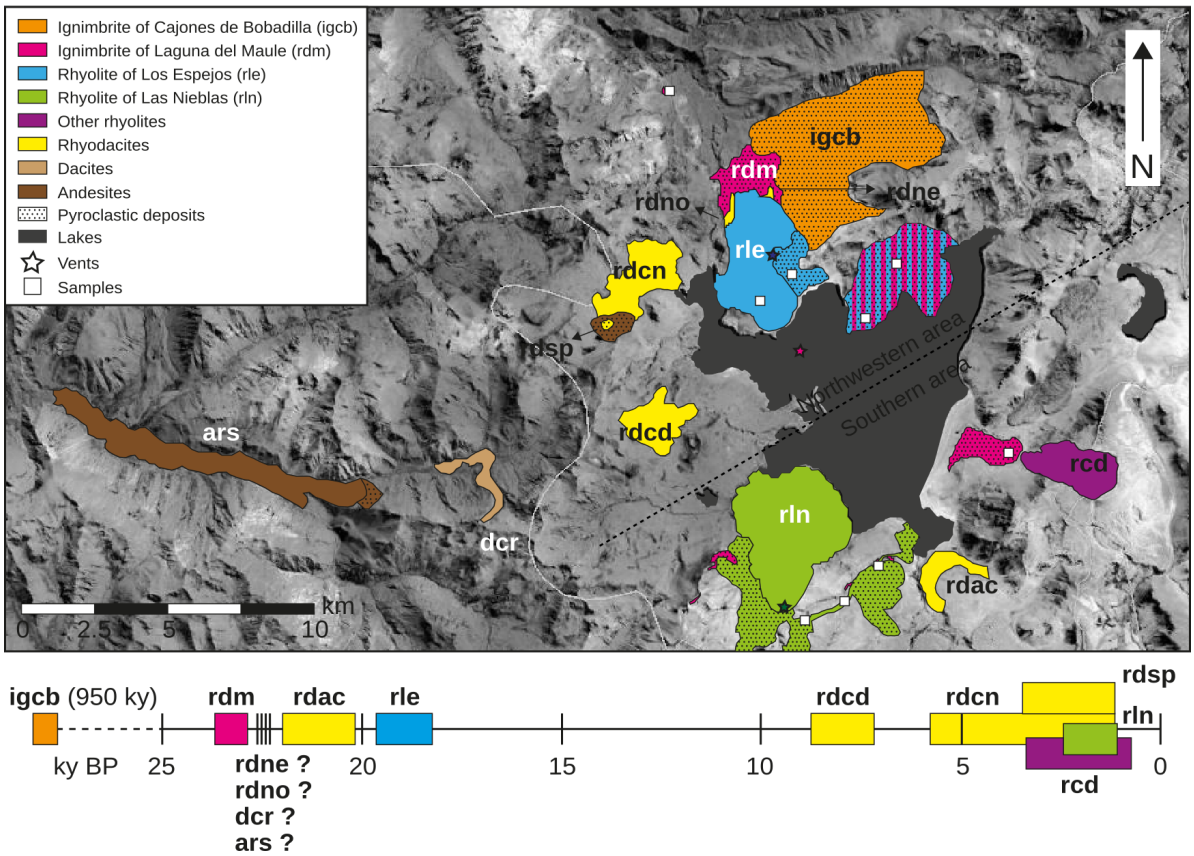

Fig. 5.1: Map of Laguna del Maule volcanic complex. Here we show the three rhyolites studied in this chapter and the units used for geothermobarometry and numerical simulations. Ages of eruptive units are taken from Hildreth et al. (2010) and Andersen et al. (2017). The dashed line separates the northwestern area from the southern area.

In this chapter, I use constraints from mineral compositions and textures to assess and model conditions of magma storage and ascent (i.e., P-T-H_2O paths) for the first two (Laguna del Maule and Los Espejos) and the youngest (rhyolite of Las Nieblas) postglacial eruptions of

LdM to determine the role of subtle variations in the rhyolite-forming reservoir on the styles and transitions of the rhyolitic eruptions.

5.2. Petrology of the Laguna del Maule volcanic complex

Except for the rhyolite of the Laguna del Maule eruption (*rdm*) which contains plagioclase and hornblende, the postglacial rhyolites of the Laguna del Maule volcanic complex (LdM) have a common mineral assemblage: four of the 11 rhyolite units are aphyric; the others have up to 3 vol.% phenocrysts of mostly plagioclase and biotite (Hildreth et al., 2010). Like in other silicic volcanic complexes (Gualda et al., 2012), a common mineral assemblage among several eruptive units suggests derivation from a single crystal mush reservoir (Andersen et al., 2017). Whole-rock geochemistry shows a continuous total alkali-silica trend from basaltic andesites to rhyolites which can be simulated numerically at shallow depths, intermediate water contents and a high oxygen fugacity (Andersen et al., 2017; Hildreth et al., 2010). A parent magma of dacitic composition (67-68 wt.% SiO_2) at 1.9-2.5 kbar best reproduces the petrology and water contents (calculated by plagioclase-whole-rock hygrometry) of the rhyolites (Andersen et al., 2018). Zircon geochronology analysis shows that rhyolite production started ~34-160 ky ago regardless of vent location and age of eruptive unit (Andersen et al., 2019). By contrast, Mg-diffusion geochronology in plagioclase records pre-eruption residence times of tens to hundreds of years (Andersen et al., 2018). The great difference between these timescales could be explained by a mush rejuvenation which affected the main minerals but not the zircons; however, the phenocrysts do not have reverse zoning. The most likely scenario to explain the zircon-plagioclase age difference is a long-term crystalline mush with a locally short-term rhyolitic interstitial melt (Andersen et al., 2019).

The rhyolite-forming mush reservoir shows lateral variations and has evolved in time (Andersen et al., 2017; Hildreth et al., 2010; Singer et al., 2000). The early postglacial rhyolites are the most silicic and were erupted in the northern area of the LdM complex. *rdm* rhyolites show evidence of magma mingling and crystal cargo (Andersen et al., 2018; Fierstein, 2018). In the other early postglacial rhyolites such as *rle*, the plagioclase crystals are less anorthitic and mostly unzoned, so the only evidence for magma replenishment and heating is localized high Ba concentration in plagioclase (Andersen et al., 2018). In the northern area, the dacitic reservoir allows the penetration of mafic magmas resulting in the eruption of aphyric basaltic andesites and andesites-to-dacites with mafic enclaves and strong disequilibrium textures in phenocrysts (Andersen et al., 2017; Cáceres et al., 2018; Hildreth et al., 2010). By contrast, the Holocene rhyolites are the most alkaline and were erupted in the southern area of the LdM complex (Hildreth et al., 2010). The phenocrysts in rhyolites such as *rln* show more complex zoning patterns and higher concentration of trace elements (e.g., Fe, Mg and Sr) for the same anorthite content than those from the early postglacial rhyolites (Andersen et al., 2018). In the southern area, basalts to dacites do not have been erupted and Fe-Ti oxide temperatures from both Holocene rhyodacites and rhyolites are higher than those from the silicic early postglacial products (Andersen et al., 2017).

The recent studies of the conditions of the rhyolite-forming reservoir below LdM (Andersen et al., 2018, 2019; Cáceres et al., 2018) indicate the spatial and temporal evolution of the mineral and whole-rock compositions in rhyolites. However, the particular conditions of silicic magma pockets within the reservoir and how those controlled the variations of the ascent paths during the rhyolitic eruptions are still unclear. Herein, I consider the origins of: 1) the hornblende phenocrysts and the glassy groundmass of *rdm* and how they related to the high explosivity of this eruption; 2) the different textures of the *rle* biotites and feldspar microcrysts and how they relate to the explosive-effusive transition of this eruption, and 3) the complex zoning of *rln*

plagioclases and how this relates to the lack of recent mafic-to-intermediate eruptions and the current volcanic unrest.

5.3. Methodology

5.3.1. Sampling and analytical methods

The *rdm* deposit was sampled from three areas (Fig. 5.1): (1) an outcrop of a pyroclastic flow on the side of the international Talca-Paso Pehuenche road located 5 km northwest of Los Espejos vent where reticulated and banded pumices were collected; (2) a beach on the north shore of the lake where a bulk sample of blue-and-grey lithic-bearing pyroclastic flow was collected; and (3) a fall deposit in front of Divisoria lava flow where a stratigraphic log was described and samples from several layers were collected. The *rle* fall deposit was accessed in two areas (Fig. 5.1): a perlite mine located 1-2 km from vent where several layers were sampled, and a valley located 3 km east of the vent where some samples were collected from the deposit base. Furthermore, samples with different textures were collected from the *rle* lava flow (Section 2.5.4.5). The *rln* pyroclastic flow was sampled from four approximately equidistant points across the deposit (Fig. 5.1).

Fourteen samples were analyzed petrographically: three pumices from the *rdm* deposits, three pumices and three pyroclastic obsidians from the *rle* fall deposit, two pieces of obsidians from the *rle* lava, and three pumices from the *rln* pyroclastic flow. Backscatter electron (BSE) images were collected by scanning electron microscopy (Hitachi S3500) at the University of Bristol by applying an accelerating potential of ~15 kV and electron beam current of 50-60 nA. Compositional analyses of minerals and glasses were performed on the Cameca SX100 electron microprobe at University of Bristol by applying an accelerating potential of 20 keV. Spot analysis in biotite, hornblende and glass were measured for compositional

characterization and the application of numerical thermodynamics methods. Spot analysis and 15-30 μm-spacing compositional traverses were analyzed for major and minor elements in plagioclase and K-feldspar for compositional characterization and the application of the Waters and Lange (2015) hygrometer. For detailed information on electron beam size and current, counting times in peaks and background, detection limits and errors associated of the electron microprobe analyses, see the Supplementary Material.

5.3.2. Thermobarometry

Pressure, temperature, oxygen fugacity and water content in samples of *rdm* were estimated from hornblende by the multiparameter calculator of Ridolfi et al. (2010). The hornblende-plagioclase thermometer of Holland and Blundy (thermometer B, 1994) was applied to 3 hornblende-plagioclase pairs of *rdm* samples. I did not apply the hornblende-glass method of Putirka (2016) because hornblende are antecrysts in dacites to rhyolites of LdM (Cáceres et al., 2018). Hornblende compositions for the application of geothermarometry methods are in Supplementary Material.

The Ti in biotite-glass geothermometer and the Ba in biotite-glass geobarometer of Righter and Carmichael (1996) were applied to biotite rims of the *rle* eruptive products (pumices, pyroclastic obsidians and lavas) and the *rln* pumices. The difference in the calculated biotite-glass temperatures between both rhyolites is consistent with Fe-Ti oxide temperatures (see below); however, they are too hot to explain anorthite content in plagioclase and water content (see below). Even more problematic is that >60% of the pressures calculated with the biotite-glass geobarometer are negative. Consequently, I do not consider the calculated thermodynamic conditions by biotite-glass methods. The fundamentals about failures in the application of both biotite-glass methods, the biotite and glass compositional data, calculated temperatures and pressures, and errors associated are shown in Supplementary Material.

The plagioclase-glass hygrometer of Waters and Lange (2015) was applied to plagioclase rims of the *rle* and *rln* samples by applying the Fe-Ti oxide temperatures of Andersen et al. (2017). Based on the calculated range of water contents and Fe-Ti oxide temperatures, water saturation pressures were estimated using the methods of Newman and Lowenstern (2002) and Ghiorso and Gualda (2015). Results from both calculators differ only by up to ~0.2 kbar. Plagioclase and glass compositions for the application of the hygrometer and the water pressure saturation methods are in Supplementary Material.

5.4. Petrography

The three studied eruptive units are almost aphyric to crystal-poor glomeroporphyritic rhyolites with glassy to trachytic groundmass. The *rdm* pumices studied are highly vesiculated (densities of 200-800 kg m^{-3}) and almost aphyric (Fig. 5.2a). Fall deposit pumices have ≤1% phenocrysts of plagioclase, hornblende, Ti-magnetite, ilmenite, olivine, clinopyroxene, apatite and zircons in order of decreasing abundance (Table 5.1) and no microcrysts in the groundmass (Fig. 5.3a). Plagioclase are up to 0.3 mm-long and anhedral to subhedral; they are either isolated or form mono- or polymineralogic clots with hornblende (Fig. 5.2b). Hornblende are 0.1-0.3 mm-long, elongate and euhedral (Fig. 5.2c). Olivines appear within mafic blobs forming crystal clots with plagioclase and hornblende (Fig. 5.2d).

The *rle* pumices are denser (average density ~970 kg m^{-3}) than the *rdm* pumices and have 1-2% phenocrysts and 5-10% microcrysts in groundmass. The *rle* pyroclastic obsidians and lavas are slightly more crystalline than the pumices (~3% phenocrysts and ~10% microcrysts in groundmass). In both pumices and obsidians (pyroclasts and lava), phenocrysts consist of plagioclase, biotite, Ti-magnetite, ilmenite, apatite and zircons in order of decreasing abundance (Table 5.1). Plagioclase crystals are ≤1.8 mm-long and sub-euhedral to euhedral;

they occur isolated or forming clots among plagioclases (Fig. 5.2e) with or without other minerals. The crystal clots have regrowth rims around the entire clot, and not each individual crystal, and are associated with both albitic plagioclase and K-feldspar (Fig. 5.2f). Biotite crystals are 0.1-0.8 mm-long and slightly elongate, with textures that vary according to rock type: they are anhedral-to-subhedral with rounded rims in pumices (Fig. 5.2g), mostly euhedral in obsidian lava samples and can be isolated (Fig. 5.2h) or forming clots with plagioclase crystals (Fig. 5.2i). Pumice groundmass contains microlites of plagioclase and k-feldspars with skeletal textures (Fig. 5.3b), and obsidian groundmass of pyroclasts and lava have elongated plagioclase, biotite and oxide microcrysts arranged in bands together with microvesicles (Fig. 5.2i, 5.3c, 5.3d).

The *rln* pumices are less dense than the *rle* pumices (average density of ~800 kg m^3) and have 6-13% phenocrysts and glassy groundmass. The *rle* pyroclastic obsidians and lavas are more crystalline than the pumices (~12-25% phenocrysts and ~2% microcrysts in groundmass; Cáceres et al., 2018). In both pumices and obsidians (pyroclasts and lava) the phenocrysts are plagioclase, biotite, Ti-magnetite, ilmenite, apatite and zircons in order of decreasing abundance (Table 5.1). Plagioclase are up to 3.0 mm-long, equant to slightly elongate, and sub-euhedral with rounded rims (Fig. 5.2j). Plagioclases are surrounded by glass 10-50 μm thick (Fig. 5.2k). Crystal clots have regrowth rims of more albitic plagioclase around the entire clot. Biotite crystals are 0.1-3.5 mm-long, more elongate than those of *rle* and mostly euhedral with regular rims (Fig. 5.2l). Pumice groundmass is aphyric (Fig. 5.3e), and the obsidian groundmass of clasts and lavas have elongate microlites of plagioclase (Fig. 5.3f).

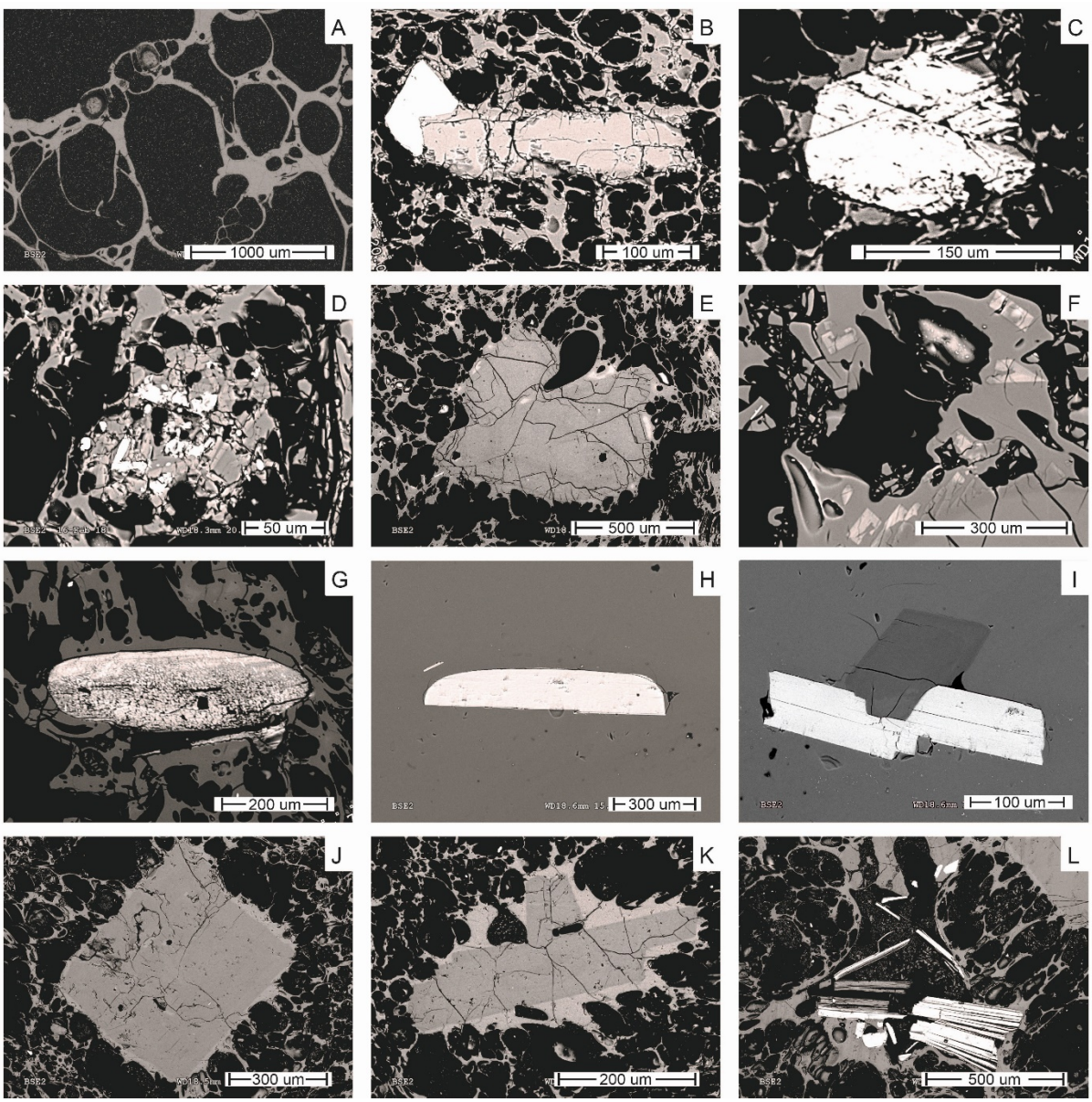

Fig. 5.2: BSE images of the studied rhyolites in the LdM volcanic complex. A A *rdm* pumice from a pyroclastic flow. **B-D** *rdm* pumices from the fall deposit. **B** Clot of plagioclase and hornblende. **C** Hornblende antecryst. **D** Mafic blob with elongate plagioclases, olivine and hornblende. **E-G** Pumices from the *rle* fall deposit. **E** Plagioclase clot. **F** Plagioclase outer rim of k-feldspar. There are skeletal microcrysts of k-feldspar in groundmass. **G** Anhedral biotite. **H-I** Obsidians from the *rle* lava flow. **H** Subhedral biotite. **I** Crystal clot of plagioclase and biotite. **J-L** Pumices from the *rln* pyroclastic flow. **J** Plagioclase phenocrysts. **K** Plagioclase clot. **L** Biotites.

Table 5.1: Crystal size, shape and occurrence of clusters and microcrysts for *rdm*, *rle* and *rln*

Rhyolite of Laguna del Maule (*rdm*)				
Phase	Maximum size [mm]	Shape	Clots	Microcrysts
Plagioclase	0.3	Anhedral to subhedral	Plagioclase and hornblende	No
Hornblende	0.3	Euhedral	Plagioclase	No
Ti-Magnetite	0.1	Subhedral	Oxides	--
Ilmenite	0.1	Subhedral	Oxides	--
Olivine	0.2	Anhedral	In mafic blobs	No
Clinopyroxene	0.2	Anhedral	In mafic blobs	No
Apatite	0.1	Euhedral	Plagioclase	--
Zircon	0.1	Subhedral	No	--
Rhyolite of Los Espejos (*rle*)				
Phase	Maximum size [mm]	Shape	Clots	Microcrysts
Plagioclase	1.8	Subhedral to euhedral	All the other phases	In pumices and obsidians
Biotite	0.8	Anhedral (pumices) or Euhedral (obsidians)	Plagioclase	In obsidians
Ti-Magnetite	0.1	Subhedral	Oxides	--
Ilmenite	0.1	Subhedral	Oxides	--
Apatite	0.1	Euhedral	Plagioclase	--
Zircon	0.1	Subhedral	No	--
K-feldspar	0.2	Skeletal	Plagioclase	In pumices
Rhyolite of Las Nieblas (*rln*)				
Phase	Maximum size [mm]	Shape	Clots	Microcrysts
Plagioclase	3.0	Subhedral	Plagioclase	In obsidians
Biotite	3.5	Euhedral	No	No
Ti-Magnetite	0.3	Subhedral	Plagioclase, biotite, oxides	--
Ilmenite	0.1	Anhedral	Oxides	--
Apatite	0.1	Euhedral	Plagioclase	--
Zircon	0.1	Subhedral	No	--

5.5. Geochemistry

New analyses of groundmass glasses (Table 5.2 and Supplementary Material) are plotted together with whole-rock geochemistry of major and trace element data from Hildreth et al. (2010) and Andersen et al. (2017) and groundmass glass analysis in rhyodacites from Cáceres et al. (Table 5.3; 2018). LdM products preserve an almost continuous whole-rock compositional range from 51 to 77 wt.% SiO_2 with two small compositional gaps at 62-64 and ~67 wt.% SiO_2 (Fig. 5.4a). All eruptive products lie just below the boundary of alkaline and subalkaline series (Fig. 5.4a) but show a range of K_2O at >62 wt.% SiO_2 (Fig. 5.4b). Rhyolites

of 72-73 wt.% SiO_2 have the highest alkali content (~9 wt.% $Na_2O + K_2O$), after which alkali content decreases slightly with increasing silica content (Fig. 5.4a). Both the *rdm* and the *rle* are the most silicic products of the postglacial stage, whilst the *rln* are among the most alkaline postglacial silicic eruptive products of LdM.

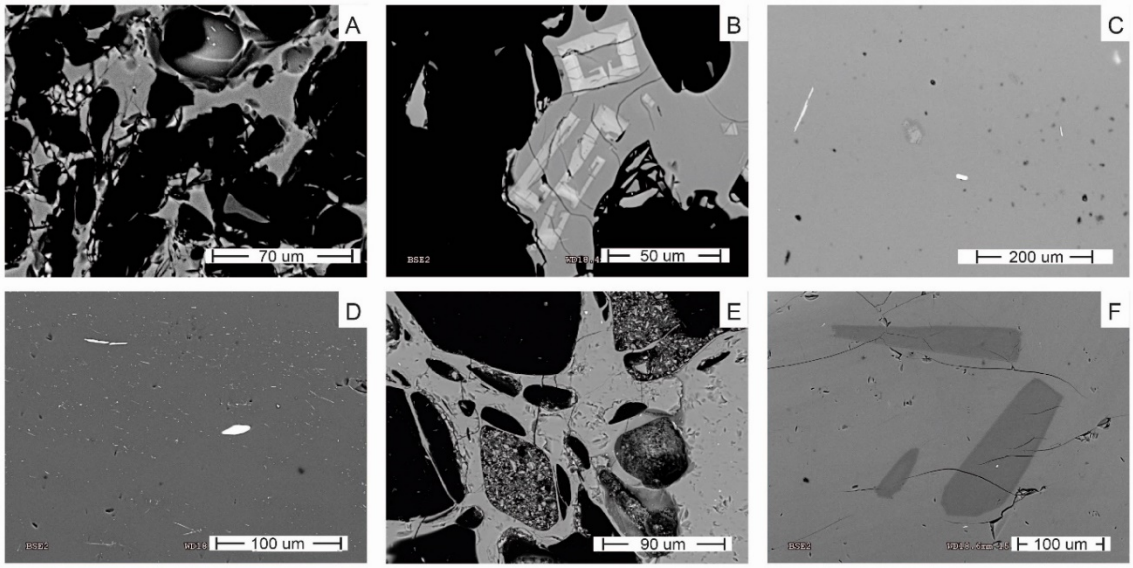

Fig. 5.3: BSE images representative of the groundmass of the studied rhyolites in the LdM. A Holohyaline groundmass of the *rdm* pumice clasts. **B-D** *rle* pyroclasts and lavas. **B** Skeletal k-feldspar microcrysts within the pumice groundmass. **C** Microcrysts of plagioclase, biotite and Fe-Ti oxides in an obsidian pyroclasts groundmass. **D** Oriented microcrysts of biotite and Fe-Ti oxides in the *rle* lava flow. **E-F** Pyroclast juveniles from the *rln* pyroclastic flow. **E** Holohyaline groundmass of the *rln* pumice clasts. **F** Elongate plagioclase microcrysts in the obsidian juvenile clasts.

The difference between groundmass glass compositions and their corresponding whole-rock geochemistry reflects the crystal content. The *rdm* and *rle* groundmass glasses are slightly more evolved (up to 1 wt.% higher SiO_2) than their corresponding whole-rock geochemistry; and the *rln* groundmass glasses have a wider range than the bulk composition (~2 wt.% SiO_2 of variance; Fig. 5.4a, b). The groundmass glass composition of Las Nieblas and rhyodacites are rhyolitic and overlap the whole-rock composition of Los Espejos; all glass compositions overlap with bulk samples from the volcanic complex. In detail, glass compositional trends vary among the three studied units. For example, the K_2O-SiO_2 correlation is negative for *rdm*, positive for *rle* samples, and relatively constant in *rln* samples (Fig. 5.4b). Compatible elements

Na_2O and FeO form negative trends with SiO_2. MgO shows a high dispersion due to its very low concentration (≤0.3 wt.%) and Al_2O_3 is relatively constant (Fig. 5.4c-f).

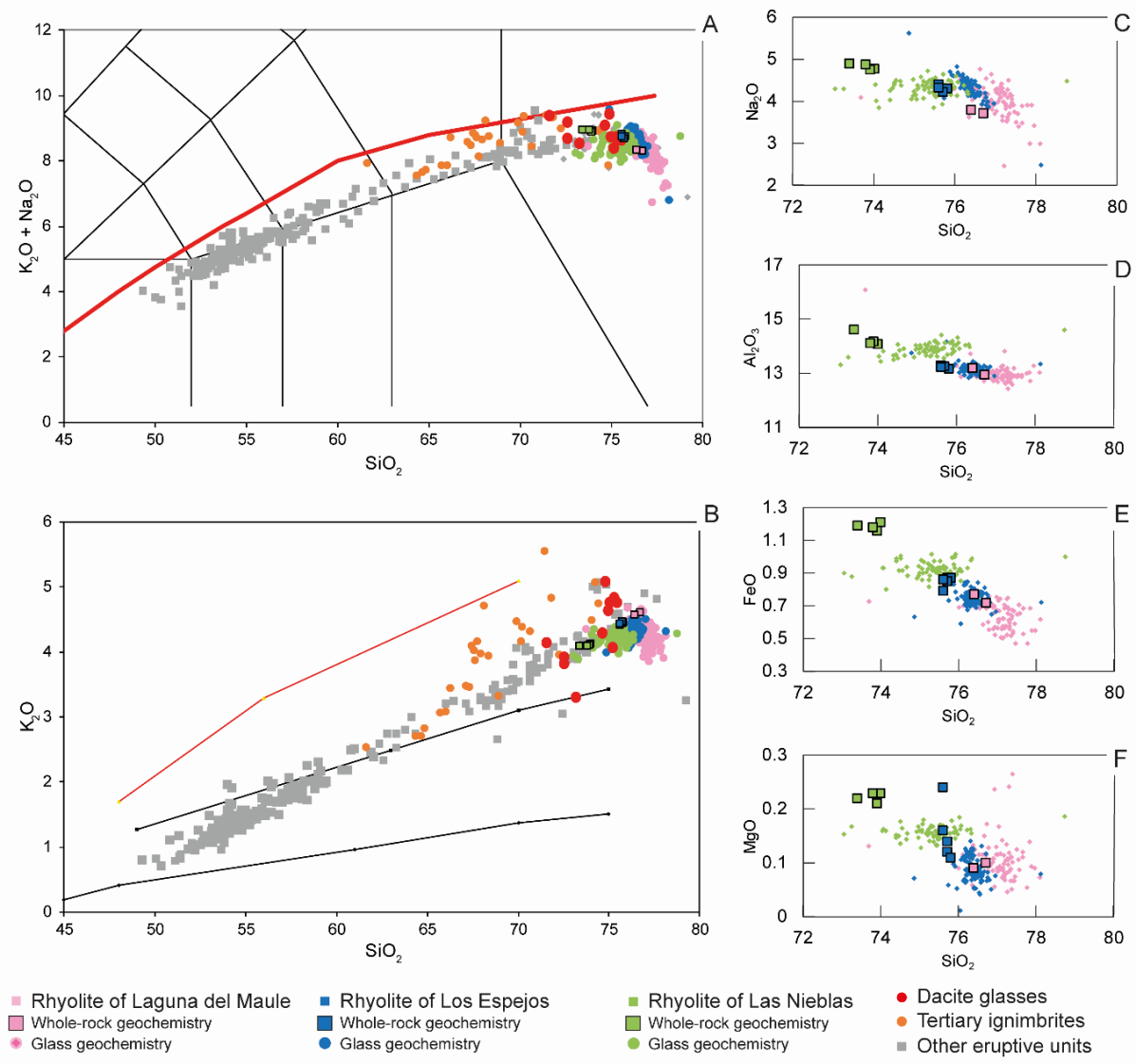

Fig. 5.4: Whole rock and glass geochemistry of the LdM volcanic complex. A Total alkali versus silica content diagram. **B** SiO_2 vs K_2O. **C-F** Harker diagrams of Na_2O, Al_2O_3, FeO and MgO with SiO_2. Whole rock geochemistry data from Andersen et al. (2017) and Hildreth et al. (2017); glass geochemistry data of dacites from Cáceres et al. (2018).

Table 5.2: Averages of groundmass glass compositions measured by EMPA[9] of pumices, pyroclastic obsidians and lavas from *rdm*, *rle* and *rln*. To reference, whole-rock major element composition is shown. WR = Whole-rock composition; PF P = Pyroclastic flow pumice; FD P = Fall deposit pumice; Pum. = Pumice; Obs. = Pyroclastic obsidian.

	rdm			*rle*							*rln*				
	WR	PF P	FD P	WR	Pum.	Pum.	Pum.	Obs.	Obs.	Lava	WR	Pum.	Pum.	Pum.	Pum.
SiO_2	76.7	77.22	76.91	75.7	76.42	76.28	76.21	76.33	76.43	76.42	73.4	74.99	75.36	75.34	75.31
TiO_2	0.15	0.11	0.13	0.18	0.14	0.15	0.15	0.15	0.14	0.15	0.26	0.19	0.20	0.19	0.19
Al_2O_3	12.93	12.90	13.08	13.23	13.21	13.28	13.31	13.21	13.20	13.14	14.6	13.95	13.94	13.91	13.79
FeO	0.72	0.57	0.70	0.87	0.74	0.76	0.73	0.78	0.75	0.76	1.19	0.92	0.94	0.93	0.91
MnO	0.05	0.04	0.04	0.07	0.07	0.06	0.06	0.06	0.06	0.07	0.08	0.07	0.07	0.07	0.07
MgO	0.1	0.10	0.11	0.12	0.08	0.10	0.10	0.10	0.09	0.10	0.22	0.16	0.16	0.15	0.16
Cr_2O_3		0.00	0.00		-0.01	0.00	0.00	0.00	0.00	0.00		-0.01	-0.01	-0.01	-0.01
CaO	0.58	0.54	0.64	0.64	0.59	0.60	0.59	0.60	0.58	0.59	0.80	0.59	0.61	0.61	0.63
Na_2O	3.71	4.16	3.80	4.27	4.23	4.26	4.45	4.26	4.29	4.40	4.89	4.21	4.33	4.42	4.27
K_2O	4.62	4.20	4.39	4.44	4.35	4.33	4.30	4.35	4.30	4.33	4.09	4.22	4.21	4.24	4.13
P_2O_5	0.07	0.02	0.03	0.05	0.02	0.01	0.02	0.01	0.01	0.02	0.05	0.02	0.03	0.03	0.04
SO_2		0.01	0.02		0.00	0.00	0.00	0.00	0.00	0.00		0.00	0.00	0.00	0.01
Cl		0.13	0.13		0.15	0.16	0.15	0.14	0.14	0.13		0.15	0.16	0.15	0.16

[9] The averages correspond to 37-55 points per pyroclast.

Table 5.3: Groundmass glass compositions from Cáceres et al., 2018 of lavas from *rdcd*, *rdcn* and *rdsp* measured by EMPA

Unit	*rdcd*					*rdcn*			*rdsp*		
Sample	g1	g2	g3	g4	g5	g1	g2	g3	g1	g2	gA
SiO_2	75.22	75.43	74.91	75.20	75.01	74.57	74.80	71.56	72.50	73.13	72.54
TiO_2	0.31	0.31	0.40	0.43	0.51	0.50	0.51	0.56	0.36	0.33	0.35
Al_2O_3	13.47	12.99	13.19	14.16	13.07	14.01	13.15	14.28	14.71	15.01	14.44
FeO	1.11	1.22	1.13	0.93	1.47	1.45	1.68	1.27	1.49	1.31	1.65
MnO	0.07	0.07	0.00	0.52	0.03	0.05	0.04	0.01	0.05	0.04	0.10
MgO	0.03	0.06	0.05	0.03	0.12	0.09	0.07	0.13	0.27	0.25	0.31
Cr_2O_3	0.00	0.00	0.00	0.03	0.00	0.00	0.02	0.00	0.00	0.00	0.01
CaO	0.59	0.65	0.68	1.07	0.65	1.13	0.65	1.26	1.27	1.52	1.24
Na_2O	3.82	3.85	4.09	4.66	3.64	4.79	4.35	5.23	4.78	5.22	5.35
K_2O	4.86	4.79	4.65	4.09	4.78	4.30	5.10	4.16	3.94	3.32	3.83
P_2O_5	0.10	0.09	0.03	0.06	0.02	0.15	0.13	0.18	0.06	0.07	0.04
Cl	0.12	0.16	0.13	0.12	0.19	0.12	0.16	0.10	0.12	0.09	0.13
F	0.06	0.00	0.00	0.00	0.20	0.00	0.34	0.49	0.00	0.07	0.30

5.6. Mineral Chemistry

5.6.1. Feldspar

New analyses of major and minor elements in plagioclases by EMPA are compared with major and minor element data by EMPA and LA-ICPMS from Andersen et al. (2018; see details in Supplementary Material). From this study, plagioclase crystals from the *rdm* pumices can be classified in two groups: ~67% show slight normal zoning of An_{41-45} (Fig. 5.5a); the rest are normally zoned with cores of An_{51-59} and outer rims of An_{41-43}. As a whole, the data show two compositional modes at ~An_{44} and ~An_{56} (Fig. 5.6a). Plagioclase phenocrysts analyzed in this work are much more anorthitic than those reported by Andersen et al., (2018). Despite these authors do not report the location and relative stratigraphy of their samples, the discrepancies between both datasets could be explained as the pumices from my samples were collected in the upper sequence of *rdm* where there are clear insights of rhyolitic-mafic magma interaction. I suggest that the An-poor plagioclase phenocrysts were not found in my samples because they were completely digested due to the mafic inputs and/or that residual rhyolitic melt did not have crystals. Andersen et al. (2018) show a broad mode of An_{28-34} with a tail of more anorthitic plagioclases (An_{35-50}). Traverses across individual plagioclase crystals from Andersen et al.

(2018) show that the modes represent the three main compositions of plagioclase cores; the rims associated with An_{28-34} cores (≤20 μm) are An_{27-32}, while the rest are An_{41-44} and An_{50} (Fig. 5.6d). Minor and trace elements data (Fig. 5.7) show that the An_{56} cores have highly variable Fe (0.40-0.80 wt.%), the ~An_{45} cores and rims have constant Fe (~0.35 wt.%) and the An_{28-34} plagioclase have increasing Fe with An (0.10-0.17 wt.%). The two high-An plagioclase groups have variable Sr (0.11-0.24 wt.%) and very low Ba (≤0.04 wt.%); whilst the An_{28-34} population have limited ranges of both Sr and Ba (0.08-0.10 wt.% and 0.04-0.05 wt.%, respectively).

The *rle* plagioclases are classified in two groups: >90% are unzoned with ~An_{22-23} and the rest are normally zoned with oscillating cores of $An_{26-39;}$ both plagioclase groups have rims of ~An_{23} (Fig. 5.5b). In the minor group, the more anorthitic bands have irregular rims. Consistent with data from Andersen et al. (2018) and Cáceres et al. (2018), the data show a narrow compositional mode at ~An_{22-23} and minor peaks at An_{26-29} and An_{12-17}; the latter from measurements in some outer rims and microlites. Analyses of An_{33-39} represent digested inner cores (Fig. 5.6b), which are unique in showing increasing Fe and Sr (0.31-0.43 wt.%, and 0.10-0.14 wt.% respectively) and decreasing Ba (0.03-0.07 wt.%) with anorthite content (Fig. 5.7). FeO, SrO and BaO are variable and show no clear trends. The low An outer rims and microcrysts, in contrast, have high FeO and BaO. The *rle* pumices are also unique in having K-feldspar microlites and outer rims. These have a broad unimodal distribution (Or_{30-61}) with mode and average of Or_{46}; the microlites are zoned with decreasing orthoclase from core to rim.

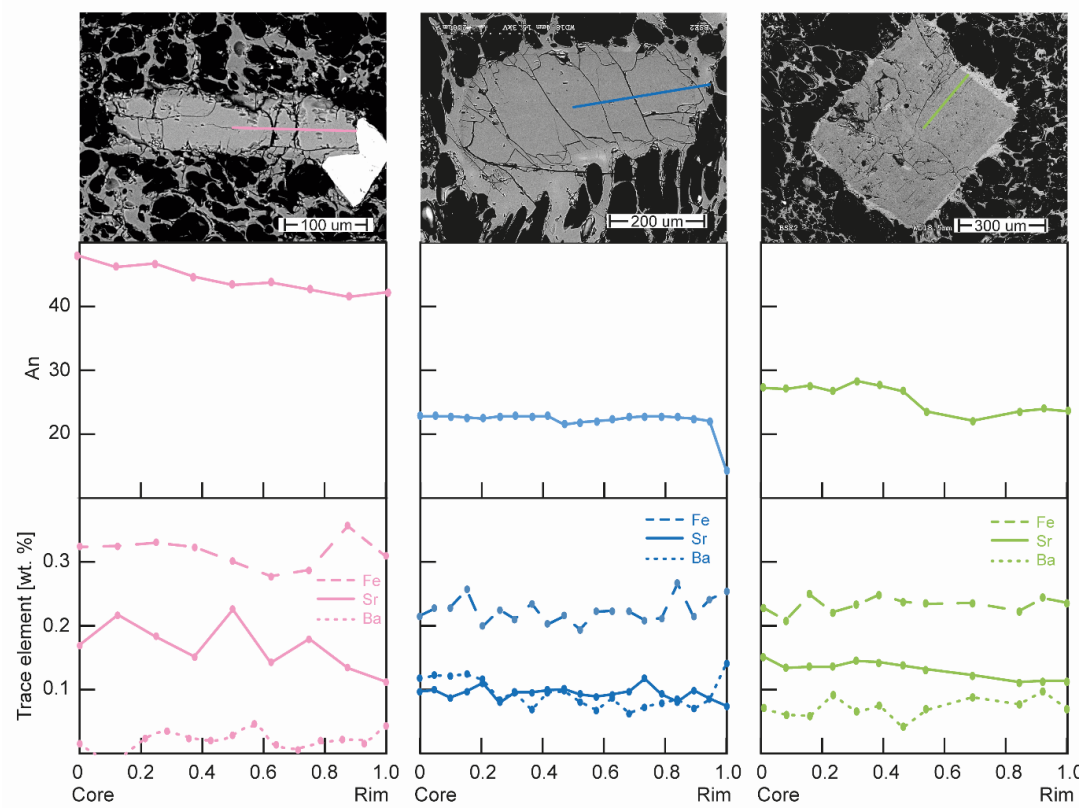

Fig. 5.5: Representative major and trace element compositional traverses in plagioclases[10]. *rdm* in pink (left), *rle* in blue (centre), and *rln* in green (right).

The *rln* plagioclase phenocrysts all have mantles of ~An_{23-27} and are classified into three groups based on differences in cores and inner mantle zones. ~60% of plagioclases are stepped-normal zoned plagioclases with cores and mantles of ~An_{27-33} (Fig. 5.5c). Each step shows slight oscillatory zoning (±1 An between minimum and maximum local values). ≥30% of plagioclase phenocrysts are slightly oscillatory zoned plagioclases of ~An_{25} with fluctuations of ±2.5 An. ≤10% of plagioclase phenocrysts show oscillatory zoning with An_{21-25}. The three plagioclase groups have mantles of ~An_{23-27}. Only the obsidian pyroclasts and lava contain microlites; these are An_{10-18}. Consistent with published data, taken as a whole, the *rln* plagioclase compositions show a broad unimodal distribution of An_{20-34} (Fig. 5.6c). With increasing An, FeO increases, SrO increases, and BaO decreases (Fig. 5.7). Both FeO and SrO are higher in the *rln* plagioclases than in the *rle* plagioclases for the same anorthite content.

[10] The traverses are 15-30 µm spacing between points.

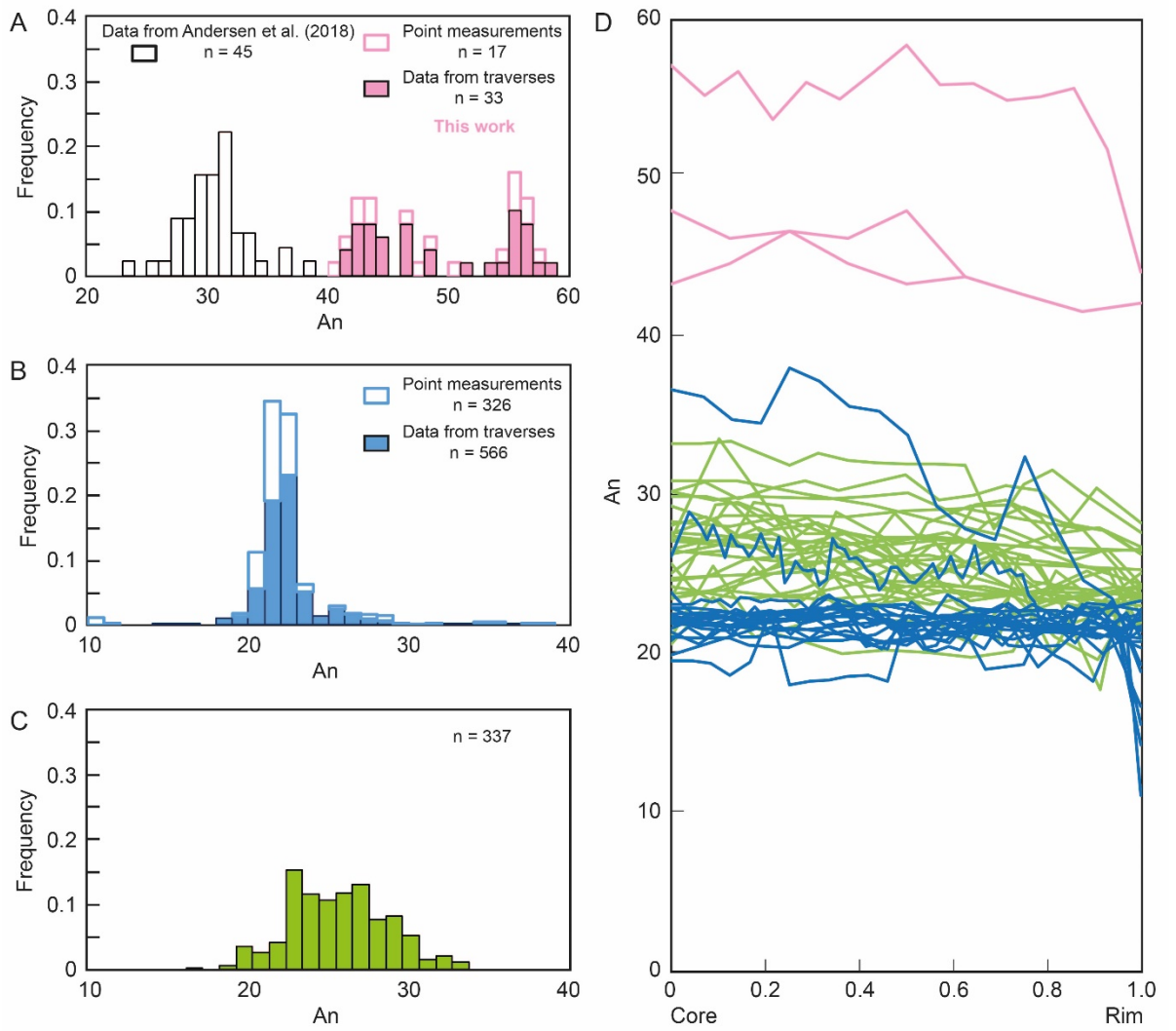

Fig. 5.6: Anorthite content in the three studied rhyolites. A-C Histograms of anorthite content from plagioclase traverses for *rdm* (**A**), *rle* (**B**), and *rln* (**C**). In **A**, point analyses representative of plagioclase phenocrysts have been added from Andersen et al. (2018). Note that X-axis (An range) is different in **A**. In **A** and **B**, point analyses from additional crystals have been added to increase the dataset. **D** Plagioclase traverses for the three studied rhyolites with position plotted nondimensionally as location relative to the core and rim, regardless of the plagioclase size.

5.6.2. Biotites

Biotites are classified according to Deer et al. (1986; Table 5.4 and Supplementary Material). The *rle* biotites show a narrow range of major element compositions, with most crystals classified as annite (Fig. 5.8a). However, they show a wide range of TiO_2 and an asymmetric and unimodal distribution of BaO (Fig. 5.8b). The *rln* biotite, in contrast, are mostly phlogopites and are slightly more compositionally variable, with slightly lower average #Fe

and higher average Al^{IV} than the *rle* biotite crystals (Fig. 5.8c); they also have higher TiO_2 and BaO (Fig. 5.8d).

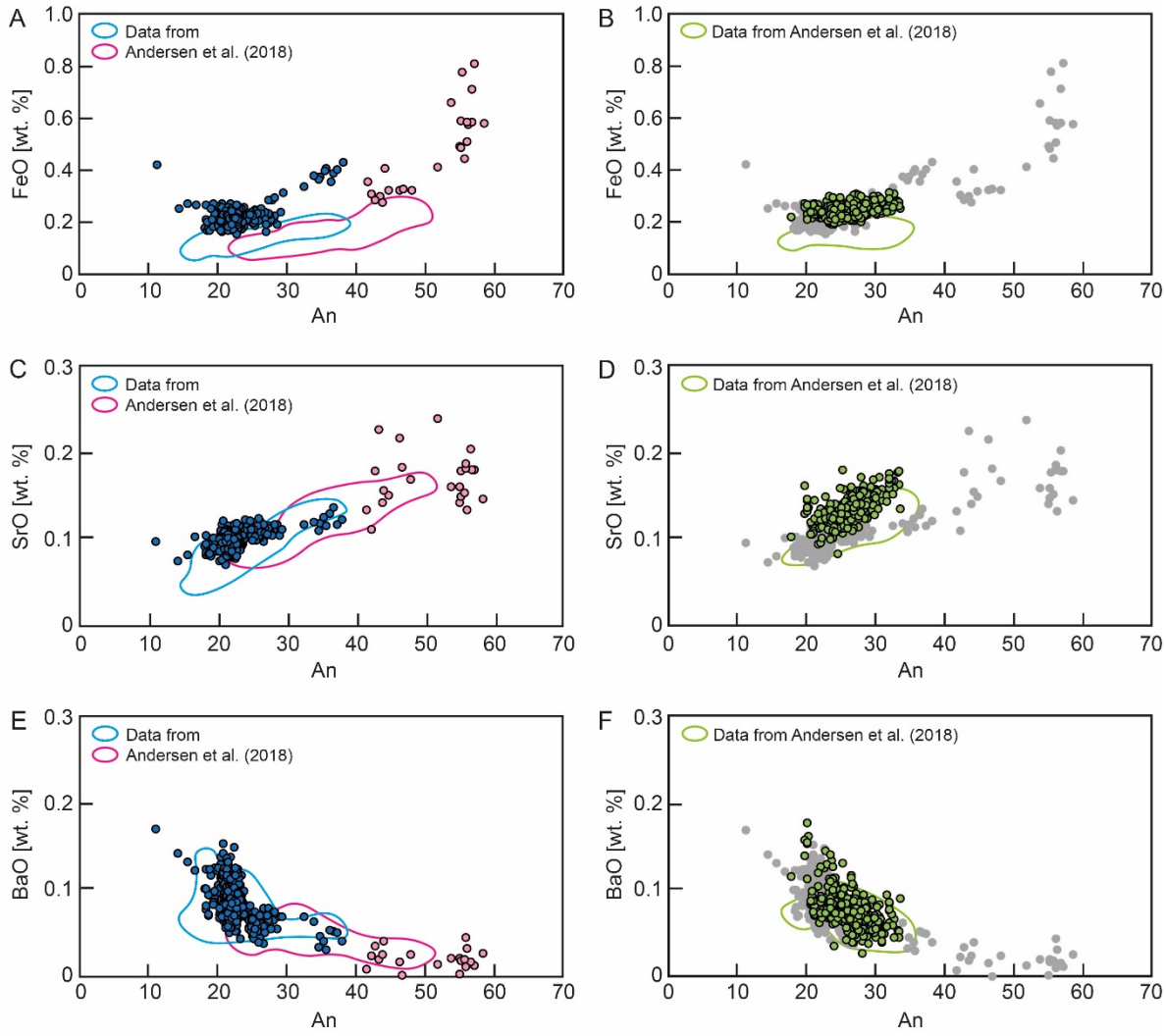

Fig. 5.7: Trace element composition in plagioclase. Pink, blue and green dots correspond to analyses in plagioclases of *rdm*, *rle* and *rln*, respectively. In **B**, **D** and **F**, grey dots are the same data highlighted in A, C and E.

Table 5.4: Averages, standard deviations and errors of compositional indexes of hornblendes and biotites from samples of *rdm*, and *rle* and *rln*, respectively. SD = Standard deviation

Si in formula	Standard Deviation	#Mg	Standard Deviation
6.33	0.08	0.81	0.03

	Al^{IV}	SD	#Fe	SD	TiO_2	SD	Error	BaO	SD	Error
Los Espejos	2.32	0.05	0.35	0.00	4.29	0.43	0.13	0.42	0.08	0.05
Las Nieblas	2.40	0.11	0.32	0.02	4.45	0.18	0.08	0.53	0.09	0.05

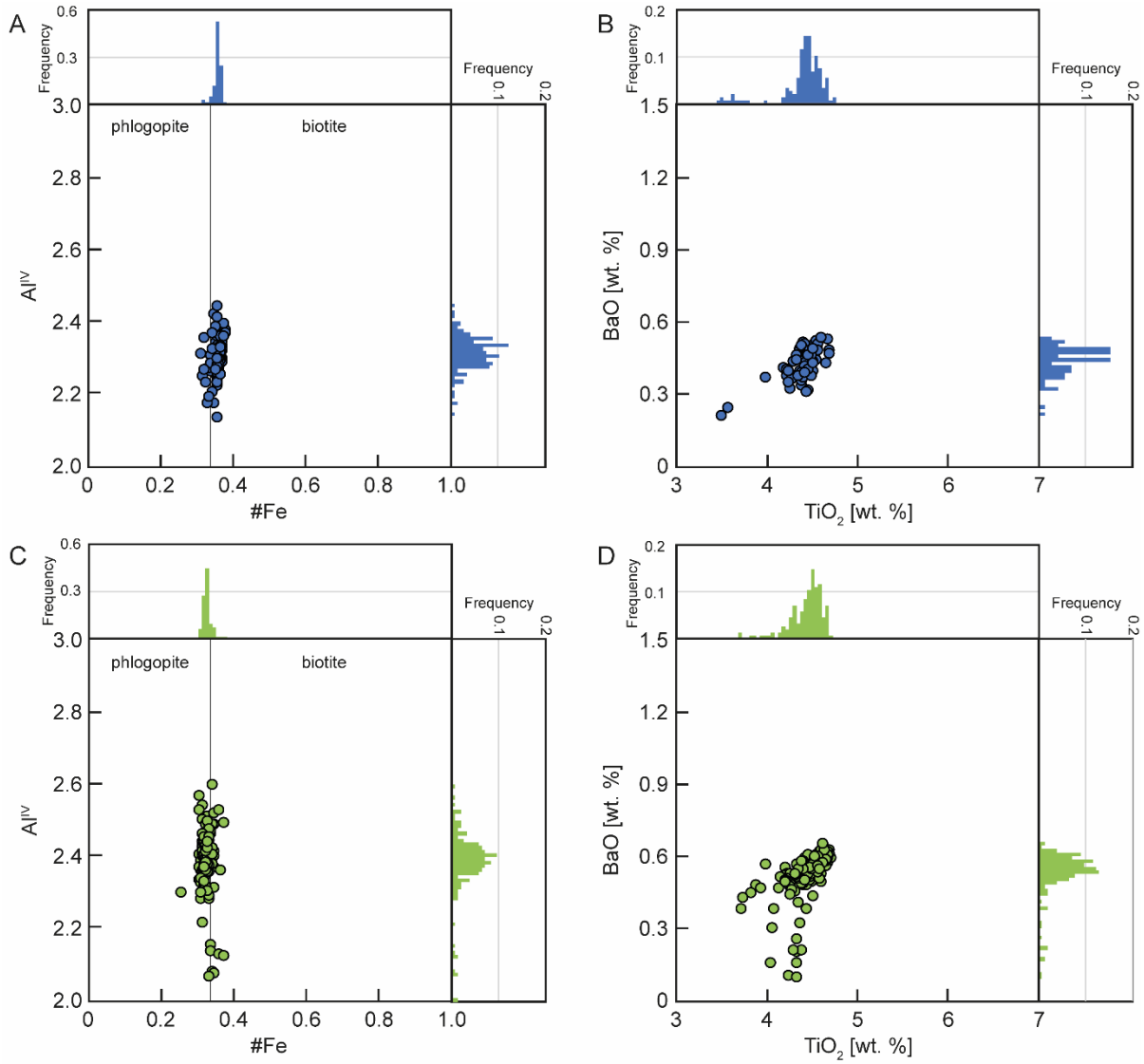

Fig. 5.8: Major and trace element compositions in the *rle* and *rln* biotites. A and **C** #Fe versus Al in IV structure in the *rle* and *rln* biotites, respectively, according to Deer et al. (1986). **B** and **D** TiO_2 versus BaO weight percent in the *rle* and *rln* biotites, respectively. We plotted these oxides because they may be used to estimate biotite crystallization temperature and pressure based on Righter and Carmichael (1996).

5.6.3. Hornblende

Of the three eruptions analyzed in this study, hornblendes are found only in the *rdm* samples. All the hornblendes have similar Si in the formula unit and a narrow range of #Mg. Because of slight variations of Na+K in position A, however, they are classified as either magnesiohastingsite (Na+K $\geq$ 0.500) or tschermakite (Na+K $<$ 0.500) according to the classification of Leake et al. (1997; Table 5.4 and Supplementary Material).

5.7. Thermodynamic conditions

The results are organized by minerals involved. A summary of estimated thermodynamic conditions by geothermobarometry methods can be found in Table 5.5 and Fig. 5.9. For details about calculations and associated errors, see Supplementary Material.

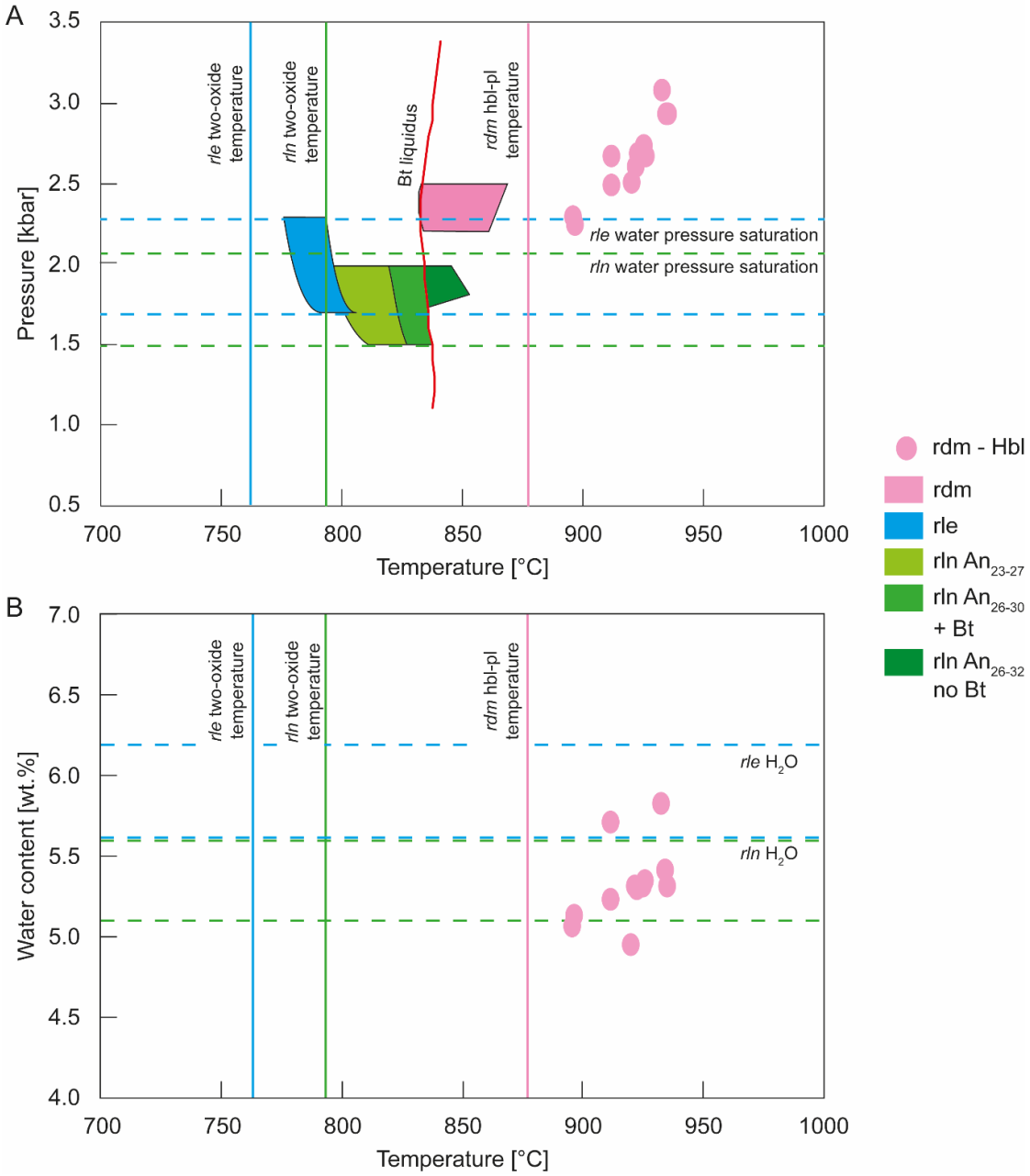

Fig. 5.9: Geothermobarometry. The Ridolfi et al. (2010) method was applied to compositions of amphiboles from *rdm* pumices. *rle* and *rln* two-oxide temperatures and *rdm* hbl-pl temperature are averages estimated with Ghiorso and Evans (2008) and Holland and Blundy (1994) methods respectively. Intervals of water pressure saturation and water content were estimated by Ghiorso and Gualda (2015) H_2O-CO_2 pressure saturation calculator and Waters and Lange (2015) plagioclase-glass hygrometer, respectively. The pressure-temperature fields of magma generation for *rdm*, *rle*, and *rln* are obtained by MELTS simulations.

5.7.1. Hornblende

The results for temperatures, pressure, water content and oxygen fugacity of 6 core-rim pairs in the *rdm* pumices are: 919 ± 13 °C (range of 896-935 °C), 2.7 ± 0.3 kbar (range of 2.2-3.1 kbar), 5.3 ± 0.2 wt.% of H_2O (range of 4.9-5.8 wt.%) and 0.8 ± 0.2 ΔNNO (range of 0.5-1.1 ΔNNO), respectively. There are no core-rim trends for any parameter and there is a positive temperature-pressure correlation (Fig. 5.9a). Three hornblende crystals in contact with plagioclase analyzed using the hornblende-plagioclase thermometer of Holland and Blundy (1994) give an average temperature of 877 °C.

5.7.2. Fe-Ti oxides

Andersen et al. (2017) applied the two-oxide oxythermobarometer of Ghiorso and Evans (2008) to five postglacial rhyodacites and fourteen postglacial rhyolites of the LdM volcanic complex. We focus on the results of Los Espejos and Las Nieblas rhyolites: the *rle* pumices give an average temperature of 763 °C and an oxygen fugacity of ΔNNO = 1.22; *rln* samples are 793 °C and ΔNNO = 1.22, respectively.

5.7.3. Feldspars

The plagioclase-glass hygrometer of Waters and Lange (2015) was applied to plagioclase rims of the *rle* eruptive products (pumices, pyroclastic obsidians and lavas) and the *rln* pumices by considering two-oxide temperatures. In the case of Los Espejos products (Fig. 5.9b), the calculated water content shows a narrow mode of 5.8 wt.% (range of 5.6-6.2 wt.%). The water content for Las Nieblas products are lower (Fig. 5.9b), with a mode of 5.4 wt.% (range of 5.1-5.6 wt.%). The calculated water contents are used to estimate water pressure saturation (P_{H2O}) by considering two-oxide temperatures (Fig. 5.9a). P_{H2O} are 1.69-2.29 kbar and 1.49-2.07 kbar for *rle* and *rln* products, respectively; both increasing with water content. The results are

insensitive to subtle variations in temperature: an increment of 5 °C decreases the calculated pressure by ~0.005 kbar.

5.8. Interpretations of mineral compositions and textures

The analysis of major element compositions and zoning patterns in phenocrysts allows classification of mineral populations and can suggest processes of mixing and/or heating (e.g., Bouvet de Maisonneuve et al., 2012); while the phenocryst rims and textures of microcrysts are related to rates and available time for crystallization during ascent (e.g., Preece et al., 2013; Shea and Hammer, 2013). The analysis of trace elements in minerals allows the classification of mineral populations as phenocrysts, antecrysts, xenocrysts and microcrysts (e.g., Ruprecht and Worner, 2007; Ubide and Kamber, 2018). Herein, I analyze the implications on the three studied rhyolites of the anorthite content in plagioclases and its relationships with trace elements, and the occurrence and textures of both mafic hydrous minerals.

5.8.1. Insights from feldspar

5.8.1.1. Rhyolite of Laguna del Maule

The An_{26-35} plagioclase crystals are the most albitic population in the pumices of *rdm,* and they were formed within the rhyolite-forming reservoir according to their consistent trends of trace elements in plagioclase with those from *rle* and *rln*. Trace elements in the An_{41-45} and An_{51-59} plagioclases from *rdm* (Fig. 5.7) show different trends than in the *rle* and *rln* plagioclases, suggesting that both plagioclase populations were not formed in the rhyolite-forming reservoir (Fig. 5.7). The Fe content of An_{41-45} plagioclase is constant and higher than those of the An_{26-35} plagioclases, whilst it is higher and more variable for An_{51-59}; this suggests that the An_{41-45} and An_{51-59} plagioclase groups were formed in two different magma reservoirs apart from the rhyolite-forming chamber (e.g., Ginibre et al., 2002; Ruprecht and Worner, 2007). The high

variability of Sr in An_{41-45} plagioclase could reflect the competition of several phases (e.g., Singer et al., 1995). As Sr is compatible with Ca, variations in volume fraction of hornblende could cause local variations in the Sr contents in melt (Andersen et al., 2018). The absence of plagioclase (and any mineral) microcrysts suggests the *rdm* magma ascended superliquidus and/or a fast magma ascent rate to avoid crystallization during ascent.

The discrepancies between the main *rdm* plagioclase group found by Andersen et al. (2018) of An_{28-34} and in this chapter (modes at ~An_{44} and ~An_{56}) may reflect sampling of different phases of the *rdm* eruption sequence (what was sampled by Andersen et al. is not well documented) and/or different rhyolitic magma portions. In particular, my samples show evidence of substantial interaction with the mafic magmas according to the fraction of co-erupted basalt-andesitic and andesitic juveniles and the pumices carrying mafic enclaves (Chapter 2). Greater interaction with the hotter and mafic magmas may explain the absence of An_{26-35} plagioclase by complete digestion of these crystals and the higher content of An_{41-45} plagioclase by crystal cargo (e.g., Berlo et al., 2007; Cashman and Blundy, 2013). The plagioclases of An_{28-34} could be phenocrysts and the rims of An_{27-32} could be late crystallization formed in a parental dacitic reservoir (Andersen et al., 2018).

Table 5.5: Summary of estimated pressure, temperature, water content, and oxygen fugacity by geothermobarometry methods. Columns "Method" refers to the following references: Hbl = Ridolfi et al. (2010); Hbl-Pl = Holland and Blundy (1994); Pl-glass = Waters and Lange (2015); PH_2O = Ghiorso and Gualda (2015); Two oxide = Ghiorso and Evans (2008) in Andersen et al. (2017).

Temperature [°C]			Pressure [kbar]			Water content [wt.%]			Oxygen fugacity [ΔNNO]		
Unit	Method	Value	Unit	Method	Value	Unit	Method	Value	Unit	Method	Value
rdm	Hbl	896-935	*rdm*	Hbl	2.23-3.08	*rdm*	Hbl	4.9-5.8	*rdm*	Hbl	0.5-1.1
rdm	Hbl-Pl	877									
rle	Two oxide	763	*rle*	PH_2O	1.69-2.29	*rle*	Pl-glass	5.6-6.2	*rle*	Two oxide	1.22
rln	Two oxide	793	*rln*	PH_2O	1.49-2.07	*rln*	Pl-glass	5.1-5.6	*rln*	Two oxide	1.25

5.8.1.2. Rhyolite of Los Espejos

The unzoned plagioclase group of An_{22-23} was formed in the rhyolite-forming reservoir because they follow the main An-trace element trend in plagioclases (Fig. 5.7). The constant anorthite and Fe contents suggest a eutectic crystallization regime in a single magma reservoir as occurs in other high-silica magmatic complexes (e.g., Anderson et al., 2000). The high variability of Ba could be explained by the crystallization of plagioclase over a wide pressure range (Singer et al., 1995), or by a heterogeneous plagioclase-biotite ratio in the rhyolite-forming reservoir due to biotite breakdown (Andersen et al., 2018). The scarce An_{26-30} cores have the same Fe and Sr and follow the same Ba trend with anorthite content as the An_{22-23} group, suggesting that they come from a hotter and deeper section of the rhyolite-forming reservoir (Fig. 5.10b). By contrast, the scarce An_{30-40} cores are antecrysts because they show a sharp transition to An_{22-23} mantles and have higher Fe and Sr and lower Ba contents than the other plagioclases.

The An_{12-17} microlites were formed during magma ascent according to their elongation and the increasing Fe and Ba trend with decreasing An. The increasing Fe is associated with the more oxidizing conditions in the ascent to the surface (Ruprecht and Wörner, 2007); while the increasing Ba should be associated with the biotite breakdown, that may also explain the crystallization of skeletal K-feldspar microlites due to the higher K available in the ascending magma (Barbey, 2007).

5.8.1.3. Rhyolite of Las Nieblas

The wider anorthite content and similar Fe, Sr and Ba trends of the *rln* plagioclases suggest that the scarce An_{30-35} cores, the An_{26-30} cores and the An_{23-27} cores and mantles were formed in the rhyolite-forming reservoir with more variable storage conditions than for Los Espejos (Fig. 5.7). Considering that all the plagioclase crystals have mantles of $An_{23-27,}$ we suggest that the more anorthitic cores come from a deeper and hotter section and were emplaced in the part

of the reservoir containing the rest of the crystals before the eruption, or that the temperature of the magma chamber decreased during crystallization and that the more anorthitic cores are older than the albitic ones. However, the stepped normal-zoning pattern of plagioclase phenocrysts suggests that the first option is more feasible than a gradual variation. Moreover, the positive Sr-An and negative Ba-An relationships suggest a temperature control of plagioclase crystallization (Berlo et al., 2007; Cashman and Blundy, 2013). The wide Sr and Ba ranges for the same An also suggest vertical grading of water pressure and/or a spatially variable plagioclase-biotite volumetric ratio (Andersen et al., 2018; Singer et al., 1995).

The An_{10-18} population in the obsidian clasts and lavas corresponds to microlites crystallized during ascent as in Los Espejos case. The absence of plagioclase microlites (and of any mineral) in the *rln* pumices suggest a fast magma ascent rate to avoid the crystallization during ascent.

5.8.2. Insights from mafic hydrous minerals

Plagioclase+biotite is the most common mineral assemblage in the postglacial rhyolites of the LdM volcanic complex (Hildreth et al., 2010). By contrast, the *rdm* is the only rhyolite which carries hornblende. Compositional and textural analyses suggest that hornblende crystals are antecrysts in the silicic products (Cáceres et al., 2018) and their mantles are formed within the rhyolite-forming reservoir (Andersen et al., 2017). Herein, I analyze the textures and conditions of hornblende crystallization in the *rdm* pumices, and textures of biotite crystals in *rle* and *rln* samples.

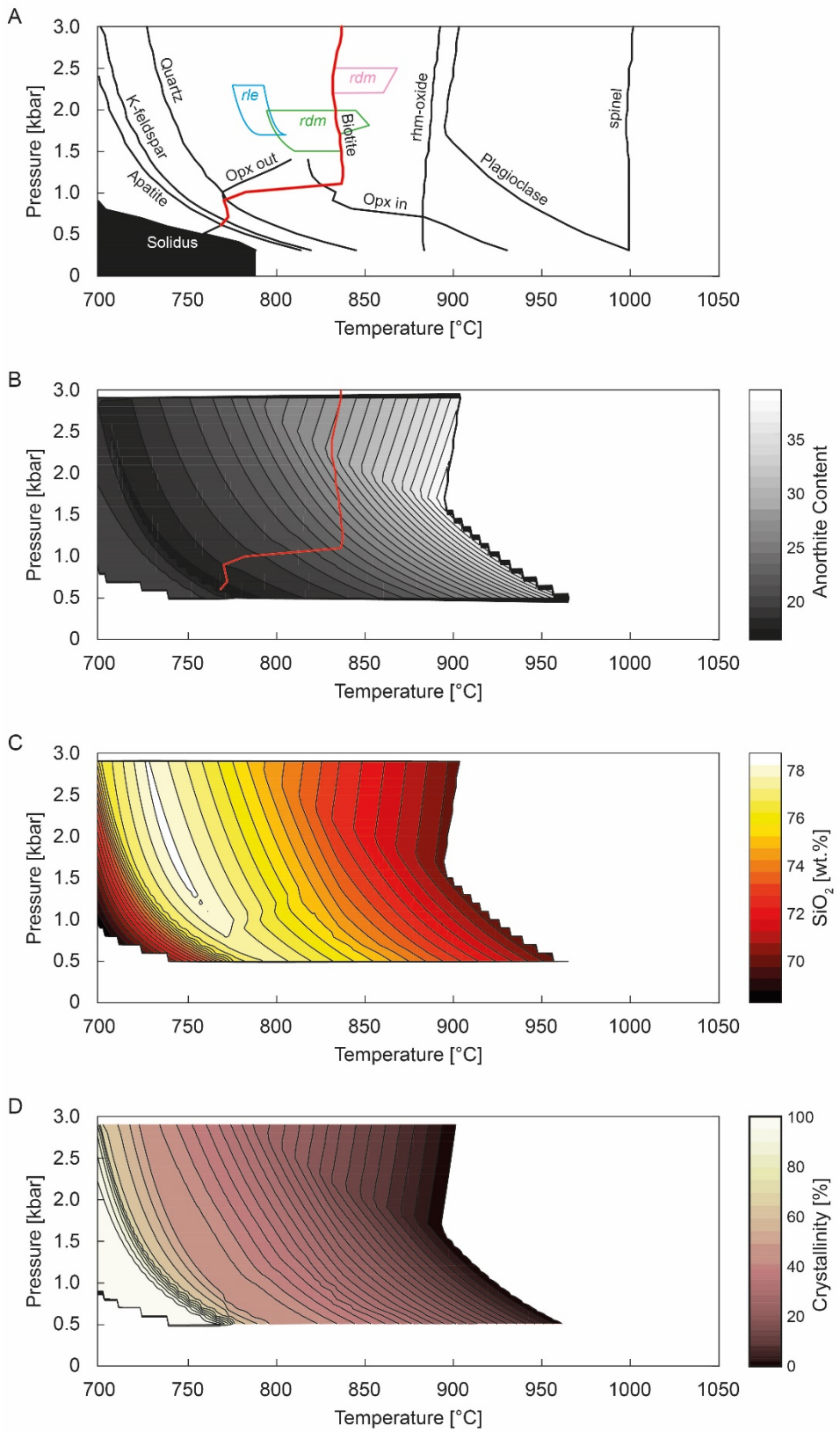

Fig. 5.10: Numerical simulations of the dacitic reservoir by MELTS. A Phase diagram including the P-T fields for the LdM rhyolites. **B** Anorthite content in plagioclase. Red line is biotite liquidus. **C** SiO_2 in melt. **D** Crystallinity. The simulations done with increments of 1 °C and 0.1 kbar with *rdcn* bulk as starting composition.

5.8.2.1. Rhyolite of Laguna del Maule

The occurrence of hornblende, rather than biotite, in *rdm* pumices suggests that this phase did not derive from the rhyolite-forming reservoir. Hornblende geothermobarometry shows that *rdm* hornblendes were formed at 2.2-3.1 kbar and 895-935 °C with an almost continuous positive pressure-temperature correlation (Fig. 5.9a). The subtle gap at 2.25-2.45 kbar and 900-910 °C suggests the transfer of hornblende crystals from a deeper and hotter magma reservoir. The conditions of the high P-T hornblende cluster match with the conditions of hornblende crystallization from mafic-to-intermediate units of the LdM complex (Andersen et al., 2017; Cáceres et al., 2018). Moreover, given that *rdm* deposits include basaltic-andesitic and andesitic juveniles and that some pumices show enclaves of the same compositions, I suggest that crystals of the An_{41-45} plagioclase-hornblende assemblage were transferred from the mafic magmas. Crystal transfer has been described in other deposits related to explosive silicic eruptions triggered by magma mixing or mingling (Feeley et al., 2008; Tepley III et al., 1999). The lack of disequilibrium textures in hornblendes and mafic microcrysts could be explained by a short residence time of the mafic magmas in the rhyolite-forming reservoir prior to the eruption.

5.8.2.2. Rhyolite of Los Espejos

As the Mg in position VI of biotite is mostly controlled by temperature (Guo and Green, 1990; Righter and Carmichael, 1996), the relatively constant #Mg in the *rle* biotite crystals suggests growth in a narrow temperature range. The biotite phenocrysts grow when the water activity is near 1, a reduction of the magmatic water content may produce disequilibrium textures in biotite (Barbey, 2007; Fabbrizio et al., 2006). Biotite textures in Los Espejos rhyolites vary according to the type of silicic product: the pumices have anhedral to subhedral biotite phenocrysts with no microcrysts, whilst pyroclastic and lava obsidians have subhedral to euhedral biotite phenocrysts with elongate microcrysts. This contrast reflects different P-T-

H_2O paths during the eruption compared with the biotite liquidus. Rounding of biotite phenocrysts in the *rle* pumices suggests that the magma ascent path exceeded the biotite liquidus temperature during the explosive stage (Barbey, 2007). Slower magma ascent during the effusive stage or the eruption of a cooler magma portion, in contrast, would have allowed sufficient magma cooling during ascent for biotite to remain stable for the entire decompression path, and so both maintain euhedral biotite phenocrysts and form new biotite microcrysts during ascent and eruption of the obsidian lava flow (Fig. 5.2 and 5.11).

5.8.2.3. Rhyolite of Las Nieblas

The *rln* biotite have slightly higher #Mg than the *rle* biotite, consistent with the warmer calculated two-oxide temperatures. The more variable #Mg in the *rln* biotite suggests a wider temperature range of crystallization than in the *rle* biotite (Guo and Green, 1990; Righter and Carmichael, 1996). The *rln* pumices have elongate euhedral biotite phenocrysts with no microcrysts. It is possible that the biotite crystallization occurred at low undercooling and the *rln* magmas ascended above the biotite liquidus temperature given the hotter storage conditions in the rhyolite-forming reservoir (Shea and Hammer, 2013). To avoid biotite breakdown as in the Los Espejos case, the magma ascent should be quicker than the diffusivity of Fe-Mg in biotite (Feeley and Sharp, 1996), but sufficient slow during the effusive stage to allow the crystallization of plagioclase microlites (Costa et al., 2003).

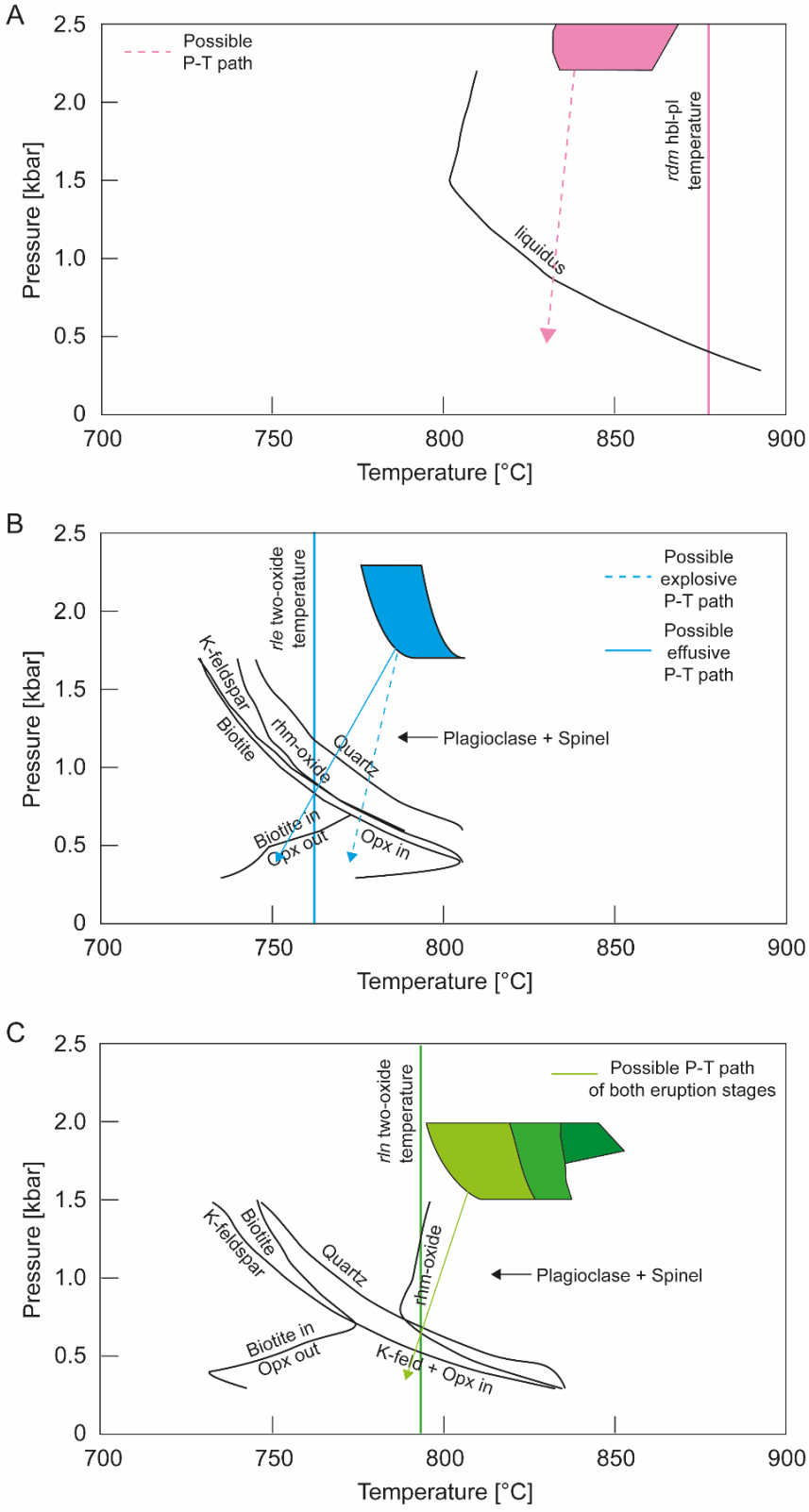

Fig. 5.11: Numerical simulations of magma ascent by MELTS. Phase diagrams from the dacitic reservoir to surface and P-T fields for magma generation. The suggested P-T paths consider information from phase diagram and groundmass mineralogy. **A** Rhyolite of Laguna del Maule. **B** Rhyolite of Los Espejos. **C** Rhyolite of Las Nieblas. The simulations done with increments of 1 °C and 0.1 kbar with the corresponding bulk for each rhyolitic event as starting composition.

5.9. Simulations of storage conditions

Andersen et al. (2018) estimated water contents in the LdM rhyolites by MELTS simulations with a dacitic starting composition; however, the output was not compared to the glass and plagioclase compositions of eruption products. As the whole-rock and plagioclase minor element compositions of *rdm*, *rle* and *rln* silicic samples follow similar trends, I assume that their magmas come from reservoirs of similar major element compositions. Herein, I simulate storage conditions in rhyolite-MELTS (Gualda et al., 2012) by applying various major element compositions to find the rhyolite-forming initial magma. Once I find the best initial magma, I construct a phase diagram using a module in Excel-MELTS (Gualda and Ghiorso, 2015) to find the P-T fields where the corresponding An contents were formed for the analyzed rhyolites (Fig. 5.10). I consider the calculated Hbl-pressure in *rdm* and the calculated saturation pressures in *rle* and *rln* but not the temperature calculated from two-oxide thermometry because the equilibration of oxides within magmatic systems can occur at very late stages of crystallization and not necessarily related to plagioclase formation (Aragon et al., 1984; Van Orman and Crispin, 2010).

From MELTS simulations, I have determined the following compositional features about the rhyolite-producer magma reservoir below LdM (Table 5.6): 1. The magma must have 4.5-6.0 wt.% H_2O to form the plagioclase-biotite assemblage at expected temperatures (at lower H_2O, it does not crystallize biotite; at higher H_2O, the An content is too high); 2. A magma composition of 67.3-69.5 wt.% SiO_2 is required to reproduce observed anorthite contents in plagioclases of the studied samples; 3. The starting material cannot be trachytic (constrained by the alkali content in glass compositions of LdM postglacial rhyolites); 4. FeO_T + MgO content must be >3 wt.% to obtain the observed plagioclase-biotite assemblage at expected temperatures.

On the basis of the above constraints, I select the *rdcn* bulk composition as the starting material to interpret *rdm*, *rle* and *rln* petrological data; it is one of the best-characterized postglacial rhyodacites of the LdM volcanic complex (e.g., Andersen et al., 2018; Cáceres et al., 2018). To determine the pressure-temperature fields of anorthite content in plagioclase and the storage conditions required for the plagioclase-biotite mineral assemblage, I applied a matrix of equilibrium conditions (Table 5.7 and Supplementary Material). The simulated phase diagram (Fig. 5.10a) shows that the plagioclase liquidus temperature decreases from 905 °C to 895 °C by decreasing pressure from 3.0 to 1.7 kbar. At lower pressures, the plagioclase liquidus increases to 1005 °C. The biotite liquidus temperature is almost isothermal (~835 °C) at 1.1-3.0 kbar. At lower pressures, biotite can be formed at 0.6-1.0 kbar and <775 °C. Quartz, K-feldspar and apatite liquidus curves decrease with pressure at 0.3-2.4 kbar.

Table 5.6: Whole-rock compositions used for numerical simulations in MELTS software. The samples were analyzed by XRF in Hildreth et al. (2010).

	rdm	*rle*	*rln*	*rdcn*	*rdla*	*igcb*$_1$	*igcb*$_2$
SiO_2	76.7	75.7	73.4	68.2	67.3	67.1	68.3
TiO_2	0.15	0.18	0.26	0.59	0.57	0.77	0.57
Al_2O_3	12.93	13.23	14.6	15.84	15.88	18.51	15.94
FeO	0.72	0.87	1.19	2.98	3.40	1.57	2.79
MnO	0.05	0.07	0.08	0.10	0.09	0.06	0.09
MgO	0.10	0.12	0.22	0.96	1.32	0.27	0.80
CaO	0.58	0.64	0.80	2.60	3.10	2.42	2.17
Na_2O	3.71	4.27	4.89	4.95	4.72	5.13	4.84
K_2O	4.62	4.44	4.09	3.18	3.09	3.49	3.95
P_2O_5	0.07	0.05	0.05	0.21	0.18	0.24	0.16

The plagioclases of An_{28-34} from *rdm* samples of Andersen et al (2018), considered as phenocrysts formed in the dacitic reservoir, are simulated at 832-869 °C and 2.2-2.5 kbar, which is above the biotite liquidus temperature (Fig. 5.9 and 5.10) consistent with the absence of this phase in *rdm* samples. Comparison of observed data with the phase diagram shows that the *rle* plagioclases of An_{22-23}, which correspond to >90% of the *rle* plagioclase crystals, are simulated at 775-805 °C and 1.7-2.3 kbar for a melt composition of 76-77 wt.% SiO_2 (or 755-

805 °C if SiO_2 is extended to 75.5 wt%; Fig. 5.9 and 5.10). The *rln* plagioclase cores of An_{26-30}, which are found in >60% of the *rln* plagioclase crystals, are simulated at 825-855 °C and 1.67-2.00 kbar (Fig. 5.9 and 5.10). If plagioclase crystallization is strictly associated with biotite, however, the stability field of An_{26-30} is 825-835 °C and 1.67-1.81 kbar (Fig. 5.9 and 5.10). In this way, the biotite crystallization is associated with plagioclase cores at shallower and colder conditions. The mantles of An_{23-27}, which correspond to the most frequent anorthite content in the *rln* plagioclases, are simulated under slightly cooler conditions (790-835 °C) at similar pressures (1.5-2.0 kbar) for a melt silica content of 74-76 wt.% (Fig. 5.10b and c). Moreover, the simulated phase diagram shows that Los Espejos plagioclase crystallization was ~30 °C colder than Las Nieblas plagioclase crystallization, consistent with geothermometry methods.

Table 5.7: Starting compositions and thermodynamics conditions used to model the storage and ascent conditions by MELTS software. To simulate the ascent conditions, the maximum value of P corresponds to the minimum pressure at storage conditions, the maximum value of T is the maximum temperature at storage conditions (except for *rdm*), and the water contents correspond to the minimum value measured by the hygrometers.

Magma conditions	Storage	Ascent	Ascent	Ascent
Starting composition	*rdcn*	*rdm*	*rle*	*rln*
P [kbar]	3-0	2.2-0	1.7-0	1.5-0
ΔP [kbar]	0.1	0.1	0.1	0.1
T [°C]	1050-700	900-700	805-700	835-700
ΔT [°C]	1	1	1	1
H_2O [wt.%]	5.8	4.9	5.6	5.1
fO_2	ΔQFM+2	ΔQFM+2	ΔQFM+2	ΔQFM+2

5.10. Simulations of ascent conditions

The shallowest storage conditions obtained from MELTS simulations are considered as the initial state of the ascending magma for each rhyolite studied. As the rhyolitic magmas were extracted from the dacitic reservoir, I use the whole-rock composition of each rhyolite studied to simulate the conditions during ascent. Following the same procedure for the simulation of

storage conditions, simulated P-T fields are used to find where the observed groundmass minerals were stable (Table 5.7 and Supplementary Material). To evaluate the magma ascent conditions, the temperature calculated by two-oxide thermometry is used as a reference.

As the *rdm* pumices are almost aphyric and most of the minerals are antecrysts, I only focus on the *rdm* liquidus. The liquidus is almost isothermal (~805 °C) at 1.5-2.2 kbar and increases with decompression up to 893 °C (Fig. 5.11a). If the ascent was adiabatic, the *rdm* magma would reach a liquidus temperature of 830 °C at ~0.9 kbar forming plagioclase and spinel. Due to the lack of microcrysts and considering the wide pressure range between the storage conditions (2.2 kbar) and the pressure where the liquidus would have been reached (0.9 kbar), the magma ascent rate was sufficiently fast to avoid crystallization at <1 kbar. If magma ascent was not fast at depth, then crystallization could be avoided by a deep (P> 1kbar) fragmentation level as magma would ascend more quickly up the conduit as hot clasts carried by gas.

Plagioclase and spinel are ubiquitous in the *rle* simulation; quartz, Fe-Ti oxides and K-feldspar liquidus curves (in decreasing order of liquidus temperature) decrease with pressure; and the biotite liquidus decreases with pressure at 0.7-1.7 kbar from 728 °C to 772 °C and decreases with decompression at <0.7 kbar (Fig. 5.11b). I propose that the *rle* explosive and effusive phases followed different P-T paths: the *rle* magma ascended at >772 °C in order to avoid biotite crystallization and the K-feldspar microlites were formed at <0.8 kbar during the explosive stage; by contrast, during the effusive eruption the *rle* magma ascended at ~760 °C (temperature estimated from two-oxide thermometry).

Plagioclase and spinel are ubiquitous in the *rln* simulation. The Fe-Ti oxide liquidus is ~790 °C at 0.8-1.5 kbar and increases up to 835 °C at lower pressures; by contrast, the biotite liquidus increases from 747 °C to 775 °C with decompression at 0.7-1.5 kbar, and decreases up to 730

°C at lower pressures (Fig. 5.11c). Based on the estimated temperature by two-oxide thermometry, the *rln* magma ascended above the biotite liquidus during both explosive and effusive phases. As plagioclase is stable for the whole range of temperatures in the model, I propose that a decrease of the magma ascent rate during the explosive-effusive transition of *rln* may explain the absence of plagioclase microcrysts in the pumices, and the crystallization of this mineral in the obsidian lavas. Unlike the *rle*, a decrease of the temperature is not needed to explain the different mineral associations in groundmass of the eruption phases.

5.11. Eruption histories of the postglacial rhyolites of LdM

A hot zone of extractable mush has produced rhyolite magma for the last 34-160 ky (Andersen et al., 2019). Trace elements in zircons and plagioclases (Andersen et al., 2018, 2019) suggest that most of the crystals of the postglacial rhyolites come from the same crystal mush located at ~5 km-depth (Le Mevel et al., 2016; Westespad, 2019). We have shown that the mush-type rhyolite-forming reservoir is dacitic to rhyodacitic of mid-high K, $FeO_T + MgO > 3$ wt.%, and nearly water-saturated. This composition is consistent with the compositional gap at ~67 wt.% SiO_2 of the LdM products (Dufek and Bachmann, 2010; Hildreth et al., 2010). Based on the absence of reverse zoning in outer rims (e.g., Till et al., 2015), the groundmass glass of rhyolites represents interstitial melt of this dacitic reservoir (Cooper and Kent, 2014; Rubin et al., 2017) rather than rhyolitic magma segregated into a transient shallower reservoir. Each rhyolite magma could come from a localized melt accumulation into a magma pocket of 30-70 vol.% crystals within the dacitic reservoir as has been suggested for the formation of intermediate products (Cáceres et al., 2018) and the origin of the current uplift in this volcanic complex (Miller et al., 2017). Subtle variations of the storage within these magma pockets control the slight differences of bulk and mineral compositions among the postglacial rhyolites. Here I suggest that the independent storage conditions of the magma pockets and the subsequent

different ascent conditions played key roles in controlling the variations of styles and transitions of the rhyolitic eruptions.

5.11.1. Rhyolite of Laguna del Maule (*rdm*)

The rhyolitic magma of *rdm* was stored within the mush-type dacitic reservoir in a magma pocket of 2.2-2.5 kbar and 830-870 °C. The lack of biotite is explained by the magma storage above the biotite liquidus. Hornblende crystals are antecrysts associated with An_{41-45} plagioclases which come from a deeper and hotter magma reservoir of >2.5 kbar and >910 °C. These conditions match those described for the formation of dacites to andesites of the LdM volcanic complex (Cáceres et al., 2018). As the samples for this study were collected in the upper part of the *rdm* sequence, I suggest that these represent a late stage of the *rdm* storage conditions. Based on the coexisting mafic and andesitic juveniles and the absence of the An_{26-34} plagioclase phenocrysts (where were found in *rdm* samples by Anderson et al (2018) from unspecified locations), we suggest that the mafic and hotter magmas were extracted during the *rdm* eruption from a deeper andesitic magma reservoir (Tarasewicz et al., 2012). Therefore, I suggest that the An_{51-59} plagioclase were antecrysts in this andesitic reservoir from an even deeper and more mafic reservoir.

Based on the coldest calculated temperatures from hornblende thermometry and the plagioclase crystallization temperatures simulated in MELTS, the andesitic magma input would have produced an overall heating of >30 °C in the rhyolitic magma. This heating of near-volatile-saturated magma could have initiated vesiculation at the top of the rhyolitic magma pocket (Gonnermann and Manga, 2007). According to the low crystal content of *rdm* pumices and my numerical simulations, the magma ascended at a temperature greater than the liquidus temperature (i.e. >805 °C). Based on the calculated temperatures in hornblendes I propose that the *rdm* rhyolitic magma ascended at a temperature some tens of degrees over the liquidus,

which is consistent with the highly expanded bubble textures in the *rdm* pumices (e.g., Baker et al., 2012). In summary, I propose that the high explosivity of the *rdm* eruption was aided by heating due to a mafic magma input in the dacitic reservoir and subsequent magma mingling. This eruptive trigger has been proposed for several highly-explosive silicic eruptions (e.g., Feeley et al., 2008; Pallister et al., 1992). As the *rdm* event is the only postglacial rhyolitic pyroclastic deposit associated with mafic clasts and enclaves within pumices, and carrying hornblende phenocrysts (Fierstein, 2018; Hildreth et al., 2010), I propose that the large magnitude of this eruption (>20 km^3; Fierstein, 2018) is linked to the mafic magma input into the dacitic reservoir.

5.11.2.Rhyolite of Los Espejos (*rle*)

The homogeneous composition of minerals (this chapter; Andersen et al., 2018) and the protracted zircon crystallization history for early postglacial rhyolites (Andersen et al., 2019) suggest stable conditions for a long period (e.g., Huber et al., 2009). The duration of stable magmatic conditions can be considered equivalent to the time gap between *rdm* and *rle* eruptions (thousands of years; Andersen et al., 2017; Fierstein, 2018) based on the heritage of *rdm* zircons within the *rle* magma (Andersen et al., 2019).

The magma pocket within the dacitic reservoir that stored *rle* magmas was 10-15 km^3 (Cáceres et al., 2018). The most common unzoned An_{22-23} plagioclase crystals were formed at 1.7-2.3 kbar and 775-805 °C; whilst the low fraction (<5%) of normally zoned plagioclases with An_{26-30} cores were formed at higher temperatures. Trace element abundances suggest that the few normally zoned plagioclases (<5%) with An_{30-40} cores are antecrysts (Fig. 5.7) that may record a small, hotter and less silicic magma input affecting the bottom part of the dacitic reservoir prior to the *rle* eruption. Evidence for this cryptic magma replenishment are the spikes of Ba concentration in plagioclases and the crystallization of K-feldspar microlites during the

explosive stage due to biotite breakdown (Andersen et al., 2018; Barbey, 2007). This biotite breakdown may be explained by the localized heating produced by those magma replenishments which overcame the biotite liquidus temperature. I propose that the transition to the effusive stage occurred by a decrease of the magma ascent rate due to a loss of pressure at the storage depth after having erupted a high volume of wet silicic magma. The decrease of the magma ascent rate occurred with a 10-15 °C cooling between the explosive and the effusive phases inferred from the occurrence of biotite microcrysts only in pyroclastic and lava obsidians. Despite the magma cooling could counter the lava formation because of the related increase of magma viscosity, this magma viscosity would be only of ~0.1 Log Pa s (Giordano et al., 2008), not sufficient to avoid the explosive-effusive transition (Cassidy et al., 2016; Di Genova et al., 2017). As the fraction of vesicular obsidian clasts increases gradually in the *rle* fall deposit with stratigraphic height (Sections 2.5.3 and 2.6.3) and the pumices did form microcrysts during ascent, I propose that the decrease of the magma ascent rate and temperature started to occur gradually before the formation of the obsidian lava.

5.11.3. Rhyolite of Las Nieblas (*rln*)

The magma pocket that stored Las Nieblas magma was bigger (~30 km^3; Cáceres et al., 2018), hotter (795-855 °C) and shallower (1.5-2.0 kbar) than the *rle* magma reservoir. These conditions affected the variety of plagioclases, the anorthite content range, and the biotite textures. I classified three populations of plagioclase phenocrysts in the *rln* samples. Unlike the *rle* samples, the most common plagioclase population are stepped-normal zoned crystals with An_{26-33} cores suggesting episodic stages of cooling and stabilization. The anorthitic cores were formed around the biotite liquidus (An_{30} at 835 °C) consistent with the elongate biotite phenocrysts due to a low undercooling (Shea and Hammer, 2013). The second most frequent plagioclase population are oscillatory-zoned crystals with anorthite contents corresponding to the composition of mantles of all the *rln* plagioclase crystals (An_{23-27}; Fig. 5.6). The common

composition of mantles suggests a common late-stage crystallization within the dacitic reservoir. Despite the wide range of anorthite content and variety of plagioclase types, trace elements in plagioclase can be explained by crystallization from a single dacitic mush.

My simulations suggest spatial and temporal variations of the dacitic mush before the *rln* eruption. Plagioclase cores of An_{26-33} crystallized at 1.8-2.0 kbar and >835 °C without biotite; whilst plagioclase cores of An_{26-30} with associated biotite crystallized at 1.6-1.8 kbar and 825-835 °C. A later cooling of the complete magma pocket allowed the crystallization of plagioclase mantles of An_{23-27} associated with biotite at 1.5-2.0 kbar and 790-825 °C. The *rln* samples show no evidence for magma replenishments. However, the stepped zoning of plagioclase cores and the higher content of trace elements in plagioclase compared with plagioclase crystals from the early postglacial rhyolites suggest a pulsatory accumulation of fluids from deeper and hotter mafic melts (Andersen et al., 2018; Huber et al., 2011). Unlike the *rle* eruption, the *rln* samples give no insights about variations of magma conditions during ascent. The crystallization of plagioclase microlites should be ubiquitous according my equilibrium simulations, but they are only found in the *rln* lavas. The absence of plagioclase microlites in the *rln* pumices are explained by a slower diffusivity of major elements in the melt to form plagioclase than the magma ascent rate. In this way, the explosive-effusive transition of Las Nieblas eruption occurred due to a deceleration of magma ascent, as in other rhyolitic eruptions (e.g., Cassidy et al., 2018; Castro and Gardner, 2008).

5.12. Evolution of the storage and ascent conditions of rhyolitic melts in LdM

The postglacial rhyolites of LdM come from a dacitic mush-type reservoir located at 2-8 km-depth which has evolved spatially and with time. The postglacial eruptive stage of LdM started with the most voluminous eruption of this period (>20 km^3), the rhyolite of the Laguna del

Maule (*rdm*; 23 ky). Of the LdM postglacial rhyolites, the *rdm* magmas are the most silicic, were stored in the deepest range within the dacitic reservoir (2.2-2.5 kbar) and were the only silicic melts that interacted with mafic magmas from below. These characteristics should be related to the high magnitude of this eruption (e.g., Feeley et al., 2008; Pallister et al., 1992). The first rhyolitic eruption after *rdm*, the rhyolite of Los Espejos (*rle*), occurred in the northwest of the LdM complex after 4 ky (Andersen et al., 2017; Singer et al., 2000). The *rle* magmas were stored shallower than the *rdm* magmas (1.7-2.3 kbar) with narrow ranges of T-H_2O because of a protracted melt accumulation and magma crystallization (e.g., Andersen et al., 2019; Anderson et al., 2000). The *rle* deposits, rocks and crystals show no features of interaction with mafic magmas and the volume of the *rle* deposits is much smaller than the volume of the *rdm* deposits (Chapter 2; Fierstein, 2018). After that, the accumulation of a less silicic and more alkaline rhyolitic melt has moved laterally according to the distribution of the younger rhyolite lava flows (Singer et al., 2014). Unlike the magma pocket supplier of *rle*, the younger magma pockets are not compositionally and thermally uniform because of a depth range of temperature, mineral associations and mineral compositions. The magma pockets are moving upwards: the supplier of *rln* (erupted 1.8 ka BP) was located at 1.5-2.0 kbar and the current local inflation, north of the *rln* lava flow, is attributed to magma and fluid accumulation at 0.9-1.1 kbar (Miller et al., 2017).

I propose that the magma accumulation producing the current local inflation follows the same evolution pattern of the previous rhyolite supplier: 1. It is located inside the dacitic crystal-mush reservoir; 2. It has moved laterally north from the *rln*, the last eruption of LdM; 3. It is shallower than the magma pocket of *rln*; 4. It is vertically heterogeneous showing a depth range of temperature, crystallinity, mineral associations and mineral compositions; 5. It could be interacting with fluids from below; 6. It is not interacting with deeper, hotter and mafic magmas. In this way, I suggest that a potential future rhyolite eruption in LdM is likely to show

the same styles and transitions as the *rln* eruption, that is, beginning with one or more subplinian phases and ending with the formation of one or more obsidian lava flows.

5.13. Conclusion

The Laguna del Maule volcanic complex overlies a mush-type dacitic magma reservoir with rhyolitic interstitial melt which feeds the postglacial rhyolitic eruptions (Fig. 5.12). The dacitic magma is 67-69 wt.% SiO_2, water nearly saturated, and the interstitial melt is rhyolitic of 74-77 wt.% SiO_2. The dacitic mush-type reservoir forms An_{20-35} plagioclase and biotite. In this study, I showed that subtle variations of the storage conditions within the dacitic reservoir controlled the mineral composition and textures of rhyolites and are key to understanding the crystallization during ascent and subsequent eruption styles and transitions.

The rhyolite of Laguna del Maule, the most silicic and voluminous postglacial rhyolite of LdM, was fed by magmas accumulated in hot (830-870 °C) and deep (2.2-2.5 kbar) conditions. The high magnitude of the *rdm* eruption in comparison with the younger rhyolitic eruptions is explained by the interaction of the silicic melt with hotter mafic-andesitic magmas. The mafic magma inputs heated the rhyolite magma by >30 °C which may have triggered a magmatic ebullition at the top of the dacitic reservoir. Due to the high magma temperature and rapid ascent microcryst crystallization was avoided. By contrast, the rhyolite of Los Espejos was fed by magmas accumulated in colder (775-805 °C) and shallower (1.7-2.3 kbar) conditions. As the *rle* magmas did not interact with mafic magmas, the explosive phase developed into an obsidian lava due to a gradual decrease of the ascent rate, a high strain rate, and a subtle cooling. The decreasing magma ascent rate is suggested by the gradual increase of the vesicular obsidian clasts in the upper part of the *rle* deposits. The high strain rate is suggested by the elongate pumices with tube bubbles within the layers with the biggest clasts. Evidence of the subtle

cooling during the explosive-effusive transition is the biotite breakdown, which developed anhedral biotite phenocrysts, Ba concentration spikes in plagioclase and K-feldspar microlite crystallization during the explosive stage due to the magma temperature above the biotite liquidus during ascent.

The rhyolite of Las Nieblas is the youngest and one of the most alkaline postglacial rhyolites of LdM. The storage conditions of the *rln* magmas within the dacitic reservoir varied spatially and temporally. In a first stage, a 1.5-2.0 kbar vertical temperature grading around the biotite liquidus temperature crystallized An_{26-33} plagioclases only associated with biotite at <1.8 kbar. In a second stage, the dacitic magma pocket was cooled and formed An_{23-27} plagioclases associated with biotite. The stepped-normal zoning of plagioclases and the higher trace elements in plagioclases compared with the plagioclase compositions of the early postglacial rhyolites suggest that the *rln* eruption was triggered by the injection of fluids derived from degassing of mafic magmas. The transition to the effusive stage occurred by a deceleration of the magma ascent according to the crystallization of plagioclase microlites in obsidian lavas.

During the postglacial stage of LdM, the rhyolite storage conditions have followed a continuous pattern of composition, location, internal settings, and interaction with deeper fluids and magmas. Due to the spatial and temporal proximity, the current state of LdM is comparable with the conditions that preluded the Las Nieblas eruption. The local uplift north of the *rln* lava flow could be due to melt and/or fluid accumulation within the dacitic mush. A protracted thermal mixing due to fluid accumulation or melt mobilization within the dacitic mush could trigger a future silicic eruption. The most probable scenario of a potential future eruption is likely a subplinian phase followed by the eruption of an obsidian lava.

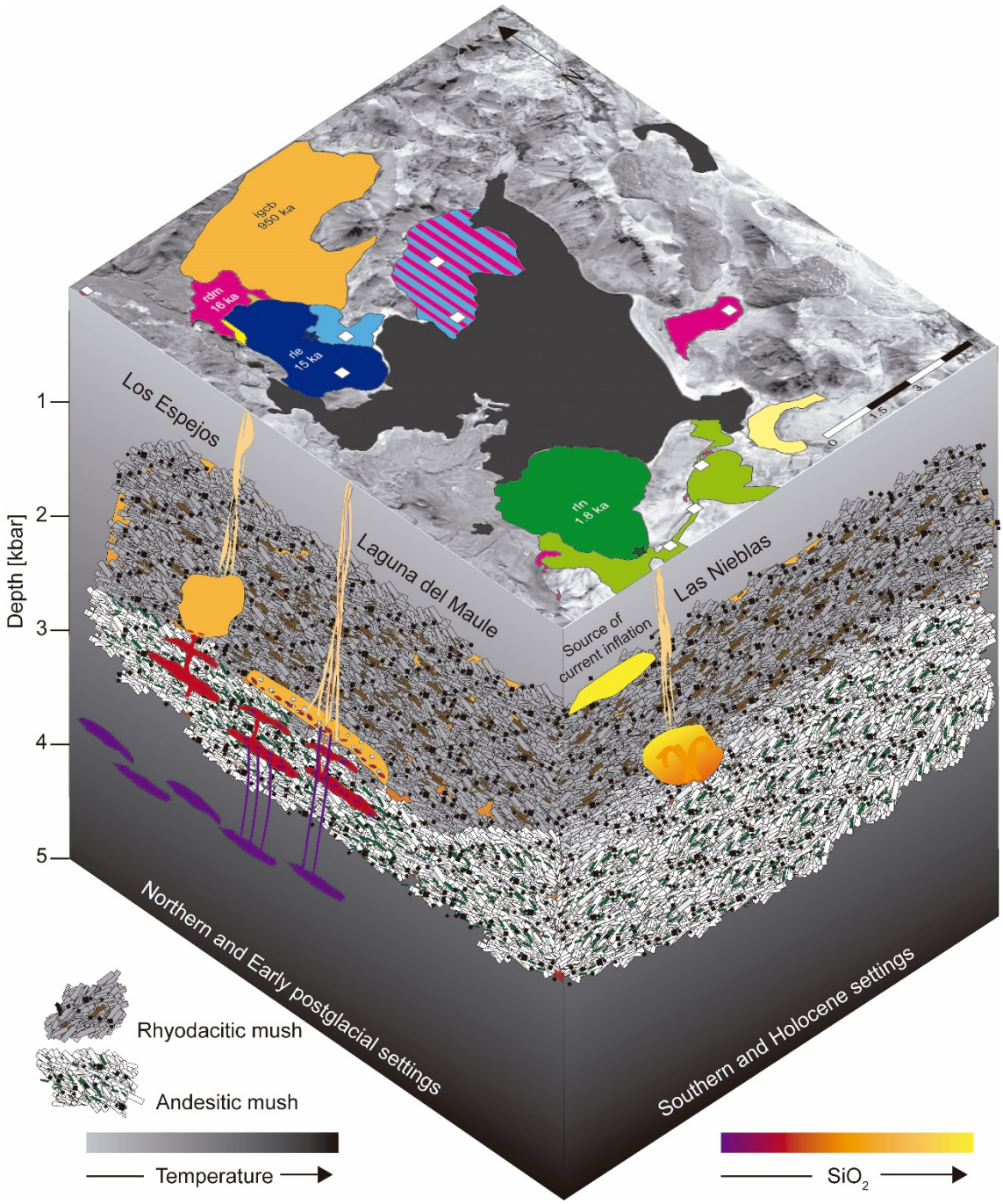

Fig. 5.12: Storage conditions of the studied rhyolites of Laguna del Maule volcanic complex. Northern area is supplied by andesitic and basaltic-andesitic magmas. The *rdm* magmas were stored into an An_{26-35} plagioclase dacitic magma pocket with interstitial ~77 wt.% SiO_2 magma. The eruption was triggered by basaltic andesite and andesitic magma inputs in the dacitic mush. The *rle* eruption was triggered by a small cryptic intermediate magma recharge. By contrast, the Southern area does not have clues of mafic magma inputs or eruptions. Before the *rln* eruption, a vertically heterogeneous magma chamber inside the rhyodacitic is characterized by grading of temperature and mineralogy. This eruption was produced by melt and fluid mobilization.

5.14. Highlights

- The magma storage and ascent conditions are key to understanding variations in the styles and transitions of the LdM rhyolite eruptions.
- The LdM rhyolite magma come from small and ephemeral melt-rich magma pockets within a crystal-rich dacitic mush.
- Mafic magma extractions played a key role in the high intensity of the *rdm* eruption because they input volatiles and heat into the rhyolite magma, aiding a fast magma ascent rate.
- The invariable anorthite content of the *rle* plagioclase phenocrysts suggests a protracted homogeneous rhyolite storage. The anhedral biotite phenocrysts, lack of biotite microcrysts and syn-eruptive k-feldspar crystallization suggest that the *rle* eruption was triggered by cryptic magma recharges that could also produce biotite breakdown.
- Unlike *rle*, the *rln* magma storage had a vertical grading of temperature and crystallinity before a thermal mixing that triggered the *rln* eruption. The lack of plagioclase microlites in the *rln* pumices suggests that the explosive-effusive transition was facilitated by a sharp decrease of the magma ascent rate.
- Geothermobarometry and MELTS modelling suggest that the rhyolite pockets within the LdM dacitic mush became shallower, hotter and more heterogeneous with time.

Acknowledgments

This work was supported by Becas Chile PhD scholarship [grant number 72160339 CC]. Thanks go to Barbara Buono-Core, Carolina Geoffroy, Rayen Gho, Christian Pizarro and Florencia Rosas, students of University of Chile, for their assistance in field, to Stuart Kearns and Ben Buse for their assistance and guidance in microprobe analysis, and to Miguel Angel Parada and Jenny Riker for their fruitful comments.

References

Andersen, N. L., Singer, B. S., Coble, M. A., 2019. Repeated Rhyolite Eruption from Heterogeneous Hot Zones Embedded Within a Cool, Shallow Magma Reservoir. Journal of Geophysical Research: Solid Earth.

Andersen, N. L., Singer, B. S., Costa, F., Fournelle, J., Herrin, J. S., Fabbro, G. N., 2018. Petrochronologic perspective on rhyolite volcano unrest at Laguna del Maule, Chile. Earth and Planetary Science Letters, 493, 57-70.

Andersen, N.L., Singer, B.S., Jicha, B.R., Beard, B.L., Johnson, C.M., Licciardi, J.M., 2017. Pleistocene to Holocene growth of a large upper crustal rhyolitic magma reservoir beneath the active Laguna del Maule volcanic field, central Chile. Journal of Petrology, 58, 85–114.

Anderson, A. T., Davis, A. M., Lu, F., 2000. Evolution of Bishop Tuff rhyolitic magma based on melt and magnetite inclusions and zoned phenocrysts. Journal of Petrology, 41(3), 449-473.

Aragon, R., McCallister, R.H., Harrison, H.R., 1984. Cation diffusion in titanomagnetites. Contributions to Mineralogy and Petrology, 85(2), 174-185.

Baker, D. R., Brun, F., O'shaughnessy, C., Mancini, L., Fife, J. L., Rivers, M., 2012. A four-dimensional X-ray tomographic microscopy study of bubble growth in basaltic foam. Nature Communications, 3, 1135.

Barbey, P., 2007. Diffusion-controlled biotite breakdown reaction textures at the solid/liquid transition in the continental crust. Contributions to Mineralogy and Petrology, 154(6), 707-716.

Berlo, K., Blundy, J., Turner, S., Hawkesworth, C., 2007. Textural and chemical variation in plagioclase phenocrysts from the 1980 eruptions of Mount St. Helens, USA. Contributions to Mineralogy and Petrology, 154(3), 291-308.

Bouvet de Maisonneuve, C., Dungan, M. A., Bachmann, O., Burgisser, A., 2012. Petrological insights into shifts in eruptive styles at Volcán Llaima (Chile). Journal of Petrology, 54(2), 393-420.

Cáceres, F., Castruccio, Á., Parada, M. A., 2018. Morphology, Effusion Rates, and Petrology of Postglacial Lavas of Laguna del Maule Volcanic Field, Chilean Andes, and Implications for Their Plumbing System. Geochemistry, Geophysics, Geosystems, 19(12), 4925-4944.

Cashman, K., Blundy, J., 2013. Petrological cannibalism: the chemical and textural consequences of incremental magma body growth. Contributions to Mineralogy and Petrology, 166(3), 703-729.

Cassidy, M., Castro, J. M., Helo, C., Troll, V. R., Deegan, F. M., Muir, D., Neave, D. A., Mueller, S. P., 2016. Volatile dilution during magma injections and implications for volcano explosivity. Geology, 44(12), 1027-1030.

Cassidy, M., Manga, M., Cashman, K., Bachmann, O., 2018. Controls on explosive-effusive volcanic eruption styles. Nature communications, 9(1), 2839.

Castro, J. M., Gardner, J. E., 2008. Did magma ascent rate control the explosive-effusive transition at the Inyo volcanic chain, California?. Geology, 36(4), 279-282.

Cembrano, J., Lara, L., 2009. The link between volcanism and tectonics in the southern volcanic zone of the Chilean Andes: a review. Tectonophysics, 471(1-2), 96-113.

Cooper, K. M., Kent, A. J., 2014. Rapid remobilization of magmatic crystals kept in cold storage. Nature, 506(7489), 480.

Costa, F., Chakraborty, S., Dohmen, R., 2003. Diffusion coupling between trace and major elements and a model for calculation of magma residence times using plagioclase. Geochimica et Cosmochimica Acta, 67(12), 2189-2200.

Deer, W. A., Howie, A., & Sussman, J. (1986). An interdiction to rock-forming minerals. 17th. Howie, J. Sussman–Longman Ltd.

Di Genova, D., Kolzenburg, S., Wiesmaier, S., Dallanave, E., Neuville, D. R., Hess, K. U., Dingwell, D. B., 2017. A compositional tipping point governing the mobilization and eruption style of rhyolitic magma. Nature, 552(7684), 235.
Dufek, J., Bachmann, O., 2010. Quantum magmatism: Magmatic compositional gaps generated by melt-crystal dynamics. Geology, 38(8), 687-690.
Fabbrizio, A., Rouse, P. J., Carroll, M. R., 2006. New experimental data on biotite+ magnetite+ sanidine saturated phonolitic melts and application to the estimation of magmatic water fugacity. American Mineralogist, 91(11-12), 1863-1870.
Feeley, T. C., Sharp, Z. D., 1996. Chemical and hydrogen isotope evidence for in situ dehydrogenation of biotite in silicic magma chambers. Geology, 24(11), 1021-1024.
Feeley, T. C., Wilson, L. F., Underwood, S. J., 2008. Distribution and compositions of magmatic inclusions in the Mount Helen dome, Lassen Volcanic Center, California: insights into magma chamber processes. Lithos, 106(1-2), 173-189.
Feigl, K.L., Le Mével, H., Ali, S.T., Cordova, L., Andersen, N.L., DeMets, C., and Singer, B.S., 2014. Rapid uplift in Laguna del Maule volcanic field of the Andean Southern Volcanic Zone (Chile) 2007–2012. Geophysical Journal International, 196, 885–901, doi: 10.1093/gji/ggt438.
Fierstein, J., Postglacial eruptive history established by mapping and tephra stratigraphy provides perspectives on magmatic system beneath Laguna del Maule, Chile, Presented at: AGU Chapman Conference on Merging Geophysical, Petrochronologic, and Modeling Perspectives of Large Silicic Magma Systems, Quinamavida, Chile, 2018.
Ghiorso, M. S., Evans, B. W., 2008. Thermodynamics of rhombohedral oxide solid solutions and a revision of the Fe–Ti two-oxide geothermometer and oxygen-barometer. American Journal of Science, 308, 957–1039.
Ghiorso, M. S., Gualda, G. A., 2015. An H2O–CO2 mixed fluid saturation model compatible with rhyolite-MELTS. Contributions to Mineralogy and Petrology, 169(6), 53.
Ginibre, C., Worner, G., Kronz, A., 2002. Minor- and trace-element zoning in plagioclase: implications for magma chamber processes at Parinacota volcano, northern Chile. Contributions to Mineralogy and Petrology 143, 300-315.
Gonnermann, H. M., Manga, M., 2007. The fluid mechanics inside a volcano. Annual Reviews of Fluid Mechanics, 39, 321-356.
Gualda, G. A., Ghiorso, M. S., 2015. MELTS_Excel: A Microsoft Excel-based MELTS interface for research and teaching of magma properties and evolution. Geochemistry, Geophysics, Geosystems, 16(1), 315-324.
Gualda, G. A., Ghiorso, M. S., Lemons, R. V., Carley, T. L., 2012. Rhyolite-MELTS: a modified calibration of MELTS optimized for silica-rich, fluid-bearing magmatic systems. Journal of Petrology, 53(5), 875-890.
Guo, J., Green, T. H., 1990. Experimental study of barium partitioning between phlogopite and silicate liquid at upper-mantle pressure and temperature. Lithos, 24(2), 83-95.
Hildreth, W., Godoy, E., Fierstein, J., Singer, B.S., 2010. Laguna del Maule volcanic field: eruptive history of a Quaternary basalt to rhyolite distributed volcanic field on the Andean range crest in central Chile. Servicio Nacional de Geología y Minería, Boletin 63.
Holland, T., Blundy, J., 1994. Non-ideal interactions in calcic amphiboles and their bearing on amphibole-plagioclase thermometry. Contributions to mineralogy and petrology, 116(4), 433-447.
Huber, C., Bachmann, O., Dufek, J., 2011. Thermo-mechanical reactivation of locked crystal mushes: melting-induced internal fracturing and assimilation processes in magmas. Earth and Planetary Science Letters, 304, 443–454
Huber, C., Bachmann, O., Manga, M., 2009. Homogenization processes in silicic magma chambers by stirring and mushification (latent heat buffering). Earth Planet. Sci.

Lett. 283:38–47. https://doi.org/10.1016/j.epsl.2009.03.029.
Leake, B. E., Woolley, A. R., Arps, C. E., Birch, W. D., Gilbert, M. C., Grice, J. D., Hawthorne, F. C., Kato, A., Kisch, H. J., Krivovichev, V. G., Linthout, K., Laird, J., Mandarino, J. A., Maresch, W.V., Nickel, E. H., Rock, N. M., Schumacher, J. C., Smith, D. C., Stephenson, N. C., Ungaretti, L., Whittaker, E. J., Guo, Y., 1997. Report. Nomenclature of amphiboles: report of the subcommittee on amphiboles of the international mineralogical association commission on new minerals and mineral names. Mineralogical magazine, 61(2), 295-321.
Le Mével, H., Gregg, P. M., Feigl, K. L., 2016. Magma injection into a long-lived reservoir to explain geodetically measured uplift: Application to the 2007-2014 unrest episode at Laguna del Maule volcanic field, Chile. Journal of Geophysical Research: Solid Earth, 121, 6092–6108. https://doi.org/10.1002/2016JB013066
Miller, C. A., Williams-Jones, G., Fournier, D., Witter, J., 2017. 3D gravity inversion and thermodynamic modelling reveal properties of shallow silicic magma reservoir beneath Laguna del Maule, Chile. Earth and Planetary Science Letters, 459, 14-27.
Newman, S., Lowenstern, J. B., 2002. VolatileCalc: a silicate melt–H2O–CO2 solution model written in Visual Basic for excel. Computers & Geosciences, 28(5), 597-604.
Pallister, J. S., Hoblitt, R. P., Reyes, A. G., 1992. A basalt trigger for the 1991 eruptions of Pinatubo Volcano?. Nature, 356(6368), 426.
Preece, K., Barclay, J., Gertisser, R., Herd, R. A., 2013. Textural and micro-petrological variations in the eruptive products of the 2006 dome-forming eruption of Merapi volcano, Indonesia: implications for sub-surface processes. Journal of Volcanology and Geothermal Research, 261, 98-120.
Putirka, K., 2016. Amphibole thermometers and barometers for igneous systems, and some implications for eruption mechanisms of felsic magmas at arc vol-canoes. American Mineralogist, 101, 841–858. https://doi .org /10 .2138 /am -2016 -5506.
Ridolfi, F., Renzulli, A., 2012. Calcic amphiboles in calc-alkaline and alkaline magmas: thermobarometric and chemometric empirical equations valid up to 1,130° C and 2.2 GPa. Contributions to Mineralogy and Petrology, 163(5), 877-895.
Ridolfi, F., Renzulli, A., Puerini, M., 2010. Stability and chemical equilibrium of amphibole in calc-alkaline magmas: an overview, new thermobarometric formulations and application to subduction-related volcanoes. Contributions to Mineralogy and Petrology, 160(1), 45-66.
Righter, K., Carmichael, I. S., 1996. Phase equilibria of phlogopite lamprophyres from western Mexico: biotite-liquid equilibria and P-T estimates for biotite-bearing igneous rocks. Contributions to Mineralogy and Petrology, 123(1), 1-21.
Rubin, A. E., Cooper, K. M., Till, C. B., Kent, A. J., Costa, F., Bose, M., Gravley, D., Deering, C., Cole, J., 2017. Rapid cooling and cold storage in a silicic magma reservoir recorded in individual crystals. Science, 356(6343), 1154-1156.
Ruprecht, P., Wörner, G., 2007. Variable regimes in magma systems documented in plagioclase zoning patterns: El Misti stratovolcano and Andahua monogenetic cones. Journal of Volcanology and Geothermal Research, 165(3), 142-162.
Shea, T., Hammer, J.E., 2013. Kinetics of cooling-and decompression-induced crystallization in hydrous mafic-intermediate magmas. Journal of Volcanology and Geothermal research, 260, 127-145.
Singer, B. S., Andersen, N. L., Le Mevel, H. et al., 2014. Dynamics of a large, restless, rhyolitic magma system at Laguna del Maule, southern Andes, Chile. GSA Today 24, 4–10.
Singer, B. S., Dungan, M. A., Layne, G. D., 1995. Textures and Sr, Ba, Mg, Fe, K, and Ti compositional profiles in volcanic plagioclase: clues to the dynamics of calc-alkaline magma chambers. American Mineralogist, 80(7-8), 776-798.
Singer, B., Hildreth, W., Vincze, Y., 2000. 40Ar/39Ar evidence for early deglaciation of the central Chilean Andes. Geophysical Research Letters, 27(11), 1663-1666.

Tarasewicz, J., Brandsdóttir, B., White, R. S., Hensch, M., Thorbjarnardóttir, B., 2012. Using microearthquakes to track repeated magma intrusions beneath the Eyjafjallajökull stratovolcano, Iceland. Journal of Geophysical Research: Solid Earth, 117(B9).
Tepley III, F. J., Davidson, J. P., Clynne, M. A., 1999. Magmatic interactions as recorded in plagioclase phenocrysts of Chaos Crags, Lassen Volcanic Center, California. Journal of Petrology, 40(5), 787-806.
Till, C. B., Vazquez, J. A., Boyce, J. W., 2015. Months between rejuvenation and volcanic eruption at Yellowstone caldera, Wyoming. Geology, 43(8), 695-698.
Ubide, T., Kamber, B.S., 2018. Volcanic crystals as time capsules of eruption history. Nature communications, 9(1), 326.
Van Orman, J. A., Crispin, K. L., 2010. Diffusion in oxides. Reviews in Mineralogy and Geochemistry, 72(1), 757-825.
Waters, L. E., Lange, R. A., 2015. An updated calibration of the plagioclase-liquid hygrometer-thermometer applicable to basalts through rhyolites. American Mineralogist, 100(10), 2172-2184.
Wespestad, C., Thurber, C. H., Andersen, N. L., Singer, B. S., Cardona, C., Zeng, X., et al., 2019. Magma Body Beneath Laguna del Maule Volcanic Field Imaged with Surface Wave Tomography. Journal of Geophysical Research: Solid Earth, 124. https://doi.org/10.1029/2018JB016485.

6. Conclusion

The postglacial (<25 ky) deposits of the Laguna del Maule volcanic complex (LdM) derive from more than 35 eruptions covering a range of compositions from basalt to rhyolites (51-77 wt.% SiO_2) of which more than 20 are rhyodacites (9) and rhyolites (12). The silicic deposits include pyroclastic density currents, fall deposits and lava flows. These can all be erupted during a single eruption sequence, but the types of deposits and their stratigraphic order vary among the silicic eruptions of LdM, reflecting a diversity of eruption styles and transitions. Despite the potential for another silicic eruption of this active volcano, the eruptive styles and transitions of the many postglacial silicic eruptive units have not been studied in detail before this thesis. Most recent studies focused on the conditions of the magmatic system below LdM and its temporal and compositional evolution in the last 25 ky (e.g., Andersen et al., 2017; Singer et al., 2014). Some geophysical studies have constrained the morphology of the reservoir that generated the rhyolites (Feigl et al., 2014), location (Le Mevel et al., 2016) and crystallinity (Wespestad et al., 2019) in order to explain the source of the current inflation in LdM (Miller et al., 2017). There has been some analysis of the physical characteristics of the deposits, but these studies mainly focused on the lava flows (e.g., Cáceres et al., 2018; Hildreth et al., 2010).

This thesis presents new insights about the physical characteristics of the pyroclastic deposits of the Laguna del Maule (*rdm*), Los Espejos (*rle*) and Las Nieblas (*rln*) rhyolite units in LdM, and the eruptive styles and transitions which formed those deposits. The key conclusions for the three eruptions are highlighted below (see a summary of the key characteristics in Table 6.1), followed by some future directions for the study of the silicic eruptive transitions in Laguna del Maule.

Table 6.1: Sedimentological, physical and petrological key characteristics of the three eruptions (*rdm*, *rle* and *rln*) studied.

	rdm	*rle*	*rln*
Deposits related to the last eruption phase	PDCs	Lava flow	Lava flow
Pumice textures	Elongate + tube bubbles	Microvesicular	Elongate + tube bubbles
Pumice density [g cm^{-3}]	0.2-0.8	0.7-1.7	0.6-1.9
Viscous permeability [m^2]	0.8-22 x 10^{-11}	0.3-7.3 x 10^{-11}	n.a.
Inertial permeability [m]	1.4-2900 x 10^{-8}	1.6-8.5 x 10^{-8}	n.a.
Main component with pumice	Mafic juveniles	Vesicular obsidians	Vesicular obsidians
An content in plagioclase phenocrysts	28-34	22-23	26-30
Mafic Mineral	Hornblende	Biotite	Biotite
Groundmass pumices	--	Plag + K-feld + ox	--
Groundmass obsidians	--	Plag + Bt + Ox	Plag
P in reservoir [kbar]	2.2-2.5	1.7-2.3	1.5-2.0
T in reservoir [°C]	830-870	785-810	815-855
Origin of the eruption transition	Rhyolite-mafic magma mingling	Outgassing + decreasing ascent rate	Decrease of magma ascent rate

6.1. Rhyolite of Laguna del Maule (*rdm*)

The rhyolite of Laguna del Maule is the first (23 ky; Singer et al., 2000), the most silicic (~77 wt.% SiO_2) and the most voluminous (>20 km^3; Fierstein, 2018) postglacial deposit of LdM. It consists of two similar subunits which are distinguished from each other due to subtle differences in their whole-rock geochemistry, componentry and the physical characteristics of the pumice clasts: the *rdm* 1 is slightly more alkaline and more silicic, does not have mafic and

andesitic juveniles and has low-density (0.25-0.65 g cm^{-3}) aphyric pumices; instead the *rdm* 2 has denser pumice clasts (modal density = 0.80 g cm^{-3}) of low crystallinity mostly containing antecrysts of plagioclase and hornblende co-erupted with mafic and andesitic juveniles and granitoid lithics. Both *rdm* subunits have not obsidian clasts or lavas. I propose that the *rdm* Plinian eruption began with residual near-liquidus rhyolitic magma from the top of the magma reservoir suggested by the high silica and alkali content and the very low crystallinity (*rdm* 1).

As the magma ascent rate increased according to the high porosity of the pumice clasts, the fragmentation level went down and deeper magmas were extracted, allowing the interaction of the rhyolitic magmas with mafic and andesitic magmas. The increasing content of granitoid lithics support the hypothesis of the downward propagation of the fragmentation level as these lithics may represent pieces of the crystal-rich dacitic mush dragged by the rhyolitic melts or come from solid igneous bodies surrounding the magma reservoir. The increasing content of mafic and andesitic juveniles reveals the rhyolite-mafic magma interaction and suggests that magma mixing was not the eruption triggering but a factor that increased the eruption intensity and developed an ignimbrite-forming eruption (*rdm* 2). As the plagioclase and hornblende antecrysts do not show disequilibrium textures, I suggest that the time period between the rhyolitic-mafic magma interaction and the eruption of the *rdm* 2 unit was short. The *rdm* 2 began forming an ash fall deposit that crops out >50 km east from vent (Gho et al., in prep). The lower porosity, tubular bubbles and high permeability of the *rdm* 2 pumice clasts suggest that the magma ascent rate decreased, the total strain increased and the outgassing became more effective allowing the transition to multiple pyroclastic density currents.

Most of the *rdm* pumices show the highest porosities and bubble number densities analyzed in this thesis, consistent with a high magma ascent rate and eruption intensity. The elongate pumice clasts with tubular bubbles have a high pore connectivity (>0.9) which together with

the high anisotropy produces a high magma permeability (>10^{-12} m^2) associated with an efficient magma outgassing. The porosities and viscous permeabilities measured in the *rdm* pumices coincide with the values of other tube pumices from Plinian eruptions (Wright et al., 2006) and with the most permeable pumices from pyroclastic flows (Nakamura et al., 2008). As the *rdm* pumices were collected in the upper part of the pyroclastic sequence, I suggest that their high porosities and high permeabilities respond to a decrease of the eruption intensity in the last stage of the *rdm* eruption. In this way, I propose that the pumices from the lower sequences could show similar porosities but with lower permeabilities. The Plinian *rdm* eruption ceased before a pervasive bubble collapse occurred as there are not pyroclastic obsidians and lava flows associated.

The *rdm* magmas were stored in a deep (2.2-2.5 kbar) and hot (835-870 °C) rhyolitic magma pocket within the dacitic mush-type reservoir. This high temperature is over the biotite liquidus temperature explaining the lack of biotites in the *rdm* pumices. The *rdm* pumices have plagioclase phenocrysts of An_{26-34} and hornblende antecrysts associated with plagioclase crystals of An_{41-49}. I propose that the antecrysts come from the andesitic magmas that interacted with the rhyolitic melts during the eruption. Both mafic and andesitic magmas heated the silicic melt by ~30 °C, which was enough to overcome the *rdm* liquidus temperature. The very-low crystallinity and the superliquidus conditions aided a fast magma ascent rate and the high explosivity of this eruption.

6.2. Rhyolite of Los Espejos (*rle*)

The rhyolite of Los Espejos is the first (19 ky; Andersen et al., 2017) and most silicic (75.5-76.0 wt.% SiO_2) eruptive unit after *rdm*. Unlike *rdm*, the *rle* pyroclastic deposits have obsidian clasts and no mafic juveniles or enclaves. I propose that the *rle* eruption began with external

water interacting with the silicic magma, forming a phreatomagmatic phase with pulses of more phreatic or more magmatic activity (*rle* 1). The magmatic component of this phase increased until it developed into a subplinian magmatic eruption (*rle* 2). The deposits formed during the *rle* 2 phase suggest pulsatory activity before the paroxysm, represented by a layer with the biggest and most elongate pumice clasts of the *rle* fall deposit. After the paroxysm, the eruption intensity decreased aided by effective outgassing and high total strain which promoted the formation of dense pumice and vesicular obsidian clasts (*rle* 3) before the complete transition to the effusive phase (*rle* 4).

In general, the *rle* pumices are dense (0.7-1.7 g cm^{-3}) with elongate and flattened bubbles that show features of bubble collapse and strain localization which are more clear with the stratigraphic height (eruption time). Even at relatively low porosities the *rle* pumices have a high connectivity and high permeability. Our simulations of gas flowing through porous media from X-ray tomograms of the pumices reveal that the gas flow is localized in the widest and straightest bubbles, which allows a high permeability to be maintained despite of the decreasing of the pumice (magma) porosity. The high permeabilities with a range of porosities is consistent with other subplinian pumices. The high permeabilities allowed an effective outgassing during ascent, aiding the gas escape during the densification of magma. Because of the low porosity of pumices and the increasing fraction of vesicular obsidians with height, I propose that the late stage of the *rle* explosive phase can be explained by an upward propagation of the fragmentation level which enlarged the distance travelled by magma within the volcanic conduit and increased the total strain. At the top of the volcanic conduit, the strain and strain rates are radially zoned, producing the wide diversity of textures within the juvenile clasts. The protracted high strain rates and magma outgassing produced a widening of the sectional area with high total strain, increasing the fraction of obsidian clasts. In the conduit margins, the high total strain could overcome the glass transition, fracturing the silicic magma and increasing the

magma outgassing. The increase of the abundance of obsidian clasts preceding the formation of the lava flow suggest a gradual explosive-effusive transition of the Los Espejos eruption, as it was observed during the recent rhyolite eruptions in Chaitén (2008) and Cordón Caulle (2011).

The *rle* magmas were stored at 1.7-2.3 kbar and 780-805 °C. The unzoned plagioclase and biotite phenocrysts suggest protracted stable storage conditions before the eruption. In the pumices, the biotite phenocrysts have digested rims, which together with the crystallization of K-feldspar microlites suggest biotite breakdown during the magma ascent of the explosive phase. By contrast, the obsidian clasts and lavas have subhedral to euhedral biotite crystals with no K-feldspar microlites. Based on MELTS simulations, these differences in mineralogy and textures between the pumice and obsidian clasts are explained by the rhyolite magmas ascended 10-15 °C colder during the effusive stage. Despite this subtle magma cooling, the decrease of the magma ascent rate and the volatile loss during ascent promoted the magma densification and the transition to the effusive stage.

6.3. Rhyolite of Las Nieblas (*rln*)

The rhyolite of Las Nieblas is the youngest and one of the most alkaline deposits of LdM (1.8 ky; Fierstein, 2018). It consists of one pyroclastic flow, a co-erupted fall deposit and lava flow, a second lava flow which is the most voluminous of the LdM volcanic complex, and minor eruptive centers (Cáceres et al., 2018). The *rln* magmas were stored at 1.5-2.0 kbar and 815-855 °C. The *rln* samples have the same mineral association as the *rle* samples but with higher crystallinities. The plagioclase phenocrysts are more anorthitic and show a wider range of An content than those of *rle* (An_{20-35}). The biotite phenocrysts are elongate suggesting that they were formed near the liquidus. Indeed, MELTS simulations show that the *rln* magmas were

stored in a vertical graded magma reservoir where the most anorthitic cores were formed in a warmer and deeper section without biotites, and the most albitic cores were formed in a colder and shallower section with biotites. Based on the lack of mafic juveniles and antecrysts in the *rln* products, I suggest that the thermal and compositional gradient of the *rln* reservoir eased the eruption. The pumices have glassy groundmass and the obsidian clasts only show plagioclase microlites. The simulated conditions of the *rln* magmas show that at equilibrium, plagioclase is a ubiquitous phase of the rln magmas, suggesting that the transition to the lava formation phase was controlled by a rapid decrease of the magma ascent rate which allowed time for plagioclase crystallization.

6.4. Postglacial evolution and current scenario of the LdM volcanic complex

The postglacial stage of the LdM volcanic complex began with its biggest (>20 km^3; Fierstein, 2018) and the most silicic (>77 wt.% SiO_2; Andersen et al., 2017) rhyolitic eruption, the ignimbrite of Laguna del Maule (*rdm*). *rdm* is the only LdM postglacial rhyolite carrying mafic and andesitic juveniles suggesting that a rhyolite-mafic magma interaction explains the high magnitude of this eruption. The *rdm* deposits have no obsidian clasts and lavas suggesting that any decrease of the eruption intensity was not enough to collapse or deform pervasively the magma bubbles to form the obsidian pockets. After *rdm*, most LdM eruptions were silicic (rhyolitic and rhyodacitic) and had various styles and transitions associated with voluminous (~1 km^3) obsidian lava flows (Cáceres et al., 2018). While the rhyolites do not show mafic juveniles, most basaltic-to-rhyodacitic pyroclastic deposits and lavas show mafic juveniles and enclaves (Hildreth et al., 2010), and antecrysts showing strong disequilibrium textures (Cáceres et al., 2018) suggesting a high interaction of magmas of different compositions and coming from different loci inside the LdM magmatic system.

The rhyolite eruptions of LdM are fed by interstitial rhyolitic melts coming from a dacitic mush-type reservoir. Based on the distribution of the rhyolite units, the magma pockets feeding the rhyolite eruptions have laterally moved through the dacitic mush. Petrological constraints from this thesis also suggest that the magma pockets are moving slightly upward in time. Miller et al. (2017) have shown that the current inflation of LdM is localized north of the *rln* lava flow – the last eruption of LdM – produced by a vertically elongate magma pocket within the dacitic mush at ~1 kbar. Like the *rln* magma pocket, this new magma pocket shows a vertical grading of temperature and crystallinity. Based on the whole evolution of the rhyolite storage conditions in LdM and on the proximity of the new magma body to the *rln* magma pocket, I suggest that a potential future rhyolitic eruption fed by this magma pocket would likely show eruption styles and transitions like those of *rln*, that is, a subplinian eruption followed by an effusive phase.

6.5. Future directions

6.5.1. Chapter 2

6.5.1.1. Study of the rdm tephra

In this thesis I described outcrops and collected samples from the proximal deposits of *rdm* but the small number of samples analyzed limited the interpretations of the eruption phases, styles and transitions of this rhyolite. I suggest the analysis of distal tephrostratigraphic logs in different directions from vent in order to improve the reconstruction of the *rdm* eruption and the analysis of the *rdm* tephra from the lower sequence. The reconstruction of the *rdm* eruption will allow to determine a possible vent location, to give insights about the eruption triggering, and a more detailed history of the eruption phases. An analysis of the *rdm* tephra from the lower sequence will allow to determine the physical characteristics of the pumice clasts and to validate my hypothesis of the lower magma permeabilities to avoid an efficient magma

degassing during ascent. Overall, a deeper analysis of the *rdm* pyroclastic deposits will improve our concerns of the origin of the ignimbrite-forming silicic eruptions and to speculate about the probability of a future highly explosive eruption like *rdm* in the Laguna del Maule volcanic complex.

6.5.1.2. Study of the rle pyroclastic obsidians

The *rle* pyroclastic obsidian clasts are gray to black, slightly transparent, and have a low crystallinity which consists of plagioclase and biotite phenocrysts. In Chapter 2 I suggested that most of the *rle* pyroclastic obsidians are juvenile clasts as they have the same glass composition and mineralogy as the pumice clasts, except for a small fraction of obsidian clasts from the *rle* unit 1 which are darker and almost aphyric. I proposed that the formation of the transparent obsidian clasts is related to shearing and degassing of silicic magma dependent on the radial and vertical-dependent total strain and to the fragmentation level; in this way, an upper fragmentation level and a closer to the conduit margin magma location enhance the development of obsidians. However, the obsidian clasts may also come from dikes and wallrock fractures filled with silicic magma, a shallow magma plug, welded fallback juvenile clasts or ash sintering (Gardner et al., 2019; Rust and Cashman, 2007). To validate my hypothesis, I recommend a further study of the pyroclastic obsidians from different layers of the *rle* pyroclastic sequence in order to reconstruct the formation of these rhyolitic clasts with time. The study should consider a classification of the obsidian clasts according to the color, groundmass glass composition, vesicularity, bubble textures, phenocrysts and microcrysts. In particular, the groundmass glass composition analysis should be focused on the comparison of the major elements with those from the pumice clasts, and on the quantification of volatile contents as an almost complete degassing is expected for the juvenile material (e.g., Castro et al., 2014; Rust and Cashman, 2007). Moreover, the analysis of bubble textures should be

emphasized on the aspect ratios in order to validate my hypothesis of the formation of obsidians related to a high total strain.

6.5.1.3. Study of volatile contents in the LdM rhyolites

The outgassing is key to controlling the silicic eruptive transitions (Cassidy et al., 2018). The explosive eruptions occur when the volatiles ascend coupled to the magma, instead the effusive eruptions occur when the volatiles may escape from and ascend quicker than the silicic magma (Rust and Cashman, 2004). In this way, it is expectable that the pumice groundmass has a slightly higher volatile content than the obsidian clasts. The *rle* pumice clasts analyzed in this thesis showed a consistent higher water content than the *rle* obsidian clasts validating my hypothesis of the pumices come from magma pockets ascending coupled to the volatiles and the obsidian clasts were mostly formed by the shearing and degassing of the same silicic magma closer to the vent margins. As only three *rle* pumice-obsidian pairs were analyzed I recommend doing more analysis in order to robust the data and interpretations.

6.5.2. Chapter 3

6.5.2.1. Control of the resolution in X-ray tomography analyses

The use of 3D images with submicrometric voxel size allows a better segmentation and separation of the objects within samples, and then a more accurate analysis of the number density and geometry of the bubble network within the silicic pumices (Ketcham and Carlson, 2001). These physical properties are linked with the eruption histories (e.g., Degruyter et al., 2010; Toramaru, 2006), so the quality of the acquired tomograms affect the interpretations of the processes that controlled the silicic magma during ascent (this thesis). As the sample size must be shortened in order to reduce the voxel size of the tomogram (Cnudde and Boone, 2013), the aim of improving the tomogram definition may bias the representativeness of the volume of interest and the analysis of the biggest objects (bubbles, crystals) within the silicic

pumices. May the voxel/sample size affect the physical properties (e.g., BND, BSD, porosity, connectivity, permeability) of the silicic pumices? Pamukcu and Gualda (2010) cut a set of cylinders of various diameters within one pumice clasts to show that the voxel/volume of interest size do affect the quantified number density and size distributions. I recommend applying a similar set up in order to explore how a set of different voxel/sample sizes could vary the bubble textures, porosities and simulated permeabilities.

6.5.3. Chapter 4

6.5.3.1. Heterogeneities inside the silicic pumices

The pumices formed by pulsatory silicic eruptions tend to show more heterogeneities than those from sustained explosive eruptions (Berg et al., 2016; Polacci et al., 2001; Schipper et al., 2013). First 2D textural analyses in this thesis show that the BND, BSD, bubble aspect ratios and bubble convexity are more heterogeneous in the densest pumices. In this thesis, I selected the barycenter of the biggest bubble (or the most connected bubble structure) as a reference to select the volume of interest (VOI) to run the permeability simulations inside some <-4φ pumice clasts. As the pumice clasts studied in this thesis are heterogeneous, the selection of the pumice size population and the VOI inside the clasts could bias the textural and permeability analyses. In this way, some questions are still unclear: Are the porosities and permeabilities also heterogeneous? Are the porosities and permeabilities simulated in this thesis the maximum possible for each clast? Are the porosities and permeabilities dependent on the size clast? For future studies, I recommend dividing the whole sample in various VOI of the same size, and to analyze porosities and bubble textures, in order to select the most representative region that be comparable to measurements in the whole pumice clasts. Moreover, to analyze how the permeability simulations in submicrometric volume of interests (e.g., Degruyter et al., 2010; Schipper et al., 2013) could be biasing the results and giving higher

values than the measurements in the same pyroclasts or in the bigger pumice clasts from the same eruption stage (e.g., Wright et al., 2006).

6.5.3.2. Understanding of the inertial permeability

The inertial permeability reduces the apparent permeability of a porous media by increasing the energy loss to inertial effects. In this thesis I measured the inertial permeability of *rdm* and *rle* pumices and compared those with a predicted inertial permeability by a Kozeny-Carman expression in order to understand the control of the bubble textures (pore geometry) on the inertial permeability. However, the inertial permeabilities measured in the laboratory are substantially lower than predicted by the Kozeny-Carman expression. The permeability simulations could not effectively explore the cause of this discrepancy because they did not include inertia. I suggest the use of Lattice-Boltzmann modelling to simulate the inertial effects and/or a correction of the Kozeny-Carman expression which considers the variation of the pore aperture and cross-sectional shapes of bubbles (as in the numerical approach in Zhou et al., 2019).

6.5.4. Chapter 5

6.5.4.1. Study of volatile contents in the LdM rhyolites

This thesis gives specific insights of the storage conditions of each magma pocket feeding some rhyolite eruptions in LdM. However, various assumptions were made to obtain those insights. I estimated water contents near saturation based on the application of a plagioclase-glass hygrometer (Waters and Lange, 2015) and MELTS simulations (Gualda et al., 2012). However, these estimates could be improved with measurements of water (and other volatiles if present) in melt inclusions. The Los Espejos plagioclase crystals lack suitable melt inclusions but there are sufficient melt inclusions in the younger rhyolites such as Las Nieblas. Furthermore, the horizontal heterogeneities of the dacitic mush proposed in this thesis and in other works (e.g.,

Cáceres et al., 2018) could be tested by measurements of trace elements in the rhyolite glasses (e.g., Anderson et al., 2000).

6.5.4.2. Study of the granitoid lithics from the rdm deposits

The upper part of the *rdm* pyroclastic deposits has <1% granitoid lithics that may be >1 m and have a variable content of k-feldspar phenocrysts (Section 2.5.2). Some authors have suggested that the granitoid lithics may represent pieces of the dacitic mush storing the rhyolitic melts (e.g., Andersen et al., 2019; Fierstein, 2018). Moreover, one of the arguments to validate the hypothesis of the downward propagation of the fragmentation level during the *rdm* eruption is the increasing volume fraction of the granitoid lithics with the stratigraphic height. However, there are not petrography and barometry analyses to determine the occurrence of remnant or reactive solidified melts inside the granitoid lithics to validate that they come from a crystalline mush, or to determine the pressure range of that crystal mush or solid igneous body. In this way, I recommend a broad study (e.g., petrography, geochemistry, mineral composition, geothermobarometry) of the petrology of the *rdm* granitoids.

References

Andersen, N. L., Singer, B. S., Coble, M. A., 2019. Repeated Rhyolite Eruption from Heterogeneous Hot Zones Embedded Within a Cool, Shallow Magma Reservoir. Journal of Geophysical Research: Solid Earth.

Andersen, N.L., Singer, B.S., Jicha, B.R., Beard, B.L., Johnson, C.M., Licciardi, J.M., 2017. Pleistocene to Holocene growth of a large upper crustal rhyolitic magma reservoir beneath the active Laguna del Maule volcanic field, central Chile. Journal of Petrology, 58, 85–114.

Anderson, A. T., Davis, A. M., Lu, F., 2000. Evolution of Bishop Tuff rhyolitic magma based on melt and magnetite inclusions and zoned phenocrysts. Journal of Petrology, 41(3), 449-473.

Berg, S.E., Troll, V.R., Deegan, F.M., Burchardt, S., Krumbholz, M., Mancini, L., Polacci, M., Carracedo, J.C., Soler, V., Arzilli, F., Brun, F. (2016). Heterogeneous vesiculation of 2011 El Hierro xeno-pumice revealed by X-ray computed microtomography. Bulletin of Volcanology, 78(12), 85.

Cáceres, F., Castruccio, Á., Parada, M. A., 2018. Morphology, Effusion Rates, and Petrology of Postglacial Lavas of Laguna del Maule Volcanic Field, Chilean Andes, and Implications for Their Plumbing System. Geochemistry, Geophysics, Geosystems, 19(12), 4925-4944.

Cassidy, M., Manga, M., Cashman, K., Bachmann, O., 2018. Controls on explosive-effusive volcanic eruption styles. Nature communications, 9(1), 2839.

Castro, J. M., Bindeman, I. N., Tuffen, H., Schipper, C. I., 2014. Explosive origin of silicic lava: textural and δD–H2O evidence for pyroclastic degassing during rhyolite effusion. Earth and Planetary Science Letters, 405, 52-61.

Cnudde, V., Boone, M.N., 2013. High-resolution X-ray computed tomography in geosciences: A review of the current technology and applications. Earth-Science Reviews 123, 1-17.

Degruyter, W., Bachmann, O., Burgisser, A., 2010. Controls on magma permeability in the volcanic conduit during the climactic phase of the Kos Plateau Tuff eruption (Aegean Arc). Bulletin of Volcanology 72, 63-74.

Dingwell, D. B., Lavallée, Y., Hess, K. U., Flaws, A., Marti, J., Nichols, A. R., Gilg, H. A., Schillinger, B., 2016. Eruptive shearing of tube pumice: Pure and simple. Solid Earth Discussions, 7(4).

Feigl, K.L., Le Mével, H., Ali, S.T., Cordova, L., Andersen, N.L., DeMets, C., and Singer, B.S., 2014. Rapid uplift in Laguna del Maule volcanic field of the Andean Southern Volcanic Zone (Chile) 2007–2012. Geophysical Journal International, 196, 885–901, doi: 10.1093/gji/ggt438.

Fierstein, J., Postglacial eruptive history established by mapping and tephra stratigraphy provides perspectives on magmatic system beneath Laguna del Maule, Chile, Presented at: AGU Chapman Conference on Merging Geophysical, Petrochronologic, and Modeling Perspectives of Large Silicic Magma Systems, Quinamavida, Chile, 2018.

Gardner, J. E., Wadsworth, F. B., Llewellin, E. W., Watkins, J. M., Coumans, J. P., 2019. Experimental constraints on the textures and origin of obsidian pyroclasts. Bulletin of Volcanology, 81(4), 22.

Gonnermann, H. M., Giachetti, T., Fliedner, C., Nguyen, C. T., Houghton, B. F., Crozier, J. A., Carey, R. J., 2017. Permeability during magma expansion and compaction. Journal of Geophysical Research: Solid Earth, 122(12), 9825-9848.

Gualda, G. A., Ghiorso, M. S., Lemons, R. V., Carley, T. L., 2012. Rhyolite-MELTS: a modified calibration of MELTS optimized for silica-rich, fluid-bearing magmatic systems. Journal of Petrology, 53(5), 875-890.

Hildreth, W., Godoy, E., Fierstein, J., Singer, B.S., 2010. Laguna del Maule volcanic field: eruptive history of a Quaternary basalt to rhyolite distributed volcanic field on the Andean range crest in central Chile. Servicio Nacional de Geología y Minería, Boletin 63.

Ketcham, R.A., Carlson, W.D., 2001. Acquisition, optimization and interpretation of X-ray computed tomographic imagery: applications to the geosciences. Computers & Geosciences 27, 381-400.
Klug, C., Cashman, K., Bacon, C., 2002. Structure and physical characteristics of pumice from the climactic eruption of Mount Mazama (Crater Lake), Oregon. Bulletin of Volcanology 64, 486–501. http://dx.doi.org/10.1007/s00445-002-0230-5.
Le Mével, H., Gregg, P. M., Feigl, K. L., 2016. Magma injection into a long-lived reservoir to explain geodetically measured uplift: Application to the 2007-2014 unrest episode at Laguna del Maule volcanic field, Chile. Journal of Geophysical Research: Solid Earth, 121, 6092–6108. https://doi.org/10.1002/2016JB013066
Miller, C. A., Williams-Jones, G., Fournier, D., Witter, J., 2017. 3D gravity inversion and thermodynamic modelling reveal properties of shallow silicic magma reservoir beneath Laguna del Maule, Chile. Earth and Planetary Science Letters, 459, 14-27.
Nakamura, M., Otaki, K., Takeuchi, S., 2008. Permeability and pore-connectivity variation of pumices from a single pyroclastic flow eruption: implications for partial fragmentation. Journal of Volcanology and Geothermal Research, 176, 302–314. http://dx.doi.org/10.1016/j.jvolgeores.2008.04.011.
Pamukcu, A. S., Gualda, G. A., 2010. Quantitative 3D petrography using X-ray tomography 2: Combining information at various resolutions. Geosphere, 6(6), 775-781.
Polacci, M., Papale, P., Rosi, M., 2001. Textural heterogeneities in pumices from the climactic eruption of Mount Pinatubo, 15 June 1991, and implications for magma ascent dynamics. Bulletin of Volcanology 63, 83-97.
Rust, A.C., Cashman, K.V., 2004. Permeability of vesicular silicic magma: inertial and hysteresis effects. Earth and Planetary Science Letters, 228, 93-107.
Rust, A. C., Cashman, K. V., 2007. Multiple origins of obsidian pyroclasts and implications for changes in the dynamics of the 1300 BP eruption of Newberry Volcano, USA. Bulletin of Volcanology, 69(8), 825-845.
Schipper, C. I., Castro, J. M., Tuffen, H., James, M. R., How, P., 2013. Shallow vent architecture during hybrid explosive–effusive activity at Cordón Caulle (Chile, 2011–12): evidence from direct observations and pyroclast textures. Journal of Volcanology and Geothermal Research, 262, 25-37.
Singer, B. S., Andersen, N. L., Le Mevel, H. et al., 2014. Dynamics of a large, restless, rhyolitic magma system at Laguna del Maule, southern Andes, Chile. GSA Today 24, 4–10.
Singer, B., Hildreth, W., Vincze, Y., 2000. 40Ar/39Ar evidence for early deglaciation of the central Chilean Andes. Geophysical Research Letters, 27(11), 1663-1666.
Toramaru, A., 2006. BND (bubble number density) decompression rate meter for explosive volcanic eruptions. Journal of Volcanology and Geothermal Research 154, 303-316.
Waters, L. E., Lange, R. A., 2015. An updated calibration of the plagioclase-liquid hygrometer-thermometer applicable to basalts through rhyolites. American Mineralogist, 100(10), 2172-2184.
Wespestad, C., Thurber, C. H., Andersen, N. L., Singer, B. S., Cardona, C., Zeng, X., et al., 2019. Magma Body Beneath Laguna del Maule Volcanic Field Imaged with Surface Wave Tomography. Journal of Geophysical Research: Solid Earth, 124. https://doi.org/10.1029/2018JB016485
Wright, H. M., Roberts, J. J., Cashman, K. V,. 2006. Permeability of anisotropic tube pumice: Model calculations and measurements. Geophysical research letters, 33(17).
Zhou, J. Q., Chen, Y. F., Wang, L., Cardenas, M. B., 2019. Universal Relationship Between Viscous and Inertial Permeability of Geologic Porous Media. Geophysical Research Letters, 46(3), 1441-1448.

Appendix A: The tephrostratigraphy of the rhyolite of Laguna del Maule (*rdm*)

This section summarizes observations from fieldwork on the rhyolite of Laguna del Maule (*rdm*) deposits. It was not included in Chapter 2, which concentrates on the Los Espejos (*rle*) sequence, with some comparison to *rdm*.

rdm unit 1: Early pyroclastic deposits

We define two eruptive subunits of the *rdm* unit 1: pyroclastic density currents at the bottom (*rdm* unit 1a) overlaid by an ash fall deposit (*rdm* unit 1b). The *rdm* unit 1a is defined as a sequence of several fine layers with multiple sedimentary structures such as laminar strata, crossbedding and lenses with coarser grains. The pyroclastic deposit is white to yellowish and is mostly composed by fragile low-density pumices with equant to elongated shapes and a broad range of bubble textures. The *rdm* unit 1b is a massive matrix supported ash fall deposit that consists of low-density pumices and lithics like the underlying *rdm* unit 1a; the deposits are yellowish to brownish due to weathering. Most of the outcrops are found to the N and NW from the possible vent; however, we cannot confirm that this would be the upwind direction of the fall deposit based on the similarities in the stratigraphy descriptions made to the South (S from the Las Nieblas vent) and to the East (near to the international road in Argentina) of the current lake (Judy Fierstein, oral communication). We analyze in detail an outcrop at 10.9 km and N34.9°W from the *rdm* vent, on the west side of the international road, ~7.5 km before arriving at the Chilean customs from Talca (Fig. 2.1a). The outcrop is fresh, and it is easy to observe in ~15 m-long and 7-10 m-high (Fig. 2.2a).

We did not observe the base of the pyroclastic flow; the lower 2 m of the outcrop was covered by talus from the same pyroclastic density current and we did not dig to see where the base is.

The deposit is poorly sorted, and matrix supported; the matrix mostly consists of angular pumices of <2 mm. The clasts consist of >95% of low-density pumices of <30 cm and the others are lithics of <5 cm. In the bottom part (40 cm-thick) of the exposure, the deposit shows laminar layers with inverse grading carrying clasts <3 cm at the top of this section. Above, in concordance with the first section, a 1 m-high cross-bedding section has lenses with coarser grains and a higher fraction of pumices. Within the lenses, the pumices are <30 cm, subelongated and have a variety of bubble textures such as spherical to colloform-shaped, banded with several planes and tubular. In the layers forming crossbedding, there is a higher fraction of <2 cm angular and elongated lithics, and angular and equant pumices. Most of the clasts are oriented parallel to the stratification. Above, in angular unconformity with the cross-bedding section, there is a ~1.5 m-high laminar parallel multilayered section, that consists of rhythmic inverse and normal grading matrix supported layers. The layers consist of low-density pumices and some lithics; the biggest pumices are mostly reticulated, and the lithics are elongated and rounded of several colors (Fig. 2.3). The top is in concordance with a more competent ash fall deposit of similar componentry (Fig. 2.2a).

At the location examined, the fall deposit is ~1.5 m thick, massive, well sorted, matrix supported, and mostly composed by lapilli-size low-density pumices (Fig. 2.3). Despite a slight normal grading, we could not determine layers of a distinctive mean grain size. The biggest clasts are pumices of <10 cm and lithics of <3 cm; most of the pumices are elongated with tubular bubbles.

rdm unit 2: Late pyroclastic deposits

We define two eruptive subunits of the *rdm* unit 2: several pyroclastic density currents (*rdm* unit 2a) overlaid by a fall deposit (*rdm* unit 2b). The pyroclastic deposits of the *rdm* unit 2 can

be recognized from the *rdm* 1 deposits due to their componentry: denser and less alkaline pumices (Table 2.1), mafic enclaves within some pumices, mafic vesiculated clasts, and granitoid lithics. The PDCs of the *rdm* unit 2a go to multiple directions and their outcrops are found in the north shoreline of the lake towards NE valleys, near to the international road towards the NE, in the eastern shoreline of the lake near and beyond the Divisoria lava flow, and in the south underlying deposits of Cerro Barrancas and Las Nieblas (Fierstein, 2018; Hildreth et al., 2010). The fall deposit of the *rdm* unit 2b is exposed to the east and shows several layers defined by variations of grain size and the fraction of the mafic vesiculated clasts. We analyze in detail some outcrops in a traverse across a NE paleovalley in the north shoreline of the lake and in a stratigraphic station at 3 km east from the east shoreline of the lake and 7 km S72°E from the possible vent (Fig. 2.1c).

One of the pyroclastic flows is exposed around tens of meters in a beach at the north shoreline of the lake. We could not observe the base, but lake sediments would be expected. Reworking by gravity and slight weathering affects ~10 cm in the surface. The deposit is clast supported, very poorly sorted and has a subtle inverse grading. The biggest clasts are ~8 cm to ~2 cm from the base to the top. Several layers can be defined by variations of grain size and angular unconformities. The fractions of vesiculated mafic clasts and granitoids decrease with the deposit height. At the top, poorly sorted and clast supported laminar strata layers have subequant pumices (Fig. 2.3).

Some kilometers to the north through the same paleovalley, a 35 cm-thick section of the *rdm* 2 fall deposit is found in angular disconformity with the pyroclastic flow. This section of the *rdm* 2b consists of three matrix-supported layers defined by abrupt changes in grain size and componentry. The upper and lower layers have mid-density subequant pumices up to 2 cm and mafic vesiculated lithics of <1 cm. The intermediate layer is a matrix supported fine-grained

layer which mostly consists of pumices. This section of the *rdm* 2 fall deposit shows a higher volume fraction of pumices compared to the pyroclastic flow and is overlaid by a 3-cm thick of oxidized soil, followed by the *rle* unit 2 in erosive and angular unconformity (Fig. 2.2c and 2.3). Because of the position of this stratigraphic section relative to the vent, the smaller grain sizes and the contact with soil and the *rle* fall deposit, we consider that the section described above corresponds to the top of the fall deposit, downwind to the deposit extension.

Below I describe a 2.6 m-high of the *rdm* fall deposit in the eastern shoreline of the lake (Fig. 2.1c and 2.2b). We could not observe the base because of a high degree of weathering that transform the pumices in clay; the top (first ~20 cm from the floor level) is reworked by gravity and partially altered by weathering, whilst the rest of the deposit is fresh. The deposit is well sorted, and clast-supported with grains of <40 cm; the clasts consist of elongated mid-density pumices with tubular bubbles that can include some mafic enclaves, subelongated high-density pumices, olivine-bearing vesiculated mafic andesites, hornblende-bearing vesiculated andesites, and granitoid lithics. Here we define seven layers by transitional changes of grain size and componentry (Fig. 2.3). The layers with coarser grains (<40 cm) show a higher volume fraction of pumices and normal grading; in contrast, the layers with finer grains show pumices of <10 cm and no grading.

Appendix B: Procedure to simulate viscous permeability and visualization of velocity and pressure fields by APES in AVIZO Lite

The following section present the preparation of the 3D images acquired by X-ray tomography to simulate viscous permeabilities and to visualize velocity and pressure fields. I show this through the 2D images of: 1. The first volume of interest from the reconstructed tomogram; 2. After the application of an iterative median filter; 3. A binomial image after segmentation by gray-scale thresholding; 4. A binomial image after separation of isolated bubbles; 5. Pressure field after the simulation of air flowing through the porous media; 6. 3D image of flow pathways from the same perspective of the previous 2D images

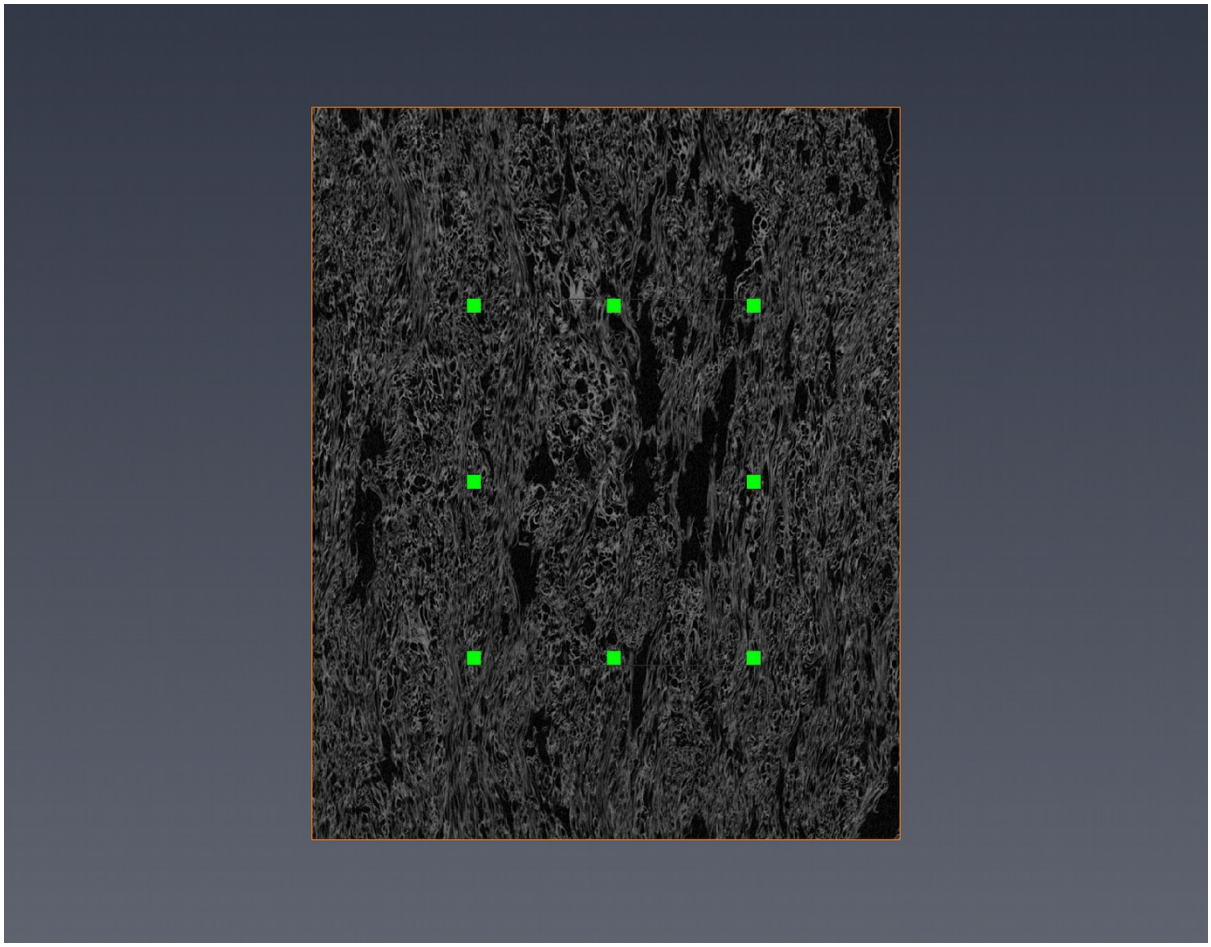

Fig. A1: First volume of interest (VOI) acquired from the original reconstructed tomogram. The first VOI is selected to delete background and areas affected by beam hardening and other artifacts. The green box is the selected VOI for the permeability simulation.

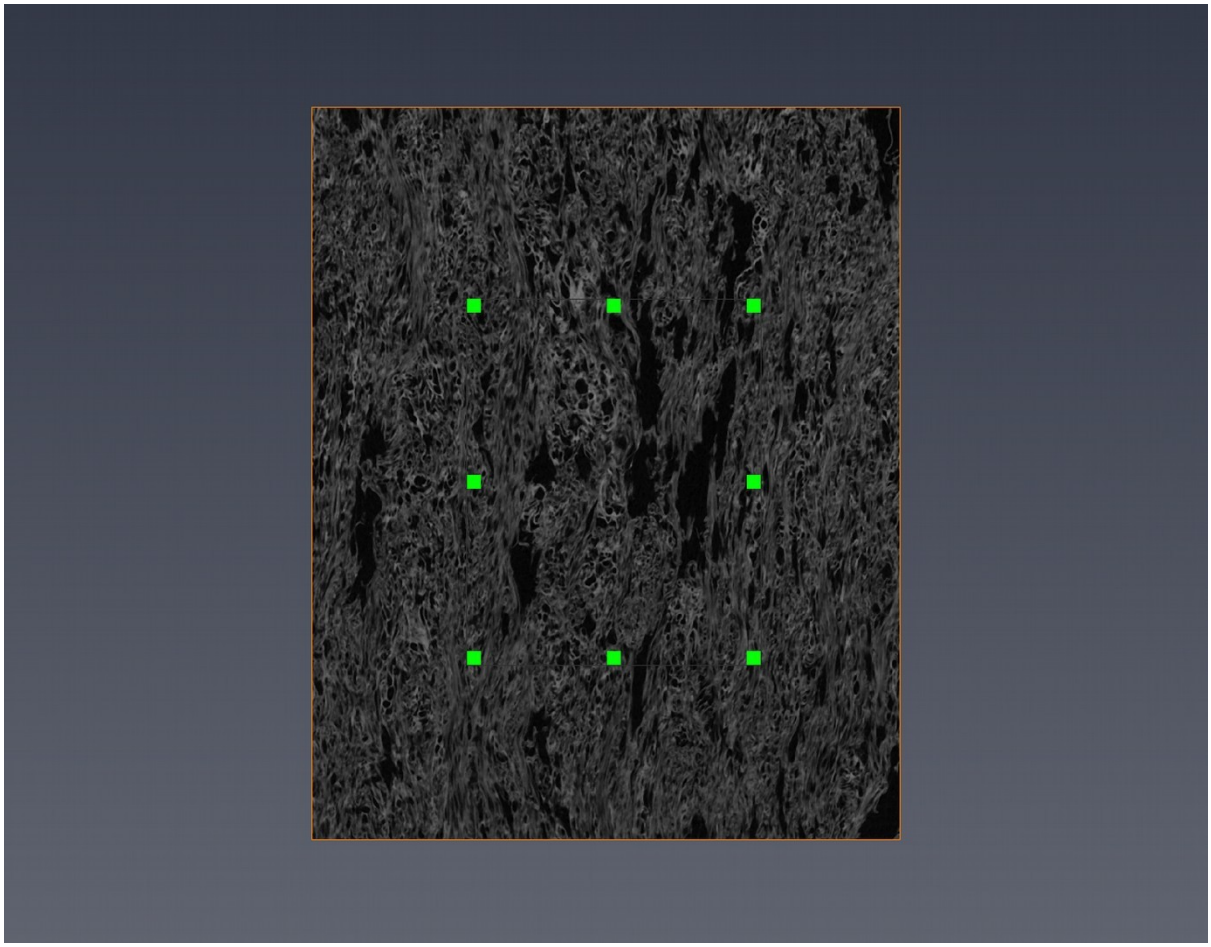

Fig. A2: Visualization of the tomogram after the application of median filter. Because of the signal-to-noise ratio of the original tomogram was high, I applied only one iteration of the median filter for this sample. As there are several small bubbles in this sample, the median filter was applied for a neighborhood of 6 voxels (the other available options are 18 and 26 voxels).

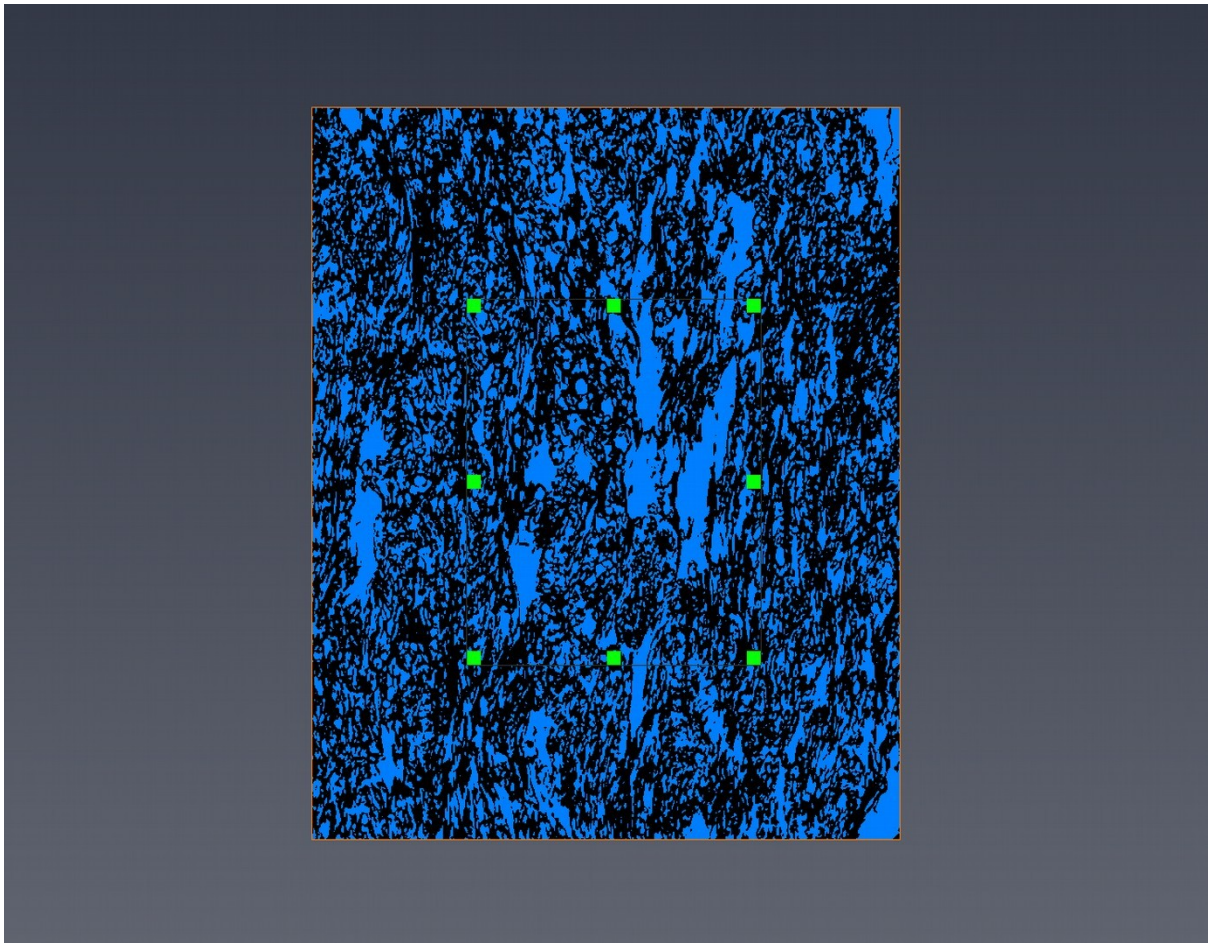

Fig. A3: Binomial image after segmentation by gray-scale thresholding. A gray-scale range was selected to separate the bubbles (the darker pixels in the filtered image) from groundmass glass and crystals. The selected bubble area fraction was compared to the measured porosity of the sample cylinder (Chapter 3 and 4). Bubbles are in blue and glass is in black.

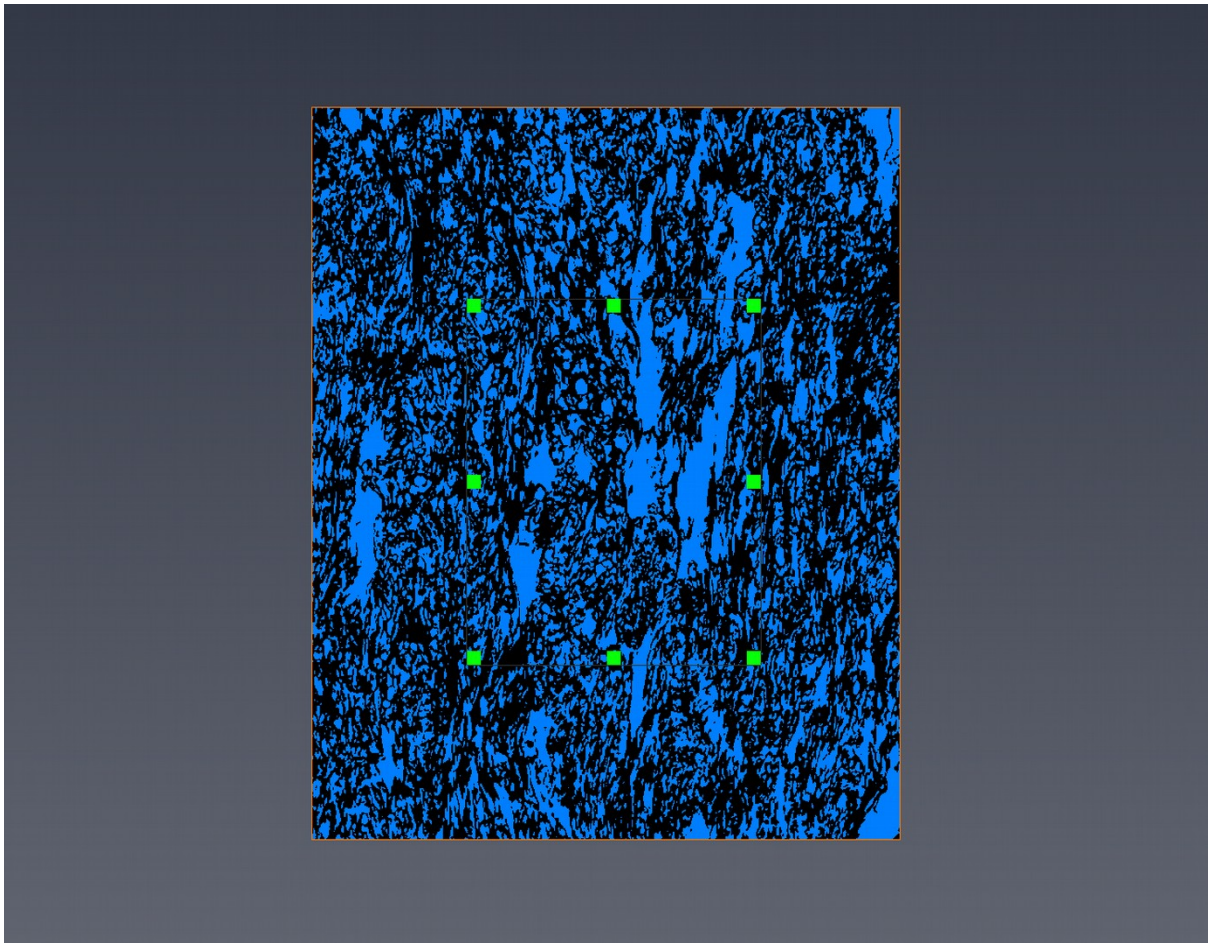

Fig. A4: Binomial image after separation of isolated bubbles. The isolated bubbles are separated by the application of the axis-connectivity script in AVIZO Lite. In this case, various small flattened bubbles in Fig. A3 were deleted in this image. Connected bubbles are in blue and glass and isolated bubbles are in black.

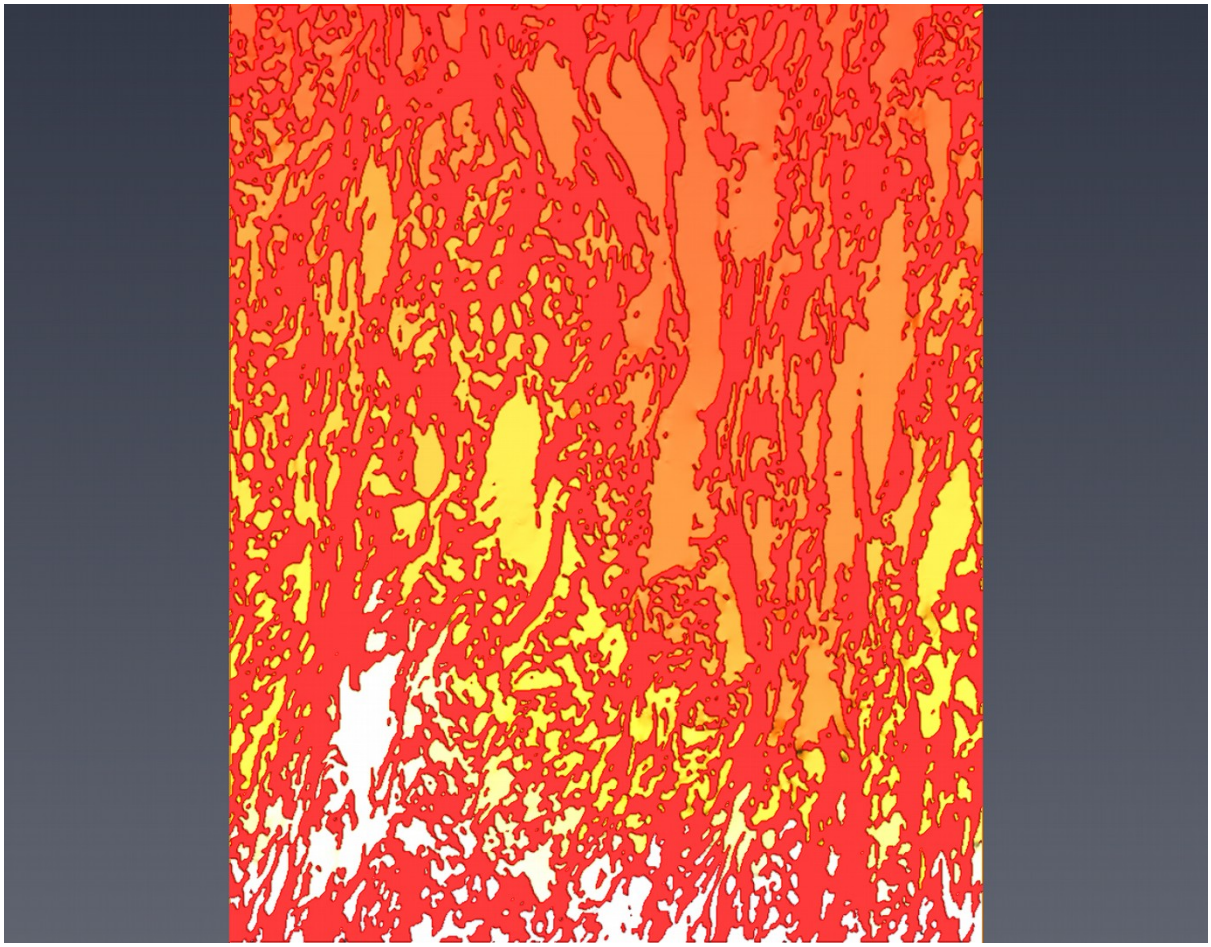

Fig. A5: 2D slice of the pressure field obtained after the simulation of air flowing through the porous media of the scanned pumice. The flow goes downward. The input conditions were P_0 = 130 kPa (red), P_f = 101.3 kPa (white) and a dynamic viscosity = 1.8 x 10^{-5} Pa s in order to emulate the conditions of permeability measurements in the laboratory. The simulation was applied within the green box of the images above. By default, AVIZO Lite paint in red (the color of the highest pressure) the glass and isolated bubbles.

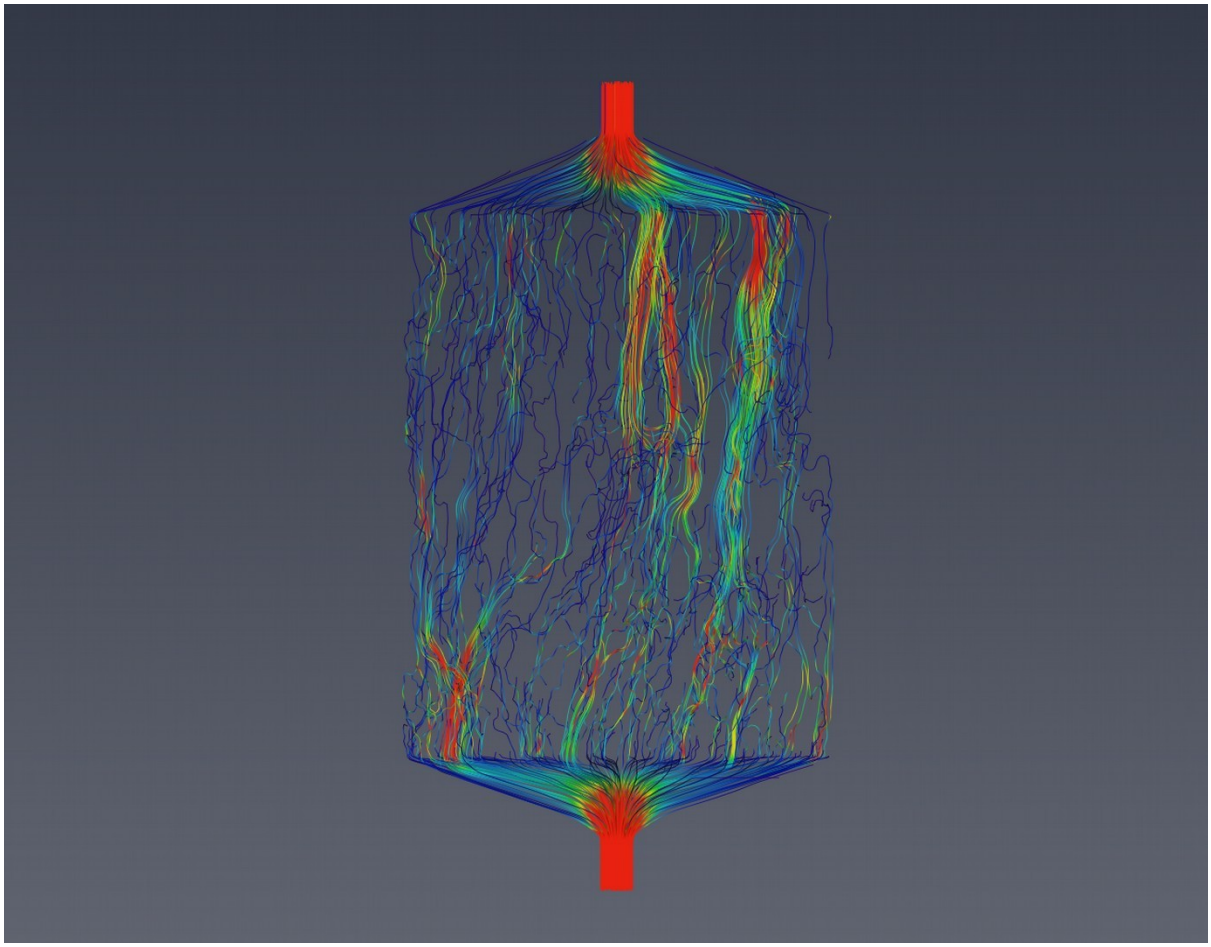

Fig. A6: 3D image of the velocity field obtained by the permeability simulations. The perspective is the same to the 2D images above. Red lines correspond to high velocities and blue lines correspond to the lowest velocities within the selected velocity range. Thus, even slower velocities are not displayed in this image. See Chapter 4 for details of the permeability simulations and visualization of the velocity fields.

Appendix C: Analytical and thermodynamic methods

Conditions in the microprobe

Compositional analyses of minerals and glasses were performed on the Cameca SX100 electron microprobe at University of Bristol by applying an accelerating potential of 20 keV. 479 spots in biotite, 27 spots in hornblende and 440 spots in glasses were measured for characterization and the application of numerical thermodynamics methods. To analyze mafic hydrous minerals and volcanic glasses, an electron defocused (5 μm) beam current of 4 nA was used to avoid alkali loss. In the case of biotite, 15-30 μm-spacing compositional traverses were analyzed by applying dual conditions for trace elements. Ti, Sr and Ba were measured with an electron beam current of 40 nA after measuring major elements. 929 spots in plagioclase and 47 spots in k-feldspars were analyzed by an electron defocused (5 μm) beam current of 10 nA to avoid alkali loss. In the case of plagioclase, 575 spots for 15-30 μm-spacing compositional traverses were analyzed by applying dual conditions for trace elements. Fe, Mg, Ti, Sr and Ba were measured with an electron beam current of 40 nA after measuring major elements. Mg and Ti were always below detection limit and are not reported. Counting times for major elements were 20 s (10 s on peak and 10 s on background), 60 s for minor elements (30 s on peak and 30 s on background) and 120 s for trace elements (60 s on peak and 60 s on background).

The Bt-glass geothermobarometer

The Ti in biotite-glass geothermometer of Righter and Carmichael (1996) was applied to 156 and 49 biotite rims of Los Espejos eruptive products (pumices, pyroclastic obsidians and lavas) and Las Nieblas pumices, respectively. The temperature data form unimodal symmetrical distributions with a peak at 855-860 °C and an average of 866 ± 10 °C for Los Espejos and a

peak at 885-890 °C and an average of 887 ± 7 °C for Las Nieblas. The propagated error was calculated based on the analytical errors of TiO_2 measurements in both biotites and glasses. In Los Espejos products, the standard deviation is lower than the calculated propagated error (~17 °C); whilst, in Las Nieblas, the statistical standard deviation matches with the calculated propagated error (~9 °C). The Ba in biotite-glass geobarometer of Righter and Carmichael (1996) was applied; however, it estimates several negative pressures with high error associated (>4 kbar).